

**Atomic Study of Defects in Two-Dimensional  
Transition Metal Chalcogenides Using Electron  
Microscopy**

Jun Chen

Supervised by Professor Jamie H. Warner



*Submitted in conformity with the requirements  
for the degree of DPhil in Materials Science*

Department of Materials

Oriel College

University of Oxford

November 2020

Copyright © 2020 by Jun Chen

## **Declaration**

The material contained within this thesis has not previously been submitted for a degree at the University of Oxford or any other university. The research reported within this thesis has been conducted by the author unless indicated otherwise.

## **Copyright Notice**

The copyright of this thesis rests with the author. No quotation from it should be published without the prior written consent of the author, and any information derived from it should be acknowledged.

## Abstract

Two-dimensional (2D) transition metal dichalcogenides (TMDs) are layered semiconductors with unique electronic and optical properties which have shown immense potential in ultrathin (opto-)electronic devices.<sup>1-3</sup> Structural defects that are ubiquitous in 2D materials have demonstrated to exert significant impacts on the materials' properties.<sup>4-6</sup> The in-depth comprehension of structural defects at the atomic level is vital for the rational exploration of their exceptional properties, which is the objective of my DPhil project.

By conducting advanced scanning transmission electron microscopy (STEM), this project resolves the structures and dynamics of defects with the atomic-scale clarity in 2D TMDs of different phases, and the use of *in-situ* heating holder in the STEM enables the direct visualization structural dynamics at elevated temperatures. The first part focuses on the grain boundary (GB)-involved defective structures in the typical 2H-phase MoS<sub>2</sub>/WS<sub>2</sub> monolayers/bilayers at the thermal condition. For the monolayers, the high-temperature mechanism is elucidated for the dynamics of 60° GB-coupled large inversion domains. In the bilayers, the existence of dual localized GBs is demonstrated with high-temperature stability. This co-localization causes one layer to adopt novel dislocation cores, not found in monolayers, due to van der Waals strain of maintaining 2H and 3R interlayer stacking either side. Then, the defects and GB structures in TMDs of another significant phase, 1T phase, are also investigated systematically, taking the emerging 1T-PtSe<sub>2</sub> as the study object. The atomic structures and dynamics of point vacancies, 1D defects, GBs and dislocations exhibit distinct "1T-feature" that differs from those found in 2H-phase MoS<sub>2</sub>/WS<sub>2</sub>.

Apart from imaging the intrinsic defects, this project also explores the controlled *in-situ* structural modification methods by manipulating focused electron beam and the heating conditions in STEM with atomic-resolution monitoring of the process. The precise

controllability is demonstrated in intentionally patterning 2D nanowell arrays at bilayer WS<sub>2</sub> in terms of shapes, depth and locations, using the combination of convergent beam and the high temperature. Besides, the phase transformation is triggered by the controlled *in-situ* heating process for promoting Se loss from few-layered PdSe<sub>2</sub>, obtaining the novel phase 2D Pd<sub>2</sub>Se<sub>3</sub> monolayers. The structural defects and their beam-driven behaviours in Pd<sub>2</sub>Se<sub>3</sub> are visualized, which are sharply distinguished from those in the conventional TMDs.

## Acknowledgement

Accomplishing this doctorate project would not have been possible without the support, advice and encouragement from my supervisor, colleagues, families and friends. First of all, I would like to express my sincere gratitude to my supervisor, Prof. Jamie Warner, for offering me patient guidance and generous help throughout my 3-year study at Oxford. I have learned from him the knowledge and skills in the field of microscopy and 2D materials, as well as the passion and rigorous attitude towards science, which are all priceless and will exert profound and positive influence on my whole research career in the future.

I would thank my fellow colleagues and collaborators who have greatly supported me on my research. I would like to deliver my appreciation to Prof. Angus Kirkland, Dr. Christopher Allen at Diamond Light source and Dr. Neil Young, Dr. Ian Griffiths at University of Oxford for their kind support on the TEM access and the expertise in training me on TEM skills of ARM 300F and ARM 200F as well; to Dr. Gyeong Hee Ryu and Dr. Jakyung Lee who have been constantly genial and supportive to assist with the TEM operating skills and data analysis methods; to my colleagues Dr. Wenshuo Xu, Dr. Yingqiu Zhou, Dr. Sha Li, Dr. Ren-Jie Chang, Mr. Si Zhou, Ms. Yi Wen, Ms. Qianyang Zhang, Ms. Linlin Hou, Mr. Yang Lu, Ms. Sapna Sinha, Mr. Kuo-Lun Tai and Mr. Peng Tang for providing generous assistance and suggestions; and to Dr. Gang Seob Jung and Prof. Markus J. Buehler at Massachusetts Institute of Technology for their significant contributions on performing theoretical calculations which have been crucial for resolving the bilayer grain boundaries.

I would give my special thanks to my parents for their love and moral support all the time, and my beloved husband, Mr. Weixin Song, for his precious companionship and encouragement to me.

Finally, I am very thankful to China Scholarship Council (CSC) for providing me with a full scholarship to cover my tuition fee and living expenses over the 3 years.

## Publications

This section lists the published works and those close to submission during the course of this doctorate project. Specific publications are labelled for which chapter relates to which of the papers. The supporting information of Chapters 4-7 are provided in the Appendix A-D, respectively.

### Chapter 4

1. **Chen, J.**; Zhou, S.; Wen, Y.; Ryu, G. H.; Allen, C.; Lu, Y.; Kirkland, A. I.; Warner, J. H. *In Situ* High Temperature Atomic Level Dynamics of Large Inversion Domain Formations in Monolayer MoS<sub>2</sub>. *Nanoscale* **2019**, *11*, 1901-1913.
2. **Chen, J.**; Jung, G. S.; Ryu, G. H.; Chang, R.-J.; Zhou, S.; Wen, Y.; Buehler, M. J.; Warner, J. H. Atomically Sharp Dual Grain Boundaries in 2D WS<sub>2</sub> Bilayers. *Small* **2019**, 1902590.

### Chapter 5

3. **Chen, J.**; Ryu, G. H.; Zhang, Q.; Wen, Y.; Tai, K.-L.; Lu, Y.; Warner, J. H. Spatially Controlled Fabrication and Mechanisms of Atomically Thin Nanowell Patterns in Bilayer WS<sub>2</sub> Using *in Situ* High Temperature Electron Microscopy. *ACS Nano* **2019**, *13*, 14486-14499.

### Chapter 6

4. **Chen, J.**; Xu, W.; Wen, Y.; Warner, J. H. Atomic-Level Dynamics of Point Vacancies and the Stretched Defects in 2D Monolayer PtSe<sub>2</sub>. *About to submit*.
5. **Chen, J.**; Wen, Y.; Xu, W.; Ryu, G. H.; Warner, J. H. Dislocations and Grain Boundaries in Two-Dimensional PtSe<sub>2</sub>. *About to submit*.

*Note: This chapter is being expended with additional pending theoretical calculations by density functional theory (DFT) and molecular dynamics (MD) simulations.*

## Chapter 7

6. **Chen, J.**; Ryu, G. H.; Sinha, S.; Warner, J. H. Atomic Structure and Dynamics of Defects and Grain Boundaries in 2D Pd<sub>2</sub>Se<sub>3</sub> Monolayers. *ACS Nano* **2019**, *13*, 8256-8264.

### Second-Author

7. Lu, Y.; **Chen, J.**; Chen, T.; Shu, Y.; Chang, R.-J.; Sheng, Y.; Shautsova, V.; Mkhize, N.; Holdway, P.; Bhaskaran, H.; Warner, J. H. Controlling Defects in Continuous 2D GaS Films for High-Performance Wavelength-Tunable UV-Discriminating Photodetectors. *Adv. Mater.* **2020**, *32*, 1906958.
8. Tai, K.-L.; **Chen, J.**; Wen, Y.; Park, H.; Zhang, Q.; Lu, Y.; Chang, R.-J.; Tang, P.; Allen, C. S.; Wu, W.-W.; Warner, J. H. Phase Variations and Layer Epitaxy of 2D PdSe<sub>2</sub> Grown on 2D Monolayers by Direct Selenization of Molecular Pd Precursors. *ACS Nano* **2020**, *14*, 11677-11690.
9. Ryu, G. H.; **Chen, J.**; Wen, Y.; Warner, J. H. *In-Situ* Atomic-Scale Dynamics of Thermally Driven Phase Transition of 2D Few-Layered 1T PtSe<sub>2</sub> into Ultrathin 2D Nonlayered PtSe Crystals. *Chem. Mater.* **2019**, *31*, 9895-9903.
10. Ryu, G. H.; **Chen, J.**; Wen, Y.; Zhou, S.; Chang, R.-J.; Warner, J. H. Atomic Structural Catalogue of Defects and Vertical Stacking in 2H/3R Mixed Polytype Multilayer WS<sub>2</sub> Pyramids. *Nanoscale* **2019**, *11*, 10859-10871.
11. Zhou, S.; **Chen, J.**; Warner, J. H. *In Situ* Atomic Level Studies of Thermally Controlled Interlayer Stacking Shifts in 2D Transition Metal Dichalcogenide Bilayers. *J. Mater. Res.* **2020**, *35*, 1407-1416.

## Co-Author

12. Ryu, G. H.; Zhu, T.; **Chen, J.**; Sinha, S.; Shautsova, V.; Grossman, J. C.; Warner, J. H. Striated 2D Lattice with Sub-nm 1D Etch Channels by Controlled Thermally Induced Phase Transformations of PdSe<sub>2</sub>. *Adv. Mater.* **2019**, 1904251.
13. Chen, E.; Xu, W.; **Chen, J.**; Warner, J. H. 2D Layered Noble Metal Dichalcogenides (Pt, Pd, Se, S) for Electronics and Energy Applications. *Materials Today Advances* **2020**, 7, 100076.
14. Wen, Y.; Ophus, C.; Allen, C. S.; Fang, S.; **Chen, J.**; Kaxiras, E.; Kirkland, A. I.; Warner, J. H. Simultaneous Identification of Low and High Atomic Number Atoms in Monolayer 2D Materials Using 4D Scanning Transmission Electron Microscopy. *Nano Lett.* **2019**, 19, 6482-6491.
15. Chen, Q.; Li, H.; Zhou, S.; Xu, W.; **Chen, J.**; Sawada, H.; Allen, C. S.; Kirkland, A. I.; Grossman, J. C.; Warner, J. H. Ultralong 1D Vacancy Channels for Rapid Atomic Migration During 2D Void Formation in Monolayer MoS<sub>2</sub>. *ACS Nano* **2018**, 12, 7721-7730.
16. Chang, R.-J.; Sheng, Y.; Ryu, G. H.; Mkhize, N.; Chen, T.; Lu, Y.; **Chen, J.**; Lee, J. K.; Bhaskaran, H.; Warner, J. H. Postgrowth Substitutional Tin Doping of 2D WS<sub>2</sub> Crystals Using Chemical Vapor Deposition. *ACS Appl. Mater. Interfaces* **2019**, 11, 24279-24288.
17. Tai, K.-L.; Huang, C.-W.; Cai, R.-F.; Huang, G.-M.; Tseng, Y.-T.; **Chen, J.**; Wu, W.-W. Atomic-Scale Fabrication of In-Plane Heterojunctions of Few-Layer MoS<sub>2</sub> *via in Situ* Scanning Transmission Electron Microscopy. *Small* **2020**, 16, 1905516.



# Table of Contents

## Chapter 1

|                                    |          |
|------------------------------------|----------|
| <b>Introduction .....</b>          | <b>1</b> |
| 1.1 Project Aims .....             | 1        |
| 1.2 The Scope of This Thesis ..... | 1        |

## Chapter 2

|   |          |
|---|----------|
| <b>Literature Review .....</b>  | <b>4</b> |
| 2.1 Introduction .....  | 4        |
| 2.1.1 An Overview of Two-Dimensional Materials.....                     | 4        |
| 2.1.2 Atomic-Resolution Microscopy Imaging Technology.....              | 6        |
| 2.1.3 Motivation for Investigating Defects in 2D Materials .....        | 7        |
| 2.2 Structures and Properties of TMDs.....                              | 8        |
| 2.3 Intrinsic Defects in TMDs.....                                      | 12       |
| 2.3.1 Point Defects .....   | 13       |
| 2.3.2 One-Dimensional Defects.....                                      | 17       |
| 2.3.3 Grain Boundaries and Dislocations .....                           | 19       |
| 2.3.4 Edge Terminations .....   | 23       |
| 2.4 <i>In-Situ</i> Structural Modifications of 2D TMDs in TEM .....     | 26       |
| 2.4.1 Electron Beam Induced Structural Change .....                     | 26       |
| 2.4.2 Thermally Controlled Modification by <i>In-Situ</i> Heating ..... | 36       |
| 2.5 Conclusion .....  | 39       |

## Chapter 3

|   |           |
|---|-----------|
| <b>Methodology.....</b>   | <b>42</b> |
| 3.1 Introduction .....  | 42        |
| 3.2 CVD Synthesis of TMDs .....   | 42        |
| 3.2.1 CVD Growth of Monolayer MoS <sub>2</sub> Films.....               | 42        |
| 3.2.2 CVD Growth of Monolayer/bilayer WS <sub>2</sub> films.....        | 44        |
| 3.2.3 Synthesis of PtSe <sub>2</sub> films by Pt Selenization .....     | 44        |
| 3.3 Transfer of TMDs.....   | 45        |
| 3.4 Optical Microscopy and Scanning Electron Microscopy .....           | 46        |
| 3.5 Transmission Electron Microscopy.....                               | 47        |
| 3.5.1 Annular Dark Field-Scanning Transmission Electron Microscopy..... | 47        |
| 3.5.2 <i>In-Situ</i> Heating Technique .....                            | 53        |
| 3.5.3 <i>In-Situ</i> Electron Beam Patterning.....                      | 54        |
| 3.6 Data Analysis and Simulation .....                                  | 55        |

|   |            |
|---|------------|
| 3.6.1 Image Processing and Simulation .....   | 55         |
| 3.6.2 Strain Analysis .....   | 57         |
| 3.6.3 DFT and MD Calculations .....   | 58         |
| <b>Chapter 4</b>  |            |
| <b>Grain Boundaries Involved Defects in MoS<sub>2</sub>/WS<sub>2</sub> Monolayer/Bilayers .....</b>   | <b>61</b>  |
| 4.1 60° Grain Boundary Inversion Domains in Monolayer MoS <sub>2</sub> .....                          | 61         |
| 4.1.1 Introduction .....  | 61         |
| 4.1.2 Results and Discussion .....  | 63         |
| 4.1.3 Conclusion .....  | 76         |
| 4.2 Atomically Sharp Tilt Grain Boundaries in Bilayer WS <sub>2</sub> .....                           | 77         |
| 4.2.1 Introduction .....  | 77         |
| 4.2.2 Results and Discussion .....  | 78         |
| 4.2.3 Conclusion .....  | 93         |
| <b>Chapter 5</b>  |            |
| <b>Atomically Thin Nanowell Patterns in Bilayer WS<sub>2</sub> .....</b>                              | <b>94</b>  |
| 5.1 Introduction .....  | 94         |
| 5.2 Results and Discussion .....  | 96         |
| 5.2.1 Spatially Controlled Fabrication of Nanowell Patterns .....                                     | 96         |
| 5.2.2 Atomic Structures and Mechanisms of Nanowells .....   | 100        |
| 5.3 Conclusion .....  | 112        |
| <b>Chapter 6</b>  |            |
| <b>Defects and Grain Boundaries in 1T-Phase PtSe<sub>2</sub> .....</b>                                | <b>113</b> |
| 6.1 Introduction .....  | 113        |
| 6.2 Results and Discussion .....  | 115        |
| 6.2.1 Atomic Structures and Dynamics of Point Vacancies .....   | 115        |
| 6.2.2 1D Stretched Defect Structures and Kinetics .....   | 119        |
| 6.2.3 Dislocations and Grain Boundaries .....   | 124        |
| 6.3 Conclusion .....  | 133        |
| <b>Chapter 7</b>  |            |
| <b>Defects and Grain Boundaries in Thermally-Driven Pd<sub>2</sub>Se<sub>3</sub> Monolayers .....</b> | <b>135</b> |
| 7.1 Introduction .....  | 135        |
| 7.2 Results and Discussion .....  | 137        |
| 7.2.1 <i>In-Situ</i> High-Temperature Formation of Pd <sub>2</sub> Se <sub>3</sub> Monolayers .....   | 137        |
| 7.2.2 Atomic Structures and Dynamics of Point and 1D Defects .....                                    | 140        |
| 7.2.3 Atomic Structures and Dynamics of Grain Boundaries .....  | 144        |
| 7.3 Conclusion .....  | 151        |
| <b>Chapter 8</b>  |            |

|   |            |
|---|------------|
| <b>Conclusion and Outlook.....</b>                          | <b>153</b> |
| 8.1 Conclusion .....  | 153        |
| 8.2 Future Outlook .....                                    | 156        |
| <b>Appendix A Supporting Information of Chapter 4 .....</b> | <b>158</b> |
| <b>Appendix B Supporting Information of Chapter 5 .....</b> | <b>174</b> |
| <b>Appendix C Supporting Information of Chapter 6 .....</b> | <b>178</b> |
| <b>Appendix D Supporting Information of Chapter 7 .....</b> | <b>190</b> |
| <b>References.....</b>                                      | <b>193</b> |

# Chapter 1

## Introduction

### 1.1 Project Aims

This doctorate project is aimed at establishing atomic-scale understanding of the configurations and dynamics of the defective structures in 2D transition metal chalcogenides (TMDs), including the point defects, linear defects and grain boundaries (GBs) in the monolayered/bilayered 2H-phase MoS<sub>2</sub>/WS<sub>2</sub>, 1T-phase PtSe<sub>2</sub>, and the novel phase Pd<sub>2</sub>Se<sub>3</sub>, with particular interest in the *in-situ* structural modification and material phases by manipulating focused electron beam and high-temperature annealing.

### 1.2 The Scope of This Thesis

This thesis covers my DPhil research on over the past 3 years at the Department of Materials and Oriel College, University of Oxford. It begins with a literature review in Chapter 2 that summarizes the recent progress on the structural study of 2D TMDs, focusing on the intrinsic defects and the *in-situ* structural modification in TEM. It also gives a brief overview of the properties of 2D materials and the development of transmission electron microscopy technique (TEM). This is followed by the introduction of the methodologies in Chapter 3, comprising the CVD method for monolayer/bilayer TMD growth, TEM sample preparation, *in-situ* heating and beam patterning procedures, materials characterization techniques as well as the typical data analysis methods.

My research focuses on the defective study in 2D TMDs, employing the ADF-STEM imaging at JEOL ARM-200F and ARM-300CF. In Chapter 4, I started with the atomic-scale study of the grain boundary (GB), which is one of the most significant defective

structures, in two typical hexagonal phase TMDs, MoS<sub>2</sub> and WS<sub>2</sub>. This includes two special types of GBs, the 60° inversion domain GBs in monolayers and the tilt-angle dual GBs in bilayers. The first topic emphasized on the high-temperature formation and evolution of the 60° inversion domain enabled by the atomic-resolution (S)TEM equipped with an *in-situ* heating stage, and the latter was targeted at demonstrating the existence of atomically sharp dual GBs in bilayer TMD systems which were stable even heated to high temperature of at least 700°C. Efforts were put onto solving their exact atomic structures and understanding the growth mechanisms.

In Chapter 5, I moved forward to develop the *in-situ* patterning technique at the atomic scale in STEM by manipulating the electron beam as a drilling tool in addition to making use of its imaging function in STEM. This work focused on the precise and controlled production of atomically thin nanowells in bilayer WS<sub>2</sub>. The *in-situ* observation at the atomic scale unveiled the exact structures of the fabricated nanowells and the drilling mechanisms.

The research then switched focus on understanding the defective structures in other phase noble metal 2D TMDs which are less studied but are very important members in the 2D materials family, including 1T-phase PtSe<sub>2</sub> and the novel phase Pd<sub>2</sub>Se<sub>3</sub>. The defect and GB structures of 1T-phase PtSe<sub>2</sub> monolayers were systematically investigated in Chapter 6. I highlighted the featured configurations and behaviours of defects and GBs in the monolayer 1T phase compared to those commonly found in the 2H phase MoS<sub>2</sub>/WS<sub>2</sub>. Their beam-driven dynamics were tracked and analysed. In Chapter 7, a thermally controlled modification method was realized to obtain the new-phase Pd<sub>2</sub>Se<sub>3</sub> monolayers by structural transformation from few-layered PdSe<sub>2</sub> *via in-situ* heating. Then I further explored their point defects, 1D defects and GB configurations and dynamic behaviours at the atomic level.

The final chapter gives a conclusion for the whole thesis and highlights the key achievements for each sub-project. An outlook of potential research directions within the field of structural study of 2D TMD defects is also discussed.

## Chapter 2

### Literature Review

#### 2.1 Introduction

This chapter presents a review of the research on 2D transition metal dichalcogenides (TMDs), with particular attention on the atomic-level studies of defect structures in monolayer/bilayer TMDs, and the *in-situ* structural modification techniques based on transmission electron microscopy (TEM). A brief overview will be introduced on the crystalline structures and properties of 2D materials, as well as the development of TEM for their advanced structural analysis. It will discuss the atomic configurations, beam-driven dynamics and behaviours of different defects, as well as their effects on the material properties of TMDs. Apart from the intrinsic defects, the *in-situ* methods to intentionally introduce defects or structural transformation are also included.

##### 2.1.1 An Overview of Two-Dimensional Materials

Layered materials can present novel physical/chemical properties that are different from their bulk counterparts as they are thinned to their physical limits, in which case they are referred to as the two-dimensional (2D) materials.<sup>7</sup> Since 2004 when graphene was exfoliated for the first time,<sup>8</sup> there has been a dramatic increase in research on a wide spectrum of 2D materials including transition metal dichalcogenides (TMDs, such as MoS<sub>2</sub>/WS<sub>2</sub>) and hexagonal boron-nitride (h-BN), realizing the 2D semiconductors and insulators.<sup>1,9-14</sup> Featuring 2D morphology and ultrathin scale, 2D crystals exhibit unique electronic properties, and therefore hold great promise for advanced electronic applications, like field effect transistors (FETs) and photodetectors.<sup>2,15-19</sup>

Graphene has the 2D-honeycombed structure lattice of carbon atoms with  $sp^2$  hybridization (Figure 2.1a). It has been well-documented to show not only excellent mechanical strength and high transparency,<sup>20-21</sup> but also strong resistance to high temperature.<sup>22</sup> Its 2D crystalline nature with high charge carrier mobility and charge carrier density makes it appropriate for large area transparent conducting electrodes in electronics and photoelectronics. The electronic properties of graphene are unique as it is a zero band gap semiconductor (Figure 2.1b), which ensures its high electron mobility while also makes it challengeable for utilizing graphene in electronic devices (*e.g.* FETs).<sup>15,23</sup> In the last several decades, graphene-based materials have been extensively investigated for a wide application in optical electronics,<sup>16</sup> biological engineering,<sup>24</sup> and energy storage materials.<sup>25-28</sup>

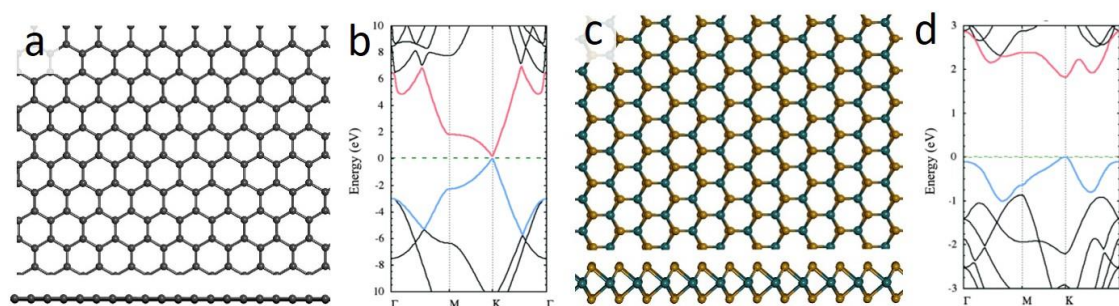


**Figure 2.1** Schematic illustration of crystal structures with atom models and band structures of (a) (b) graphene (top and side view), and (c) (d) MoS<sub>2</sub> (top and side view). (b,d) Reproduced with permission from ref. <sup>29</sup> © 2014 American Chemical Society.

Following graphene, semiconducting TMDs have also drawn surging research attention over the past few years. Their direct or indirect band gaps make them complementary to the zero-bandgap graphene, which show promise in various nanoelectronics.<sup>3,9,30-31</sup> Synthesis of large-area monolayer/bilayer TMD films has been realized by chemical vapour deposition (CVD) techniques,<sup>32-45</sup> enabling the achievement of reliable performances of TMDs-based devices. To be exact, 2D TMD materials are of

three-atom thick. As shown in Figure 2.1c, a layer of transition metal atoms are lying within another two layers of chalcogenide atoms, constituting a whole layer of TMD. Basically, TMDs of monolayer are semi-conductive with direct band gaps of around 1.0-2.0 eV (Figure 2.1d),<sup>2</sup> which means the TMDs can be utilized directly in electronics as transistors and in optics as detectors.<sup>1,46-47</sup> At the same time, tunable, superior and unusual material electronic properties are of high demand in order to realize the versatile applications of 2D materials in next-generation novel electronics. This can be achieved by developing new hybrid materials by combining different types of 2D materials in vertical or lateral stacks, which offers massive possibilities to broaden the versatility of 2D materials.<sup>31,48-54</sup>

### **2.1.2 Atomic-Resolution Microscopy Imaging Technology**

Owing to the ultrathin structural feature, 2D materials are ideal for the characterization of defects at atomic level. One of the powerful characterizing technologies is to use aberration-corrected TEM (AC-TEM), including phase contrast high resolution TEM and STEM. The resolution of TEM is one of the most significant indicators of the technological advancement, which has developed from ~10 nm in 1930s, to sub-nanometre in 1960s, and lately down to even 80 pm in the cutting-edge high-resolution TEM.<sup>55</sup>

Fundamental TEM resolution is limited by the wavelength of electrons which is adjusted by the accelerating voltage. Theoretically, increasing the accelerating voltage can reduce the electron wavelength which leads to higher resolution. At an early stage of the development of TEM technology, higher resolution was pursued by increasing the accelerating voltage with great efforts. In practice, the achievable resolution is normally lower than the theoretical resolution because the electrons are focused in imperfect ways.

These imperfections include spherical aberration ( $C_s$ ), chromatic aberration ( $C_c$ ) and astigmatism. In recent years, the progress in aberration correction and lens system optimization has substantially enhanced the (S)TEM resolving power to achieve sub-Ångstrom resolution without the necessity of increasing to higher voltage.<sup>56-62</sup> In 1998, Haider reported the first aberration-corrected images obtained by a commercial TEM.<sup>63-</sup>  
<sup>64</sup> There has been a significant improvement in resolution with 3rd-order aberration correction, which enabled the first sub-Ångstrom-resolution direct imaging of single gold atoms at 120 keV energy.<sup>65</sup> Greater improvements are achieved with 5th order aberration correction, transcending 0.5 Å at 300 kV accelerating voltage.<sup>66-67</sup> This is nearly reaching the ultimate resolution in modern microscopy techniques, but is more difficult to attain at low accelerating voltage. Even so, the development of 5th order correctors can still enable atomic resolution at low voltage. In 2008, Meyer *et al.* obtained the image of 1 Å resolution at 80 keV.<sup>68</sup> In 2010, single atom substitutions in monolayer h-BN are directly resolved by Krivanek *et al.* at low voltage of 60 kV.<sup>69</sup> With the advancements in aberration correction, the visualization of 2D materials with atomic resolution at a low accelerating voltage has become increasingly accessible. This is significantly crucial to microscopy studies of 2D materials because they are susceptible to the knock-on damage induced by electron beam and hence require TEM to be conducted at the voltages no higher than 80kV. The achievements in modern imaging technologies have opened up extensive exploration of the structural defects in various 2D materials with atomic resolution.

### **2.1.3 Motivation for Investigating Defects in 2D Materials**

2D materials have been offering researchers a fertile ground for harvesting novel properties and versatile applications. The properties of 2D materials are significantly influenced by their specific atomic structures and in particular the lattice imperfections

which are unavoidable in reality as a consequence of the second law of thermodynamics and are especially evident in 2D materials grown using chemical methods due to the imperfections of the growth process. Those defects can occur in the forms of vacancies, grain boundaries, edge terminations, etc, all of which can lead to tunable electronic structures of the materials as the altered coordination of the transition metal atoms of the defects can change the density of electronic states at the Fermi level.<sup>70</sup> Accordingly, the device performances can vary much with the existence of different structural defects. A typical example is that some TMD based devices show n- or p-type behaviour, deviating from what their perfect crystal structures without unsaturated bonds. And the tested typical device mobilities in experiments are below the theoretical values, which are supposed to be associated with the existence of structural defects.<sup>71</sup> Understanding how the materials properties are adjusted by the structural defects requires the atomic insights of the defective structures, which is also significant to the defect engineering of 2D materials for a wider range of applications. Besides, the ability to controllably produce large-area 2D materials is a key aspect to the development of TMDs, and the occurrence of defects during growth plays a significant role in a larger polycrystalline film developed from seed nuclei. The unambiguous knowledge of the atomic defects of the as-grown 2D materials can in turn offer guidance for the designing and optimizing the growth methods. Motivated by these factors, this thesis focuses on the atomic-level investigation defective structures with the help of advanced microscopy imaging techniques.

## **2.2 Structures and Properties of TMDs**

TMDs are often generalized in a formula of  $\text{MX}_2$  with M as a transition metal element and X as a chalcogen (S, Se, Te). They can exist in several crystalline phases derived from different coordination of the M atoms.

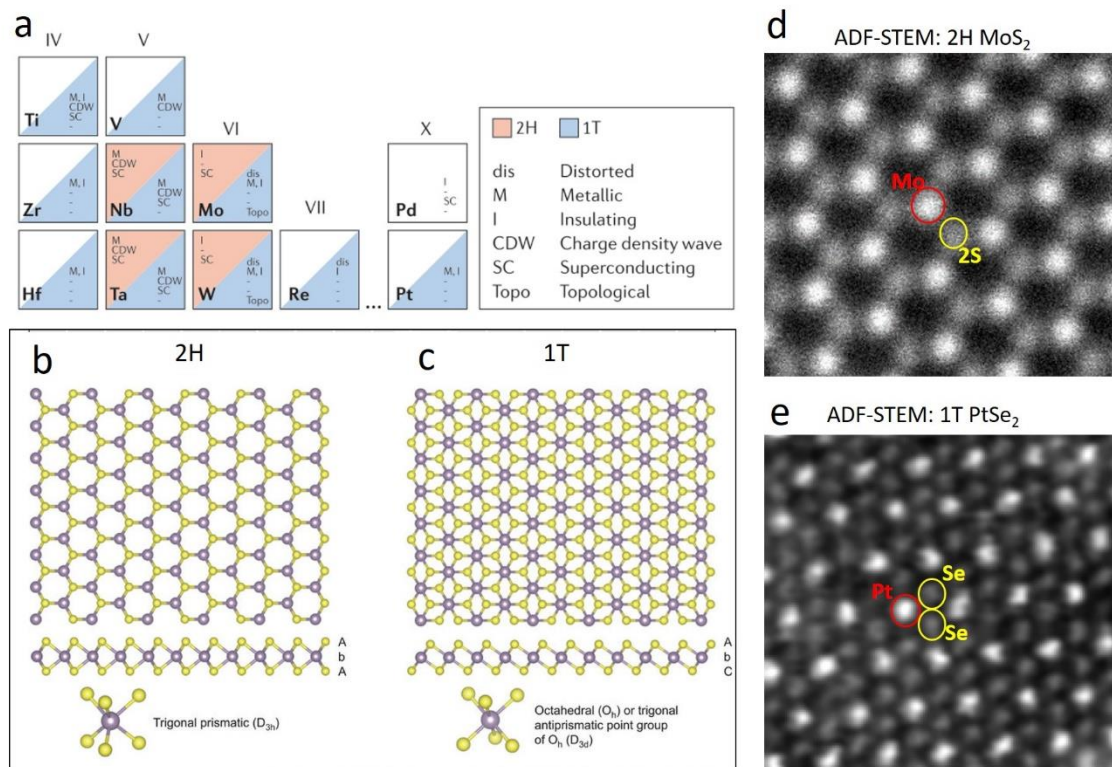


**Figure 2.2** (a) A table of layered TMDs, organized based on the transition metal element involved, summarizing their existing structural phases and observed electronic phases. (b,c) Atomic models of (b) 2H and (c) 1T phase monolayer TMD. The metal and chalcogen atoms are represented by pink and yellow spheres, respectively. (d,e) ADF-STEM images taken from (c) 2H-phase MoS<sub>2</sub>, and (d) 1T-phase PtSe<sub>2</sub>. (a) Reproduced with permission from ref.<sup>3</sup> © 2017 Nature Publishing Group. (b,c) Reproduced with permission from ref.<sup>72</sup> © 2013 Nature Publishing Group.

Figure 2.2a summarized the existing structural phases for the TMDs composed of a variety of metal elements from group 4 to 10 in the periodic table, ranging from insulating (e.g. HfS<sub>2</sub>), semiconducting (e.g. 2H-MoS<sub>2</sub>), to metallic phases (e.g. TiSe<sub>2</sub>). Two of the most common phases for the currently known TMDs are the 2H phase with trigonal prismatic coordination and the 1T phase with octahedral coordination of the metal atoms. Their crystal structures are shown in Figure 2.2b,c. The different phases can be distinguished by atomic-resolution ADF-STEM imaging. Figure 2.2d,e present the typical ADF-STEM images obtained from the 2H-MoS<sub>2</sub> and 1T-PtSe<sub>2</sub> monolayers, comparing their different contrast features. There are two contrast columns in the 2H-MoS<sub>2</sub> in a honeycomb unit, contributed by Mo and 2S respectively (Figure 2.2d), while

the 1T-PtSe<sub>2</sub> have three contrast columns in a rhombus unit, Pt, Se, and the other Se (Figure 2.2e). The group VI metal (Mo, W) TMDs with S, Se chalcogenides are thermodynamically stabilized as the semiconducting 2H phase, while can also have metallic 1T phase with a higher energy.<sup>73-77</sup> The two phases, 2H and 1T, can be transformed mutually by sliding one layer of S atoms across, giving the overlapped or split positions of the S positions. In experimental work, the approach of alkali metals intercalation was used to trigger the transition from 2H to 1T phase.<sup>78-80</sup> A potassium (K)-assisted CVD method was designed for the phase-selective growth of 1T' MoS<sub>2</sub> monolayers and 1T'/2H heterophase bilayers.<sup>81</sup>

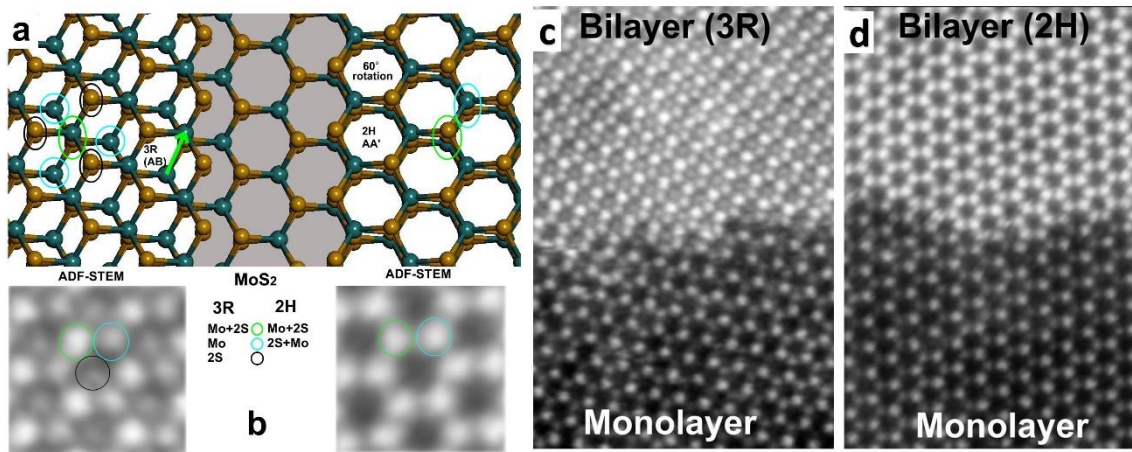


**Figure 2.3** (a) 3D perspective atomic model showing monolayer 2H MoS<sub>2</sub> (central shaded area) with two types of bilayer stacking. Left side is 3R AB stacking from translation shift. Right side is 2H AA' stacking from 60° rotation. (b) ADF-STEM images taken of 3R stacked MoS<sub>2</sub> bilayer (left) and 2H stacked MoS<sub>2</sub> bilayer (right). (c) ADF-STEM image of monolayer-bilayer interface in MoS<sub>2</sub> with 3R stacking. (d) ADF-STEM image of monolayer-bilayer interface in MoS<sub>2</sub> with 2H stacking.

For the bilayer TMDs, there are numbers of stacking orders between the two adjacent layers, among which the two most energetically favourable polymorphs are the 2H and 3R configurations (Figure 2.3a), with the space groups of *P6<sub>3</sub>/mmc* and *R3m*, respectively. Here, the letters of 2H and 3R represents the crystal symmetry of hexagonal and rhombohedral, respectively, and the digits means layer numbers in each unit cell. Different stackings can be distinguished by using ADF-STEM as a direct and

unambiguous characterization tool. The Z-contrast ADF-STEM images obtained to differentiate various configurations of bilayer MoS<sub>2</sub> are shown in Figure 2.3b-d. Apart from modifying the crystal symmetry, these different stacking sequences can also alter the physical properties of TMDs including bandgaps, phonon vibration, and magnetism.<sup>82</sup> A recent study found that the twisted 2H or 3R stacked TMD bilayers with twist angles  $\theta < 3^\circ$  showed qualitatively diverse physical properties prescribed by the lack of inversion symmetry in the constituent layers.<sup>83</sup>

The variety of 2D layered TMDs have developed as a large family of atomically thin semiconductors with variable electronic structures (Figure 2.4). It has been maintained that the multiplicity of electronic properties of bulk layered TMDs is primarily attributed to the different filling states of the non-bonding d bands of transition metals. Bulk TMDs are metallic when their non-bonding d orbitals are partially occupied, and those with fully occupied non-bonding d orbitals exhibit semiconducting properties.<sup>72</sup> Their band structures can also vary with the configuration difference on the crystal unit cell. Taking MoS<sub>2</sub> for example, the degeneracy of the electronic structure at the K(K') point in the Brillouin zone has been eliminated because of the two different lattice points of Mo and two overlapped S atoms, thus opening up a bandgap in the bulk MoS<sub>2</sub>.<sup>84</sup> Notably, TMDs presents tunable bandgaps with the change of layer numbers because of the quantum confinement effect and interlayer interaction.<sup>85-87</sup> As shown in Figure 2.4a, as the layers of MoS<sub>2</sub> decrease, the lowest conduction band near the  $\Gamma$  point moves upward, while the conduction band at the K point scarcely shifts, which can make the MoS<sub>2</sub> transit from an indirect band gap in bulk crystals to a direct band gap in the monolayer. Similar to MoS<sub>2</sub>, the layer-dependent band features are also seen in many 2D-TMDs. The relative valence and conduction band edge of some common monolayer TMDs are displayed in Figure 2.4b. The bandgaps in most semiconducting TMDs are comparable to the 1.1 eV bandgap

in silicon, which make them appropriate for in digital transistor applications. Besides, the transition to a direct bandgap in the monolayer form enables extensive application potentials in variety of (opto-)electronic devices.

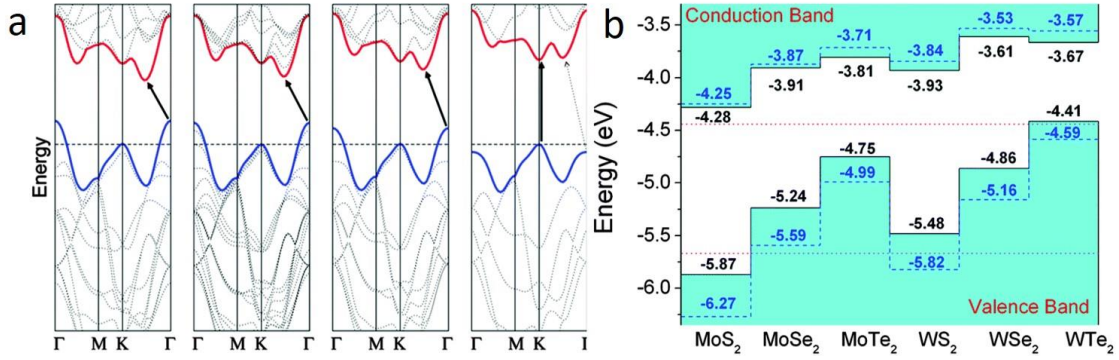


**Figure 2.4** (a) Calculated MoS<sub>2</sub> band structures, corresponding to bulk, quadrilayer (4L), bilayer (2L) and monolayer MoS<sub>2</sub>, with the figures from left to right. (b) The valence and conduction band edge of some typical monolayer TMDs. Reproduced with permission from ref.<sup>86</sup> © 2010 American Chemical Society and ref.<sup>88</sup> © 2013 American Institute of Physics, respectively.

## 2.3 Intrinsic Defects in TMDs

The fast-developing modern aberration corrected TEM and STEM technologies make it feasible to characterize the atomic defects and record their dynamics in 2D materials. There have been numerous reports regarding various structural defects in graphene, including point defects, partial dislocations, grain boundaries (GBs), edges, and sub-nanometre pores, as well as their influence on the mechanical, optical, thermal, and electrical properties.<sup>89-103</sup> In comparison with graphene which only contains one element and one atomic layer thickness, the types of defects in TMDs could be more diverse as they own two elements, more atom layers, and more complex configurations. Their intrinsic defects include the point vacancies, GBs, edges, etc. In this part, I will review the reported defects that have been visualized experimentally, which will be sorted from zero-dimensional (point defects) to one-dimensional (line defects), GBs and dislocations, and edge terminations. These structural defects have been demonstrated to have

noteworthy influences on the band structures, magnetic, electrical or optical performances, further extending the applications of TMDs.

Note that there are many notations used to describe different types of defects and grain boundaries. In this thesis, for vacancies,  $V_S$  and  $V_{Mo}$  denotes sulphur vacancies and Mo vacancies, respectively, and the GB dislocation cores are described using the symmetry fold in the atom loops in the dislocations, with the symbol ‘|’ between the numbers meaning the connection of the atom rings. For example, the ‘4|6’ dislocation core means it is composed of rhomb-hexagon fold rings.

### 2.3.1 Point Defects

Point defects are frequently found in 2D crystals. It has been manifested in graphene that there exists a great variety of defects in the 2D lattice with different combinations. Therefore, this part only focuses on the simplest intrinsic defects when the crystal structure is perturbed without the presence of foreign atoms.

Utilizing the combination of direct atomic resolution imaging and first-principle calculations, various vacancies and antisite defects can be identified. Different types of point defects has been found in monolayer  $MoS_2$ , including sulphur vacancies (monosulphur vacancies  $V_S$ , and disulphur vacancies  $V_{S_2}$ ), Mo vacancies  $V_{Mo}$ , complex vacancies ( $V_{MoS_3}$ ,  $V_{MoS_6}$ ) and antisite defects (with Mo atoms substituting S atoms, namely  $Mo_S$ ,  $Mo_{S_2}$ , or with S atoms occupying the site of Mo, namely  $S_{Mo}$ ,  $S_{2Mo}$ ). Atomic resolution ADF images of various point defects including  $V_S$ ,  $V_{S_2}$ ,  $Mo_{S_2}$ ,  $V_{MoS_3}$ ,  $V_{MoS_6}$ , and  $S_{2Mo}$  reported by Zhou *et al.* are presented in Figure 2.5a,<sup>104</sup> with their corresponding atomic models displayed in Figure 2.5b which have been optimized from DFT calculations and are in qualitative agreement with the experimental STEM images. Pure Mo vacancies were not observed in isolation as they usually formed complexes with S

vacancies. The 3-fold symmetry was still preserved in most of the defect structures.

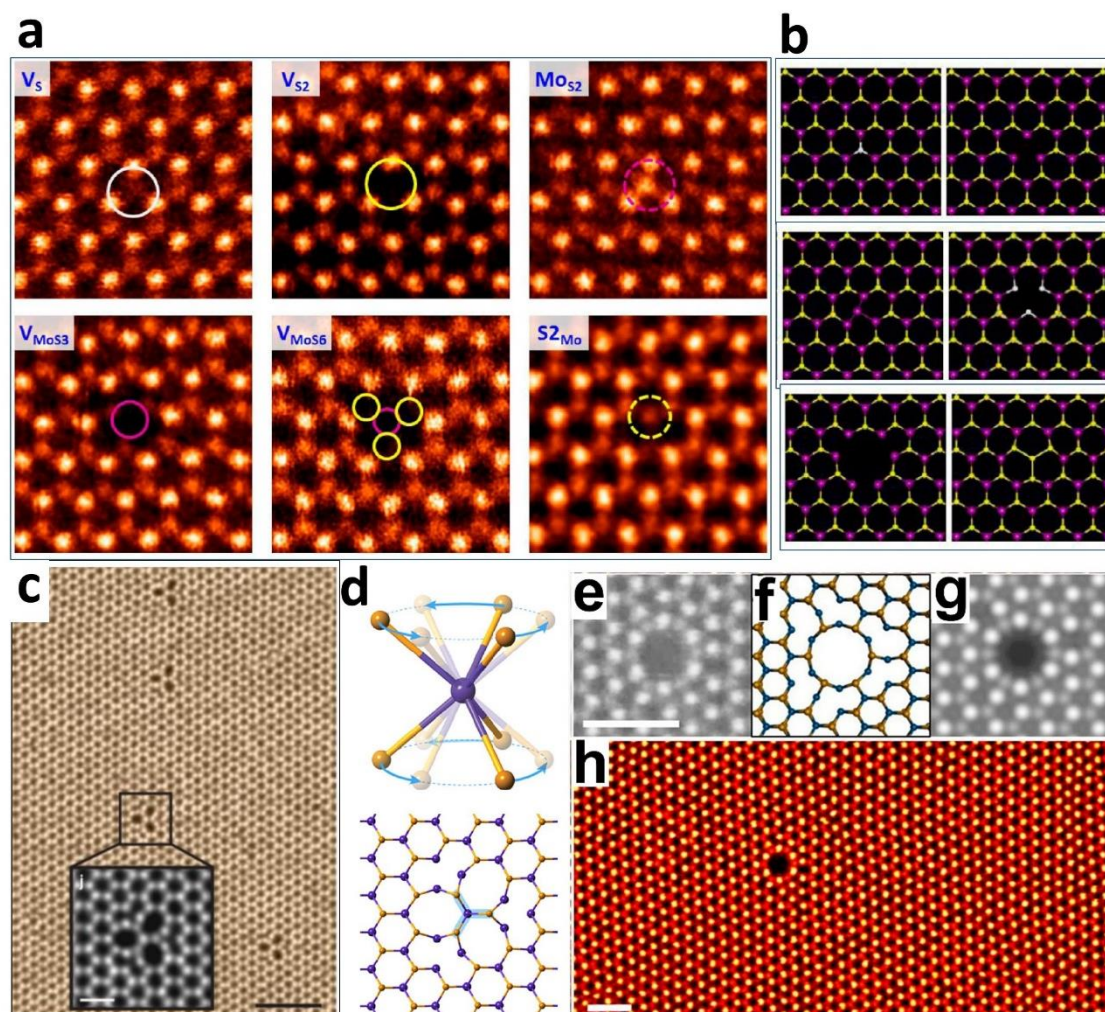


**Figure 2.5** Point defects of monolayer 2H-phase TMDs. (a) ADF-STEM images of various point defects in monolayer MoS<sub>2</sub> and (b) corresponding DFT-fully-relaxed atomic models, showing V<sub>S</sub>, V<sub>S2</sub>, MoS<sub>2</sub>, V<sub>MoS3</sub>, V<sub>MoS6</sub>, and S<sub>2</sub>Mo, from top left to bottom right. (c) ADF-STEM image of trefoil defects at monolayer WSe<sub>2</sub> at 500°C, with (d) schematic model showing the formation mechanism by bond rotation. (e) ADF-STEM image of self-limiting nanopore (SLP) in WS<sub>2</sub> at 500°C, with atomic model in (f) and multislice image simulation in (g). (h) ADF-STEM image showing large area of WS<sub>2</sub> with single SLP. (a,b) Reproduced with permission from ref.<sup>104</sup> © 2013 American Chemical Society. (c,d) Reproduced with permission from ref.<sup>105</sup> © 2015 Nature Publishing Group. (e-h) Reproduced with permission from ref.<sup>106</sup> © 2018 American Chemical Society

The predominant intrinsic defects in MoS<sub>2</sub> were reported by Hong *et al.* to be affected by the material growth methods, where mechanical exfoliation, and physical or chemical vapour deposition (PVD or CVD) were evaluated.<sup>107</sup> High defect density was found in these synthetic monolayer MoS<sub>2</sub>, in which sulphur vacancy dominated the

defects in the mechanical exfoliation and CVD samples, while the principal defect category was Mo antisites in PVD samples. Their observed antisite defects were believed to be native rather than caused by electron beam. The *in-situ* STEM experiment indicated the Mo adatoms were highly mobile. The results from DFT calculation and electric transport measurement demonstrated that minimizing point defects, especially antisites, was vital for electric transport applications, while the antisites controllably brought in could generate local magnetic moments.

Bond rotations are abundantly found in graphene to form defects without losing atoms,<sup>94-95,98,108-109</sup> which help stabilize the vacancies and are important in the dynamics of vacancy migration. Different from the Stone-Wales rotation in graphene with a 90° in-plane C-C rotation, bond rotations in monolayer TMDs involves three dimensional process and are much less common due to the bi-element feature of the bonds between metals and chalcogenide atoms. Lin *et al.* found a type of trefoil-like point defect contributed by bond rotation in monolayer WSe<sub>2</sub> at 500 °C, as displayed in Figure 2.5c,d, where the metal-chalcogen bonds rotated by 60° to produce the defect.<sup>105</sup> Although this has demonstrated the existence of that bond rotations in the 2D TMDs, the common observation throughout the TMD systems has been restricted. The visualization of such bond-rotation defects in Mo-based TMDs is rare, for example, never in MoS<sub>2</sub> to date. As the vacancy stability is related to temperature, the reported bond rotation in TMDs is often observed at high temperature. Note that the stable W-W bonding occurs in the defects after bond rotation, and this kind of W-W bond also enables self-limiting nanopores to form during S loss at high temperature (Figure 2.5e-h).<sup>106</sup>

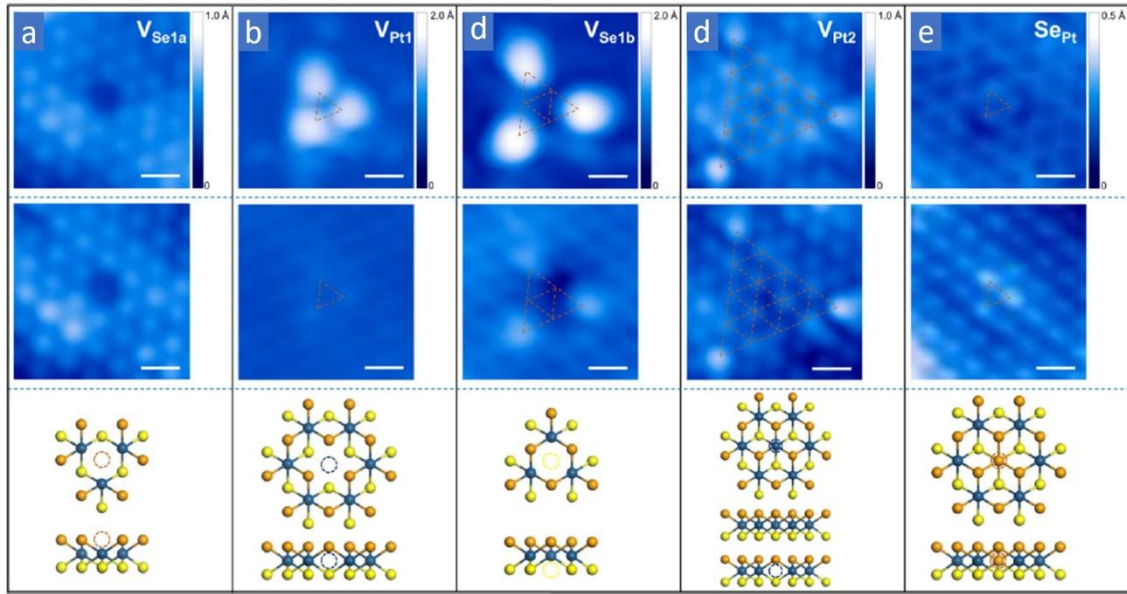


**Figure 2.6** Point defects of ultrathin 1T-phase PtSe<sub>2</sub> characterized by scanning tunneling microscopy (STM). Top panel: empty-state images. Middle panel: filled-state images. Bottom panel: Top and side view of the models of each type of defects shown in the top and middle panels. The scale bars: 0.5 nm. Reproduced with permission from ref. <sup>110</sup> © 2019 IOP Publishing Ltd.

Many of the experimental investigations have focused on the 2H-phase TMDs, while with regard to the point defects in the 1T-phase TMD monolayers, much less reports have presented experimental characterizations especially at the atomic level, mainly due to the difficulty in obtaining the high-quality monolayer samples, as well as the beam sensitivity of many 1T-phase TMDs when thinned to monolayers. There are some theoretical studies calculating the stability and properties of the point defects in 1T-TMDs. First-principles calculations by Zhang *et al.* suggested that the S adatoms, S vacancies, and the V adatoms can stably exist in 1T-phase VS<sub>2</sub>, and introducing those point defects onto VS<sub>2</sub> basal planes can enhance hydrogen evolution reaction (HER) of the materials.<sup>111</sup> Ali *et al.* calculated the point vacancies in the semiconducting 1T-SnSe<sub>2</sub> monolayer, and proposed that that single Sn vacancy can bring about half-metal property, and can also induce magnetic ground states.<sup>112</sup> Gao *et al.* predicted the structure, stability, and kinetics of both Pt and Se vacancies in monolayer 1T-PtSe<sub>2</sub> by first-principles study, and suggested that the single vacancies for either Pt or Se prefer to combine to form double vacancies

energetically.<sup>113</sup> For the experimental characterization, several types of point defects have been visualized in the ultrathin 1T-PtSe<sub>2</sub> in the scanning tunneling microscopy (STM) work by Zheng *et al.* although not from the monolayer sample, as shown in Figure 2.6, which are Pt vacancies, Se vacancies in the topmost layer, and Se antisites at Pt sites within the topmost layer. Their calculation shows that the Se antisite defects have the lowest formation energy in a Se-rich growth condition.

### 2.3.2 One-Dimensional Defects

Chalcogen vacancy lines can be regarded as the most frequently observed one-dimensional defects in TMDs. When an increasing number of S vacancies are created under continuous electron beam irradiation in TEM/STEM imaging, line defects are generated with the migration and aggregation of single S vacancies. For a S vacancy migrating to the adjacent site, the calculated energy barrier of 2.0 eV is too high for spontaneous diffusion at ambient temperature.<sup>114</sup> However, it has been noticed that with the prolonged irradiation of the electrons in TEM, S vacancies migrate slowly with a diffusion coefficient of  $3.8 \times 10^{-18} \text{ cm}^2/\text{s}$ . They tend to migrate in short distances and form several line defects simultaneously (Figure 2.7a-b).

Wang *et al.* reported various types of SVLs structures (Figure 2.7c-f)<sup>115</sup>. The simplest S line vacancy is single S line vacancy (1SVL), composed of a single line of S vacancies with out-of-plane distortion as predicted by DFT calculation (Figure 2.7c,e). These SVLs can increase in both length and width. When increasing in width, broader SVLs with more than one parallel lines of S vacancies are formed, like the two S line vacancies (2SVLs) in Figure 2.7d,f, and the three sulphur line vacancy (3SLV) is shown in Figure 2.7g,h. It is suggested that the multi-SVLs have staggered up and down to stabilize the system and reduce buckling. As the length increases, the compression of

lattice occurs due to the missing S atoms, which gives rise to the compressive strain in the x (perpendicular) to the line vacancy direction (Figure 2.7i,j). As the SVLs propagate along the three zigzag directions with the angle of  $120^\circ$ , they are highly likely to encounter each other. Ryu *et al.* have observed the interactions among several SVLs, with a pore being opened and enlarged at the interacting point.<sup>116</sup>

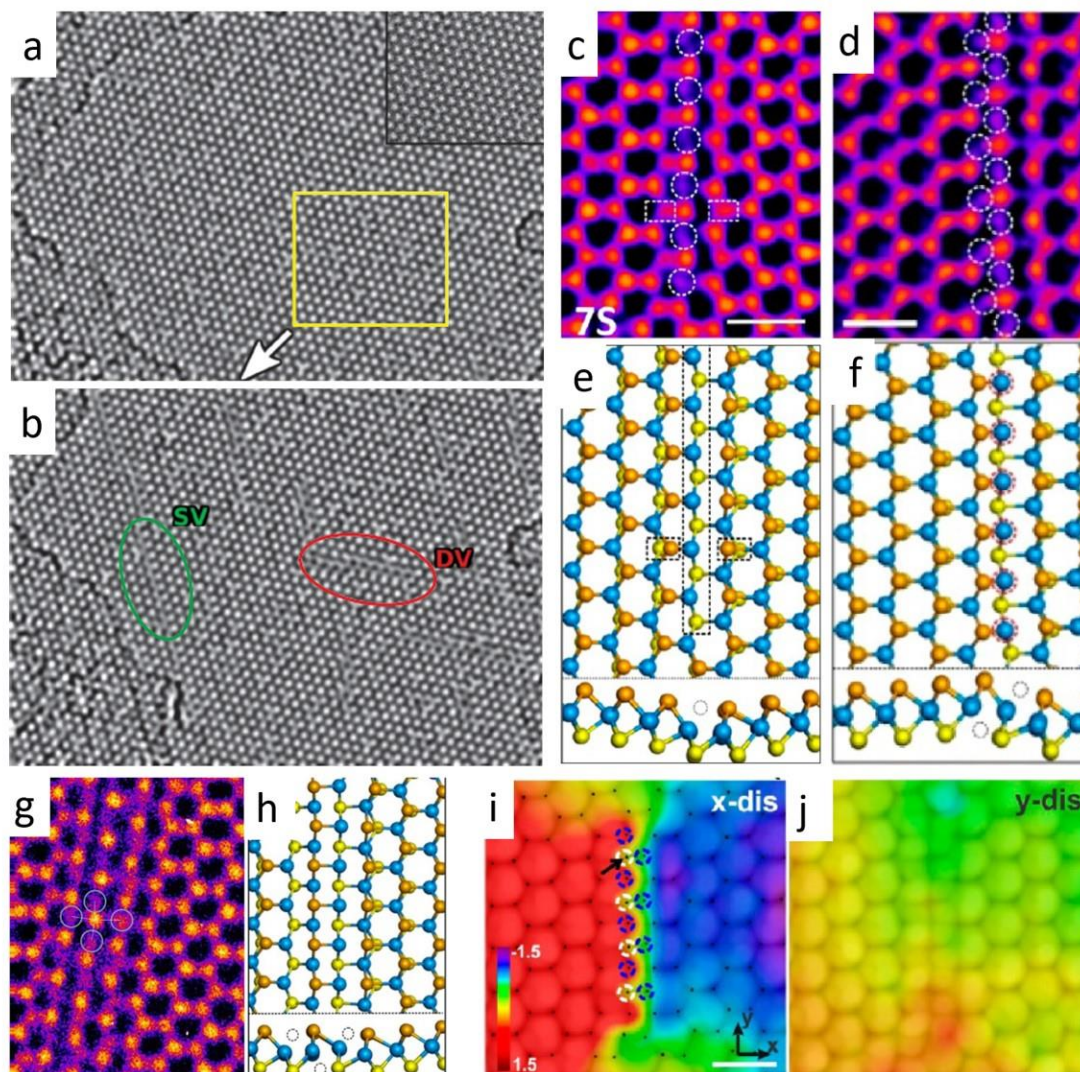


**Figure 2.7** Sulphur vacancy lines (SVLs) in monolayer MoS<sub>2</sub>. (a,b) TEM images showing the creation of SVLs under 80 keV electron beam at (a) initial point, (b) 220 s. SV: single line vacancy (1SVL); DV: double line vacancy (2SVL). (e-f) False-colour AC-TEM images and corresponding DFT relaxed models of MoS<sub>2</sub> with different SVLs: (c,e) 1SVL; (d,f) 2SVL; (g,h) three sulphur line vacancy (3SLV). (i,j) Displacement maps across the 1SLV for x and y directions respectively. Scale bar: 0.5 nm. (a,b) Reproduced with permission from ref.<sup>114</sup> © 2013 American Physical Society. (c-j) Reproduced with permission from ref.<sup>115</sup> © 2016 American Chemical Society.

The SVLs have a different stoichiometry locally, thus are supposed to present altered

electronic band structures. It has been predicted that the band structure changes within these line vacancies as a function of their width, gradually shifting from the pristine semiconducting to metallic. The band gap decreases gradually from 1.7 eV in pristine MoS<sub>2</sub> to 0.047 eV in 3SVL, and metallic properties are shown in the 4SVL structure.<sup>115</sup> In this regard, large linear vacancy clusters may be able to bring about complex transport behaviour by acting as metallic channels in the semiconducting MoS<sub>2</sub> material.<sup>118</sup>

### 2.3.3 Grain Boundaries and Dislocations

Grain boundaries (GBs) in 2D materials are formed between two grains with orientation variation and are demonstrated to be stitched together with the atomic bonding, which can exert vital influences to the physical/chemical properties of the materials.<sup>119-133</sup> CVD-grown TMDs are often polycrystalline, and two differently oriented single crystals can merge during the growth (Figure 2.8 a-d), producing different types of GBs.

The GBs in MoS<sub>2</sub> monolayers can be divided by two categories, small-angle GBs and mirror twin GBs (MTBs, also called 60° GBs). Their effects on the material properties vary with the GB structures. The MTBs caused slight increase in the electrical conductivity but small-angle tilt GBs led to the reverse effect.<sup>134</sup> Tilt GBs introduced degraded electrical characteristics and n-type doping in MoS<sub>2</sub>, while MTBs did not show these effects.<sup>135</sup> Apart from the transport properties, GBs can also influence the electroluminescence (EL) of WS<sub>2</sub>.<sup>136</sup> Strong photoluminescence quenching was caused by MTBs in MoS<sub>2</sub> whereas tilt GBs led to substantial enhancement.<sup>134</sup> Some other distinct features of GBs are also being discovered, for example, preferential oxidation at GBs,<sup>137</sup> vulnerable to produce nanopores,<sup>138</sup> and serving as the seeding sites of Pt nanoclusters.<sup>139</sup> Atomic study on these GBs can facilitate tailoring the TMD properties.

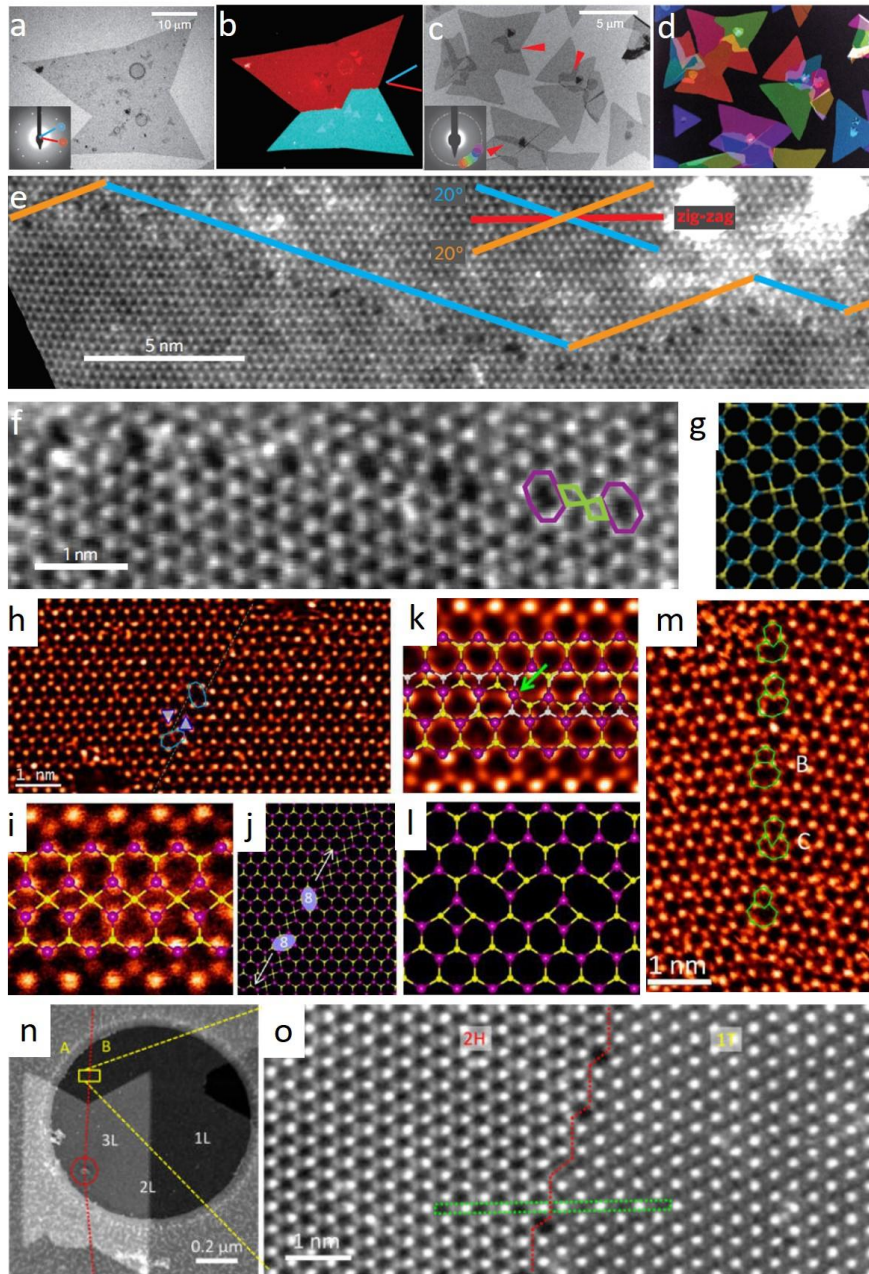


**Figure 2.8** GBs in monolayer MoS<sub>2</sub> and WS<sub>2</sub>. (a) Bright-field TEM (BF-TEM) image of two triangles that have grown together. Inset is the diffraction pattern. (b) Colour-coded overlay of dark field TEM (DF-TEM) images. (c) BF-TEM image of irregular-shape MoS<sub>2</sub> domains, with the diffraction pattern inset. (d) Coloured DF-TEM image with the colours correspond to the orientations. (e,f) High-resolution ADF-STEM images and (g) atomic model of a MTB. (h,i) ADF image of a 4|4P 60° GB. (j) Schematic structure of the GB and GB kinks as shown in h. (k) ADF image and overlaid structural model of a 4|4E type 60° GB. (l) Relaxed structure for 4|8 GB, representing a 4|4P GB with the highest kink density. (m) ADF image of an 18.5° GB with a row of dislocation cores highlighted in green lines. (n) Low-magnification and (o) high-magnification ADF-STEM images of a GB between 2H and 1T phase WS<sub>2</sub> domains formed during CVD growth. (a-g) Reproduced with permission from ref.<sup>134</sup> © 2013 Nature Publishing Group. (h-m) Reproduced with permission from ref.<sup>104</sup> © 2013 American Chemical Society. (n,o) Reproduced with permission from ref.<sup>140</sup> © 2018 American Chemical Society.

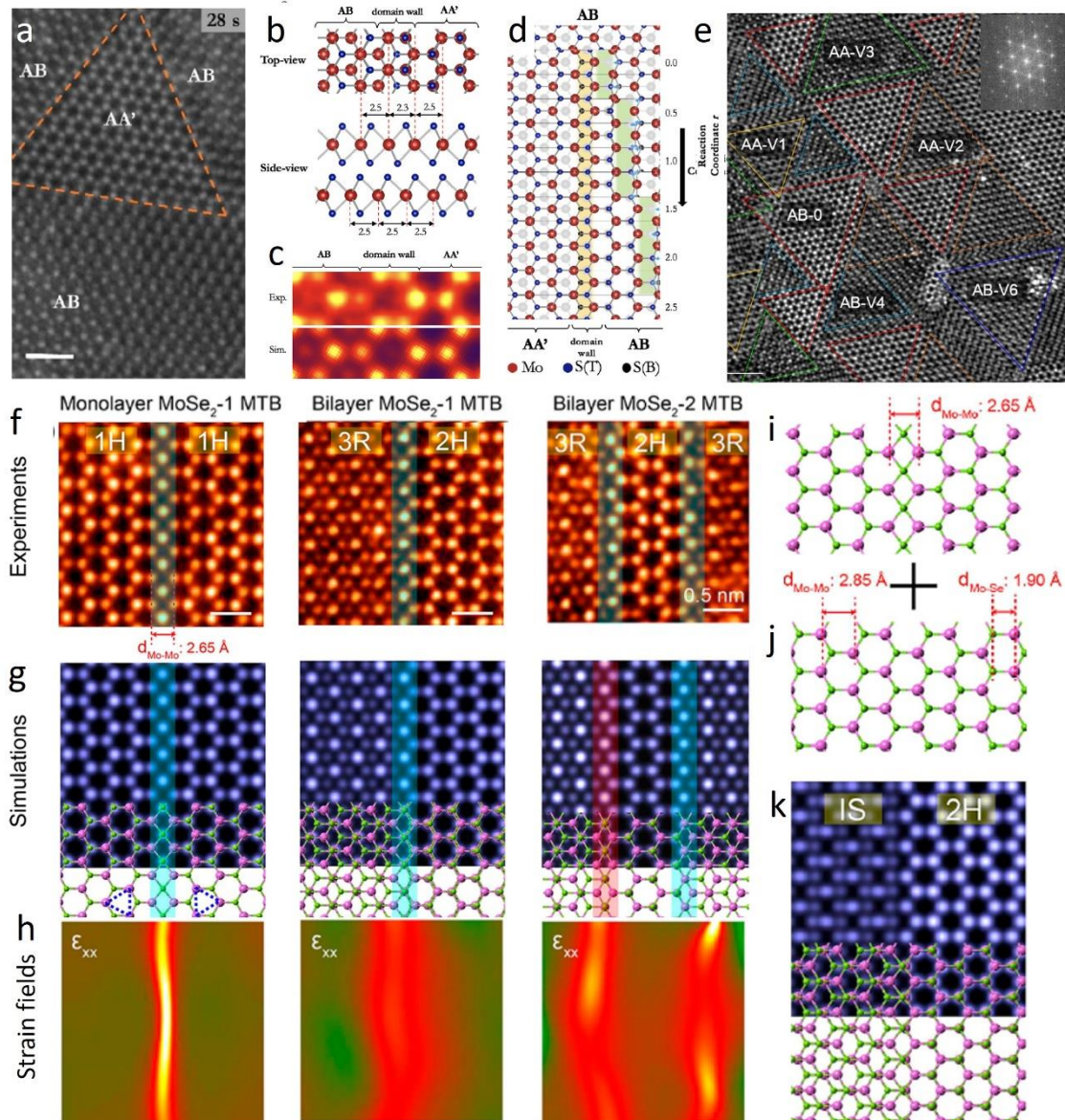


**Figure 2.9** GBs in bilayer TMDs. (a) ADF-STEM image of AA' stacked triangular domains stitching to AB stacked regions in bilayer MoS<sub>2</sub>. (b) Scheme of the boundary structure derived from DFT calculations. (c) Experimental ADF-STEM image at a stacking boundary compared to the simulated image of the atomic model in (b). (d) Scheme of domain boundary nucleation and domain growth, starting from a pristine, strained AB-stacked bilayer. (e) Diverse atomic structure of bilayer domains with inversion-domain boundaries in MoSe<sub>2</sub>. (f) Experimental ADF-STEM images of monolayer 1H MoSe<sub>2</sub> with one mirror twin boundary (1 MTB), bilayer MoSe<sub>2</sub>-1 MTB, and bilayer MoSe<sub>2</sub>-2 MTB films, from left to right with (g) corresponding simulated images with overlaid DFT-optimized atomic models, and (h) strain analysis on component  $\epsilon_{xx}$ . (i,j) DFT-optimized atomic models of (i) a monolayer MoSe<sub>2</sub>-1 MTB film and (j) a monolayer 1H MoSe<sub>2</sub> film. (k) Simulated image of the unstrained bilayer MoSe<sub>2</sub>-1 MTB by manually stacking (i) and (j) without DFT relaxation. (a-d) Reproduced with permission from ref.<sup>141</sup> © 2017 American Chemical Society. (e) Reproduced with permission from ref.<sup>142</sup> © 2017 American Chemical Society. (f-k) Reproduced with permission from ref.<sup>143</sup> © 2018 American Chemical Society.

The atomic structures of GBs can vary much with the intersecting angle of the two grains. The extended GBs in 2D materials are generally connected by chains of dislocation cores.<sup>121,144-146</sup> Several GB dislocation structures, including 4|4 (rhomb-rhomb), 4|6 (rhomb-hexagon), 4|8 (square-octagon), and 6|8 (hexagon-octagon) fold rings have been predicted in monolayer MoS<sub>2</sub> by first principles theory.<sup>147</sup> For the small angle GBs, due to the diversity in the coordination manner between Mo and S atoms, the complicated GB configurations, such as a recurring 8|4|4 motif, can be formed (Figure 2.8 e-g).<sup>134</sup> Linearly-aligned dislocation cores composed of 5|7 rings, 6|8 rings, 4|6 rings are also observed, for example, in the 18.5° tilt angle GB in Figure 2.8 m.<sup>104,145</sup> Similar structures have also been observed in WS<sub>2</sub> GB dislocation cores which exhibit series of electron-beam driven dynamics.<sup>148</sup>

Mirror twin GBs are the mirror-symmetric 60° GBs, which appear between two grains twisted by integer multiples of 60°.<sup>149-150</sup> Two kinds of mirror twin GBs consisting of 4-fold rings linear dislocation cores have been directly visualized by Zhou *et al.* using STEM, with either point sharing (4|4P) or edge sharing (4|4E), as displays in Figure 2.8i,k, respectively. The 4|4P GB may serve as a metallic wire embedded in the semiconducting MoS<sub>2</sub> lattice according to the first principle calculation.<sup>147</sup> These 60° GBs are not always straight lines along the zig-zag direction, but has steps along the armchair with kinks of the 8-member rings (Figure 2.8 j, l). The 4-8-member dislocation rings are also found to connect to be the anti-phase GB between 2H and 1T phase WS<sub>2</sub> domains, which intrinsically grow during CVD synthesis.<sup>140</sup> Combining 4-8 rings, the GB can appear as any angle at the nano-microscale level, while staying consistent with zig-zag directions at the atomic level with armchair joined step-wise developments.

GBs for bilayer TMDs are more complicated compared with monolayer system. The commonly observed intrinsic GBs in synthetic bilayer TMDs samples are the overlapping

GBs in one of the two stacked layers.<sup>143,151</sup> When two monolayers of TMD containing GB themselves are stacked together, the randomly appearing GB in each layer provide more possibility for modulating stacking geometry which are correlated to the electronic, optical, or mechanical properties of bilayer TMDs. Yan *et al.* utilized the thermal stimulation and electron irradiation to create nanoscale stacking boundaries in bilayer MoS<sub>2</sub> that separated domains with different inversion symmetries (Figure 2.9a-d).<sup>141</sup> An atomically sharp stacking boundaries were observed between two differently stacked domains AB and AA' (Figure 2.9a). The GB structure was stabilized by having a T-phase-like structure based on DFT calculations (Figure 2.9b,c). They found that there were highly localized metallic states at the stacking boundaries. For the GB in as-prepared bilayer TMDs sample, Hong *et al.* introduced inversion-domain GBs into molecular-beam-epitaxy grown MoSe<sub>2</sub> homobilayers, inducing the diversity of large-area and uniform stacking sequences (Figure 2.9e).<sup>142</sup> These multifarious stacking sequences have proved to produce stacking-dependent bandgaps and valence band tail states. Besides, interlayer-induced strain variation in the MTB of bilayer TMDs were found by Zhao *et al.* (Figure 2.9f-h).<sup>143</sup> The MTB modifies the interlayer vdW coupling in bilayer films, developing local strain for a few nanometers near the MTB (Figure 2.9h), which should impact the local conductance and thermoelectric properties.<sup>152-153</sup> Figure 2.9i-k illustrate that to form the 2H|3R stacking across the MTB, the monolayer containing MTB must be strained. The understanding of interlayer interactions in the presence of MTBs can hopefully afford alternative routes for strain engineering of layered structures.

### 2.3.4 Edge Terminations

Edge terminations of 2D materials have been explored extensively with predicted metallic states that cross the bulk energy gap along MoS<sub>2</sub> or WS<sub>2</sub> zigzag edges.<sup>154</sup> Novel electronic,

magnetic, optical, and catalytic properties can present at the edge structures of TMDs.<sup>155-162</sup> Distinct magnetic and electronic properties are predicted for zig-zag edge and armchair edge: zigzag edges show the ferromagnetic and metallic behaviour, while armchair edges are nonmagnetic and semiconducting.<sup>162-163</sup> Intense PL emissions and preferential formation of biexcitons were found to be around the edges of individual WS<sub>2</sub> grains attributed to larger population of charge carriers.<sup>127</sup> Besides, the structural discontinuity at the edges of TMDs presents a unique chemical reactivity, like the high catalytic activity in the hydrogen evolution reaction (HER).<sup>158,164-165</sup> Precise recognition of the edge structures at the atomic level is the key to the realization of promising application of TMD nanoribbons in the devices of nanoelectronics, HER, etc.

A number of theoretical studies have indicated an energetic preference for zigzag terminations of MoS<sub>2</sub>.<sup>154,160,166</sup> The two elemental nature of TMDs determines two zigzag edges: S-zigzag and metal-zigzag, with different energetics and stability. Depending on the chemical potential of the constituent atoms during growth, the metal-zigzag or S-zigzag edges can be further terminated by S or metal atoms with reconstructions.<sup>159</sup> The regular Mo-edge with bare Mo termination, and the reconstructed edge containing 50% of S vacancies were observed by Zhou and co-workers.<sup>104</sup> That reconstructed Mo-rich edge can be normally formed under either Mo-rich or S-deficient conditions, while the presence of adatoms near the edge indicate it is the Mo-rich environment. For their electronic structure, in contrast to the bare Mo-terminated edge which has been shown to have a ferromagnetic ground state,<sup>162</sup> the Mo magnetic moments are quenched in that reconstructed Mo edges, while the metallic behaviour of the edge is still well-preserved.<sup>104</sup>

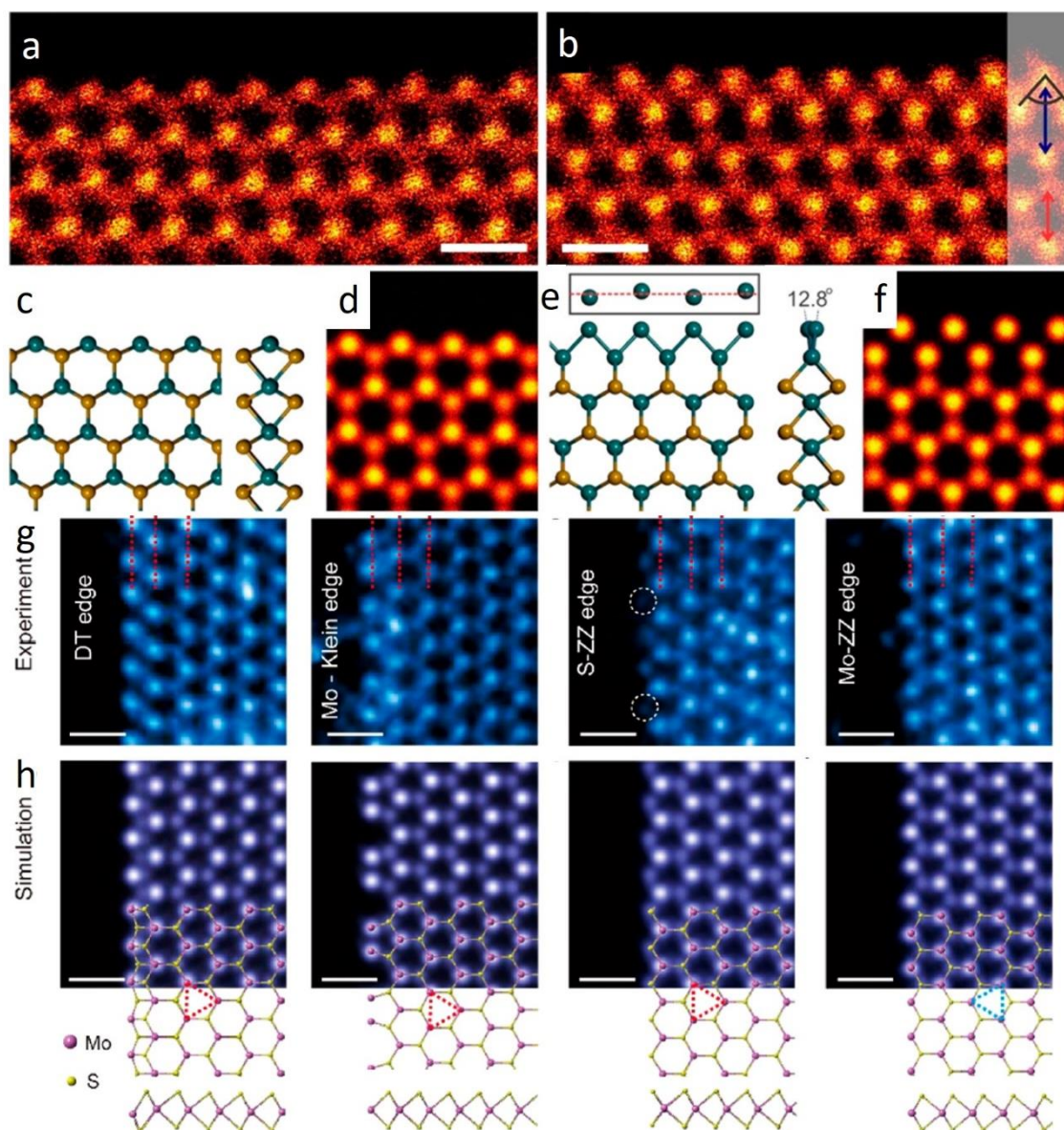


**Figure 2.10** Edge termination structures of monolayer MoS<sub>2</sub>. (a,b) ADF-STEM images of a Mo edge and Mo-replaced S edge at high temperature of 800 °C. (c) The atomic model of a Mo edge calculated using DFT and (d) corresponding image simulation. (e) DFT model of a Mo-replaced S edge and (f) corresponding image simulation. (g) ADF-STEM images showing the distorted 1T (DT) edge, Mo-Klein, S-zigzag (S-ZZ), and Mo-zigzag (Mo-ZZ) edges, and (h) corresponding simulated images with overlaid DFT atomic structures. (a-f) Reproduced with permission from ref.<sup>167</sup> © 2017 American Chemical Society. (g,h) Reproduced with permission from ref.<sup>168</sup> © 2018 American Chemical Society.

A recent work reported atomically flat zigzag edges in MoS<sub>2</sub> when heated above 500°C, using high temperature *in-situ* TEM heating holder (Figure 2.10 a,b),<sup>167</sup> unlike the typical terraced step edges at room temperature of the CVD-grown samples. Two distinct zigzag terminations were seen at the edge with different contrast patterns. The S depletion

caused the reconstruction of the S terminated zigzag edges to be double Mo terminated (Figure 2.10e,f). Electron beam irradiation led to the formation of constrictions in MoS<sub>2</sub> at 800°C, making it highly faceted along the zigzag direction. The progressive narrowing resulted in ribbons that were 1nm in width adopting the Mo-rich terminations. DFT calculations predicted interesting spin dependent properties for these nanoribbons. A type of reconstructed Mo-terminated edge, namely, a distorted 1T (DT) edge, as well as a Mo-Klein edge were found in a nano-porous MoS<sub>2</sub> films grown by molecular beam epitaxy under high Mo flux.<sup>168</sup> There are four main edges, Mo-zigzag, DT, Mo-Klein, and S-zigzag, as shown in Figure 2.10g,h, distributed with population percentages from the highest to lowest, indicating the predominance of Mo-terminated edges. Their calculation suggested that the DT, Klein, and Mo-zigzag were mostly Mo-terminated under Mo-rich synthesis conditions. The calculated spatially resolved spin densities showed that the magnetic moment was confined to the edge region.

## **2.4 *In-Situ* Structural Modifications of 2D TMDs in TEM**

### **2.4.1 Electron Beam Induced Structural Change**

The interaction between the high-energy electron beam and the atomically thin 2D materials offers massive possibilities of their structural changes. Before concretely reviewing diverse *in-situ* structural changes in 2D TMDs induced by beam, here discuss the effects of the beam radiation on the samples in general. During (S)TEM imaging, multiple damage mechanisms can occur simultaneously, associated with both the microscope configuration and the nature of the materials. Basically, when electrons pass through materials, energy can be either elastically or inelastically transferred to the atoms, which gives rise to the two main types of radiation damage, namely “knock-on” damage (the displacement of atoms from their original positions in the lattice), and radiolysis.<sup>169-</sup>

<sup>170</sup> In an elastic collision, the incident beam is scattered by the Coulomb force with the atom nuclei, which process involves no loss of the total kinetic energy. For the high-angle elastic scattering, the energy transfer from the incident beam can be significant and lead to atom displacement when the transferred energy exceeds the displacement energy threshold of a sample atom. This displacement energy is determined by the bond strength, the atomic number and the crystal orientation of the sample itself, while the transferred energy increases with the acceleration voltage and decreases with the  $Z$  atomic number of the recoil atom.<sup>169,171</sup> Thus the knock-on damage can be mitigated by lowering the accelerating voltage of the beam in (S)TEM. As for the inelastic scattering process, the incident electron interacts with the electrons of the target atom, resulting in radiolysis damage by the ionisation effect, which is often the dominant mechanism in insulators, semiconductors and the organic specimen, and is difficult to avoid. This damage process generally involves two steps: electron excitation and bond recovery, independent of the beam accelerating voltage, and there is no sharp threshold below which no damage occurs, although it can be eased by cooling the specimen.<sup>170</sup> At lower energy beam irradiation, radiolysis is expected to become more dominant, as the larger inelastic interaction cross-section allows for a larger number of radiolysis caused secondary electrons. Other resulted effects of inelastic scattering can also include electrostatic charging and specimen heating, which mainly happen in less thermal and electrical conducting materials like h-BN. The inelastic damage mechanism in metallic materials such as graphene, is virtually irrelevant due to the rapid electron-hole recombination.<sup>169</sup>

For the semiconducting TMDs, it is likely that both knock-on and ionization damage mechanisms can occur in (S)TEM observation. The displacement threshold for chalcogen atoms in the typical monolayer  $\text{MoX}_2$  ( $X = \text{chalcogens, S/Se}$ ) is calculated to be  $\sim 6.5$  eV, which is approximately achievable by the knock-on energy transferred from 80 keV

electrons ( $\sim 6.0$  eV), thus the chalcogen vacancies can generate frequently during TEM imaging at 80 kV accelerating voltage mainly caused by the knock-on effect.<sup>172-174</sup> Some reports have demonstrated the use of graphene encapsulation could be an effective way to improve the stability of 2D materials under the beam exposure.<sup>172,175-177</sup> Transition metal vacancies are much less often observed at 80 kV, like the Mo vacancies, as the energy transferred to Mo atoms ( $\sim 2.0$  eV) is far below the threshold for sputtering them ( $\sim 13.9$  eV).<sup>173</sup> It is notable that the chalcogens can be sputtered more easily from the edge as the displacement threshold is calculated to be as low as 4.2 eV, which can be overcome by the electron beam of 60 keV.<sup>174</sup> At lower accelerating voltages (for example, 60 keV electron beam which can transfer up to 4.3 eV to S atoms), the chalcogen vacancies can also occur through more complex mechanisms, such as chemical etching effects and valence ionization from inelastic excitations.<sup>174,178-180</sup> The significant roles of ionization in defect generation in MoS<sub>2</sub> was validated by a study on the defect production in MoS<sub>2</sub>/graphene heterostructures.<sup>175</sup> Inelastic scattering leads to not only electrostatic repulsion producing vacancies, but also lowers the knock-on threshold by electronic excitations as suggested by theory and experiment.<sup>178</sup> On the other hand, chemical etching also plays an important role in defect creation in 2D TMDs, where the electrons break down residual impurities such as oxygen molecules in the vacuum chamber, forming radicals in turn that react with the materials surface and cause atomic loss.<sup>172,174</sup> These studies suggest that the mechanisms of vacancy generation in 2D TMDs below the knock-on threshold may involve the combined effect of valence ionization and chemical etching, although the precise understanding of the actual channels still needs to be elucidated and quantified in theory and experiment.

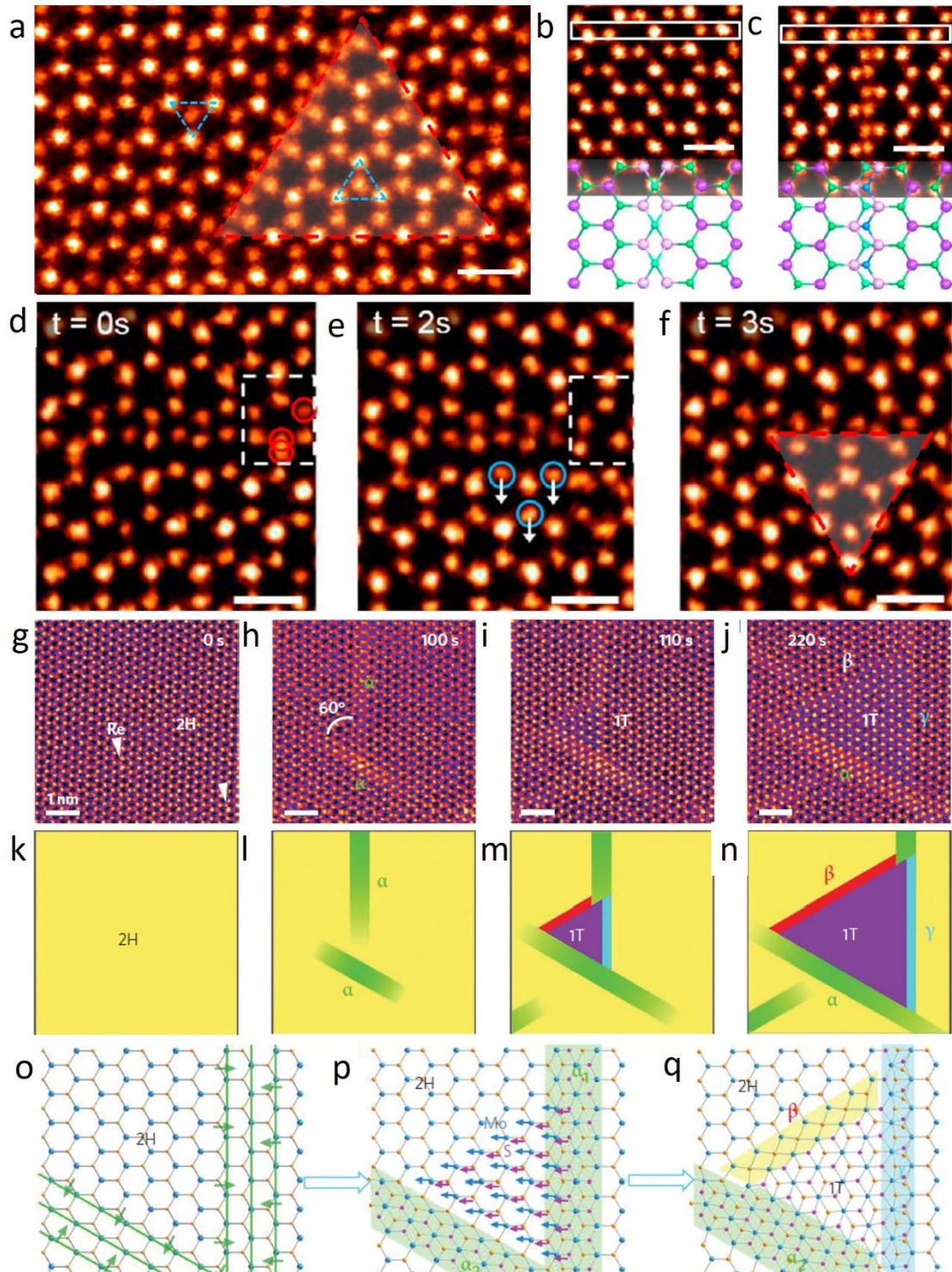


**Figure 2.11** Electron beam induced local embedded anti-phase domains with GBs in monolayer TMDs. (a) Beam-induced inversion domain within MoSe<sub>2</sub> monolayer with (b) 4|4P GB (c) 4|4E GB. Scale bar: 0.5nm. (d-f) Time series showing the nucleation of the inversion domain. (g-j) ADF-STEM images showing step-by-step transition from 2H to 1T phase domain in monolayer MoS<sub>2</sub> at 600 °C. (k-n) Corresponding schematic illustrations. (o-q) Atomic models demonstrating the atomic movement. (a-f) Reproduced with permission from ref.<sup>181</sup> © 2015 American Chemical Society. (g-q) Reproduced with permission from ref.<sup>182</sup> © 2014 Nature Publishing Group.

Chalcogen vacancies are frequently produced when illuminated by electron beam even at low accelerating voltage of 60kV, which often initiate many of the subsequent structural transformations of TMDs with the increase of electron dose rate. The structural evolution mechanisms often involve the migration of vacancies, displacement of atoms, bond breaking and re-generating, charge re-distribution, lattice distortion, change of crystallinity, and adjustment of strain fields, etc. The combination of these effects gives rise to a variety of electron-beam driven structural changes, such as nanopores, holes, nanoribbons, nanowires, cracks with sharp edges, recrystallization, as well as the *in-situ* repair of the defects.<sup>106,173,183-189</sup>

The electron beam irradiation at 80kV can trigger the formation of anti-phase triangular domains embedded in TMD monolayers. Two types of triangular domains have been discovered to be implanted in the 2H-TMDs: inversion domain and 1T phase domain. An inversion domain is a domain of mirror symmetry with the original lattice and have the lattice rotation by 60°. Lin *et al.*<sup>181</sup> found that the 4|4P and 4|4E 60° GBs in monolayer MoSe<sub>2</sub> could be artificially produced by either the electron beam irradiation or thermal annealing, generating inversion domains inside the pristine MoSe<sub>2</sub> lattice (Figure 2.11a-c). They argued that the nucleation of the inversion domains and migration of the 60° GBs were driven by the collective Se vacancies and subsequent displacement of Mo atoms. Similar nucleation and growth mechanism of the inversion domain was also proposed by Lehtinen *et al.*<sup>132</sup> The other triangular domain, metallic 1T-phase domain, was formed from semiconducting 2H-phase MoS<sub>2</sub> by local phase transition by Lin *et al.* with *in-situ* heating at 600 °C in STEM (Figure 2.11d-n).<sup>182</sup> The transition started from the generation of two linear structures ( $\alpha$  in Figure 2.11e,i) along zigzag directions with intersecting angle of 60°, followed by the formation of 1T phase with two new boundaries,  $\beta$  and  $\gamma$ . The  $\beta$  boundary is similar to the 4|4P 60° GB structure. Following this, Silvan and co-

workers investigated the mechanism of the beam-induced 2H-1T phase transformation by first-principle calculations,<sup>190</sup> and concluded that this transition is promoted by charge redistribution due to electronic excitations combined with formation of vacancies under the beam and build-up of the associated mechanical strain.

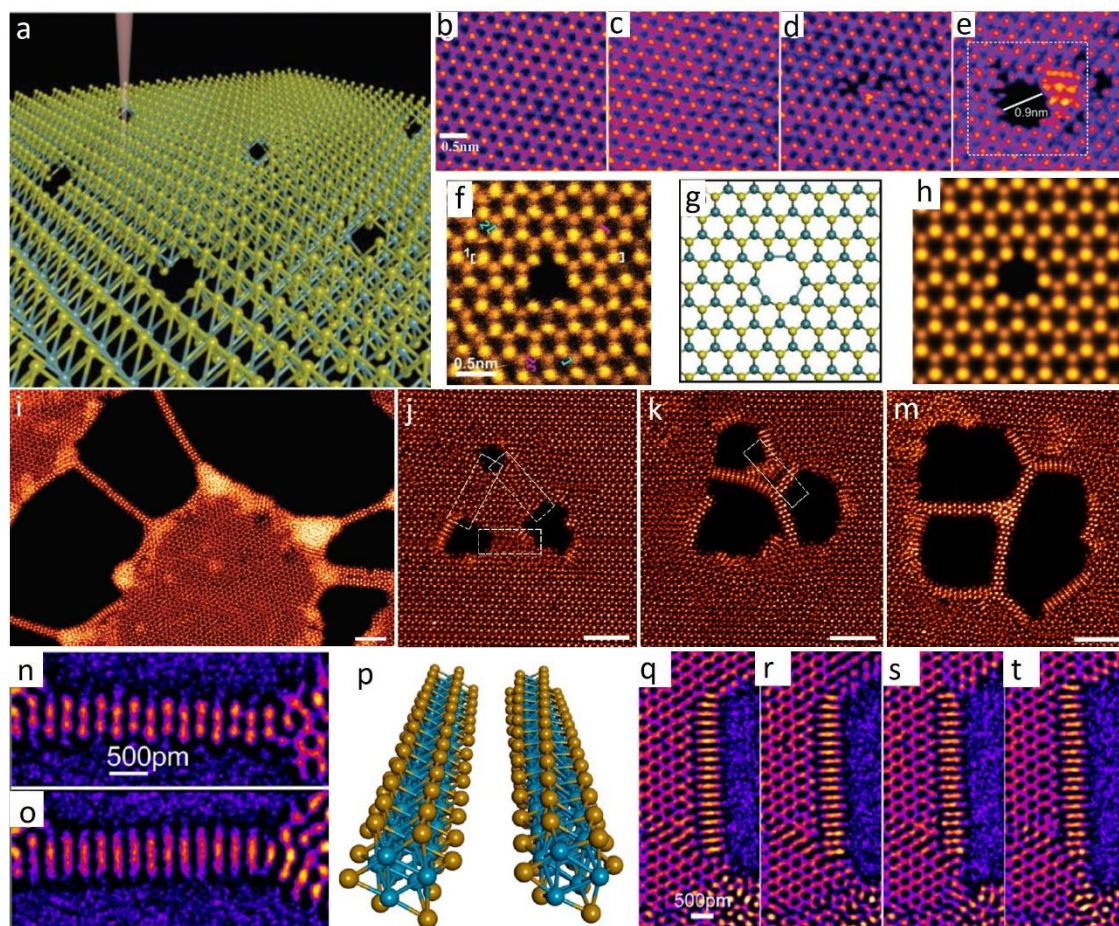


**Figure 2.12** Electron beam sculpted nanopores and nanowires in TMDs. (a-h) Controlled creation of sub-nanometre pores in monolayer MoS<sub>2</sub>. (a) Schematic illustration of the electron beam drilling process. (b-e) ADF-STEM images showing step-by-step drilling of a nanopore in monolayer MoS<sub>2</sub>. (f) Ultra-small nanopore by displacing a single Mo atom. (g) DFT-calculated atomic model corresponding to f. (h) Image simulation based on g. (i) Pattern of a MoSe nanowire network. (j-m) Sequential ADF images of the fabrication process of Y-junction of MoSe nanowires. (n,o) AC-TEM images of a suspended MoS wire in monolayer MoS<sub>2</sub> (n) before and (o) after a whole rotation about its long axis. Time between images is 1 s. (p) A 3D perspective view of pristine and twisted MoS wires. (q-t) Series of AC-TEM images showing the dynamics of a MoS wire located at the edge of monolayer MoS<sub>2</sub>. Time between frames is ~0.5 s. (a-h) Reproduced with permission from ref.<sup>184</sup> © 2017 The Royal Society of Chemistry. (i-m) Reproduced with permission from ref.<sup>191</sup> © 2014 Nature Publishing Group. (n-t) Reproduced with permission from ref.<sup>192</sup> © 2016 American Chemical Society.

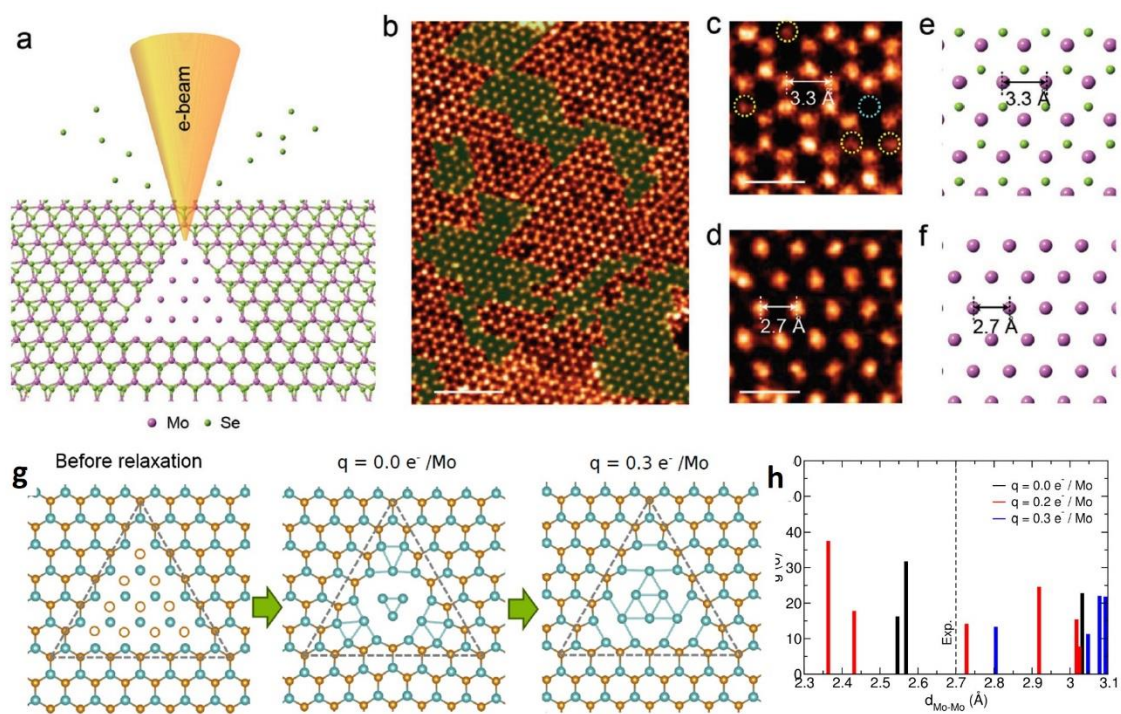


**Figure 2.13** Electron beam fabrication of monolayer Mo membranes. (a) Schematic illustration of the Mo membrane by sputtering of Se atoms from a monolayer MoSe<sub>2</sub> film. (b) ADF-STEM image of the fabricated Mo membranes in the monolayer MoSe<sub>2</sub> films at accelerating voltage of 80 kV. (c,d) ADF-STEM images showing a monolayer MoSe<sub>2</sub> film (c) and monolayer Mo membrane (d). Corresponding in-plane Mo–Mo distances in the monolayer MoSe<sub>2</sub> film (c) and the monolayer Mo membrane (d) Atomic models of the monolayer MoSe<sub>2</sub> film (e) and monolayer Mo membrane (f). Scale bars: 2 nm in (b), 0.5 nm in (c, d). (g,h) Theoretical investigation of the pure Mo membrane structure. (g) Illustration of the evolution of the metal membrane structure upon introduction of additional charge, showing that extra charge increases inter-atomic distances. (d) Radial distribution function for the neutral and charged system. (a-f) Reproduced with permission from ref.<sup>193</sup> © 2018 WILEY-VCH Verlag GmbH & Co. KGaA. (g,h) Reproduced with permission from ref.<sup>194</sup> © 2019 American Chemical Society.

Focused electron beam irradiation can locally sputter S atoms, which also destabilizes the Mo bonding and causes Mo displacement to the surface, diffuse away and then open up the metal vacancy site. The ability to spatially control defect formation is integral to successful nano-engineering of their properties. Increasing electron beam irradiation can cause the formation of voids in 2D TMDs.<sup>184,195-196</sup> ADF-STEM images in Figure 2.12a-e show step-by-step drilling of a nanopore nucleated from Mo atoms ejection induced by S vacancy, as reported by Wang *et al.*<sup>184</sup> Reducing electron beam dose rate for irradiation can lead to just single metal atom loss (Figure 2.12f-h). The holes

opening up is caused by the creation of large number of S vacancies, and when the holes keep expanding with more S sputtered away, the excessive metal atoms cluster around the edges. This leads to the edge structures of monolayer TMDs transformed to be the unique MoS wires before the local area ruptures (Figure 2.12i-t).<sup>183,191-192,197</sup> These subnanometer wires are flexible, self-adapting, and can rotate their entire crystal structure under electron beam irradiation (Figure 2.12n,o), or can also have torsional rotation effects that are that help the self-adapting nature during growth and contraction of the wire (Figure 2.12q-t).

In contrast to the nanopores and nanowires that are sculpted with the ejection of chalcogen atoms and subsequent migration of both chalcogens and metals in the 2D TMDs, there could also be selective ionization etching by controlling the electron beam, which can result in novel reconstructed phase. Zhao *et al.* reported the Mo pure metal membrane fabricated from MoSe<sub>2</sub> monolayers atom by atom *via* the electron beam ionization of Se atoms by STEM at low accelerating voltage of 80 keV (Figure 2.13a-f).<sup>193</sup> Their *in-situ* observation demonstrated that the initiating stage of this fabrication process was the formation and aggregation of numbers of Se vacancies. There remained metallic Mo clusters in the lattice with enhanced conductivity which impeded the further ionization damage. Those Mo clusters developed to be close-pack hexagonal structures composed of Mo atomic plane with a reduced lattice constant (2.7 Å in contrast to the original 3.3 Å in MoSe<sub>2</sub>). As indicated in the following DFT theoretical calculation by Joseph *et al.*, this pure metal film is expected to be a corrugated structure instead of a flat plane, although the hexagonal configuration is not the most energetically favourable structure, with a square lattice having the lowest energy when the system is neutral.<sup>194</sup> However, this hexagonal metal matrix can be stabilized by charge transfer, which can give rise to the theoretical lattice constant close to that in the experiments of Zhao *et al.*,

as shown in Figure 2.13g,h.

In addition to the *in-situ* lithography function, the electron beam in (S)TEM can also be utilized to manipulate phase transformation of the layered TMDs (Figure 2.14). This is often achieved when the chalcogen atoms are ejected progressively under continuous beam irradiation with large energy transferred to the atoms overcoming the sputtering threshold or ionization effects. The resulted different atomic ratio between the two elements are then followed by structural reconstruction, forming a new crystalline phase with the stoichiometry distinct from that of the initial TMD phase. This mechanism is seen in the phase transition from few-layered tin dichalcogenides ( $\text{SnS}_2$ ) to the anisotropic orthorhombic monochalcogenides ( $\text{SnS}$ ) reported by Sutter *et al* (Figure 2.14a).<sup>198</sup> They observed the structural change after sample continuously exposed to electron beam with energy of 80, 200, and 300 keV in the HRTEM, as shown in Figure 2.14b,c, regardless of the operating temperature (room temperature or moderate annealing temperature of  $\sim 300^\circ\text{C}$ ). It is proposed that the transformation started from the assembly of vacancies into ordered S line defects, then formed a S-deficient intermediate state of  $\text{Sn}_2\text{S}_3$ , finally converting to the  $\text{SnS}$ . Another example of phase change derived from periodic accumulation of chalcogen vacancy lines is seen in the fabrication of 2D  $\text{Mo}_2\text{S}_3$  from  $\text{MoS}_2$  using the electron beam in STEM.<sup>199</sup> In contrast, a different mechanism of phase transition *via* interlayer fusion was presented by Lin *et al* regarding layered  $\text{PdSe}_2$  reconstructing to form a novel 2D  $\text{Pd}_2\text{Se}_3$  monolayer phase.<sup>200-201</sup> Figure 2.14e presented the schematic illustration of this mechanism, with the *in-situ* observation of this beam driven process step by step shown in Figure 2.14f. The continuous Se loss upon extended electron beam exposure resulted in the gradually decreased interlayer distance in layered  $\text{PdSe}_2$  due to its strong interlayer binding, enabling the melding between two adjacent layers and the establishment of the new stoichiometry which proved to be monolayer

$\text{Pd}_2\text{Se}_3$ . This beam-driven interlayer fusion mechanism provides more possibilities of exploiting novel-phase 2D materials from parent layered materials with moderate van der Waals coupling effects.

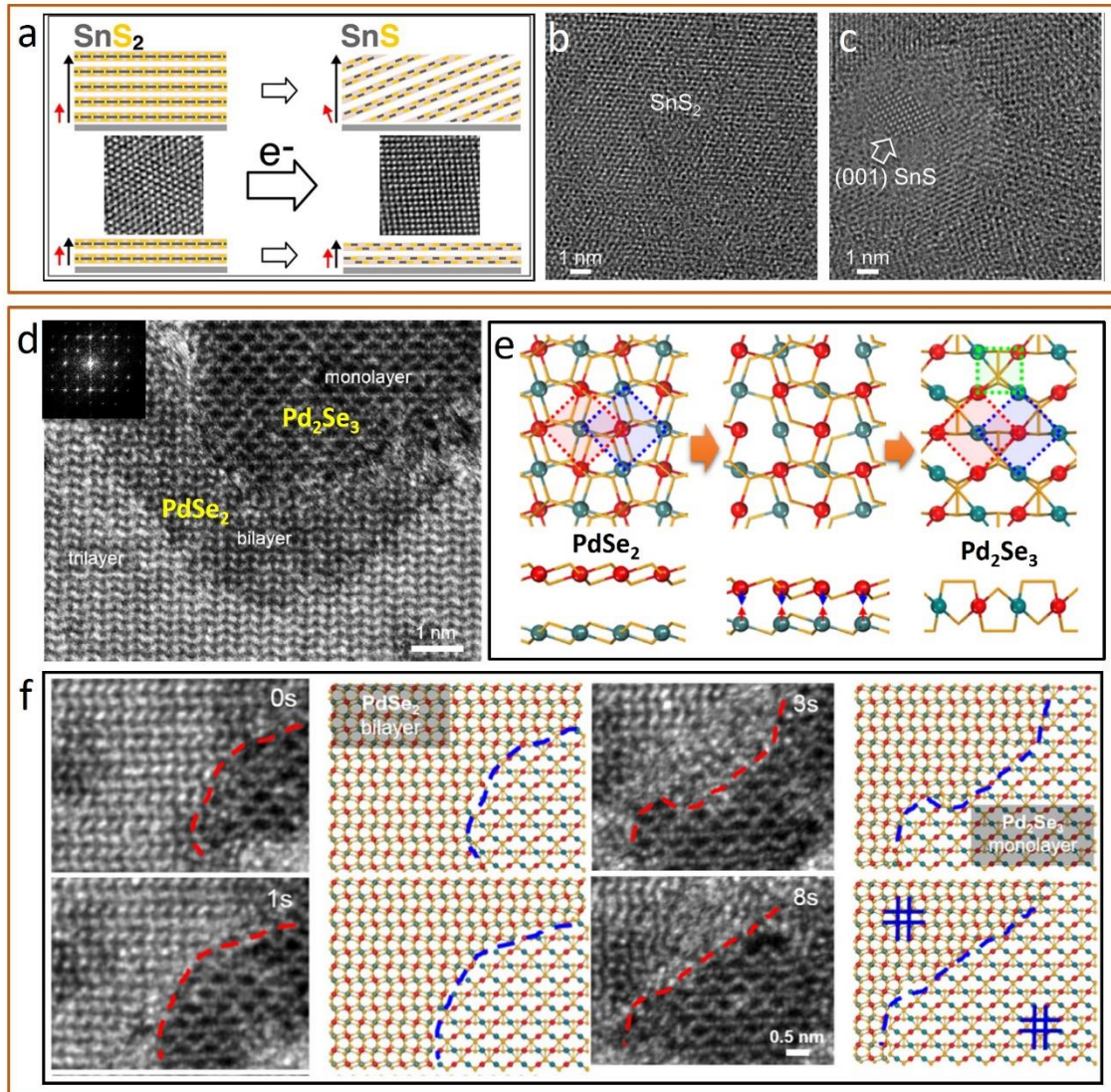


**Figure 2.14** Electron beam induced phase transformations of layered TMDs. (a) Schematic illustration and (b-c) sequential HRTEM images showing the phase transformation from few-layered  $\text{SnS}_2$  to  $\alpha\text{-SnS}$  crystal under electron beam irradiation. (d-f) E-beam driven phase transition from layered  $\text{PdSe}_2$  to 2D  $\text{Pd}_2\text{Se}_3$  monolayers. (d) ADF-STEM image of exfoliation of layered  $\text{PdSe}_2$  sample, where the monolayer region exhibits  $\text{Pd}_2\text{Se}_3$  lattices. (e) Schematic illustration of the interlayer fusion mechanism from bilayer  $\text{PdSe}_2$  to monolayer  $\text{Pd}_2\text{Se}_3$ . (f) Sequential ADF-STEM images showing this reconstruction process. (a-c) Reproduced with permission from ref.<sup>198</sup> © 2016 American Chemical Society. (d-f) Reproduced with permission from ref.<sup>200</sup> © 2017 American Physical Society.

#### 2.4.2 Thermally Controlled Modification by *In-Situ* Heating

Apart from the study of the beam-driven structural change dynamics at room temperature, the development of *in-situ* heating technique in (S)TEM has enabled the real-time investigation of the high-temperature behaviours of 2D materials. Thermal annealing during operating (S)TEM can be utilized to remove carbon contamination so as to revealing the dynamics without interference from surface contamination, as well as provide thermal energy that can activate the vacancy diffusion and increase the atom motion of the radiation-enhanced surface diffusion.<sup>202</sup> In addition, some theoretical studies suggest the knock-on irradiation effect is relevant to temperature which can affect displacement cross section of the atoms, with the impacts from thermal perturbation of atoms from their equilibrium positions and the variation in the momenta of the atoms neighbouring the displaced atom.<sup>203-204</sup> Considering this, the knock-on effect in causing defects in 2D TMDs under the beam is expected to be facilitated by heating the sample to very high temperature like 800 °C which provides extra kinetic energy, although the resulted atom motion is likely to be much smaller compared with the high-energy incident beam.<sup>202</sup> Qu *et al.* reported the ultralong 1D defect channel triggered by *in-situ* heating, which differed from the beam-driven line defects at room temperature.<sup>117</sup> As illustrated in Figure 2.15, at ambient temperature the S vacancies migration rate is limited thus the reported line defects at normal conditions are mostly short in length with separate distributions. While at high temperature (~800 °C), thermally driven fast diffusion of S vacancies result in ultralong (~60 nm) 1D S vacancy lines at high vacancy densities, which was reported to serve as the channels for rapid atomic migration for initiating void formation.<sup>167</sup>

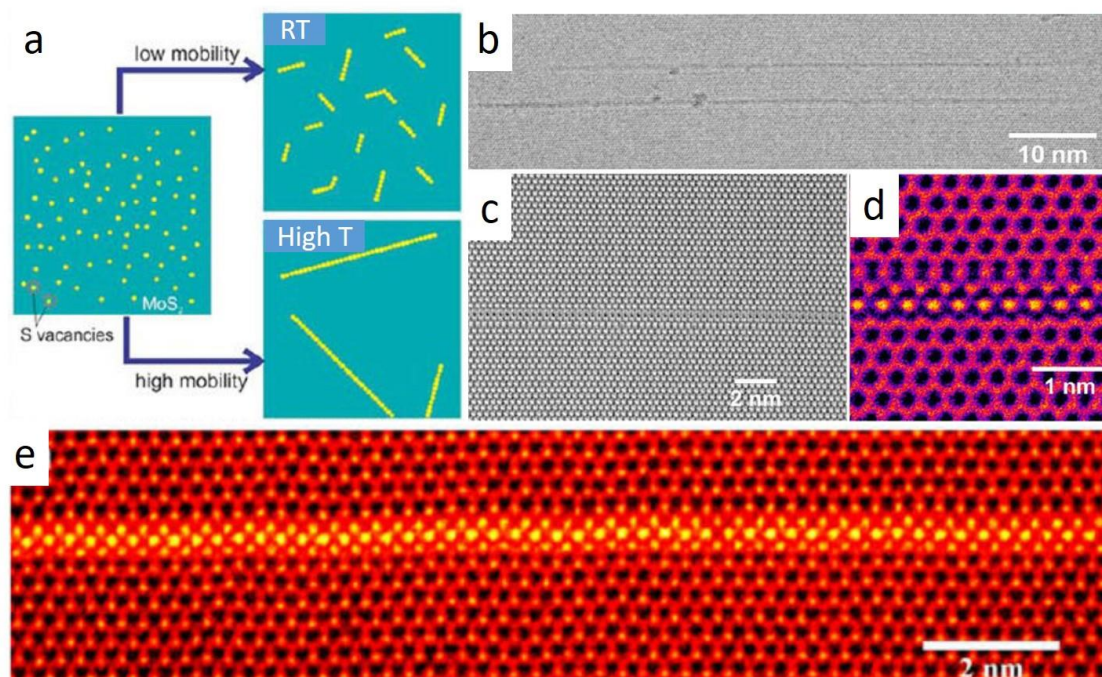


**Figure 2.15** Thermally triggered formation of ultralong 1D defect channel by *in-situ* heating. (a) Schematic diagram showing how S vacancy aggregate into short or long 1D defects for different motilities. Low mobility occurs at room temperature, and high mobility occurs at 800 °C. (b) Phase contrast AC-TEM image of MoS<sub>2</sub> at 800 °C, showing two ultralong line defects. (c,d) Higher-magnification AC-TEM images, and (d) false coloured ADF-STEM image at 800 °C of an ultralong line defect in MoS<sub>2</sub>, showing uniform atomic periodicity. Reproduced with permission from ref.<sup>117</sup> © 2018 American Chemical Society.

Thermally triggered defect formation, migration, and repair were also observed *in-situ* in the planar GBs in 2D TMDs. In the MoTe<sub>2</sub> 2D crystals, the high-concentration 60° inversion domain GBs were generated when heating the sample to 400 °C.<sup>205</sup> As reported by Zhao *et al*, the overlapping GBs in bilayer and few-layered MoSe<sub>2</sub> can migrate and vanish driven by thermal annealing to 700 °C, which finally gave rise to the healing of the stacking inconformity and disordered faults (Figure 2.16a).<sup>206</sup> Their *in-situ* heating STEM experiment traced the gradual sliding of GBs (Figure 2.16b-d), and they argued that the driving force for GB migration was the gain in interlayer binding energy for forming a more stable phase with homogeneous stacking registry. This report highlights the utilization of *in-situ* thermal treatment for investigating defect repair in 2D TMDs.

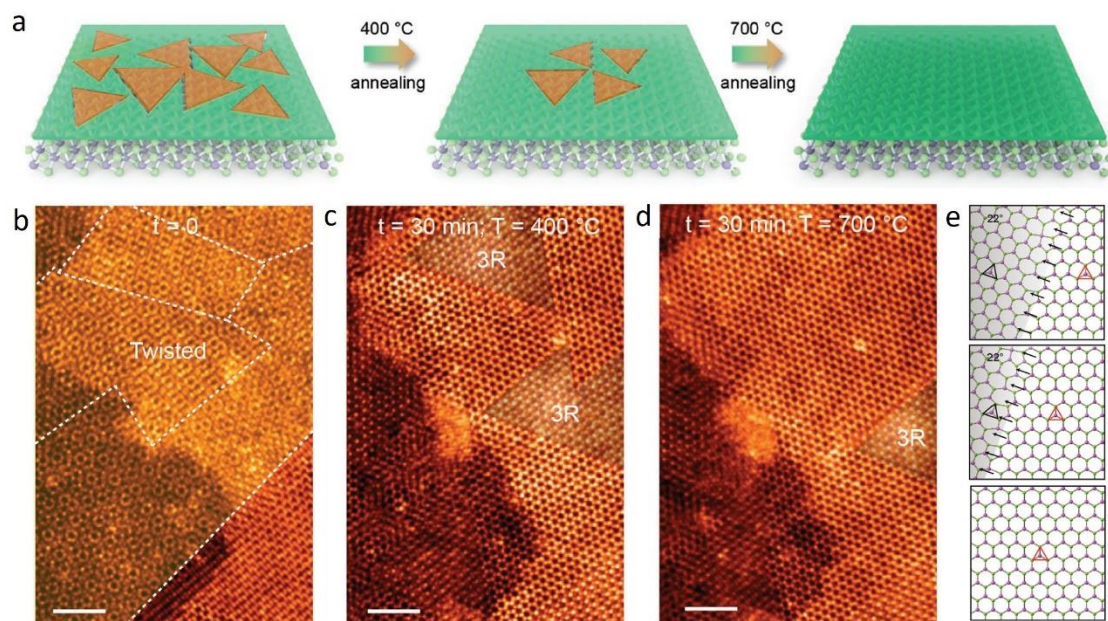


**Figure 2.16** GB migration-induced healing of stacking faults upon *in-situ* thermal annealing. (a) Schematic illustration depicting the MoSe<sub>2</sub> grain growth *via* GB migration and subsequent vanishing upon thermal annealing up to 700°C. (b-d) ADF-STEM images of (d) before, (e) after *in situ* heating at 400 °C, and (f) 700 °C. The stacking fault first transformed into the 3R stacking at 400 °C and ultimately transformed into the 2H stacking at 700 °C. (e) Corresponding schematic illustration of this process. Reproduced with permission from ref.<sup>206</sup> © 2019 WILEY-VCH Verlag GmbH & Co. KGaA.

Some layered materials can experience phase transitions upon heating to high temperature before entire collapse or melt, particularly for those possessing rich phase diagram with different atomic ratios before melting point. For example, the metallic Mo<sub>6</sub>Te<sub>6</sub> nanowires can form from multilayered 2H-MoTe<sub>2</sub> driven by thermal-activated phase transition (400–500°C) under vacuum.<sup>205,207-209</sup> The *in-situ* heating (S)TEM enables the deduction of the exact thermal degradation temperature, rate and mechanism. By intentionally manipulating the annealing process, it is promising to achieve controlled structural modification of the materials with *in-situ* monitoring of the transition process. Recently, Ryu *et al.* reported a thermally driven phase transition of 2D few-layered PtSe<sub>2</sub> into ultrathin 2D nonlayered PtSe crystals with *in-situ* atomic-scale observations, as shown in Figure 2.17.<sup>210</sup> The structural change was driven by Se loss and stoichiometry

modification upon annealing to 550°C, involving the mechanism of lateral diffusion and atomic digestion, yielding the PtSe crystals that are thicker than the original PtSe<sub>2</sub> layered precursors. This process is different from the afore-mentioned interlayer fusion mechanism in the other noble metal TMDs, PdSe<sub>2</sub>, owing to the stability of the 1:1 metal:chalcogen intermediate phase in Pt:Se before forming the pure metal. This demonstrated how the *in-situ* heating can be used to create new ultrathin materials using 2D layered precursors controllably.

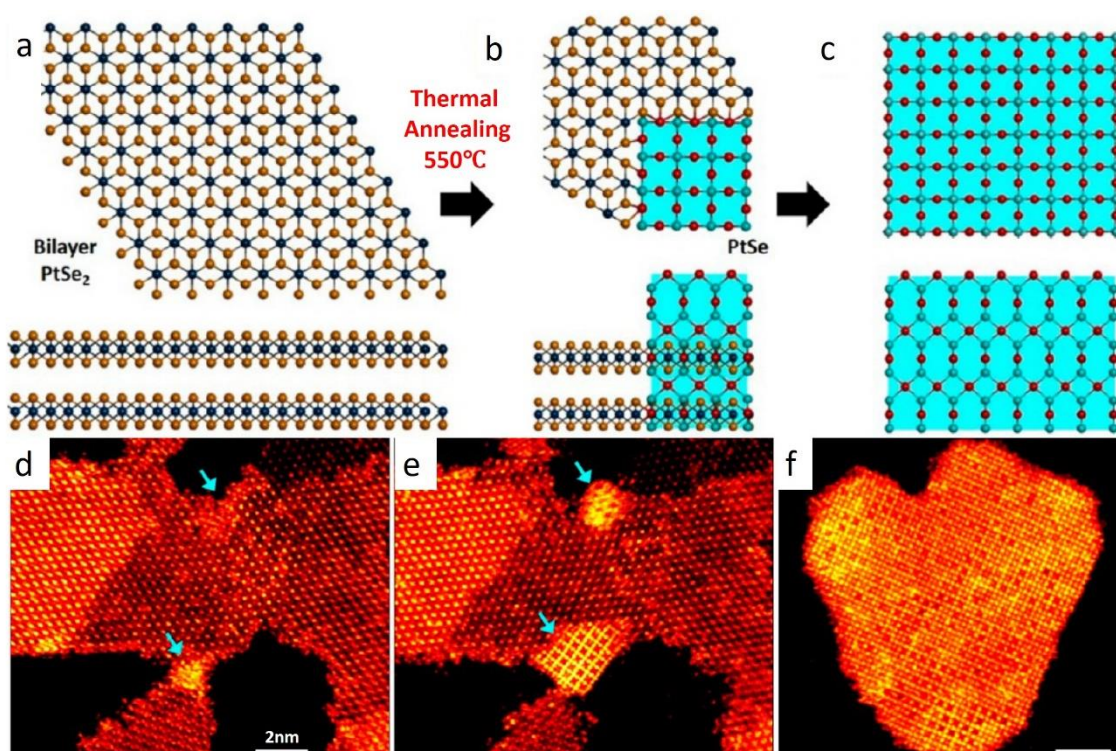


**Figure 2.17** Thermally controlled phase transition by *in-situ* heating. (a-c) Schematic illustration of the phase transition process of 2D few-layered 1T PtSe<sub>2</sub> into ultrathin 2D non-layered PtSe crystals by thermal annealing at 550 °C. (d-f) ADF-STEM images showing the phase transition from the edge of the bilayer PtSe<sub>2</sub>, and finally perfectly transformed PtSe nanoparticle after the heating. Reproduced with permission from ref.<sup>210</sup> © 2019 American Chemical Society.

## 2.5 Conclusion

Recent studies on the defect structures in monolayer/bilayer TMDs by using electron microscopy are reviewed in this chapter, including the intrinsic defects of different

dimensions and configurations, and the *in-situ* materials modification methods in (S)TEM. The noteworthy development in the AC-TEM and ADF-STEM technologies enables them to be powerful tools in identifying a wide range of defects in 2D TMDs with single-atom resolution. The influences of defects, either synthetically brought about or electron beam induced, are significant on altering the electrical, magnetic, vibrational, optical and chemical properties of materials. What is encouraging is that these effects can be beneficial in certain cases, like improved transport behaviour caused by some 1D defects acting as metallic channels or the higher electrochemical reactivity enabled by edge terminations.

The electron beam illumination when imaging can enable atoms to overcome displacement energy threshold and produce vacancies, or may also bring about some other effects like ionization, so the impact of high-energy beam on the TMDs need to be carefully evaluated for analysing the origin of defects and their dynamics. Also, controlling the dose of irradiation beam is critical for the manipulation of the type and density of defects. The research interest is increasing in the *in-situ* modification of materials in (S)TEM in recent years, particularly in the *in-situ* high temperature study. The exploration of materials modification driven by electron-beam or thermal annealing TMDs for obtaining novel structures offers more opportunities to enrich the library of 2D materials.

So far, significant progress has been made in the study of defects on TMDs, although we are possibly only witnessing the tip of the iceberg. The three-atom thick nature of layered TMDs and various stacking modes provide more possibilities for complex defect configurations. It is expected that more interesting work will continue to arise on exploring new defect structures in the continuously expanding family of 2D TMDs, particularly towards the intentional manipulation of the defect structures at the atomic

scale and their impact on the material properties, which could be desirable as well as challengeable. In particular for the extreme conditions like ultrahigh temperature, future work will further give insights on the defect and lattice evolution mechanisms by *in-situ* electron microscopy techniques. A better understanding of the manipulation of defects will advance the field of defect engineering in 2D materials and targeted applications.

## Chapter 3

### Methodology

#### 3.1 Introduction

This chapter introduces the experimental and analytical methods specifically used in my research project. This will cover materials synthesis technique *via* chemical vapour deposition (CVD) method, TEM samples transferring process, optical microscopy (OM) and SEM characterizations of the as-prepared samples, TEM operation procedures including *in-situ* modification methods involved, as well as typical data processing methods. To clarify, I have done the sample preparation including CVD synthesis, transfer, OM, SEM and STEM operation for obtaining images, while the CVD furnace set up and recipes were developed by the senior group members, and I followed the previous recipes with minor adjustment of the parameters like the distance between the substrate and the precursors. The TEM systems have been maintained well and corrected from time to time by the supportive scientists in EM centre of the Oxford Materials and in Diamond Light Source, including Dr Ian Griffiths, Dr Neil Young, Dr Christopher Allen, and Dr Judy Kim, just to name a few, so that I am able to operate the TEM and get the data as planned. The theoretical calculations of DFT and MD simulations were done by the collaborator, Dr Gang Seob Jung at Massachusetts Institute of Technology, and I put the detailed methods and process in section 3.6.3 for repeatability of my work.

#### 3.2 CVD Synthesis of TMDs

##### 3.2.1 CVD Growth of Monolayer MoS<sub>2</sub> Films

The CVD system used for TMD growth is composed of two independent furnaces and two quartz (Figure 3.1). Here the two furnaces are used to control temperature separately on the precursors and substrate, and two different-diameter quartz tubes with one inside the other (1 in. diameter for the outer tube, and 0.6 in. diameter for the inner tube).

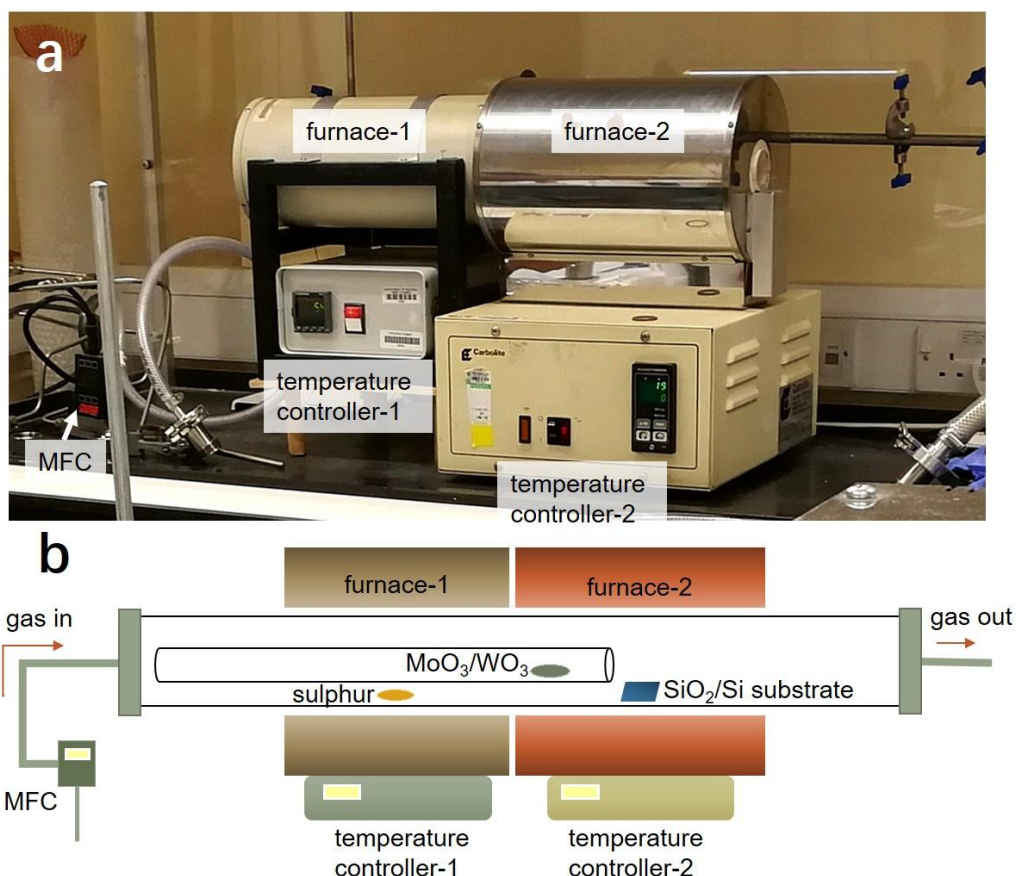


**Figure 3.1** (a) A photo graph of the two-furnace system equipped in our laboratory for CVD growth. (b) A schematic diagram showing the CVD setup for MoS<sub>2</sub> or WS<sub>2</sub> films growth.

To grow MoS<sub>2</sub> monolayers, argon (Ar) was used as carrier at atmosphere pressure. Molybdenum trioxide (MoO<sub>3</sub>, ≥99.5%, Sigma-Aldrich) of 20 mg and sulphur (S, ≥99.5%, Sigma-Aldrich) powder of 300 mg were utilized as the precursors to growth MoS<sub>2</sub> on a Si substrate with 300 nm-thick SiO<sub>2</sub> on the surface. The substrate is cleaned with acetone and isopropanol, followed by O<sub>2</sub> plasma for 5 min, then placed horizontally into the outer quartz tube and located at the centre of Furnace-2. S powder was loaded in the outer quartz tube at the Furnace-1 midpoint, while MoO<sub>3</sub> was in the inner tube with a distance of ~11

cm to the tube flow exit. This After flushing with 500 sccm Ar for 30 min, Furnace-1 was heated to 200 °C to pre-introduce S vapour, and Furnace-2 was heated up to 800 °C, maintaining for 15 min under 150 sccm argon flow, and then another 25 min under decreased flow of 10 sccm before the growth stopped. The fast-cooling process is then done by moving the tube so that the substrate is away from the heating zone with the increase the Ar flow of 500 sccm. After finishing fast cooling, monolayer MoS<sub>2</sub> grown on the SiO<sub>2</sub>/Si substrate was collected.

### **3.2.2 CVD Growth of Monolayer/bilayer WS<sub>2</sub> films**

A similar strategy was used for growing WS<sub>2</sub> thin films. Sulphur (S, ≥99.5%, Sigma-Aldrich) powder of 300 mg was loaded in the outer quart tube at the centre point of Furnace-1. Tungsten trioxide (WO<sub>3</sub>, ≥99.9%, Sigma-Aldrich) of 200 mg was inserted in the inner tube at the central heating zone of Furnace-2. Si substrate with 300 nm-thick SiO<sub>2</sub> was pre-cleaned by acetone and isopropanol, followed by short O<sub>2</sub> plasma, then horizontally placed in the outer quart tube at the further downstream position of Furnace-2 with a calibrated distance to WO<sub>3</sub>. Firstly, the two tubes were flushed with 500 sccm Ar for 30 min. Then, Furnace-1 and Furnace-2 were heated up to 180 °C and 1145 °C, respectively, maintaining the temperatures for 6 min as the WS<sub>2</sub> growth stage under 250 sccm Ar flow, and then stopped the growth by decreasing the flow to 10 sccm and lowering the temperatures. After a fast cooling process, the WS<sub>2</sub> samples grown on the SiO<sub>2</sub>/Si substrate were collected.

### **3.2.3 Synthesis of PtSe<sub>2</sub> films by Pt Selenization**

The two-furnace CVD system was also used for PtSe<sub>2</sub> growth using direct selenization method of ultrathin Pt layer at the atmospheric pressure. An ultrathin Pt layer of 10nm

thickness was first deposited on top of a 300 nm SiO<sub>2</sub>/ Si chip *via* e-beam evaporation. Selenium powder (Se, 20 mg, ≥99.5%, Sigma-Aldrich) and the substrate with uniform Pt coating were loaded in a 2 inch-diameter quartz tube, which were placed at the centres of two split furnaces, respectively, for individual temperature controls. The system was sealed and flushed with a 500 sccm argon (Ar) flow for 30 min in order to drive off all the reactive gases such as oxygen. After that, the Se and substrate were ramped up to 230 and 260 °C, respectively. Ar of 110 sccm was used as the carrier gas to transport the Se vapor downstream to the substrate surface. The temperatures had then been maintained for 10 min since they were reached. Next, the substrate was heated up to 350 °C, at which the selenization began. This process lasted for 20 min, leading to formation of PtSe<sub>2</sub> thin films. Finally, the reaction ended up by slow cools of both the Se and the as-produced PtSe<sub>2</sub> at elevated Ar flow rate of 500 sccm.

### **3.3 Transfer of TMDs**

To transfer the as-prepared TMDs onto the SiO<sub>2</sub>/Si substrate, a thin film of poly(methyl methacrylate) (PMMA, 8% wt. in the anisole, 495k molecular weight) was firstly spin-coated on the surface of TMD/SiO<sub>2</sub>/Si substrate taken from the CVD furnace. The rotation speed of the main spin-coating stage was set to 4500 rpm (round per minute) for 50 seconds. Then edge the substrate covered by PMMA was scratched carefully using a fine diamond drill to expose the SiO<sub>2</sub> beneath the PMMA before putting the sample onto 1 mol L<sup>-1</sup> potassium hydroxide (KOH) solution, floating on the liquid surface and etching for several hours until it peeled off. This process was done at room temperature, and the time requested for peeling can vary from 6h to 24h, depending on the coverage of the CVD-grown domains and the extent of edge scratch of the substrate. Subsequently, PMMA/TMD film was scooped up and placed on the deionized ion (DI) water which was

renewed repeatedly for at least three times, with 30 min in between. The rinsed PMMA/TMD film was transferred onto a TEM grid, dried at room temperature overnight, which was then baked at 150 °C for 30 min. Note that when I use the heating chip with Si<sub>3</sub>N<sub>4</sub> membrane, the baking time can increase to 45 min to enhance the adherence between the sample and the Si<sub>3</sub>N<sub>4</sub> membrane. Finally, the TEM grid was rinsed in acetone for over 24 h to remove PMMA.

### **3.4 Optical Microscopy and Scanning Electron Microscopy**

Optical microscopy (OM) is often used for direct observation of the CVD grown TMD samples in large scale, which is particularly useful for checking the shapes of the TMD films, size distribution, the nucleation density, and the homogeneity of the layer thickness based on the layer-dependent optical contrast in the OM image. For characterizing the samples in my DPhil project, I primarily used the OM system of the CMOS camera (DCC1645C Thorlabs high-resolution 1280×1024 CMOS camera with a color sensor) with the Mitutoyo objective lens (50×magnification). Figure 3.2a presents a typical OM image of the MoS<sub>2</sub> on SiO<sub>2</sub>/Si substrate grown by CVD methods, in which a number of triangular MoS<sub>2</sub> domains with the average size of approximately 90µm in side length are distributed across the substrate, and the homogeneous contrast manifest the uniformity of the layer number of each domain. The brighter dots in the centre of the domains are attributed to the tiny MoS<sub>2</sub> nucleation on the substrate at the beginning of growth.

Scanning electron microscopy (SEM) is an important tool in characterizing the surface topography of the material surface. It collects the signals from the secondary electrons (SEs) which are generated by the incident beam on the material surface within a few nanometres. In my project, field emission scanning electron microscope of Hitachi S-4300 was conducted for imaging micrometre-scale morphologies of the as-grown TMD

specimens, using the accelerating voltage of 3 kV with a beam current of 10  $\mu\text{A}$ , which enables clearly imaging the surface structure of the 2D TMDs with minimal electron charging and irradiation damage. Figure 3.2b presents a typical SEM image of the CVD-grown  $\text{MoS}_2$  on  $\text{SiO}_2/\text{Si}$  substrate corresponding to the OM image in (a), which further confirms the domain sizes layer number and film continuity of the samples.

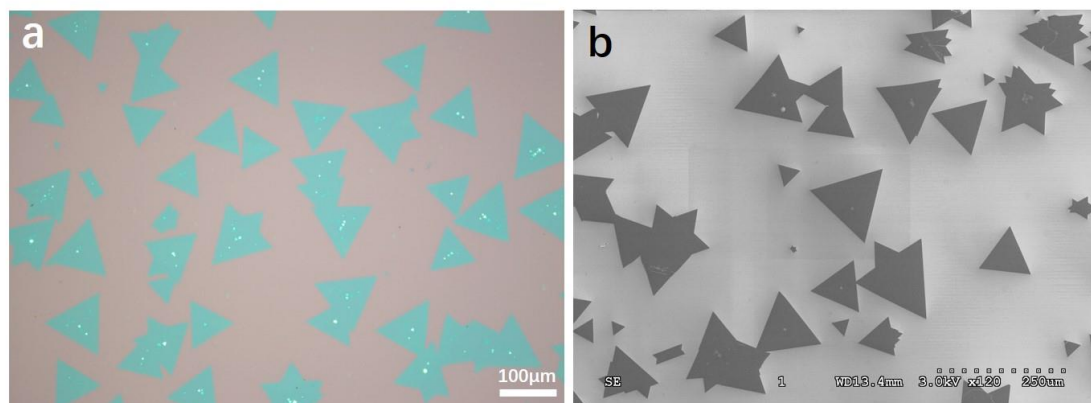


**Figure 3.2** (a) OM and (b) SEM image of the CVD grown  $\text{MoS}_2$  domains on  $\text{SiO}_2/\text{Si}$  substrate.

## 3.5 Transmission Electron Microscopy

### 3.5.1 Annular Dark Field-Scanning Transmission Electron Microscopy

TEM is one of the most powerful characterizing technologies in terms of atomic characterization of thin materials, including phase contrast high resolution TEM and STEM. A typical setup of the TEM and its ray diagram is exhibited in Figure 3.3a. The first part is the components overhead the sample which are used for preparing specific electron beam to illuminate the specimen. At the classical TEM mode, the electron beam generated are normally parallel, by applying several condenser lenses (C1, C2, etc.) and the upper objective lens system. The other part below the specimen is utilized for the collection, selection, and magnification of the transmitted or scattered electron signals.

In STEM, focused electron beam ( $\sim 1 \text{ \AA}$ ) rather than parallel beam is used in raster-

scanning over the specimen to produce an image, which can probe the 2D materials atom by atom. As illustrated in Figure 3.3b, a detector on axis (BF detector) or an annular detector (ADF detector) is used to gather the scattered electrons after interacting with the specimen so as to construct BF or ADF images. By placing off-axis annular detectors with different selecting angle ranges, specific STEM images, like low angle annular dark field STEM (LAADF-STEM) or high angle annular dark field STEM (HAADF-STEM), can be obtained with corresponding electrons scattering angles gathered. The ADF-STEM image is known as the Z-contrast image as its contrast goes with  $Z^{1.6-2}$ , which can directly distinguish the different elements.<sup>211-213</sup> In this project, I mainly use the ADF-STEM as a straightforward strategy in imaging 2D TMDs materials comprised of more than one element which can be sharply determined by different Z-contrasts.

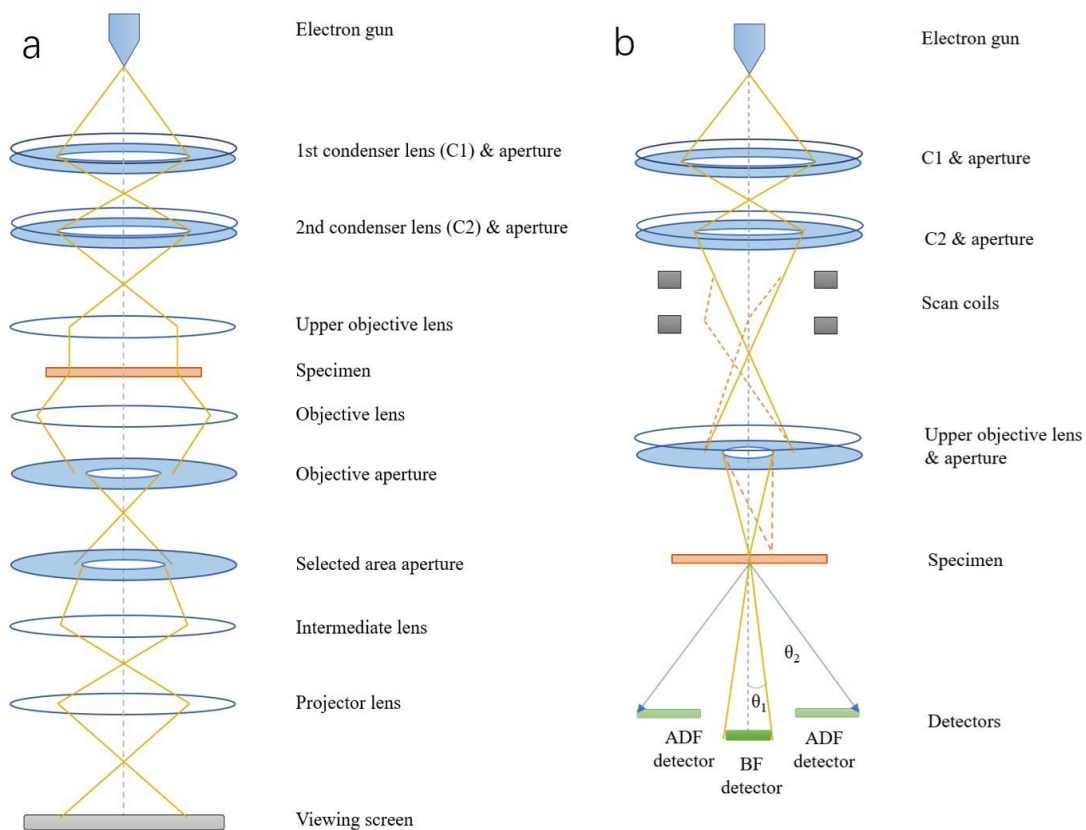


**Figure 3.3** Schematic illustration of (a) basic TEM setup and ray diagram, (b) compared STEM setup and ray diagram, showing ADF and BF detector setup with different electron scattering angles for imaging in a STEM.

When producing high resolution images in (S)TEM, many parts of the microscope have potentially negative influences on the electron wave. The most significant limiting factors in the resolution are imperfections in the way the electrons are focused. These imperfections mainly include spherical aberration ( $C_s$ ), chromatic aberration ( $C_c$ ) and astigmatism. If objective lens is perfect with no aberration, the wavefront in the diffraction plane should be spherical centred at the image point, while the imperfect formation of the magnetic field or the unavoidable aberrations of round electron magnetic lenses can result in spherical aberrations of various types, which have severe influence on the resolution. The wave aberration function is used to describe the how the actual aberrated wavefront is shifted away from the ideal spherical wavefront  $W(\omega)$ , which can be expanded as a Taylors series (Eq.3.1), with  $\omega = \lambda \mathbf{k} = \lambda k e^{i\varphi}$  as a complex variable ( $\mathbf{k}$  is the reciprocal space vector at the diffraction plane).<sup>214-215</sup> The coefficient like  $A_{1,2,3}$  in each term of the Taylors series represents one type of aberration from low to high orders. The specific notations corresponding to the types of aberrations are given in Table 3.1.

$$W(\omega) = Re \left\{ A_0 \omega^* + \frac{1}{2} A_1 \omega^{*2} + \frac{1}{2} C_1 \omega^* \omega + \frac{1}{3} A_2 \omega^{*3} + \frac{1}{3} B_2 \omega^{*2} \omega + \frac{1}{4} A_3 \omega^{*2} \omega^2 + \frac{1}{4} S_3 \omega^{*3} \omega + \frac{1}{4} C_3 \omega^{*2} \omega^2 + \dots \right\} \quad \text{Eq(3.1)}$$

**Table 3.1** Aberration coefficient up to forth order and the target values for alignment

| Coefficient | Aberration modes       | Order in $\omega$ | Target values |
|-------------|------------------------|-------------------|---------------|
| $A_0$       | Image shift            | 1                 | /             |
| $A_1$       | Two fold astigmatism   | 2                 | <1nm          |
| $C_1$       | Defocus                | 2                 | /             |
| $A_2$       | Three fold astigmatism | 3                 | <50nm         |
| $B_2$       | Axial coma             | 3                 | <20nm         |
| $A_3$       | Four-fold astigmatism  | 4                 | <1 $\mu$ m    |
| $S_3$       | Axial star aberration  | 4                 | <1 $\mu$ m    |
| $C_3$       | Spherical aberration   | 4                 | <1 $\mu$ m    |

In my research, I mainly operated the aberration corrected JEOL STEM of ARM series for ADF-STEM imaging, including the JEOL ARM-200F STEM with a cold field emission source (CFEG)  $C_s$  probe corrector with resolution capability at 80kV accelerating voltage, which is situated at David Cockayne Centre for Electron Microscopy (DCCEM) in Department of Materials at University of Oxford, and the JEOL ARM-300CF STEM equipped with a JEOL ETA corrector at the electron Physical Sciences Imaging Centre (ePSIC) at Diamond Light Source with the low-voltage capability down to 60kV. Both are equipped with  $C_s$  correctors capable of well correcting aberrations to the third order with high accuracy. In principle, the way that a corrector compensates for spherical aberration in a magnetic lens is to construct a deviating lens which spread out the off-axis beams in order to re-converge them to a point, rather than a disk in the Gaussian image plane. Taking the ARM-200F STEM as an example, the  $C_s$  aberration correctors consist of pairs of hexapoles designed by CEOS, which is integrated in the probe-forming system between the last condenser lens and the objective lens, with the optical design depicted in Figure 3.4a.<sup>216</sup> The corrector system mainly consists of two principal hexapole elements (HP1, HP2) and five transfer lenses (TL11/TL12, TL21/TL22, ADL). The beam is firstly deformed by the first hexapole and then projected into a second hexapole that compensates for this deformation leaving only a higher order effect, which acts like a negative  $C_s$ , compensating for the opposite effect (positive  $C_s$ ) in the objective lens. By adding the two components together, the total  $C_s$  of the two modules can be adjusted to various values. Once the corrector system is not far from an aligned state, the (auto-) alignment tools can be used to compensate for the parasitic aberrations measured from the probe-tableau method. The calculation involved in this method is composed of measuring the propagation of an electron wave through a phase plate (phase shift image) and the calculation for the intensity of the resulting wave, where

the phase shift is caused by the coherent axial aberrations from  $A_1$  to higher orders. As the complete electron intensity distribution can be given by the incoherent superposition of the distributions for the individual energies, the influence of the various axial aberrations on the shape and on the electron intensity distribution within the probe can be calculated. The tableau consists of an initial Gaussian image and deconvoluted under- and over-focused probe shapes with incident beams of tilted angles. Measurements are taken with varying values for the ‘outer tableau tilt’ and changing the azimuths step by step. Then, the phase plate is calculated from the aberration coefficients of the last measured probe tableau for different outer tilt angles. Figure 3.4b gives an example of the visualized phase plate.

In my alignment using the diffractogram tableau method at ARM-200F with the CEOS corrector, a thin amorphous area is predefined at a magnification of  $\sim 600K$ , and the tableau is operated for several runs with a tilted incident beam of 32 mrad at the enhanced mode (recording 21 diffractograms). For each run it automatically records series of diffractograms corresponding to different beam tilt angles for correcting  $C_s$  based on the wave aberration function by the software. When each tableau run finishes, a phase plate with the values of aberration coefficients is given as an indicator for further corrections, as illustrated in an example in Figure 3.4. The alignment needs to run a couple of times, and each time it needs around 3 min to finish the measurements in the typical enhanced mode. The alignment degree is judged by whether the coefficients are reaching the targeting “good” values shown in Table 3.1. Note that we consider the coefficients to be acceptable as long as they fall into the rough range of the suggested “good” value. For example,  $A_1$  in the range of 1–5nm should be acceptable. Figure 3.4d gives a good example of the coefficients obtained after running the corrector for several times. With the aberration coefficients well-corrected, the high-resolution ADF-STEM images were

taken on a clean WS<sub>2</sub> monolayer to check the sharpness of the contrasts (Figure 3.4e), where the brighter and dimmer contrasts were yielded by W and S atoms, respectively.

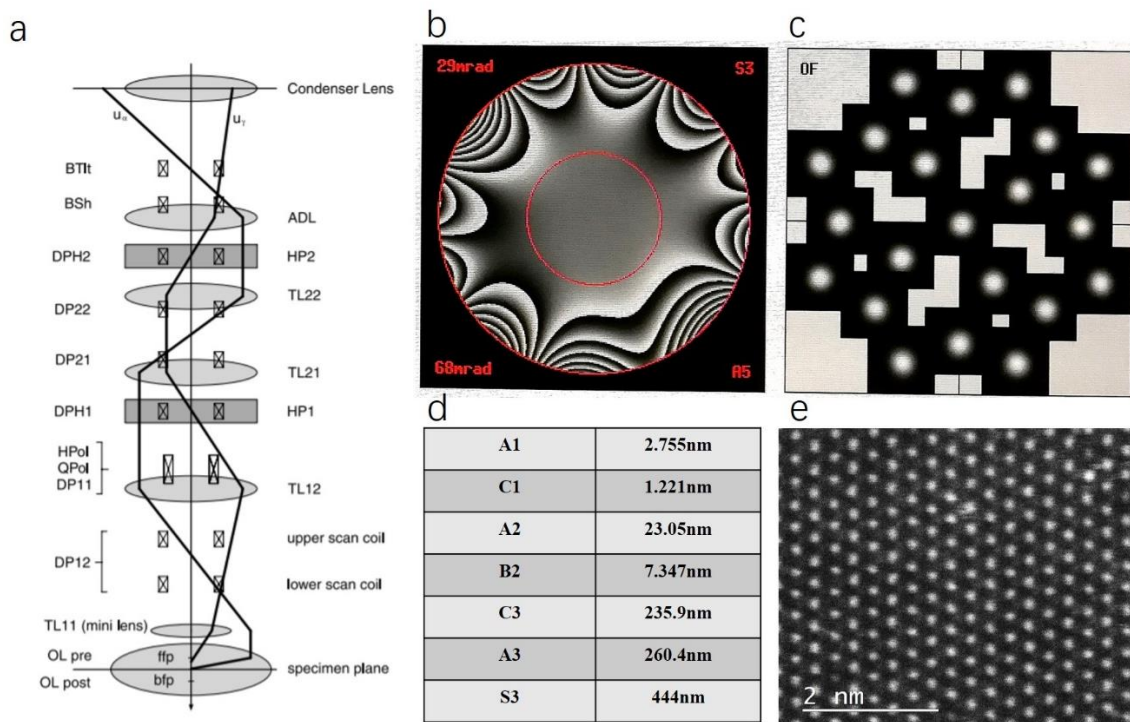


**Figure 3.4** (a) Schematic of the optics of a hexapole STEM corrector with transfer lenses TL, adaptor lens ADL, hexapole elements HP, alignment deflectors DP, beam tilt BTlt, and beam shift BSh coils, and stigmators QPol, HPol. (b-d) A diffractogram tableau obtained by running C<sub>s</sub> corrector with an outer tilt angle of 32 mrad. (b) Phase plate, (c) over-focused diffractograms, and (d) the corresponding values of aberrations. (e) An image of monolayer WS<sub>2</sub> lattice captured after this correction. (a) Reproduced with permission from ref<sup>216</sup> © 2016 Microscopy Society of America.

Apart from the aberration correction, the ADF-STEM image quality is also associated with the selection of the collection angle (inner collection angle and outer collection angle) of the annular detectors relative to the convergence semi-angle ( $\alpha$ ) of the electron probe. This involves the trade-off between the  $Z$ -contrast and the SNR of the images. By changing the of the collection angle, the  $n$  values in  $Z^n$  dependence contrasts and the signal-to-noise ratio (SNR) can be manipulated. High inner collection angle ( $>3\alpha$ ) ensures  $Z$ -dependence sensitivity which avoids coherent effects like diffraction contrast or contrast reversal, so as to sharply distinguish different elements, *e.g.* to detect individual impurity atoms in crystals, whilst at the expense of SNR, because fewer

electrons are scattered to high angles. Considering the very small signals of highly scattered electrons from atomically thin 2D materials, it is particularly important to ensure enough SNR with the minimum tolerable inner collection angle when imaging them.

In this research project, the experimental ADF-STEM imaging in Chapter 4 and 6 were operated using JEOL ARM-200F at the accelerating voltage of 80kV. A dwell time of 10–18  $\mu\text{s}$  was used for imaging with a pixel size of  $0.006 \text{ nm px}^{-1}$ , beam current of 35 pA, convergence semi-angle of 22.5 mrad, and collecting angles of 73–271 mrad (inner-outer angles). For Chapter 5 and 7, the ADF-STEM experiment was conducted using JEOL ARM-300CF at the accelerating voltage of 60kV. The dwell time of 10–20  $\mu\text{s}$  was used for imaging with a pixel size of  $0.006 \text{ nm px}^{-1}$ , beam current of 48.5 pA, convergence semi-angle of 39.1mrad, and acquisition angles of 56.4–207.1 mrad (inner-outer). Basically, the drift artefacts are unavoidable during STEM imaging, whilst it can be negligible in terms of recognizing the vacancies and defects in the materials when the sample and stage have stabilized for enough time (e.g.  $\sim 1\text{h}$ ). This can be qualitatively determined by looking at the pristine region in the lattice in the STEM images by checking the corresponding diffraction spots whether the hexagons can be symmetric in all directions. The images used for defect analysis in chapters 4-7 have been selected with negligible drift artefacts.

### **3.5.2 *In-Situ* Heating Technique**

*In-situ* heating experiments was conducted at the increased temperature up to 900 °C utilizing a commercial *in situ* heating holder (DENS Solutions, SH30-4M-FS), and TEM heating chips (DENS Solutions, DENS-C-30) imbedded with a platinum resistive coil in the central area covered by a thin  $\text{Si}_3\text{N}_4$  film, as shown in Figure 3.5a,b. Slits were cut into the thin  $\text{Si}_3\text{N}_4$  membranes on the heating chips by using focused ion beam (FIB)

milling, with the size of  $0.6 \times 3 \mu\text{m}$  each (Figure 3.5c). Figure 3.5 d-f shows the distribution of the  $\text{WS}_2$  samples overlaid on the heating chip, where the slits in the TEM windows are well-covered by the  $\text{WS}_2$  triangular domain. Sample was heated by controlling a current through the platinum coil, whose resistance was detected in a four-point contact device, and the temperature was calculated according to the Callendar-Van Dusen equation with the calibration coefficients from the manufacturer.

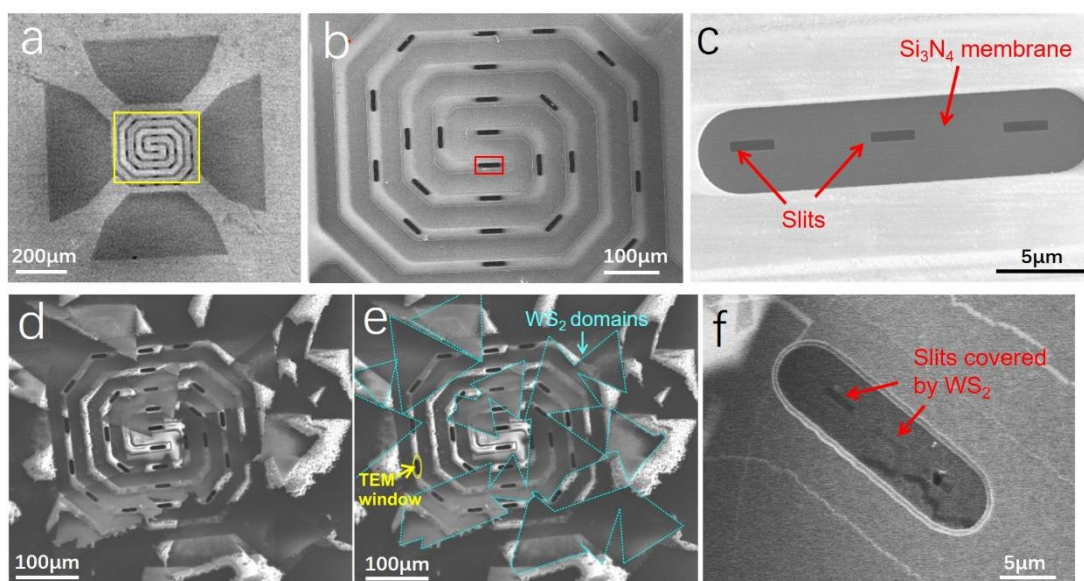


**Figure 3.5** SEM images of the overall and detailed structures of the heating chips with slits manufactured by FIB (a-c) before and (d-f) after transferring  $\text{WS}_2$  samples, with (e) highlighting the  $\text{WS}_2$  domains overlaid on TEM windows.

During the *in-situ* heating experiment in STEM imaging, the sample stage and the focus need to adjust finely when increasing the temperature over  $500 \text{ }^\circ\text{C}$  as there could be slight buckling of the coils with temperature change. The target temperature can be reached in a second whilst it is better to increase the temperature by  $50 \text{ }^\circ\text{C}$  each time so as not to cause crack of the samples due to sharp temperature change.

### 3.5.3 *In-Situ* Electron Beam Patterning

Chapter 5 involves the *in-situ* electron beam patterning experiment for atomically thin

nanowell patterns, which are essentially obtained by drilling single-layer nanopores out from bilayer WS<sub>2</sub>. For the patterning process, a small box was defined onto a limited area, typically a  $\sim 150 \times 150$  pixel box covering a  $\sim 2 \text{ nm} \times 2 \text{ nm}$  area (these values can be modified with varying areas of the whole region) with a longer dwelling time of  $\sim 35 \mu\text{s}$  per pixel for higher dose irradiation in the reproducible nanowells drilling. We controlled the drilling time from 20 s to 320 s to give adjustable electron dose for obtaining different-sized nanowells at 800 °C, and also compared the pore production difference when changing the temperature to 300 °C. After drilling at a given time, we took a typical ADF-STEM image of the whole region or recorded images consecutively to evaluate the beam damage on the drilled nanowells under the fast scanning. The *in-situ* observation of the samples enables us to track the atom displacement during drilling and monitor the progression of the pore creation.

## **3.6 Data Analysis and Simulation**

### **3.6.1 Image Processing and Simulation**

The ADF-STEM images were processed using Image J software package, which includes various filtering regimes to remove noise. In a typical imaging process in my project, a Gaussian blur filter with a blur radius of 1–2 pixels was applied to the ADF-STEM images of  $1024 \times 1024$  pixels to smooth the images and enhance the contrast of atoms without affecting the interpretation of the original image. The Gaussian filter is essentially a 2D convolution operator that is used to 'blur' images. The blur radius values of the filter correspond to the radius of the 2D Gaussian operator it uses for the smoothed fitting. In applying the Gaussian filter, the image is convolved with a Gaussian function in the real space, which can be regarded as using the weighted average of a spot's neighbourhood as the new value for this spot. This convolution operation corresponds to multiply the

Fourier transform of this image with another Gaussian function in the reciprocal space. As a result, this filter can remove noises from high spatial frequencies and at the same time preserve the edge features better than other uniform blurring filters. The false colours were performed using false colour look up tables (LUT) on some of the original greyscale images to increase the visual contrast. For the false-coloured ADF-STEM images in each chapter, chapters 4-5 applied a LUT of “Gem”, chapter 6 applied “Gem” and “Red hot” and chapter 7 applied “Orange hot”. Finally, the contrast and brightness were adjusted. The atomic models were constructed by using CrystalMaker X and Accelrys Discovery Studio Visualizer software. Then the atom coordinate values in the atomic models were converted using Python scripts (written by Dr Christopher S. Allen) into a readable format for JEMS simulation software. ADF-STEM image simulations were carried out using the multislice method implemented in the JEMS software (programmed by Dr P. A. Stadelmann), in which the multislice approximation is conducted by dividing the input crystal into a series of consecutive sub-nanometre slices in order to imitate the multiple scattering as the electrons propagate through the specimen.<sup>217-219</sup> The multislice algorithm mainly consist of two steps, the diffractor (transferring the incident wave function by one slice), and the propagator (propagating between slices and convoluting by the Fresnel propagator). As a result, the interaction of the electron wave with each slice is combined in order for image formation with the intensities given by incoherent illumination (optical transfer function) for the STEM image simulations. Multislice simulations in JEMS are started by selecting the *Multislice* menu item of the *Imaging* menu. When first activated the *Multislice* dialogue sets the zone axis to [0,0,1]. Many parameters can be adjusted to take into account different alignment qualities and experimental imaging conditions, such as the aberrations, the detector collection angles, defocus and defocus spread. Typically, the slice numbers in the multislice methods in my simulations were set to  $n=c/3$ , where  $c$

represents the unit cell parameter ( $\text{\AA}$ ) in  $z$  direction of the crystal model, with the slice thickness similar to the real  $z$ -direction interlayer spacings of  $\text{MoS}_2/\text{WS}_2$ . Most of the parameters of the simulation were set based on the experimental conditions of the JEOL ARM300CF at accelerating voltage of 60kV or the JEOL ARM-200F at 80kV. Here in JEMS, simulations were taken from the FEI Titan microscope to approximate the conditions for ARM200/300. Two of the most frequently adjusted parameters include defocus and defocus spread. The defocus varies in different images as they were captured at a different  $z$  height. And the defocus spread is associated with the intrinsic energy spread of the electron gun, the fluctuation of the accelerating voltage, as well as the objective lens current. The setting of these two parameters can act as a limit to the image resolution, and can mostly affect how accurate the simulation reflects the experimental data. In a typical simulation of Chapter 4, the chromatic aberration ( $C_C$ ) and spherical aberration ( $C_S$ ) at 60 kV were set to be 0.95 mm and -0.03 mm, respectively. And defocus spread and defocus were set to be 8.5 nm and 9 nm respectively.

### 3.6.2 Strain Analysis

The strain distributions for the ADF-STEM image are evaluated using geometric phase analysis (GPA) method used with Fast Fourier transform algorithms,<sup>220-221</sup> which quantitatively measures the variation the crystal periodicity of reciprocal space vector. The 2D strain maps in this project are obtained by performing the GPA tool in the FRWRtools plug-in package developed by the Stuttgart Center for Electron Microscopy, which is installed in the Digital Micrograph software, which is able to compute strain maps from complex wave functions resulting from a high-resolution focal series reconstruction and data stacks. After loading and calibrating the high-resolution STEM images correctly, the GPA tool was started from the plugin. Two spots of the  $\{100\}$

reflections were selected on the Fourier transform by positioning the circular masks and pressing “Read Apertures” to command the tool to read the reciprocal space coordinates of the selected reflections in to the grain. The two parameters, “resolution” which defines the radius of the aperture used, and the “smooth” which represents the outer outer fraction of the aperture radius, can be adjusted for obtaining the gradient maps with different sensitivity and noise levels. In my analysis, resolution was set to 1–1.5 nm and smooth was set to 0. Then a reference area (unstrained lattices) was defined in the phase image. In the GPA process, the magnitude of lattice expansion/contraction is expressed by two directions, x and y, separately. It calculates displacement value difference divided by their location variations along certain directions,  $\partial Ux/\partial x$ ,  $\partial Uy/\partial y$ ,  $\partial Ux/\partial y$  and  $\partial Uy/\partial x$ , referring to the two selected G-vectors (lattice reflections), finally obtaining the 2D gradient maps of the four strain field components, including the normal strain field component along x direction ( $\mathcal{E}_{xx}$ ) and y directions ( $\mathcal{E}_{yy}$ ), and the  $\mathcal{E}_{xy}$  and  $\mathcal{E}_{yx}$  which indicate the 2D shear strain fields. The accuracy of the GPA outcome relies on the input image qualities including resolutions, magnifications and drift artifacts. It can work well in atomic-resolution images without drift artifacts. The GPA results can also be affected by the setting of parameters including the selection of aperture “resolution” and the reference area.

### 3.6.3 DFT and MD Calculations

In the study of bilayer GB in WS<sub>2</sub> (Chapter 4), molecular dynamics (MD) simulations are performed *via* a LAMMPS package.<sup>222</sup> To investigate the mechanical stability of dual GBs in WS<sub>2</sub>, we perform structural relaxation and tensile tests of the geometries obtained from STEM images. A reactive empirical bond order (REBO) style forcefield<sup>223-224</sup> was used to describe the interatomic interaction of WS<sub>2</sub> monolayer. For the parameters for W

and S, we use previously developed ones for the growth of MoS<sub>2</sub> channels.<sup>144</sup> Unlike the monolayers, the interlayer interaction may play a critical role in the bilayer system. The previous DFT (density functional theory) study<sup>225</sup> indicates that the difference of binding energy of WS<sub>2</sub> and MoS<sub>2</sub> has only 10meV/atoms with dispersion correction DFT-D2 and almost same with vdW-DF.<sup>226-227</sup> Also, the interlayer distance of 2H (AA') is the same. Therefore, instead of further tuning of vdW parameters for WS<sub>2</sub>, we utilize the vdW parameters developed for MoS<sub>2</sub> bilayer system, which describes well the binding energy profile as a function of the interlayer distance between two layers.<sup>186</sup>

For the atomic models, we relax the geometries through MD simulations. During the relaxation, we fix the boundaries because the boundaries of models with a finite size are not well bounded and can change due to residual strains coming from the mismatching lattice parameters between TEM and MD. Then, we take one of the unit cells to rebuild the system. We further relax atomic structures of the rebuilt models at 10K for 150ps with the relaxation of the periodic unit length along the  $y$  direction. The periodic boundary condition along the  $z$  direction with enough space is applied to all models to avoid the unphysical interactions between imaginary layers. The non-periodic and shrinkable boundary is used only for the  $x$  direction. After the relaxation, one of the edges parallel to the GB with the width 0.5nm is fixed. The other edge is moved with a constant loading speed with 0.02Å/ps (2m/s). The stress-strain data are recorded during the loading.

To estimate the defect formation energy, we perform DFT calculation with Quantum-Espresso package<sup>228</sup> using Perdew Burke Ernzerhof (PBE) functional<sup>229</sup> and norm-conserving type pseudopotential.<sup>230</sup> The energy cutoff for the wave functions is 60 Ry, and 1×15×1 Monkhost-Pack grids are adopted for the K space sampling. For modeling the isolated ribbon, 15 Å vacuum is inserted to avoid undesirable interaction between periodic images in both  $x$  and  $z$  directions. The structure is relaxed with the fixation of

boundary atoms movement in  $x$  and  $z$  directions and fully relaxed along the  $y$  direction. We note that there is residual strain due to the fixed boundary atoms, but the 4|6 dislocation and its nearest atoms are fully relaxed under a given GB. We introduce the sulfur vacancy at A, B, Ref-A, and Ref-B, as illustrated in Figure 4.12 in Chapter 4, to compare the vacancy formation energy of A and B to the nearest vacancy position. The defect formation energy ( $E_f$ ) is obtained by

$$E_f(\alpha) = E_V + E_S - E_0,$$

where  $E_0$  is the total energy of the reference system;  $E_V$  is the total energy of the system with a S vacancy,  $E_S$  is the energy of isolated S atom;  $\alpha$  is vacancy type with a single S vacancy. For example, A1 is the first vacancy at the position A from pristine, and A2 is the second vacancy at the position A from A1. Here, we do not consider the detailed values of chemical potentials due to S/W rich limit or temperature.<sup>231</sup> Instead, we compare the formation energy at A and B sites with that of the nearest S vacancy position.

## Chapter 4

### Grain Boundaries Involved Defects in MoS<sub>2</sub>/WS<sub>2</sub>

#### Monolayer/Bilayers

Grain boundaries (GBs) of TMDs, including 60° GBs and small-angle tilt GBs, have considerable impacts on their chemical-physical properties. This chapter focuses on the GB-involved defect structures in MoS<sub>2</sub>/WS<sub>2</sub> monolayers/bilayers at the atomic level by using ADF-STEM, including two GB types, namely 60° GBs and tilt GBs. The first part studies the high-temperature formation and dynamics of 60° GBs connected large inversion domains (IDs) in monolayer MoS<sub>2</sub>. *In-situ* heating experiment is conducted at 800°C to thermally activate S vacancy migration and this leads to formation mechanism of IDs different from room temperature. In the second part, the study extends to tilt-GBs in bilayers, showing that tilt GBs in bilayer WS<sub>2</sub> can be atomically sharp, where top and bottom layer GBs are located within sub-nm distances. An *in-situ* heating holder is used and the GBs are stable to at least 800 °C. This expands the current knowledge of GBs in 2D bilayer crystals, beyond the established large overlapping GB types typically formed in CVD growth, to now include atomically sharp dual bilayer GBs.

#### 4.1 60° Grain Boundary Inversion Domains in Monolayer MoS<sub>2</sub>

##### 4.1.1 Introduction

As introduced in section 2.3, the 60° GB is a special type of GB in TMD monolayers owing to their three-fold symmetry, which is formed when two 60° oriented monolayer grains merge together. In monolayer MoS<sub>2</sub> or WS<sub>2</sub>, it comprises 4-member rings and

dislocations, which are calculated to be metallic conducting nanowires embedded in the semiconducting monolayer TMDs.<sup>104,145,147</sup> Experimental results have demonstrated a slightly increased in-plane electrical conductivity and photoluminescence quenching caused by 60° GB.<sup>134</sup> Such distinct transporting properties add useful functionality for engineered GBs rather than a negative role that is more often reported.

Coupled by linear 60° GBs, inversion domains (IDs) with 60° lattice rotation can form locally.<sup>182</sup> It was shown that the MoSe<sub>2</sub> monolayer IDs could emerge with the Se-deficient growth environment and heating condition.<sup>132</sup> The formation of IDs is usually considered to be associated with two factors, the chalcogen deficiency and thermal energy. However, the mechanism of the ID formation at high temperature still needs to be understood, especially the large-scale transformations that occur when long line defects are present. Prior work using ADF-STEM imaging at room temperature showed the electron beam driven formation of IDs in MoSe<sub>2</sub>.<sup>181</sup> These IDs were relatively small (1–2nm) and are surrounded by many other S vacancies, holes, and line vacancies due to the low mobility of S vacancies at room temperature resulting from the high-energy barrier of S vacancy migration.<sup>114,232</sup> This makes it difficult to elucidate the strain dynamics due to the heavily distorted lattice on the larger scale from so many defects in the vicinity.

Recent work has shown that at high temperature (>700°C), thermal energy activates the rapid migration of S point vacancies and they assemble into ultralong line defects.<sup>117</sup> The newly created S point vacancies tend to migrate to join an existing vacancy line rather than start a new one.<sup>117</sup> Therefore the formation process and strain fields of IDs at higher temperatures should be much easier to understand because of the more uniform defect structures. Thermal treatments are usually involved in fabricating and processing monolayer TMDs for opto-electronic devices, so it is crucial to understand the structural transformations that occur at high temperatures and whether IDs can be stable and

controllably formed.

Here, aberration corrected ADF-STEM with an *in-situ* heating stage is used to investigate the mechanism of ID formation and evolution in monolayer MoS<sub>2</sub> at the atomic level under the high temperature of 800 °C. The details of the ID evolution after formation was tracked, including further expansion by GB migration, interplay with the formed void, as well as the final disappearance. The high temperature in this study also ensures a highly clean MoS<sub>2</sub> lattice surface for revealing unambiguous dynamics of the ID without interference from attached contamination.

#### 4.1.2 Results and Discussion

CVD-grown MoS<sub>2</sub> monolayers are transferred to a heating TEM chip, and then heated up to 800 °C *in-situ* when doing ADF-STEM at 60 keV. Figure 4.1a exhibits the ADF-STEM image of a typical inversion domain (ID) formed at 800 °C with electron beam induced vacancies. The IDs formed at high temperature are generally much larger than those formed at room temperature, with a triangular side length of around 20 Mo atoms, compared to 7-10 at room temperature.<sup>132,205</sup> The lattices of Mo and S atoms inside (Figure 4.1b) and outside (Figure 4.1c) the domain have a rotation of 60°, showing the inverted orientations. Two different GB structures are observed at this ID (Figure 4.1d-i). One is composed of a 4|4 edge (4|4E) sharing structure with two rows of single sulphur atoms bridging at the boundary (Figure 4.1d,e), and the other is a 4|4 point (4|4P) sharing mirror twin boundary (Figure 4.1g,h), which are similar to the previously reported boundary structures.<sup>104</sup> These two types of 60° GBs possess the same local stoichiometry, and both were calculated to be energetically favourable (only 0.04 eV/Å difference in energy).<sup>104</sup> Their simulated images in Figure 4.1f,i also show a good accordance with the experimental images.

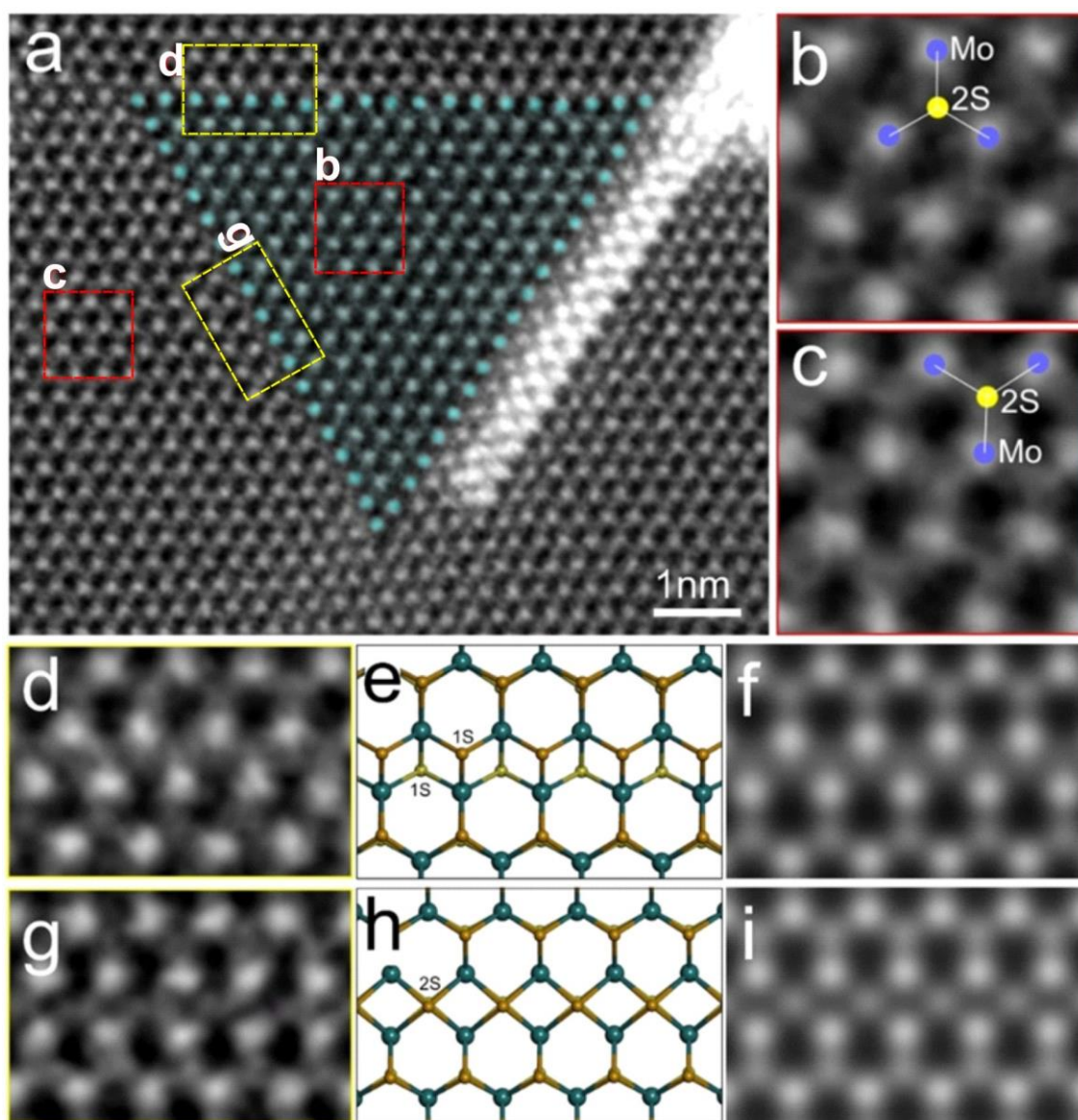


**Figure 4.1** (a) ADF-STEM image of large-area inversion domain (ID) formed at 800 °C in monolayer MoS<sub>2</sub>. The domain size is around 7 nm of the edge length. Cyan dots indicate the edge of the ID. (b, c) Magnified views of the boxed regions in (a), showing the inverted lattice within the ID. (d, g) Magnified views of the boxed regions in (a), indicating two types of ID boundary structures. (e) Atomic model and (f) Multislice simulated ADF-STEM image corresponding to (d). (h) Atomic model and (i) Multislice simulated ADF-STEM image corresponding to (g).

Figure 4.2a-d shows a series of ADF-STEM images obtained at 800 °C that reveal how the ID forms from the S vacancy line defects. At high temperature, the MoS<sub>2</sub> film is clean without surface contamination which has been evaporated. Under the electron beam irradiation, several long sulphur-vacancy lines (SVLs) are produced and grow fast both in number and length (Figure 4.2a-c). The sulphur vacancies are generated in growing

number, which is supposed to mainly result from the combined effect of chemical etching and ionization damage at this low accelerating voltage of 60 kV below the knock-on threshold.<sup>172,174</sup> Those generated vacancies quickly migrate at high temperature, consequently forming an area with a large density of line vacancies crossing each other (Figure 4.2c).

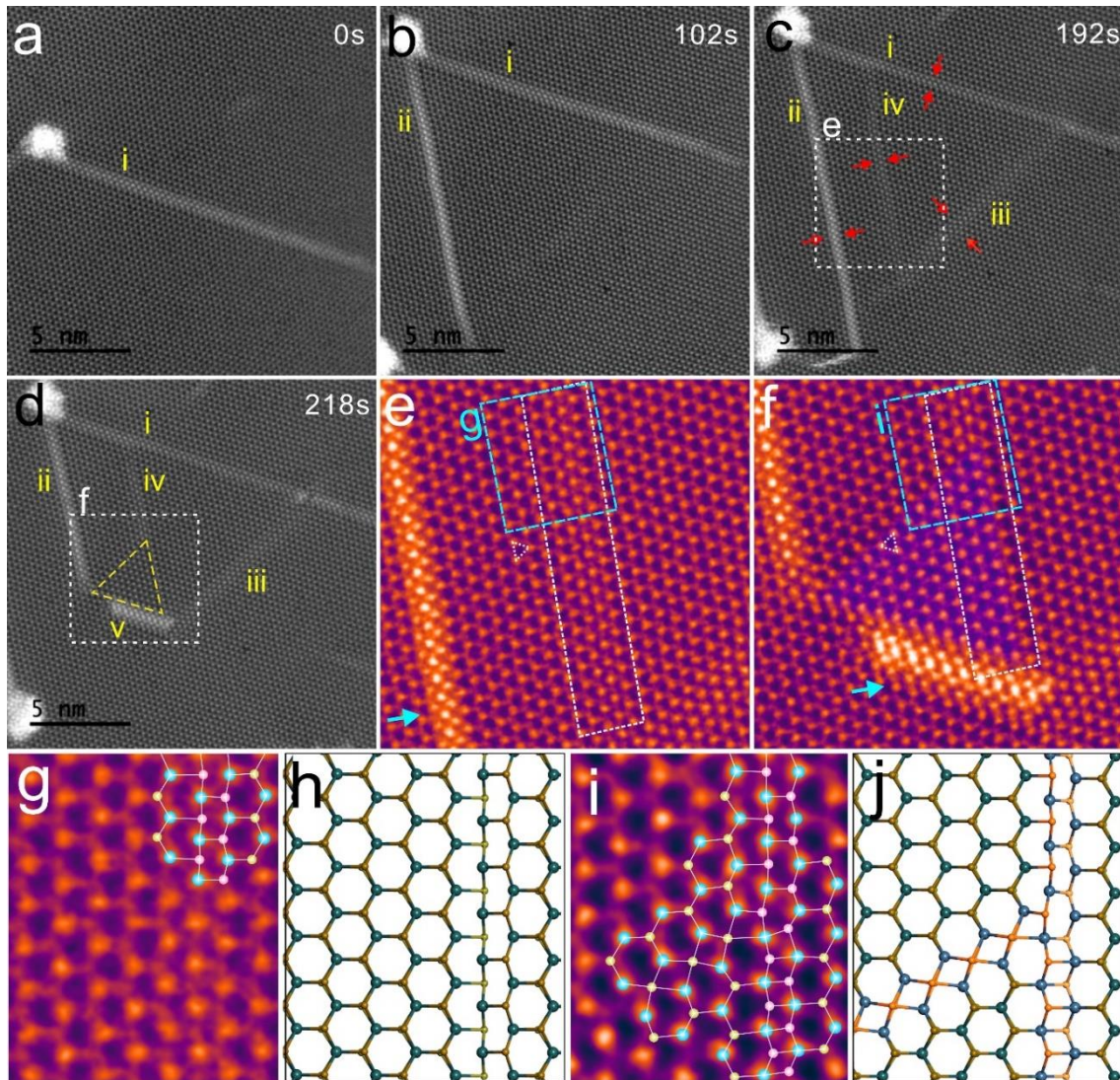


**Figure 4.2** ID formation process at high temperature of 800°C. (a-d) Time series of ADF-STEM images at 800 °C, where i-iv with red arrows represent line defects, and the formed ID is marked by dashed yellow triangle in (d). (e,f) Magnified views of the boxed regions in (c) and (d), shown in false colour, where the atoms in the ID are overlaid by a blue colour mask, and the line defect across this region is marked by white dashed lines. (g, i) Magnified views of the blue-line-boxed regions in (e, f), with schematic atomic models of Mo (blue), 2S (yellow), and single S (pink) atoms overlaid. (h) and (j) The atomic model corresponding to (g) and (i), respectively.

It is noticeable from Figure 4.2d that at the region where several line defects are

intersecting and interacting, a large ID with the size of  $\sim 4$  nm suddenly forms, along with the readjustment of the direction of one of the two SVLs (iv and v). The enlarged views of the lattice involved in the ID before and after formation are presented in Figure 4.2e and 2f respectively, which show a compact SVL (marked by blue arrow) migrates and turns  $120^\circ$ , to the side of the ID triangle, and another 2SVL (SVL losing two sulphur rows, marked by white dashed rectangular) forms the boundary of the domain. This 2SVL structure is highlighted in Figure 4.2g,h, as previously reported.<sup>115</sup> The ID in Figure 4.2f also consists of a 4|4E GB and a 4|4P GB, similar to the previously reported structures.<sup>104</sup> These two GBs are connected in the corner of the ID (Figure 4.2i, j), with the 2SVL being the extending line of the 4|4E GB.

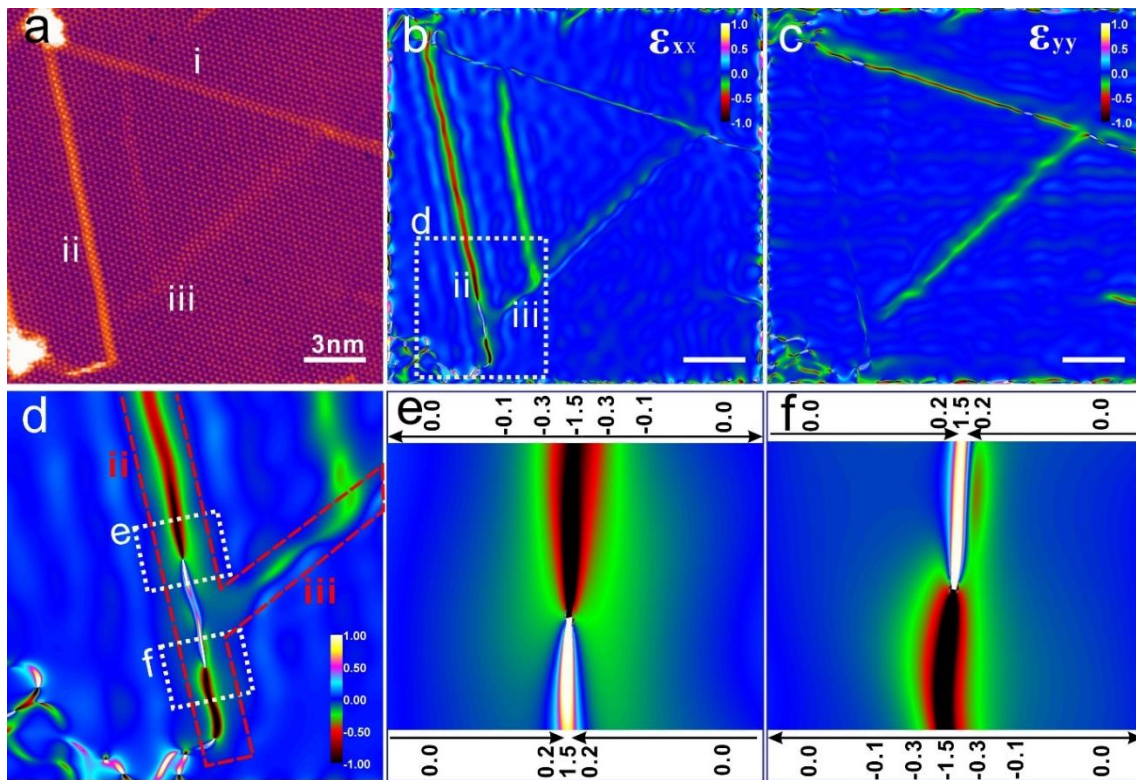


**Figure 4.3** Strain field analysis of line vacancies from Figure 4.2c, i.e before forming an ID. (a) ADF-STEM image prior to the ID formation. Same image as in frame 2c, but in false colour (b,c) Strain components  $\epsilon_{xx}$  and  $\epsilon_{yy}$ , respectively, based on geometric phase analysis of (a). (d) Enlarged view of the boxed region in (b), showing complex strain variation at the region where the tip of SVL (ii) nearly reach SVL (iii). (e, f) Magnified image of the boxed regions in (d) with scales of the strain intensity.

It is common to see SVLs in the vicinity of IDs, and the SVLs form one GB side of

the IDs (Figure A1). Creating an atomic model of an ID without utilizing a SVL (Figure A2), requires significant lattice shrinkage in the pristine MoS<sub>2</sub>. In the experimental data, the SVLs have provided the required lattice contraction, for example, the 2SVL in Figure 4.2f. It can be seen from Figure 4.2a-d that the appearance of the ID is not a simple result of certain point defects or one individual SVL alone, but is related to the whole network of the interlacing line defects.

The strain field is examined on the MoS<sub>2</sub> lattice containing line defects, before ID formation (Figure 4.3). The strain distributions for the ADF-STEM image (Figure 4.3a) are evaluated using geometric phase analysis (GPA).<sup>220-221</sup> Detailed parameters for using GPA analysis is shown in Figure A3. Figure 4.3b and 3c are the obtained strain maps of the normal strain field component along x direction ( $\mathcal{E}_{xx}$ ) and y directions ( $\mathcal{E}_{yy}$ ), respectively. Each SVL in this network gives compressive strain to the adjacent lattice (with colour black, red, and green in the map) in the perpendicular direction, in agreement with the previous report on line defects,<sup>115,167</sup> as well as the GPA analysis on another ADF-STEM image with line defects, which likewise shows compressive strain for each vacancy line (Figure A4). As reported previously, the obvious lattice compression in perpendicular direction of line defects mainly results from the out-of-plane distortions of the lattice with missing S atom rows.<sup>115</sup> The intersecting line defects yield non-orthogonal strains, making the strain fields in this whole lattice complicated. The strain fields in the marked region in Figure 4.2b are particularly strong and complex with several SVL close to each other in an angle of 60°. Interestingly, a distinct strain field is narrowly localized at the small end area of SVLs (ii) and (iii), as highlighted in the large view in Figure 4.3d. The corresponding strain transition points are shown in Figure 4.3e,f. Along the long SVL, the contraction increases from 50% to 150%, then suddenly decays to 0, followed by tension strain varying from 150% to 50% when another SVL is nearly reaching from the

right side, and the strain finally becomes compression strain at the SVL tip. It is at this region indicated by Figure 4.3e, where the ID forms, as marked by red arrows in Figure A5 showing the strain fields before and after the generation of an ID. At the same time, the strain has been reduced at the ID boundary (Figure A5e) compared to the original line defect in Figure A5b.

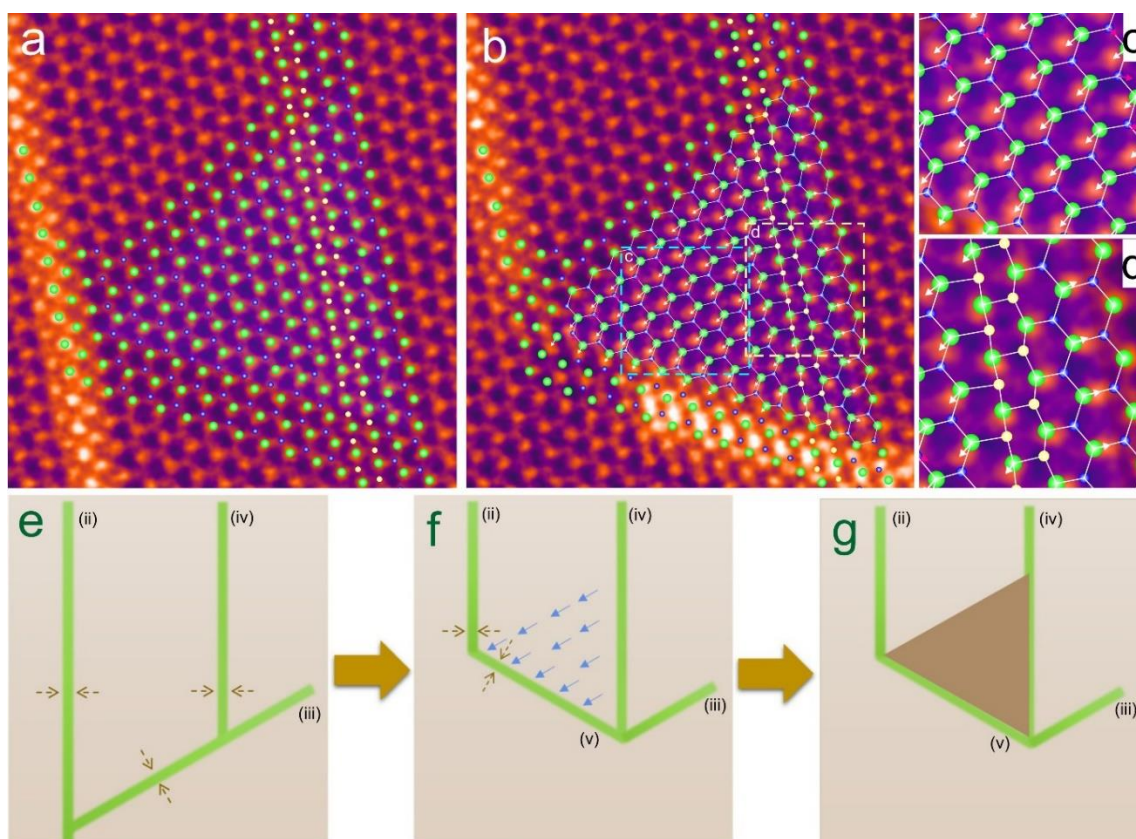
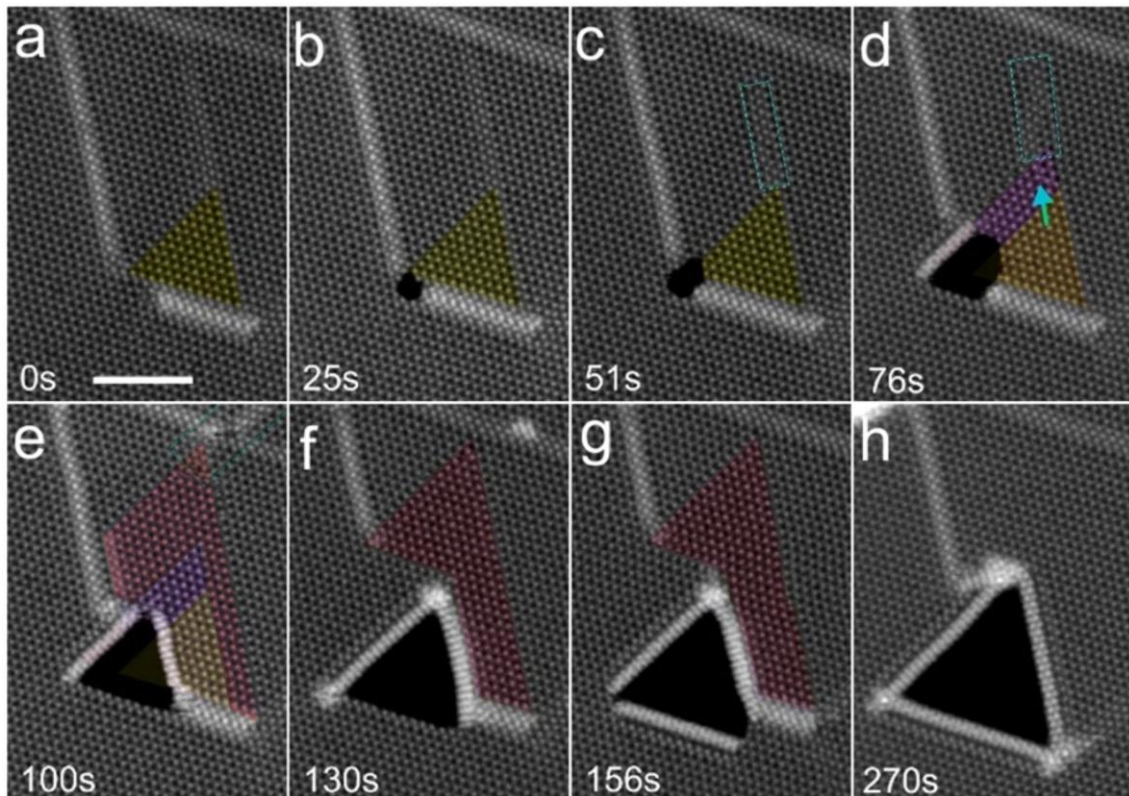


**Figure 4.4** (a, b) ADF-STEM images of (a) pristine and (b) ID region, taken from Figure 4.2 (e,f). (c,d) Expanded view of the boxed region in (b). The schematic atomic models in (a-c) overlaid represent the original position of Mo (green) and 2S (navy) atoms in the pristine structure, showing the structural reconstruction of MoS<sub>2</sub> lattice to form ID, and the displacement direction of these atoms are indicated by arrows. The sulphur vacancies (1S) of line defects are shown by yellow atoms. (e-g) Schematic illustration of the ID formation process corresponding to the transformation from (a) to (b), the green lines represent the line defects, the dashed arrows show their compressive strain, and the blue arrows in (f) signify the shift direction of Mo atoms within ID, corresponding to (b). The roman numerals marked near each line defect correspond to those in Figure 4.2 (c,d).

The lattice change and atomic displacements at this region, required for generating the ID, are displayed in Figure 4.4a-d. The overlaid atoms mark the original positions of Mo and S atoms in Figure 4.4a, and the arrows in Figure 4.4b-d show the atomic

displacements needed for creating the ID. The results show that the atoms in the pristine area have moved towards the two compact SVLs in a  $120^\circ$  angle with intense strain fields, and Mo are the main shifting atoms driven by the need to reduce the strain fields. The Mo atomic displacement value is around  $1.6 \text{ \AA}$ . The transformations from a  $\text{MoS}_2$  lattice with a 2SVL to an ID is illustrated in the schematic models in Figure A6, indicating that the migration of Mo atoms by half a lattice on one side of the 2SVL can create the 4|4E GB and 4|4P GB simultaneously, thus forming the ID. For the 2SVL lattice transforming to the 4|4E GB, only tiny displacements of atoms are needed (Figure 4.4d), suggesting that the presence of 2SVL makes the structural change more feasible. Another example of an ID formation process with similar behaviour of Mo atoms shifting during lattice inversion is presented in Figure A7.

Based on the above analysis of strain fields and the atomic displacements, the schematic illustration in Figure 4.4e-h shows how this ID (Figure 4.2-4.4) forms influenced by the network of line defects. Under high temperature, extended line defects are easily formed and grow along zig-zag lattice directions at  $60^\circ$  until they intersect one another while each of them has a compressive strain field (Figure 4.4e). At the corner when two line defects are approaching, the strain fields become intense and complex, driving the vacancies and atoms to migrate (Figure 4.4e to f). In this crossing region of a line defect network (Figure 4.4f), the strain fields coming from each line defect are non-orthogonal and thus are competing. As a result, the composited strain triggers the displacement of atoms and reconstruction of lattice, finally generating an ID (Figure 4.4g). The high mobility of vacancies at high temperature can also facilitate the reconstruction.



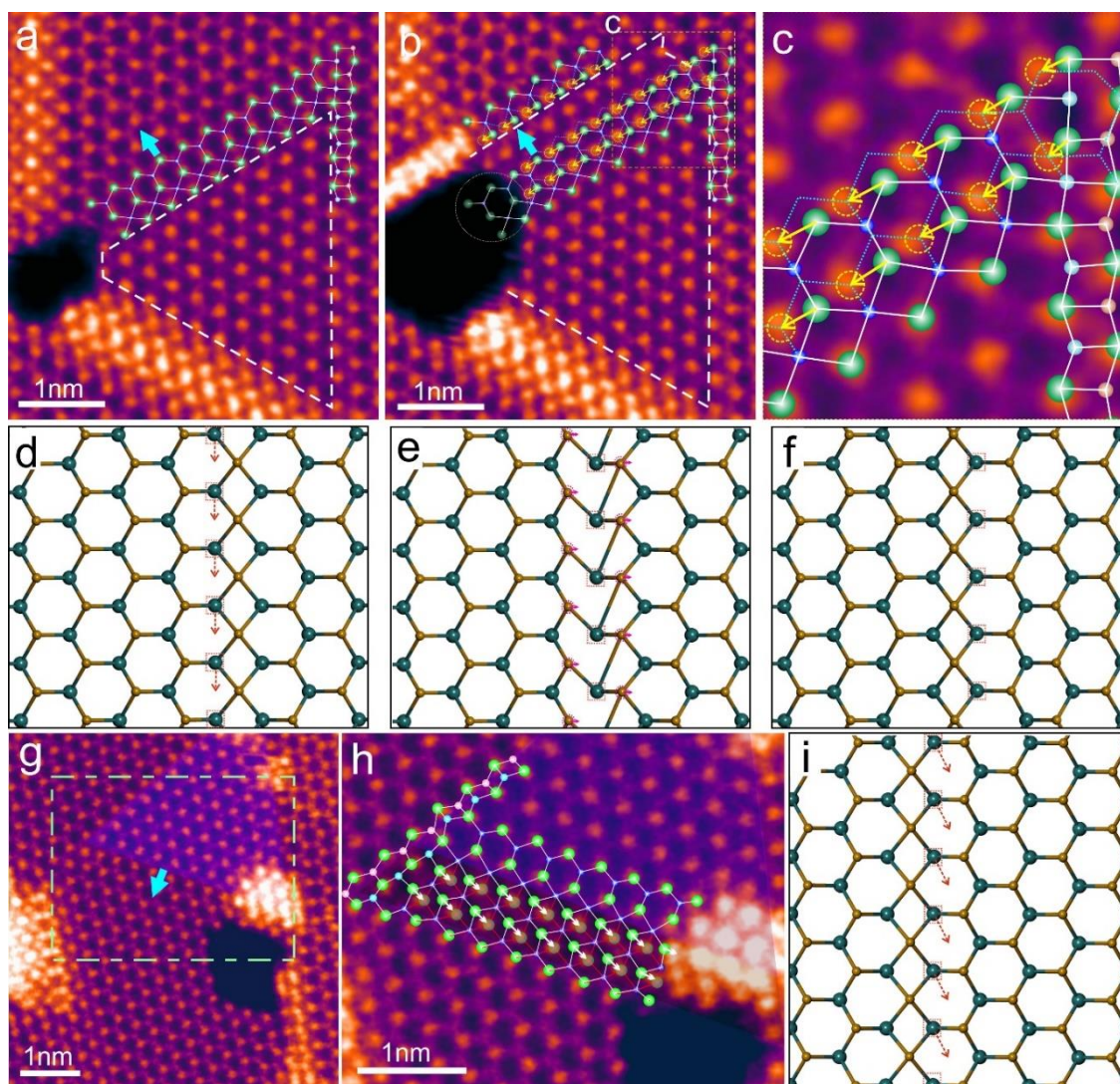
**Figure 4.5** Sequence of ADF-STEM images showing the dynamics of an ID at a high temperature of 800 °C after formation. The ID is highlighted by colour, and the overlaid shapes in different colours indicate the expansion and evolution of the ID. Scale bar: 3 nm.

Figure 4.5 displays the ADF-STEM image sequence captured at 800 °C, which shows a strong interplay between IDs and the nearby defect network including line defects as well as the formed void. From Figure 4.5a to b, a hole opens up at one corner of ID. That corner is the junction of two compact multi-SVLs in an angle of 120° (Figure 4.5a). It shows numbers of distorted lattices at this region (Figure A8). Also considering the tense strong field at the tip, it is expected that the lattice in this small area would be unstable when continuing to be irradiated by electron beam. This was revealed by the formed void at the corner in Figure 4.5b. During that time, the ID remains steady by retaining all of its boundaries at the original position (Figure 4.5b, c). Under continuous beam irradiation, the ID expands along the direction of the 2SVL (Figure 4.5c,d). This expansion is achieved by the migration of its 4|4P GB toward the outer region as well as the elongation of the 4|4E GB along the 2SVL, when the adjoining void is increasing as

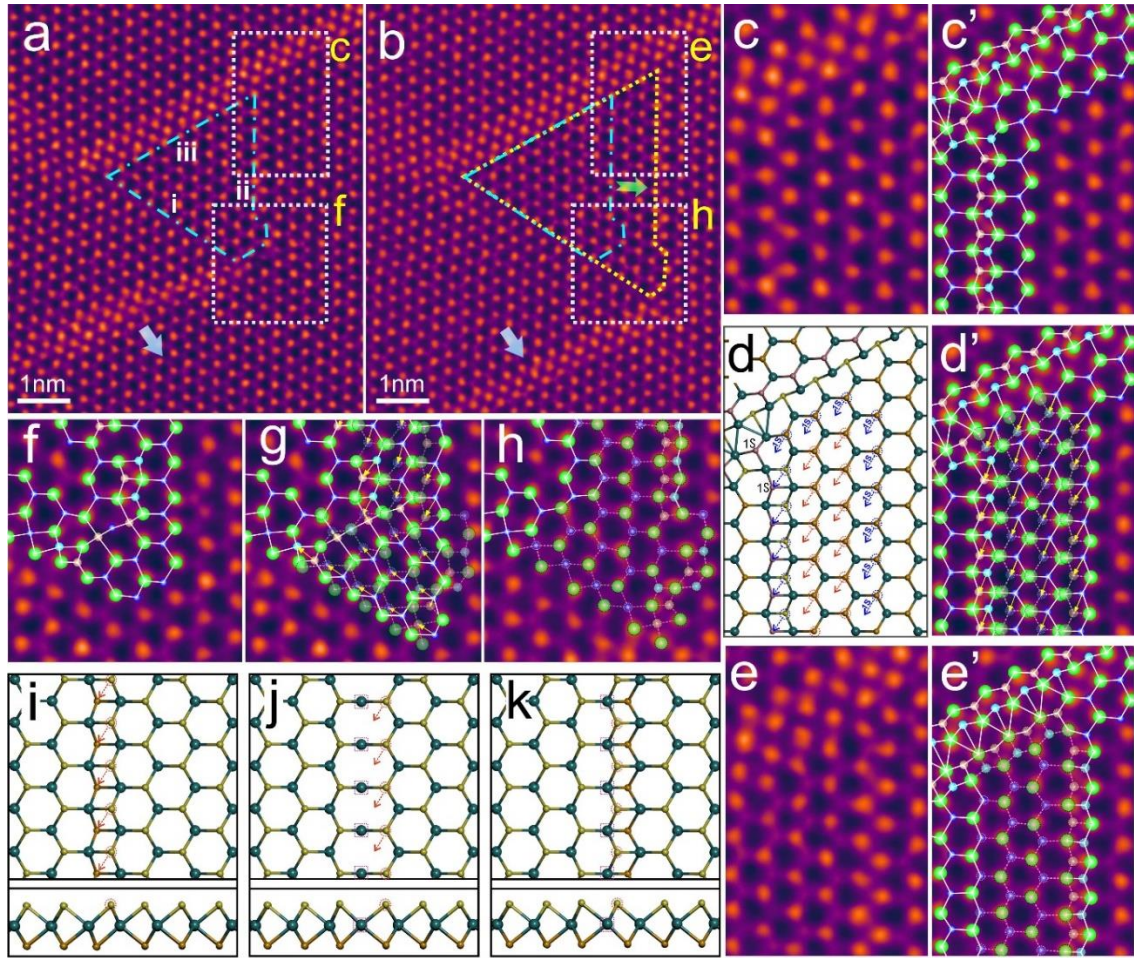
well. The ID further enlarges until its top vertex reaches another line defect (Figure 4.5e), during which the void grows to be a 60° triangular shape along zig-zag direction. The tendency of the void of triangular shape is attributed to the three-fold symmetry of the hexagonal MoS<sub>2</sub> lattice. With the further growth of the void under continuous electron beam irradiation, the ID finally disappears, as shown from Figure 4.5f to h. This dynamic process shows that the ID growth is always along the line defect direction, while the line defect network together with the formed void restrict the size of IDs to typically less than 5nm. This shows that the ID serves as a metastable state between the line defect rearrangement and void formation under continual vacancy production.

Figure 4.6 presents the expansion mechanism of ID by migrating its 4|4P GB. MoS<sub>2</sub> lattice at the outer side region of the 4|4P GB undergoes atomic displacement and bond reconstruction, making the 4|4P GB migrate outward (Figure 4.6a,b). As highlighted in Figure 4.6c, Mo atoms outside the 4|4P GB including half of the Mo atoms in the GB itself shift to the centre point of two shoulder Mo atoms and re-bond with the adjacent S atoms, causing the lattice to be inverted. Figure 4.6b shows that the shifting direction of the Mo atoms is towards the void formed at the left corner of the ID. Corresponding 4|4P GB migrating process is illustrated in Figure 4.6d-f, through the shifting of Mo atoms at one side of 4|4P GB to the shoulder positions (Figure 4.6d), tiny adjustment of S atoms positions (Figure 4.6e), and reconstruction of Mo – S bonding (Figure 4.6f). Figure 4.6g,h presents another example of the ID increase by migrating the 4|4P GB, realized by moving Mo atoms outside the 4|4P GB as well. The involved Mo atoms shift to the geometric centre of the hexagon, as demonstrated in the ADF-STEM image region overlaid with atoms (Figure 4.6h) and the corresponding atomic model (Figure 4.6i). This moving pathway slightly differs from that in the former example (Figure 4.6c) as they are surrounded by a different environment, where their Mo atomic displacement directions

are both affected by the adjoining void.



**Figure 4.6** ID expansion through the 4|4P GB migration. (a,b) ADF-STEM images showing (a) the original and (b) expanded ID. The outlines of the IDs are marked by white triangles. The large green arrow presents the migrating direction of the 4|4P GB. The circled lattices in (b) show the removed atoms in the void. (c) Magnified view of the boxed region in (b). The schematic atomic models of Mo (green, larger balls) and 2S (royal, smaller balls) overlaid mark the original position of the atoms before expansion, and the circles drawn by dashed yellow lines represent the shifted Mo atomic positions with the yellow arrows showing the displacement pathways. (d-f) Schematic illustration depicting the corresponding atomic movement during 4|4P GB migration in (a-b). (g,h) Another example of ID expansion with 4|4P GB migration. (g) Original ID highlighted by a colour mask. The large green arrow shows the expanding direction. (h) Partial view of the enlarged ID in the boxed region in (g), with the solid atomic models overlaid marking the original atoms positions before domain expansion, and the transparent models representing the shifted positions. (i) Schematic atomic model showing Mo atoms movement corresponding to (h).



**Figure 4.7** ID expansion *via* the migration of its 4|4E GB. (a,b) ADF-STEM images of (a) original ID and (b) expanded domain. Three GBs of the ID in (a) are labelled (i-iii). The blue arrows in (a,b) show the movement of the related line defect. The green arrow in (b) presents the migration direction of the 4|4E GB. (c, e) Magnified views of boxed region in (a,b) of the corner crossed by two 4|4E GB with one leaning a 2SVL as a extending line, with (c', e') overlaid by atomic models of Mo (green), 2S (royal) and single S (orange or light blue in different S rows). (d, d') Schematic atomic models illustrating the atomic displacement during the transformation from (c) to (e). (f, h) Magnified views of boxed region in (a,b) of the other corner crossed by 4|4E GB, 4|4P GB and a line defect in another direction. (g) Atoms shift and lattice change from (f) to (h). (i-k) Schematic illustration showing the atomic movement during 4|4E GB migration.

The other mode of ID expansion is through the migration of 4|4E GB, shown in the ADF-STEM sequence in Figure 4.7. The boundary structures of the increased ID (Figure 4.7b) and the original one (Figure 4.7a) are interpreted in Figure A9, comprising a 4|4P GB (i) and two 4|4E GBs (ii and iii) with one 4|4E GB adjoining an extended 2SVL. For growing the ID from Figure 4.7a to b, the 4|4E GB (ii) migrates outward when the other two GBs extend. The 4|4E GB (iii) elongates along its 2SVL, and the 4|4P GB (i)

lengthens together with the migration of multi-SVL crossing the vertex of the GBs (i) and (ii). As shown in Figure 4.7c-e, the 4|4E GB (iii) adjusts by sliding one single S row near the extended 2SVL with slight Mo displacement (Figure A10). Meantime, the 4|4E GB (ii) migrates by shifting the S atoms outside the ID. This migration process is illustrated in Figure 4.7i-k. The Mo and S atoms shift along opposite directions during the SVL migration, which makes the 4|4P GB (i) extend with lattice inversion in the domain. The overall dynamics of the connected line defects and the 4|4E GB result in the further growth of the ID.

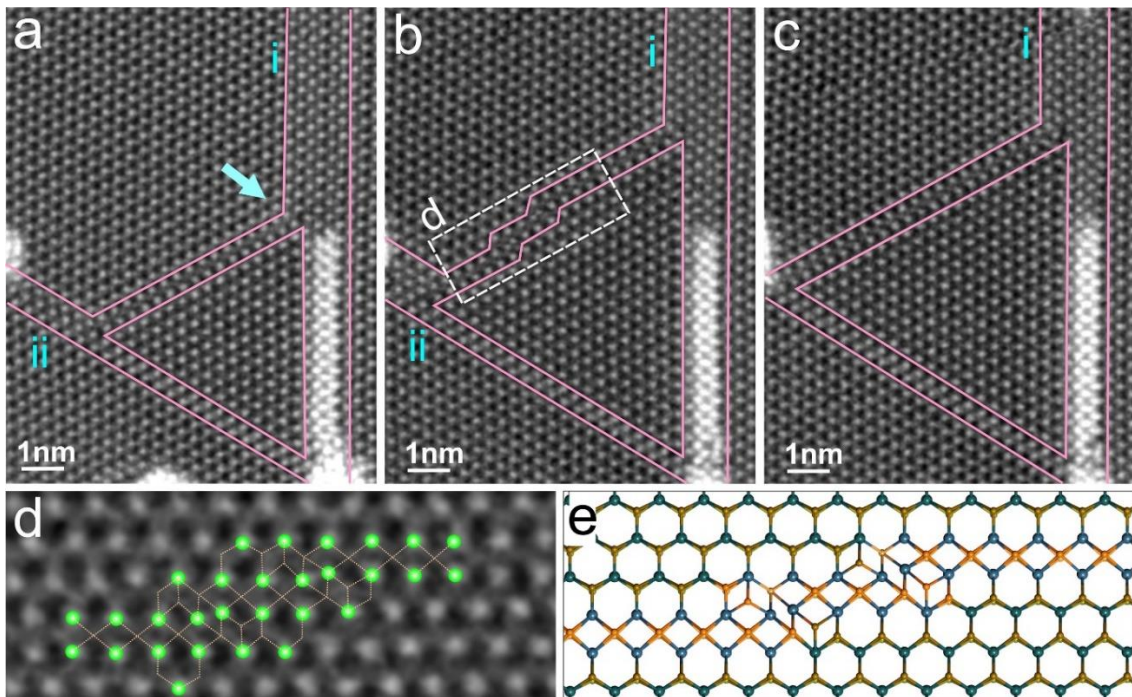


**Figure 4.8** Staggered boundary of an ID. (a-c) ADF-STEM image sequence during ID growth, where (b) presents a staggered boundary as highlighted by the white dashed box. The roman numerals indicate the adjoin line defects. (d) Magnified view of the boxed region in (b), with schematic atoms showing the step boundary structure. (e) Atomic model corresponding to (d).

The boundaries of ID can exhibit staggered structure (Figure 4.8). It grows along the two extended line defects from Figure 4.8a to c, by shifting the 4|4P GB outward. In Figure 4.8b, the 4|4P GB evolved to be a 3-step structure, connected by several 4-member rings with single S atom conjunctions (Figure 4.8d,e). The growth of this ID is initiated from the cross-point (marked by blue arrow in Figure 4.8a) of the 4|4P GB and the broad

multi-S vacancy line (i), then propagates to the other boundary tip step by step. At a certain stage the 2S atoms at the boundary step junctions split and one S slides to form these metastable 4-member rings, making the staggered boundary. It finally evolves to be the atomically flat boundary with prolonged electron beam irradiation (Figure 4.8c).

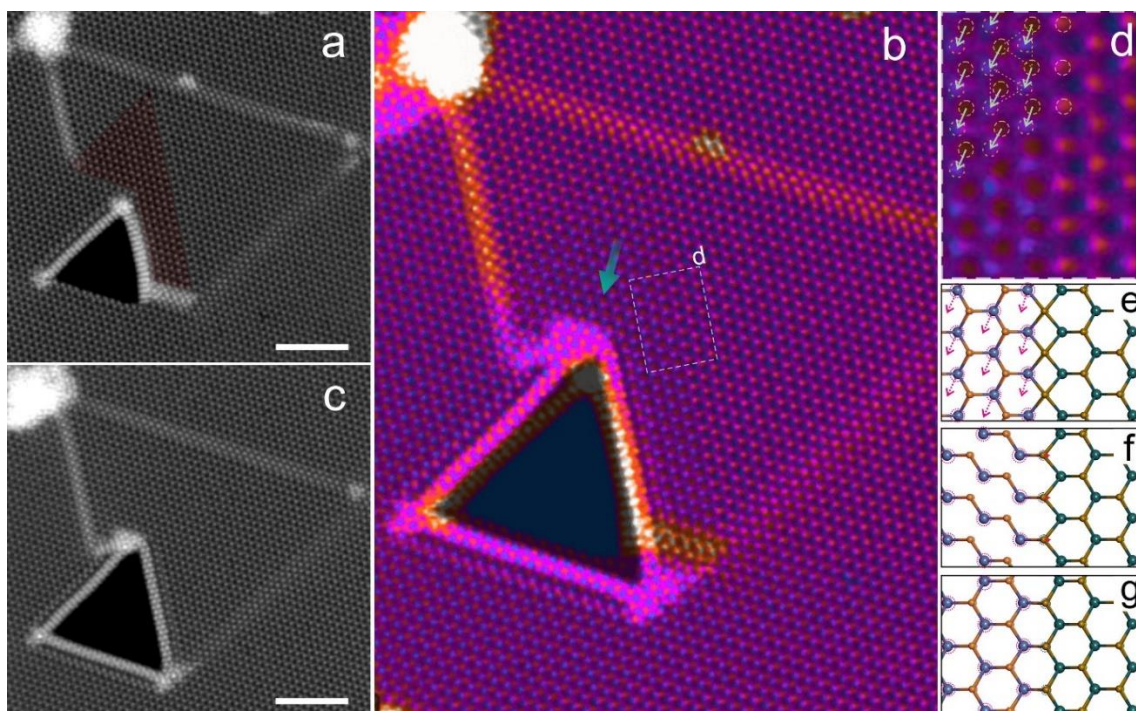


**Figure 4.9** ID vanishing into the void. ADF-STEM images of an ID (a) before and (c) after vanishing. The ID area is highlighted by colour mask in (a). (b) Atomic movement and lattice changes are revealed by overlaying (a) and (c). (d) Magnified view in the boxed region in (b), showing the Mo atoms shifting near the 4|4P GB. (e-g) Schematic atomic models showing the corresponding vanishing process.

Figure 4.9 shows a vanishing process as the last stage of high-temperature evolution of the ID taken from Figure 4.5. As the triangular void beside the ID further enlarges, the ID appears to be consumed by the void (Figure 4.9a to c). According to the overlapped image of the two frames in Figure 4.9b, the Mo atoms inside the ID have all migrated toward the void. The void growth is due to an increasing concentration of S vacancies produced by extended electron beam irradiation, and Mo atoms that are difficult to be sputtered agglomerate at the void edge and form the MoS nanowire structure.<sup>192</sup> The strain near the void edge drives Mo atoms to migrate toward it, and the inverted lattices

reconstruct to be the pristine structure to balance the strain. This mechanism reveals an initiating effect on the faceted void formation given by the dynamics and collapse of vacancy line defects and IDs. Figure 4.9d highlights the displacement of the Mo atoms near the 4|4P GB, which shows that the Mo atoms at the inverted side of the GB have shifted by half lattice while the outer MoS<sub>2</sub> stays unchanged. The corresponding lattice transformation process for ID disappearing near the 4|4P GB is illustrated by schematic atomic models in Figure 4.9e-g.

### 4.1.3 Conclusion

This study shows the formation, enlargement and vanishing evolution mechanisms of large IDs (~ 4nm) at high temperatures using an *in-situ* high-temperature holder in an ADF-STEM. Thermal energy provides the sulphur vacancies with high mobility which makes defects evolve fast, as well as eliminates the effect derived from surface contamination on the defect behaviour. The IDs formed at high temperature are much larger than those at room temperature (e.g. a triangular side length of 20 Mo atoms, in contrast to those of 7–10 at room temperature). The formation of large IDs is not simply caused by single point vacancies or individual line defects, but rather as a result of a network of non-orthogonal line vacancies with competing strain fields that trigger ID formation. The maximum size of IDs formed are ~3-5nm, after which void formation takes over. When interplaying with the surrounding defect network, IDs can further expand through the migration of any of its two types of grain boundaries, 4|4E GB and 4|4P GB, by S or Mo atoms displacement, respectively. This study gives insights into the high-temperature dynamics of large ID, and also highlights the important interplay between line defects, GBs, voids, and the ID in a large scale.

## 4.2 Atomically Sharp Tilt Grain Boundaries in Bilayer WS<sub>2</sub>

### 4.2.1 Introduction

The GB effects on the TMDs properties vary much with the exact GB structures, in particular sharply different between the small-angle GBs and 60° GBs. For example, the electrical conductivity had slight increase in 60° GBs but a little decrease in small-angle tilt GBs.<sup>134</sup> Tilt GBs introduced degradation of electrical characteristics and n-type doping in MoS<sub>2</sub>, while these features were not presented by 60° GBs.<sup>135</sup> Using electron microscopy techniques, linear 5|7, 6|8, 4|6 dislocation cores have been visualized in the tilt GB in monolayer MoS<sub>2</sub> and WS<sub>2</sub> monolayers with dynamic behaviours.<sup>104,145,148</sup>

Extending from the monolayer to the few-layer TMDs, tunability of electrical, optical, and chemical properties is yielded due to the layer-dependent band structures.<sup>12,85,87,233-234</sup> For instance, bilayer MoS<sub>2</sub> has promising applications in valleytronics owing to adjustable valley Hall effect which is not easily tuned in monolayers.<sup>19</sup> Compared to the intensive study of GBs in 2D monolayer crystals, the GB structures of bilayer are less explored. Understanding how the GBs are constructed in the bilayered CVD-grown TMD is crucial in advancing the CVD growth techniques, controlling their electric and optical performances, as well as extending their applications.

The bilayer GB structures are more complicated compared with monolayers, because of interlayer van der Waals forces that compete with local GB strains. The observed GBs in synthetic bilayer TMDs samples to date are mostly overlapping types, where the GB only locally exists in one of the layers, giving rise to diverse stacking orders in a homo-bilayer.<sup>141-143,151</sup> Interlayer van der Waals coupling has been found to be modified by the overlapping GBs in bilayer MoSe<sub>2</sub>.<sup>143</sup> If we consider the extreme situation where two GBs are overlapping at the same region, termed as dual GBs, this should

greatly impact the local conductance and mechanical properties.

This part presents ADF-STEM study of atomically sharp dual GB structures in polycrystalline bilayer  $\text{WS}_2$ . The dual GBs are formed between two tilt bilayer grains with different or same stacking types (2H or 3R), where the GBs in adjacent layers are narrowly aligned, showing unique periodic defective patterns. These uncommon dual-GBs are rarely found, but the results show they do exist and therefore must be considered in the 2D GBs. The formation pathways of different types of dual GBs are discussed, which can shed light on the CVD growth mechanism of polycrystalline bilayer  $\text{WS}_2$ .

#### 4.2.2 Results and Discussion

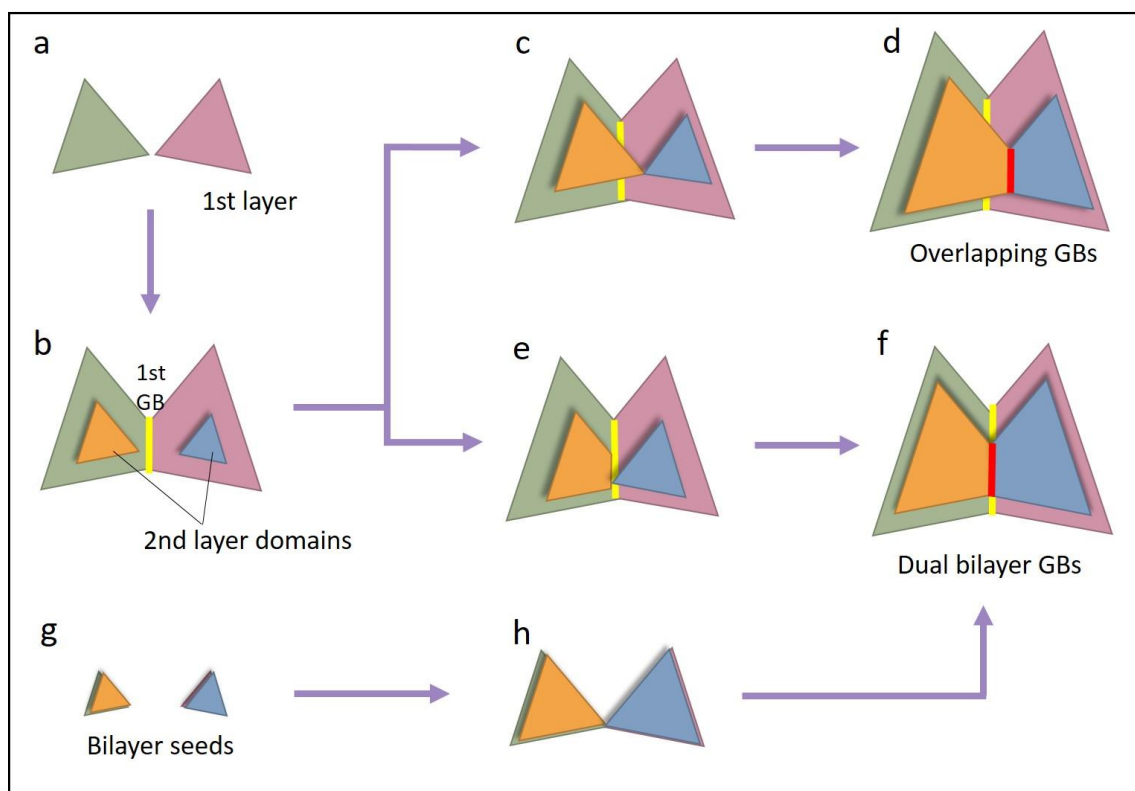


**Figure 4.10** Schematic illustration of possible bilayer grain boundaries (GBs) and their different formation processes during growth.

Figure 4.10 depicts three possible configurations of the bilayer GBs in TMDs and their different formation processes during growth. In the first step (Figure 4.10a-b), a tilt

GB within TMD monolayers is produced when two separate monolayer domains with tilt angle grow and meet together, as reported in many literatures before.<sup>134,145,235-236</sup> Meanwhile, a secondary TMD domain nucleates on the top of each 1<sup>st</sup>-layer grain with crystallographic stacking (2H or 3R) (Figure 4.10b). As the secondary seeds grow, they either form an overlapping GB (Figure 4.10c-d), where one of the secondary layers grows across the GB and these two domains merge to form a new GB at a random place. In this case, the GBs within each layer are independent to each other, and the bottom-layer GB interferes little on the growth of the secondary domains. The other possibility is the dual GBs, where the secondary domains stop growing when they reach the location of the GB already formed in the underlying monolayer, (Figure 4.10e-f). Eventually both layers connect at the same site as the monolayer GB to form the dual GB. The final mechanism for dual GB formation is that two bilayer TMD domains nucleate and grow together as a unified bilayer domain with constant area of top and bottom (Figure 4.10g-h-f).

ADF-STEM at 60 keV was used with an *in-situ* heating holder to characterize the CVD-grown bilayer WS<sub>2</sub>. No change was observed to the atomic structure of the GBs as a function of temperature (Figure A11), however the high temperature ( $\geq 500^\circ\text{C}$ ) removes surface contamination and beam induced contamination effects and this enables clearer atomic structure to be obtained. Figure 4.11 shows a bilayer GB structure with a tilt angle. In Figure 4.11a-b, the GB is relatively straight on the micro-scale, extending across the slit in the Si<sub>3</sub>N<sub>4</sub> film. The magnified ADF-STEM image in Figure 4.11c shows different contrast either side of the GB region for the bilayers due to one side having 2H (higher contrast) and the other 3R stacking structure (lower contrast). Some regions of the GB show the second layer has not fully grown together, revealing the typical monolayer GBs (Figure 4.11d), and some are within two stacked bilayers (Figure 4.11e).

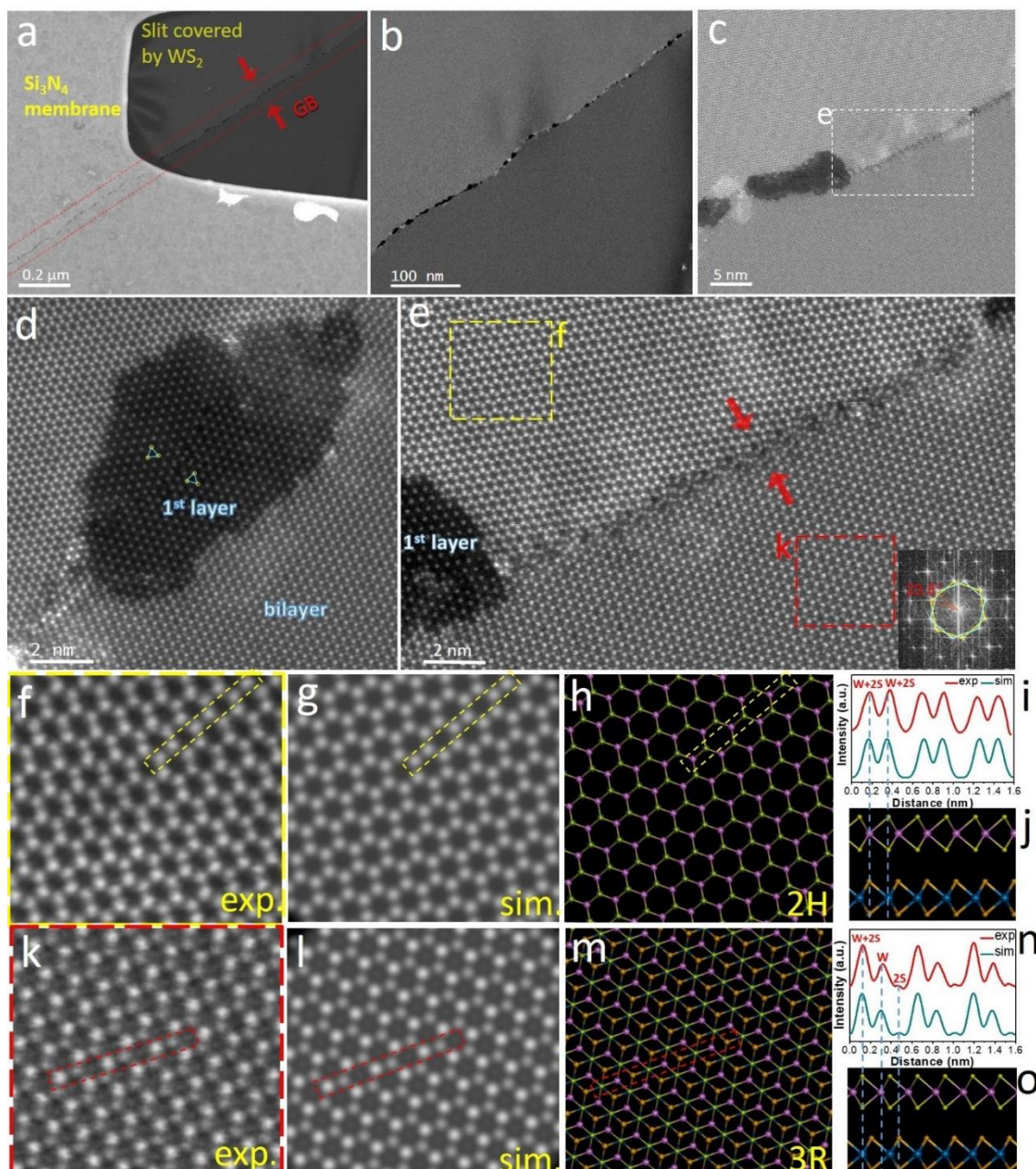


**Figure 4.11** (a-c) ADF-STEM images of the GB in bilayer  $\text{WS}_2$  film, spanning from micro scale to nanoscale. (d) ADF-STEM image of the GB formed on monolayer region. (e) Magnified view of the boxed region in (c), showing the GB within  $\text{WS}_2$  bilayers. The inset is the power spectrum calculated by a FFT, where two sets of spots have an angle of  $23.5^\circ$ . (f) Expanded view of the yellow box in (e), (g) multislice simulated ADF-STEM image and (h) corresponding atomic model of the 2H-stacked bilayer  $\text{WS}_2$ . (i) Intensity line profile measured from the labelled regions in (f-h), with (j) side view of atomic model. (k) Expanded view of the red box in (e), (l) multislice simulated ADF-STEM image and (m) corresponding atomic model of the 3R-stacked bilayer  $\text{WS}_2$ . (n) Intensity line profile measured from the labelled regions in (k-m), with (o) side view of atomic model. The perpendicular blue line marks the correspondence between atoms and intensities.

A dual GB structure was found between two differently stacked  $\text{WS}_2$  bilayers,

exhibiting atomically sharp configuration with periodic interesting patterns in ADF-STEM image (Figure 4.11e). For the samples with dual GBs, overlapping GBs do not co-exist, possibly because of preferable growth of dual GBs locally in the specific growth environment. The power spectrum calculated by a FFT shows two sets of hexagonal spots indicating an intersecting angle of  $23.5^\circ$ . The magnified views of the two grains in Figure 4.11f-o show that these two bilayers are 2H (AA') and 3R (AB) stacked, respectively. In 2H stacking, lattices on two layers are rotated by  $60^\circ$ , where each W atoms are situated on top of 2S atoms, and vice versa, so the intensities of Z-contrast of all columns are at the same level (Figure 4.11i,j). While in the ADF-STEM image of 3R-stacked bilayer, there are three different contrast intensities contributed by the columns W plus 2S, W, and 2S atoms, respectively, from high to low Z-dependent contrasts (Figure 4.11n,o).

At the exposed monolayer regions (Figure 4.11d, Figure 4.12a-f), the  $23.5^\circ$ -tilt monolayer GB structures can be clearly distinguished. The extended GB has a meandering pathway, similar to some previous results on monolayer  $\text{MoS}_2$ .<sup>24,46</sup> Taking the W-zigzag direction as the reference, the GB mostly develops along the direction of  $\sim 20.5^\circ$  and at some points have steps along the  $\sim 80.5^\circ$  ( $20.5^\circ + 60^\circ$ ) direction (Figure 4.12c). This monolayer GB is connected by a series of dislocation cores, which can be classified to be two categories subject to the extending directions. According to the previous classification, these two types on  $\sim 20.5^\circ$  and  $\sim 80.5^\circ$  are sulfur-polar  $\top$  and metal-polar  $\perp$  dislocations, respectively, based on two unit vectors along the zigzag node motifs (Figure A13a,b).<sup>32</sup> The one on  $\sim 20.5^\circ$  GB is composed of four- and six-fold (4|6) rings and their variations (type II and type III) by losing S kinks, with the atomic structures and DFT relaxed models shown in Figure 4.12g,h. And the other GB category along  $\sim 80.5^\circ$  consists of five- and seven-fold rings (5|7) rings with W-W bonds. We compared the simulation of S-vacancy derivatives of 4|6 GB in Figure A14 to confirm the

observed metal-rich  $V_{2s}(B)$  (type-II) and  $V_{2s}(A)$  (type-III) GBs in the first layer.

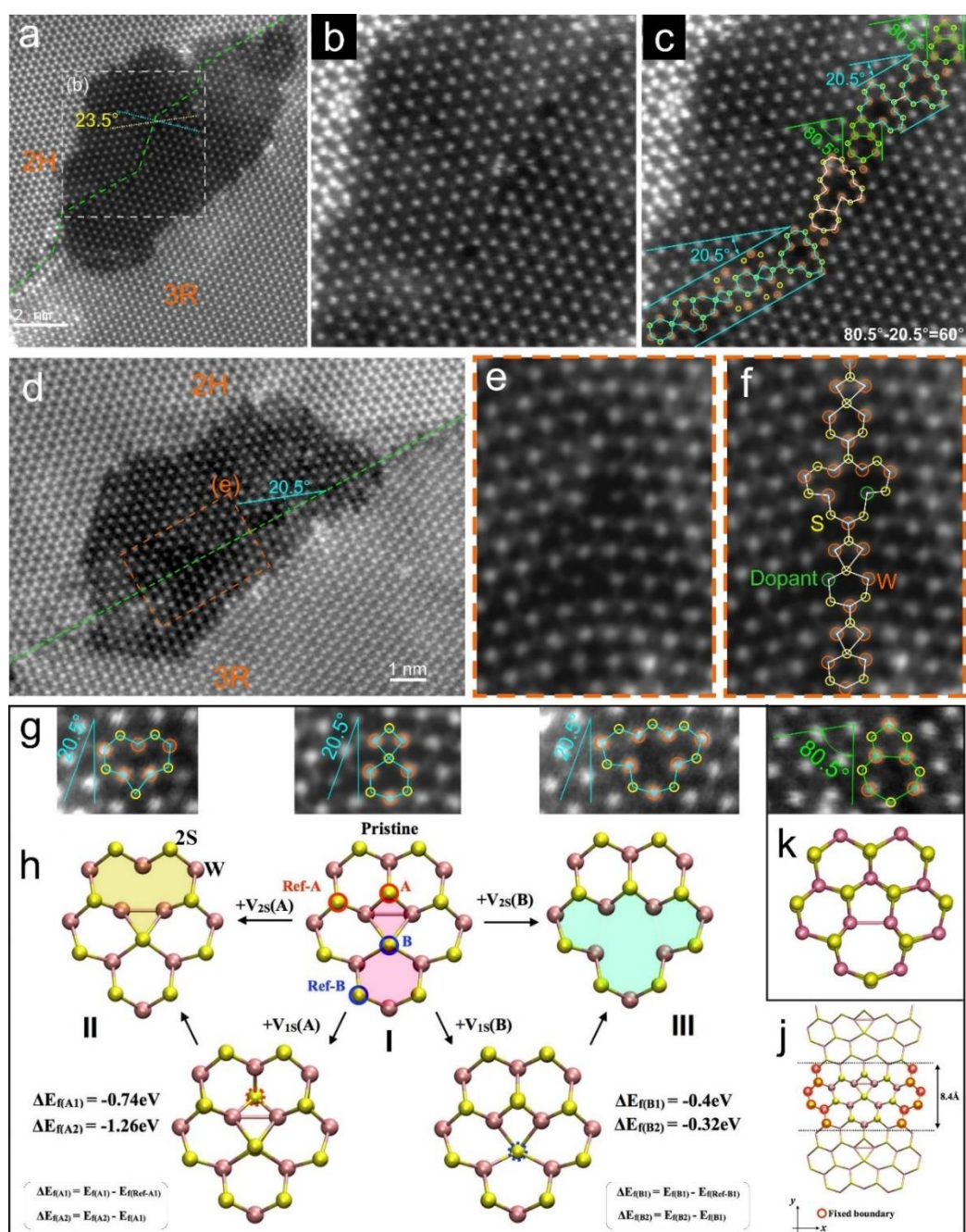


**Figure 4.12** GBs in the monolayer  $WS_2$  region. (a) ADF-STEM showing a GB formed by two monolayer  $WS_2$  crystal with an angle of  $23.5^\circ$ . (b) Enlarged view of the boxed region in (a), with (c) overlaid by atomic models of W (orange) and 2S (yellow) atoms showing the dislocation cores structure. (d) Another monolayer GB. (e) Enlarged view of the boxed region in (d), with (f) overlaid by atomic models. (g-k) Two categories of dislocation cores in monolayer  $WS_2$  GBs. (g) Enlarged ADF-STEM images with (h) schematic of  $4|6$  GB (I) and its derivatives  $4|6+V_{2s}$  GB (II and III) by introducing S vacancies. The atomic geometries are relaxed through DFT calculations. The defect formation energy of type II and III is given, compared to the nearest S vacancy ( $V_{Ref-A1}$  or  $V_{Ref-B1}$ ). (j) Unit cell ( $25\text{\AA} \times 8.4\text{\AA} \times 15\text{\AA}$ ) of the grain boundary with a dislocation core, the red-circled atoms are fixed in both x and z direction.

The results of DFT calculation show that the S vacancy formation energy at A (II) and B (III) kinks are both lower compared to the nearest reference S position. Also, the formation energy of the next vacancy at the same position becomes smaller than the first one, indicating once the monovacancy forms at A or B sites, the second S vacancy becomes easier to form (Figure 4.12h, Figure A15). More importantly, the GB is the location of stress concentration. Once the S is lost at the dislocation core kinks, the other S is under severe atomic stress and deformation, which can be another reason for the predominant divacancy observation in the GB. Note that all these observed dislocation cores are W-rich, and the 4|6 rings including the derivatives II and III make up the majority in this GB (Figure 4.12d-f), as the overall GB is extending along this direction in large scale (see Figure 4.11a,b). As suggested in previous report, the 4|6 (Figure 4.12h, I) and 4|6+V<sub>2S</sub> GB (Figure 4.12h, II and III) are more likely to form over 5|7 S-S GB in W-rich conditions.<sup>32</sup> The high concentration of the intrinsic W-rich dislocation cores manifests a local W-rich environment during CVD growth.

If the second layer overlaps the bottom GB, the ADF-STEM image will show a turbostratic moiré pattern at the other side (Figure A16). In this sample, we did not find overlaying GB sections or any turbostratic patterns. The dual GB, Figure 4.13, shows specific periodic contrasts, in particular 6-member half-rings. The dual GB structure has different configurations along the nanoscale meandering pathway (Figure 4.13b), so we classify them into type 1 and type 2(i and ii), according to the second-layer atoms from which stacking (3R or 2H) taking the dominance over bottom GB (this will be explained more below). Type 1 dual GB (Figure 4.13c-l) has the 6-member half-rings, due to alternating W atoms from the two layers (Figure 4.13h,i). The dual GB is extending along the angle of 20.5° to the reference axis (as defined in Figure 4.12), indicating sulfur-polar T bottom-GBs composed of symmetric 4|6 dislocation cores.

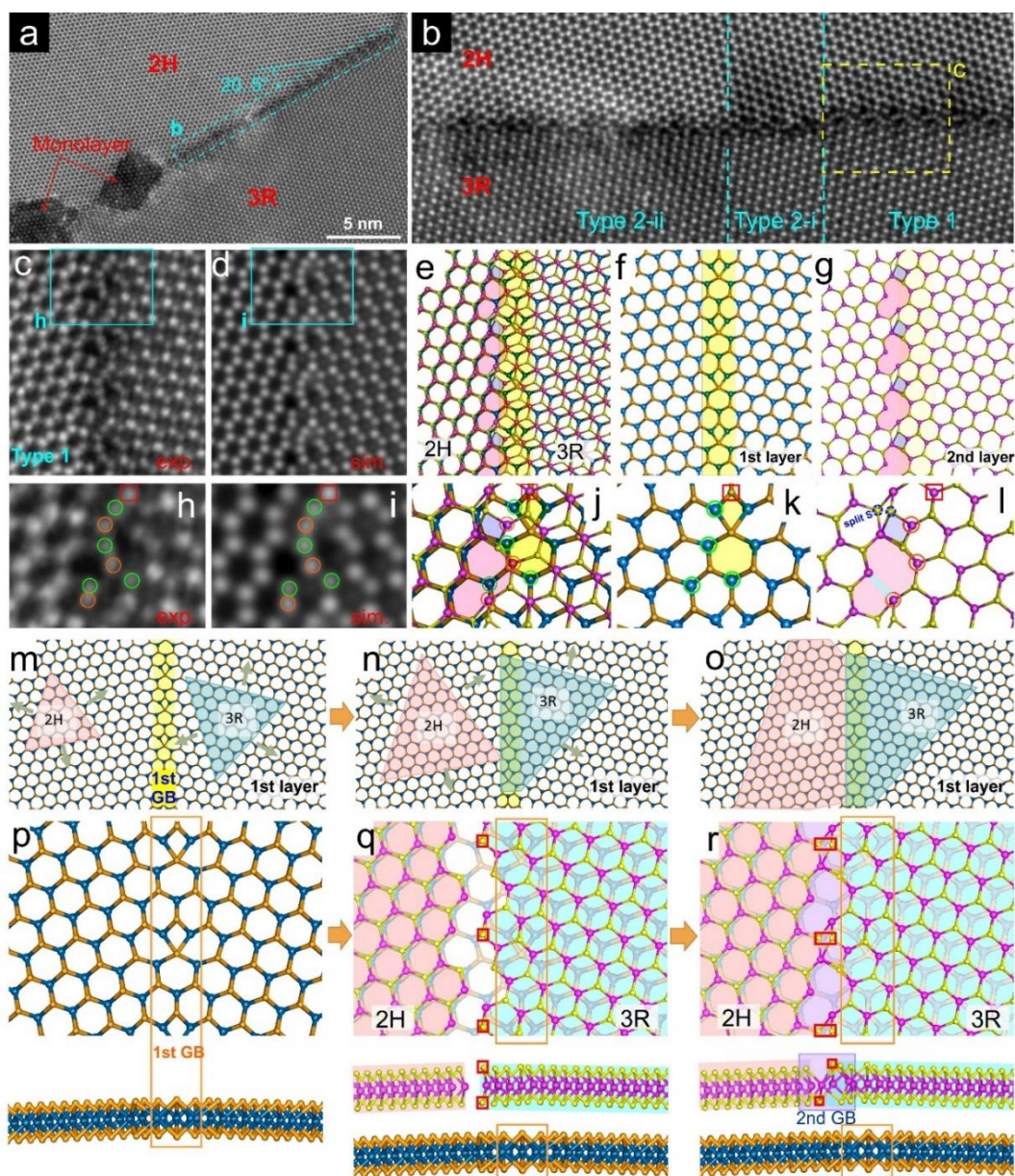


**Figure 4.13** Dual GBs in the bilayer  $\text{WS}_2$  region. (a) ADF-STEM showing the GB formed by two bilayer  $\text{WS}_2$  crystal with different stacking registries (2H and 3R) and tilt angle. (b) Enlarged view of the dual bilayer GB highlighted in (a), showing three different configurations (type 1, type2i/ii). (c) Enlarged view of the yellow boxed region in (b) showing the periodic semicircle structure at the GB (type 1). (d) Simulated ADF-STEM image obtained from (e) the relaxed bilayer atomic model through molecular dynamics (MD) simulations, with (f) and (g) showing the bottom and top layer models respectively. Yellow linear shade marks the bottom GB, purple and pink shades highlight the dislocation cores in top GB. (h, i) Enlarged view of the blue boxed region in (c, d) showing a unit of the periodic dual GB and simulation, with (j) corresponding relaxed bilayer atomic model, (k) bottom and (l) top layer models. The green and orange circles indicate the W atoms at the bottom and top layer, respectively. The blue strip shade shows the W-W bonding region. (m-o) Schematic illustration of the formation mechanism of the type 1 bilayer dual GB, and (p-r) detailed atomic models with side views below. (p) Bottom layer GB, (q) upper freestanding secondary layers separately grown on bottom layer without strain in 2H and 3R configuration, and (r) top GB formed by in-plane bonding with strain.

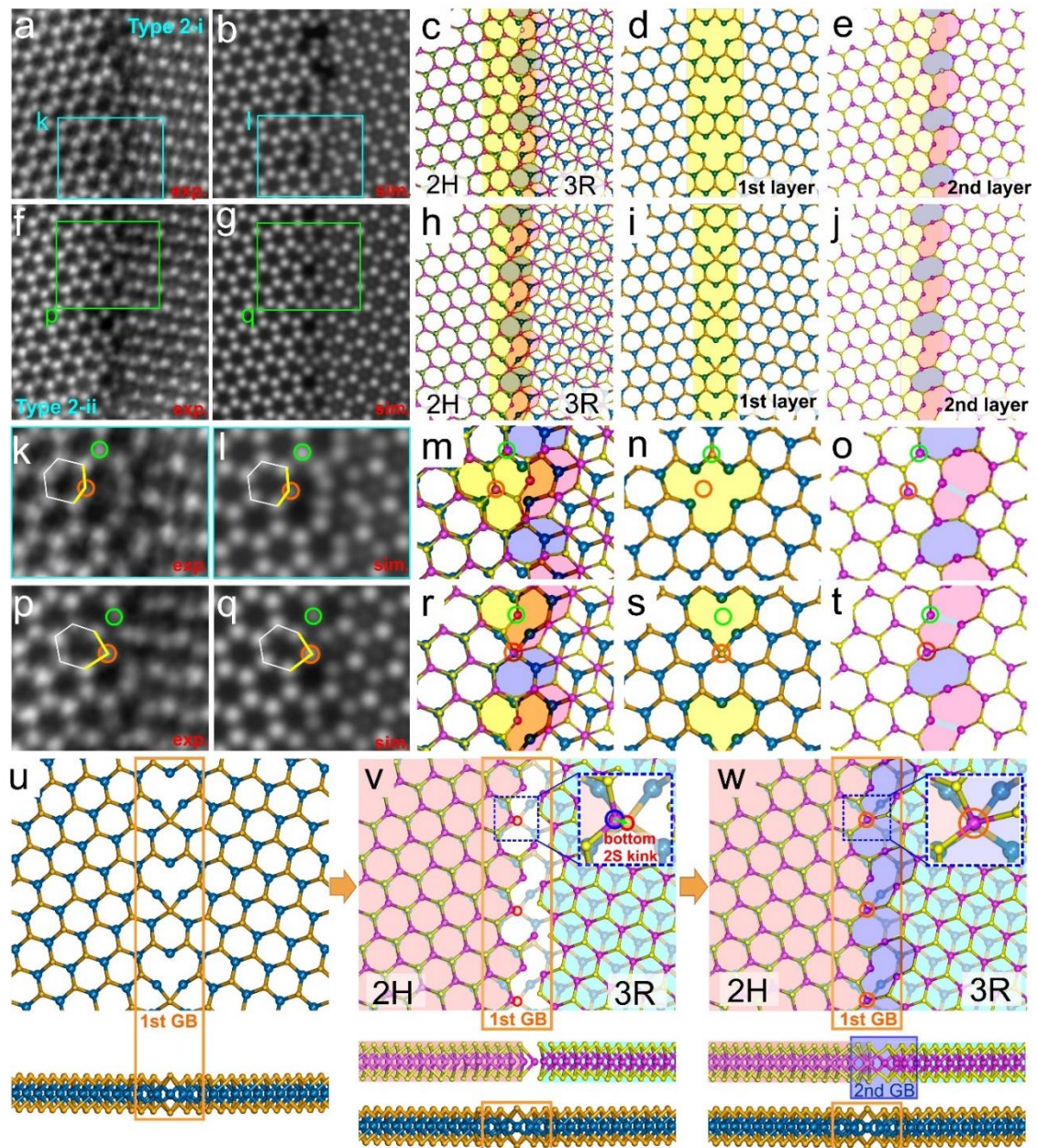


**Figure 4.14** Detailed structures of the other type (2H-dominated, Type 2) of configurations of the dual GBs shown in Figure 4.13(b). (a-e) type 2i GB. (f-j) type 2ii GB. (a, f, k, p) ADF-STEM images of the periodic dual GB structures. (b, g, l, q) Simulated ADF-STEM images corresponding to (c, h, m, r) the relaxed bilayer atomic model through MD simulations, with (d, l, n, s) and (e, j, o, t) showing the bottom- and top- layer atomic models, respectively. (u-w) Schematic illustration of the formation mechanism of the type 2 bilayer dual GB with side views below. (u) Bottom layer GB, (v) freestanding secondary layers grown on bottom layer without strain in 2H and 3R configuration, separately and (w) relaxed atomic model by MD showing top GB formed by in-plane bonding with strain. The insets in (v, w) highlight the top layer strained by interlayer coupling effect and in-plane bonding.

Owing to different stacking types of the two bilayers, the second-layer lattices are

asymmetric at two sides of the bottom GB, so the second GB cannot be formed with any of the usual monolayer dislocation cores which are all symmetric. According to the bilayer ADF-STEM image and considering the contributions from bottom-layer atoms, the W positions on second-layer GB can be deduced and the atomic model can be constructed. We relaxed the bilayer GB geometries obtained from experimental ADF-STEM images through molecular dynamics (MD) simulations and rebuilt the model as shown in Figure 4.13e-g, with qualitatively matched simulated ADF-STEM image (Figure 4.13c,d,h,i). We found the bridge 2S column needs to split and bond to the neighbour W atoms from 2H and 3R side separately to form a stable model after relaxation. Besides, the generation of the GB triggers a slight out-of-plane buckling attributed to the strain concentrated at the dislocation cores, which can increase the interlayer interactions of the atoms of the two layers and thus affect the atom positions in the defect. The detailed position of the split S atoms is displayed in Figure A17. The second-layer GB has asymmetric chains of metal-rich dislocation cores that are not found or predicted on the free-standing TMD monolayers, which is composed of a 4-member ring (purple shade in Figure 4.13g,l) with a single S tip, similar to the component of the 4|6 W–W defects with S vacancy, and a W-rich loop (pink shade in Figure 4.13g,l) where there is a W–W bonding region highlighted by blue shade in Figure 4.13k. The W metal rich structures have been commonly found in rotational defects in WSe<sub>2</sub> and WS<sub>2</sub>,<sup>105</sup> as well as the circular nanopores in WS<sub>2</sub>.<sup>106</sup> It is suggested that the W-based TMDs can accommodate a variety of defects owing to W–W bonding (*e.g.* stronger than Mo–Mo bonding). The second-layer GB is formed by synergetic effects from interlayer stacking interaction and in-plane bonding between atoms from two lattice sides. In this dual GB, the second-layer atoms coming from the 3R side make up the majority which maintain their original lattice orientation when reaching the bottom GB, so we call it the 3R-

dominated GB (type 1). Its formation mechanism during growth is illustrated in Figure 4.13m-o, where the dual GB could be formed when the second layer of 3R WS<sub>2</sub> takes the kinetic priority in reaching and covering the top region of the bottom GB (Figure 4.13n). It then connects to the as-grown top layer of 2H WS<sub>2</sub> when the 2H-stacked atoms reach, generating a new GB subject to the bottom GB. For supporting this growth mechanism, we have experimentally captured the intermediate state that the secondary domain (second layer) stops growing when it reaches the location of the GB already formed in the underlying monolayer (Figure A18). This process is further illustrated by atomic models in Figure 4.13p-r. To form GBs in a second layer, the edge atoms of both sides need to be strained to generate in-plane bonding, and the protruding 2S column (red boxes in Figure 4.13q) from the 3R edge split to two near columns (red boxes in Figure 4.13r), with one single S bonded to W atoms at 2H side, serving as the bridge of two grains and meanwhile producing new dislocation cores.

The other type of dual GBs (type 2) including two configurations, type 2i (Figure 4.14a-e) and type 2ii (Figure 4.14f-j), are 2H dominated, which means the second-layer atoms at the bilayer GB region are mainly from the 2H stacked side. Similar to the previous analysis, the 2H-dominated dual GBs are due to the predominant occupation of the GB area by the top layer of 2H stacked WS<sub>2</sub> (Figure 4.14u,v). Like the 3R-dominated dual GBs, these two 2H-dominated dual GBs are also W-rich in both layer, with the W-W metal bonding on top layers (blue strips in Figure 4.14o,t). Both the bottom layer and top layer are abundant in these W-rich cores with well-maintained structures during imaging, regardless of the types of the GBs, which should be intrinsically derived from local W-rich environment during CVD growth of this material. The MD relaxed atomic models of type 2i and 2ii are displayed in Figure 4.14c-e and Figure 4.14h-j, respectively, with qualitatively-matched ADF-STEM images in Figure 4.14b,g. The bottom GBs

belong to the  $4|6 + V_{2S}$  GBs, and their top layers show resembling W-rich dislocation cores chains which are composed of a 8-member ring (light purple shade) and a  $5|7$  metal-polar  $\perp$  dislocation by pink shade), while differing in the exact atom positions (see the more distorted  $5|7$  dislocations in Figure 4.14j). The minor differences of these two structures (type 2i and 2ii) are because of the variation of the dislocation cores at bottom layer and the existence of the interlayer coupling. Figure A19 gives supporting example of type 2-ii pattern at another region. All of them have the S-deficient  $4|6$  GB in the bottom layer, but have the  $V_{2S}$  at different column sites ( $V_{2S-A}$  or  $-B$  as described in monolayers in Figure 4.12h). In type 2i (Figure 4.14k,l), the orange circle has the contrast of one W atom on top layer, which retains its original bond length to the neighbouring S atoms in the pristine hexagon, with  $V_{2S-B}$  beneath it (Figure 4.14n). For type 2ii (Figure 4.14p,q), the top-layer W at the equivalent position undertakes strains to stack onto the 2S column at the (B) site at the bottom GB (Figure 4.14s) owing to interlayer electronegativity between W and S. This is further illustrated in the formation mechanism in Figure 4.14v-w. If the second-layer atoms is freestanding, the W atoms at the 2H edge (blue circles in Figure 4.14v insert) undergo minor displacement to stack onto the bottom 2S kinks (Figure 4.14w insert), and bond to S atoms from 3R edge, serving as the bridge of the two grains as well as the strain centre. Note that the bridging atoms of type 1 and type 2 second-layer GBs are S (split) and W atoms, respectively, because of different exposed edges of the kinetically dominant side when stopping at the bottom GB (S-edge of 3R side in Figure 4.13q vs. W-edge of 2H side in Figure 4.14v).

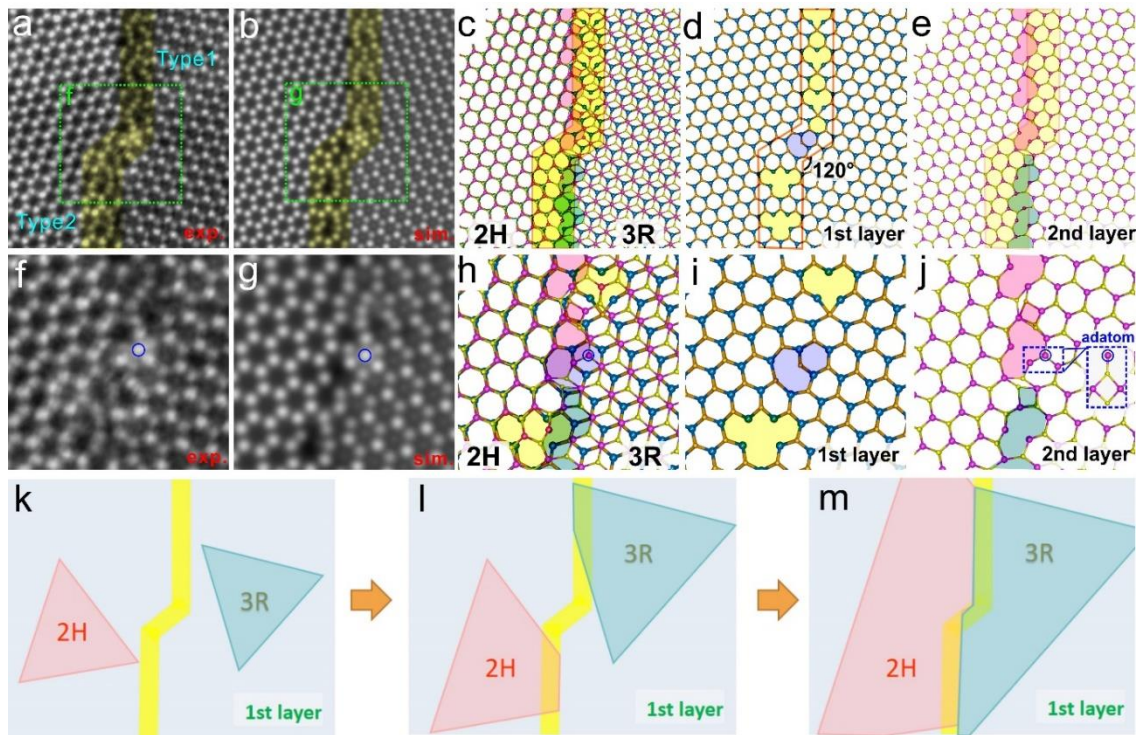


**Figure 4.15** Dual GBs with stepped structure connected by two types of GBs in bilayer WS<sub>2</sub>. (a) Experimental and (b) simulated ADF-STEM images, with yellow-coloured mask highlighting the bottom-layer GB. (c) Corresponding bilayer atomic model which has been relaxed by MD simulation, with (d) and (e) showing the bottom- and top-layer atomic models, respectively. (f,g) Enlarged view of the green boxed regions in (a, b) showing the turning point of the step GB and simulation, with (h) corresponding bilayer atomic model, (i) bottom layer, and (j) top layer models. The blue circles indicate the adsorptive W-adatom on the surface, with corresponding side view shown in insert in (j). (k-m) Schematic illustration of formation mechanism of the stepped GB.

Nanoscale meandering of the GBs requires steps that cause deviation of the GB angle relative to the tilt angle at the atomic scale. This section of the stepped dual GB structure connected with type 1 and type 2 GBs (Figure 4.15a-e) shows the bottom GB can turn its extending direction at 120° by using the metal-polar ⊥ dislocation cores, and here it uses 6|8 W-polar defects as marked by light purple shade in Figure 4.15i (evolved from 5|7 W-W rings by inserting 2S atoms), on which the absorbed second-layer atoms positions are affected by interlayer reaction. The formation mechanism of this stepped dual GB is illustrated in Figure 4.15k-m. Two top layers with 2H and 3R stacking separately expand until reaching the bottom GB at different positions (Figure 4.15l), forming various types of GB. They further develop till the two separate GBs merge at the turning point (Figure

4.15m). From Figure 4.13b and Figure 4.15a, the two types of dual GBs can coexist at a local region and construct along a straight line (Figure 4.13b), or can be connected with meandering steps to form a stepped line (Figure 4.15a). The local dual GB type is determined by which side second layer dominates.

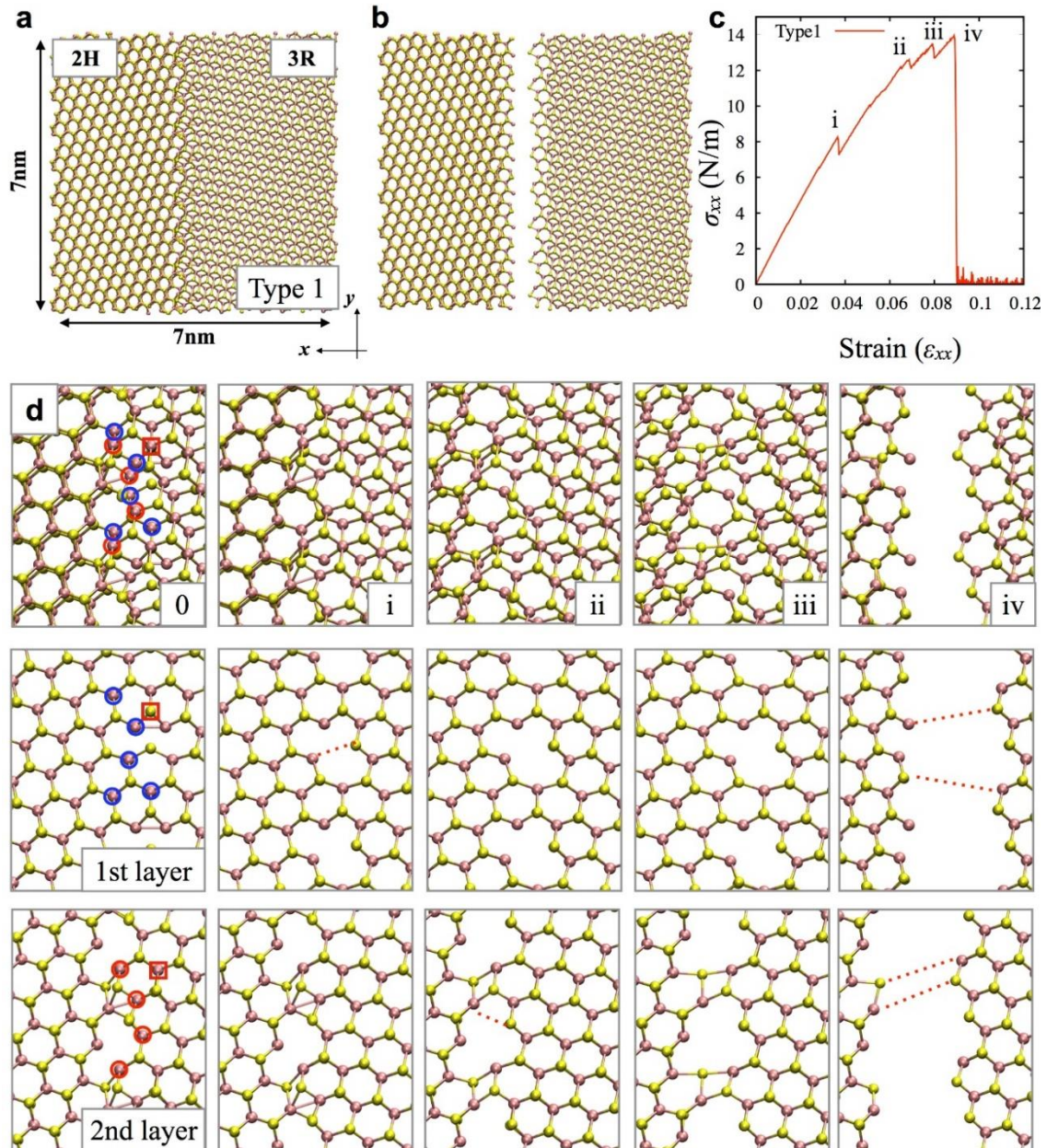


**Figure 4.16** (a) Rebuilt model of Type1 through MD simulations with 7nm x 7nm size. (b) Snapshot of the model after both layers fail. (c) Stress-strain curve of the bilayer under tensile loading. There are several stages of failure (i- iv), which described more detail in **d**. (d) Detailed atomic structures of the MD model. The marked positions of atoms (red and blue circles and square) are in correspondence with the ADF-STEM observation. The red lines indicate the bond breaks at the failure stage from i to iv described in the stress-strain curve.

In order to examine the mechanical stability of the dual GBs, we conducted the tensile tests using molecular dynamics (MD) simulations based on first-principles reactive force fields (see Chapter 3). Figure 8 shows the rebuilt MD models and the tensile tests of Type 1 dual GB (results of Type 2i and 2ii are given in Figure A21-A22). Under the tensile loading, the crack nucleation and propagation occur along the GBs. Before the catastrophic failure, the atomic bonds at the GB fail first. Overall, the 2nd layer completely breaks at the strain around 8% and the 1st layer holds the loading slightly longer with the strain around 9%, manifesting similar mechanical stability. The 2nd layer of Type 1 can elongate as much as the other layer due to the split S atoms which stabilized the system. The 1st layer GBs in Figure 4.16 and Figure A21-A22 are constructed from dislocation core I, III and II in Figure 4.12g,h, respectively. From the snapshots of models under tensile loading, we can find these dislocations have different stability under mechanical loading. The dislocations I, II and III start to change their structures at around 4%, 5%, and 9% of the tensile strains, respectively. The dislocations in two layers of the dual GBs are all mechanically stable although they have different failure strain.

Apart from the GBs in small-angle 2H/3R interfaces, we also observed the atomically sharp dual GBs between two tilted 2H stacked WS<sub>2</sub> bilayers (Figure 4.17a), which are formed by stitching two WS<sub>2</sub> domains with an angle of 20.9°. The two domains in Figure 4.17b,c show the AA' (2H) stacking feature, though at one side (Figure 4.17c) the lattices are not perfectly stacked where the second layer has slight in-plane translation (Figure 4.17d-g). Figure A23 provides more examples of the dual GBs in the shifted 2H bilayers. The contrast patterns of sharp dual GB between matches well with those in the simulated ADF-STEM image. (Figure 4.17i,j). The atomic model in Figure 4.17k show the two lattices (*A*) and (*B*) near the GB have undergone moderate in-plane shift, mainly attributed to the local strain in the vicinity of the GB. Similar to the tilted dual GB in the

2H/3R interface in the previous analysis, here the linear GB on the top layer aligns with the bottom symmetric 4|6-rings GB, and the top-GB is also composed of asymmetric W-rich dislocation cores, which are not precisely right above of the 1<sup>st</sup>-layer dislocation cores but are shifted towards the domain (A) side. The asymmetric structure can form as a result of in-plane translation of the top-layer lattice near the GB and kinetic differences of the atoms migrating to the GB during growth, resembling the mechanism as the previous 2H/3R GB. This example further demonstrates that the atomically sharp dual GB can be developed not only in 2H/3R border but also in bilayers with same stacking type.

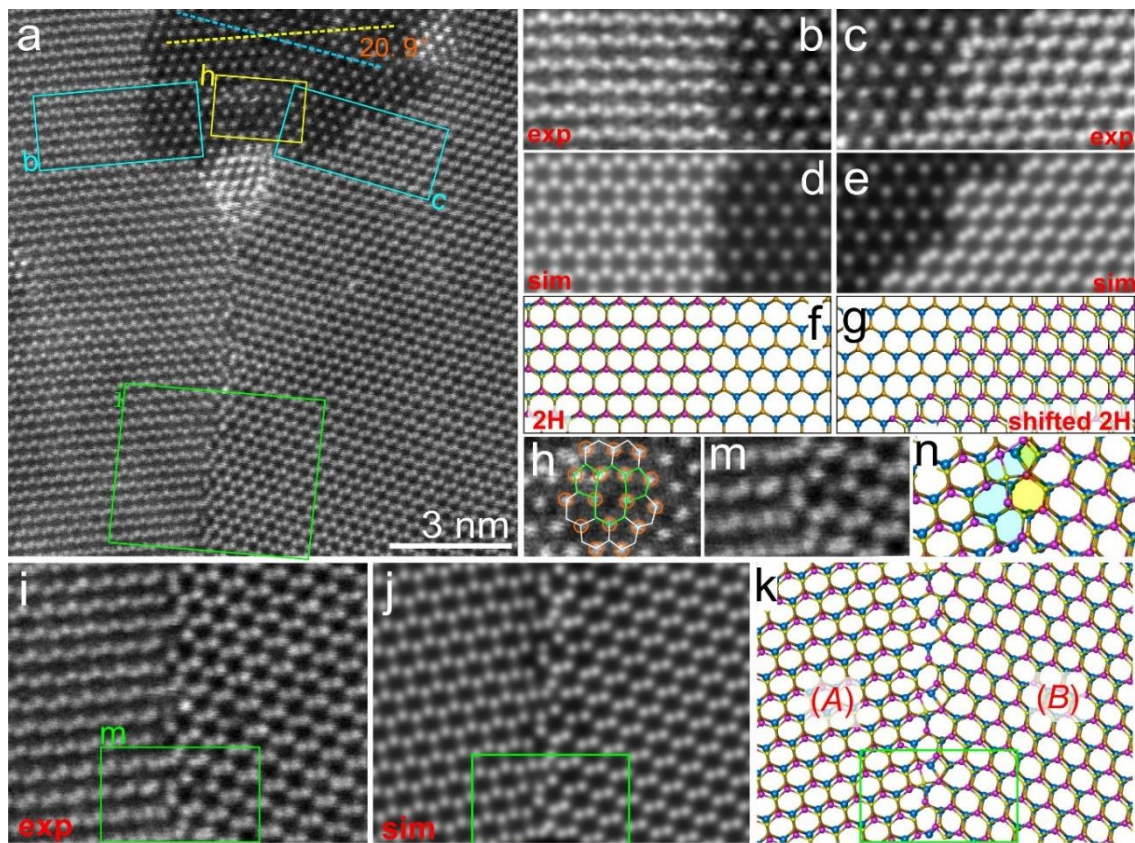


**Figure 4.17** Dual GB formed between two WS<sub>2</sub> bilayers with translated 2H (AA') stacking. (a) ADF-STEM image of a tilt GB region in bilayer WS<sub>2</sub>. (b,c) Magnified views of blue boxes in (a), with (d,e) simulated ADF-STEM images. (f,g) Atomic models corresponding to (d,e), respectively. Cyan and pink balls represent W atoms on bottom and top layers, respectively. (h) Magnified view of the yellow boxed region in (a), with schematic models overlaid illustrating the GB dislocation cores. (i) Magnified view of the green box in (a), highlighting the dual GB in two AA'-stacked bilayers with in-plane translation, with (j) simulated ADF-STEM image and (k) corresponding atomic model. (m,n) Enlarged views of the green boxed regions in (i,k). The yellow and blue masks applied on (n) highlight the dislocation cores on bottom and top layers, respectively.

### 4.2.3 Conclusion

By using ADF-STEM, it is shown that dual GBs can exist in 2D crystals and that special types of W-rich dislocation cores are needed to enable such atomically precise GB structure. The dual GBs are mostly found in the interfaces of two bilayer domains of well-defined stacking registries each (2H or 3R), attributed to the interlayer van der Waals forces and the local GB strains, enabling them maintaining energetically favourable stacking configurations in both sides of the GBs without stacking faults. The two sides of the tilt dual GB can have different or the same stacking orders, and both 2H/3R and 2H/2H interfaces are characterized. Our *in-situ* heating shows these structures are stable up to 800°C at least. The W and S positions are resolved within the atomically sharp dual GBs in the bilayers, enabling studies of 2H-3R and 2H-2H interfaces. The dual GBs exhibit voids in their structure, similar to those of monolayer TMDs grown by CVD, which enables the GB structure of both monolayer and bilayer regions to be deduced. These GB interfaces may have different semiconducting behaviour compared to the overlapping GB types commonly found and further studies may help reveal new band gap behaviours to stimulate ways to increase the density and controlled growth of these 2D bilayer interfaces.

## Chapter 5

### Atomically Thin Nanowell Patterns in Bilayer WS<sub>2</sub>

The previous chapter has revealed how the beam can introduce vacancies in monolayer/bilayers when doing ADF-STEM imaging, and in this chapter, I will apply this knowledge and introduce how to control the electron beam as an *in-situ* patterning tool at the atomic scale. In this study, the controlled production of atomically thin nanowells in bilayer WS<sub>2</sub> is achieved by a focused electron beam in a STEM combined with an *in-situ* heating holder. I systematically study the formation and evolution involved in removing a single layer of WS<sub>2</sub> within a bilayer region with 2nm accuracy in location which is adjustable by dose-dependent parameters without punching through to the other layer. The mechanism is discussed regarding removing one layer of WS<sub>2</sub> bilayer region which is different to removing equivalent sections in a monolayer film due to the van der Waals interaction of the underlying remaining layer in the bilayer system.

#### 5.1 Introduction

Void regions that are only a monolayer thick create ultras-small volumes and channels that are opening up new applications in nanofluidics and 2D chemistry.<sup>237-239</sup> By removing a monolayer area section within a few layered 2D stack, a 2D void is formed with confined chemistry and interactions that are not present in bulk volumetric spaces.<sup>240-241</sup> In single monolayer materials the voids become nanopores that have led to improved filtration membranes, selective ion transport channels, measurements of molecule propagation and biological ion migration through the pores and in particular the DNA sensitivity.<sup>242-254</sup> In few layered crystals, voids within the surface layer can then be used as nanowells,

restricting molecule diffusion and chemistry to 2D.

The nanowells have been used in prior work to trap  $\text{CoCl}_2$  from solution deposition and form nanocrystals.<sup>255</sup> The pristine lattice surface of 2D crystals often have low energy barrier for adatom diffusion,<sup>256-258</sup> and this means that when atoms are deposited on the surface they can migrate freely and do not stick until they find either a defect, grain boundary, step edge at the bilayer region, or the edge of the surface carbon residue on the nanowell.<sup>259-262</sup> This initial binding of atoms to the edge of a nanowell can then enable the lateral 2D crystal growth across the pristine area and lead to the formation of monolayer/bilayer metals such as Pt.<sup>99,263-264</sup> The filling of nanopores in monolayer graphene also led to the discovery of monolayer Fe crystals bound to the edges of the graphene void.<sup>265</sup>

Being able to create new types of nanoscale voids with precise shapes, depth and location will further expand this area. There are two approaches for 2D void formation, bottom up by the assembly of different layers, one by one, into a specific pattern. The other approach is top down etching, where 2D voids are created by etching material from a pre-existing stack. Top down etching can be done using resist based lithography methods (optical and electron beam) combined with plasma etching,<sup>266-268</sup> electrochemical reaction,<sup>269</sup> or with high energy irradiation by ions (He, Ar, Ga) or by electron beam irradiation.<sup>270-274</sup> Scanning probe methods can also be used to etch out monolayer materials.<sup>275-278</sup> Focused electron beam irradiation has one of the highest precision and control out of all methods, with *in-situ* atomic resolution monitoring.

In an aberration corrected STEM, the electron probe can be as small as 50pm, with the ability to place the beam on an atom of choice. This method of electron beam manipulation has been used in 2D materials to move single impurities around the lattice,<sup>97,101,279</sup> to displace a single atom from its lattice site to create a sub-nm

nanopore,<sup>184</sup> and write patterns in 2D materials by sputtering atoms from the lattice.<sup>280-283</sup> The sub-nanostructures like nanoribbons and nanowires have been sculptured on 2D graphene, MoS<sub>2</sub>, and black phosphorus.<sup>191,284-285</sup> In monolayer 2D crystals, nanopores have been created with spacing precision of ~5nm at high temperature, enabling patterned arrays on demand.<sup>280</sup> Elevated temperature is used in the 2D void patterning to obtain the well-defined nanostructures when maintaining pristine crystallinity.<sup>270,280</sup> However, extending these methods to the precise fabrication of nanowell voids in few layered 2D crystals has not achieved such accuracy and control to date. Further work is needed to demonstrate patterning of nanowells into arrays, along with the understanding of the mechanisms that govern the limits of fabrication.

In this chapter, a detailed study is presented regarding the nanowell fabrication method in bilayer WS<sub>2</sub>. The mechanisms on the atomic migration that underpin the nanowell formation are presented and then I demonstrate the patterning of single monolayer nanowells with ~5nm spacings and uniform area. The results are enabled by the use of an *in-situ* heating holder and suspended 2D WS<sub>2</sub> bilayers, providing clean material that is free from surface carbon residue that impinges on the understanding and formation process. I show how thermally induced vacancy migration plays a crucial role for the creation of nanowells. I demonstrate the etching of a single layer in bilayer WS<sub>2</sub> occurs differently to the etching of a single layer within monolayer WS<sub>2</sub>, due to the van der Waals interaction that enables the W metal to form a stable 2D crystal in the bilayer material, but not in the monolayer.

## **5.2 Results and Discussion**

### **5.2.1 Spatially Controlled Fabrication of Nanowell Patterns**

CVD-grown bilayer WS<sub>2</sub> films were transferred to a TEM chip for *in-situ* heating

experiments within an aberration corrected STEM at the accelerating voltage of 80 kV, which is suitable for mild sputtering of atoms from the WS<sub>2</sub> material. I conducted the nanowell drilling experiment at the high temperature up to 800 °C so as to eliminate the interference of covered hydrocarbon contamination which can restrict the defect production and migration. The schematic illustration in Figure 5.1 depicts the fabrication process of nanowells by using a focused electron beam as a drilling tool in STEM. Before drilling, an ADF-STEM image is taken on pristine WS<sub>2</sub> bilayers with a fast-scanning electron probe (typical pixel dwell time ~15 μs), as shown in Figure 5.1a,d. Then, the electron probe is confined in a small boxed region (typically ~2 nm×2 nm), scanning at a low rate to give irradiation of higher dose (dwell time ~35 μs/pixel), finally sputtering atoms of one layer out from this limited film and generating a monolayer-nanopore supported by the other intact layer, namely an atomically thin nanowell (Figure 5.1c,f).

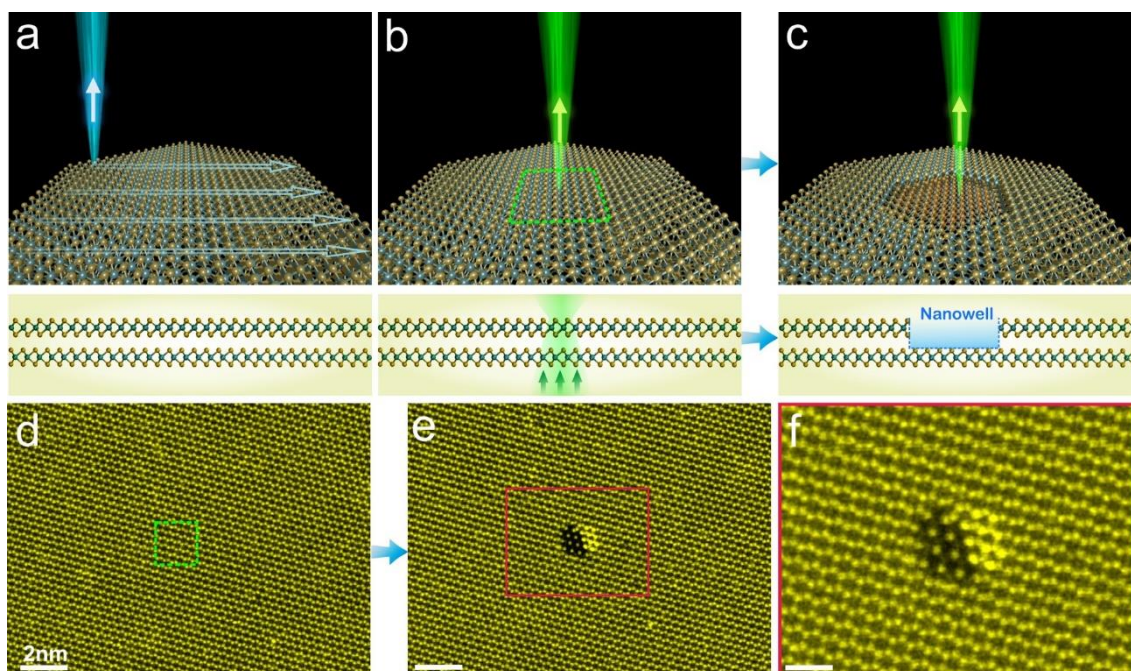


**Figure 5.1** (a–c) Schematic illustration of the drilling process of nanowells on bilayer WS<sub>2</sub> using electron beam with side views beneath the 3D perspective images. (a) A fast-scanning electron beam used to image bilayer WS<sub>2</sub>, obtaining an ADF-STEM image such as (d). (b) The beam is confined in a small region marked by green dashed box at a low scanning rate to drill one-layer nanopores out from the bilayer, forming the nanowell in (c). (d–e) ADF-STEM images taken at 800°C giving an example of the drilling process on WS<sub>2</sub> bilayers corresponding to the steps in (b–c). (f) Enlarged view of the red boxed region showing the nanowell in (e).

The nanowell fabrication process is highly reproducibly and controllable in positions and sizes by manipulating the drilling area and irradiating electron dose. Figure 5.2 gives a sequence of ADF-STEM images showing the one-by-one production of the sub-nanowell arrays at bilayer WS<sub>2</sub>. At the beginning, I identified a clean WS<sub>2</sub> bilayer film in Figure 5.2a. The green boxes mark the limited scanning region of the electron probe, which was moved to another given position once one nanowell drilling process was finished. Each nanowell in the array was drilled by giving the same dwell time and same beam current (10.3 pA, drilling for 40s each), yielding the equivalent irradiation electron dose. Consequently, one layer atoms only were sputtered away while retaining the other layer every time, with controlled sizes and spacings of the produced nanowells in a very small range (~1.1nm diameter, ~5nm spacing in average). The four nanowells (No. 1-4) were 1.1, 1.1, 1.3, 1.1nm, respectively in diameter when produced. Those nanowells show good structure stability, maintaining their configurations during low-dose imaging, although slightly enlarged (Figure B1).

It is noted from Figure 5.2 that all the five stable nanowells possess a re-crystallized metal-rich edge after formation, which are supposed to be reconstructed from the sputtered W atoms from one layer of the pristine bilayer WS<sub>2</sub>. According to the contrast features, the nanowell edges are categorized into two types. Type I nanowell edge (no. 1, 3, 4, 5 in Figure 5.2f) maintained the hexagonal configurations (Figure 5.2g-i), while type II (no.5 nanowell, Figure 5.2j) underwent reconstruction with changed phase. The two re-developed structures are not found in the edges of nanopores drilled on WS<sub>2</sub> monolayer at room temperature (Figure 5.2k), in which the ejected W atoms were aggregated on the surface of pore edge but in a random way. For the monolayer nanopores at high temperature (700~1000°C), prior work showed that metal atoms form 3D clusters at the edge,<sup>106</sup> and the positions of nanopores are less accurate to control due to the very high

mobility of vacancies which tend to migrate away from the irradiation area to build ultralong narrow line vacancies.<sup>106,117</sup> Here in the bilayer film, the migrating of S vacancies seems to be affected by the interactions with the supporting layer, and the remaining S-deficient metal atoms tend to re-structure locally, creating the nanowell at the exact drilled area.

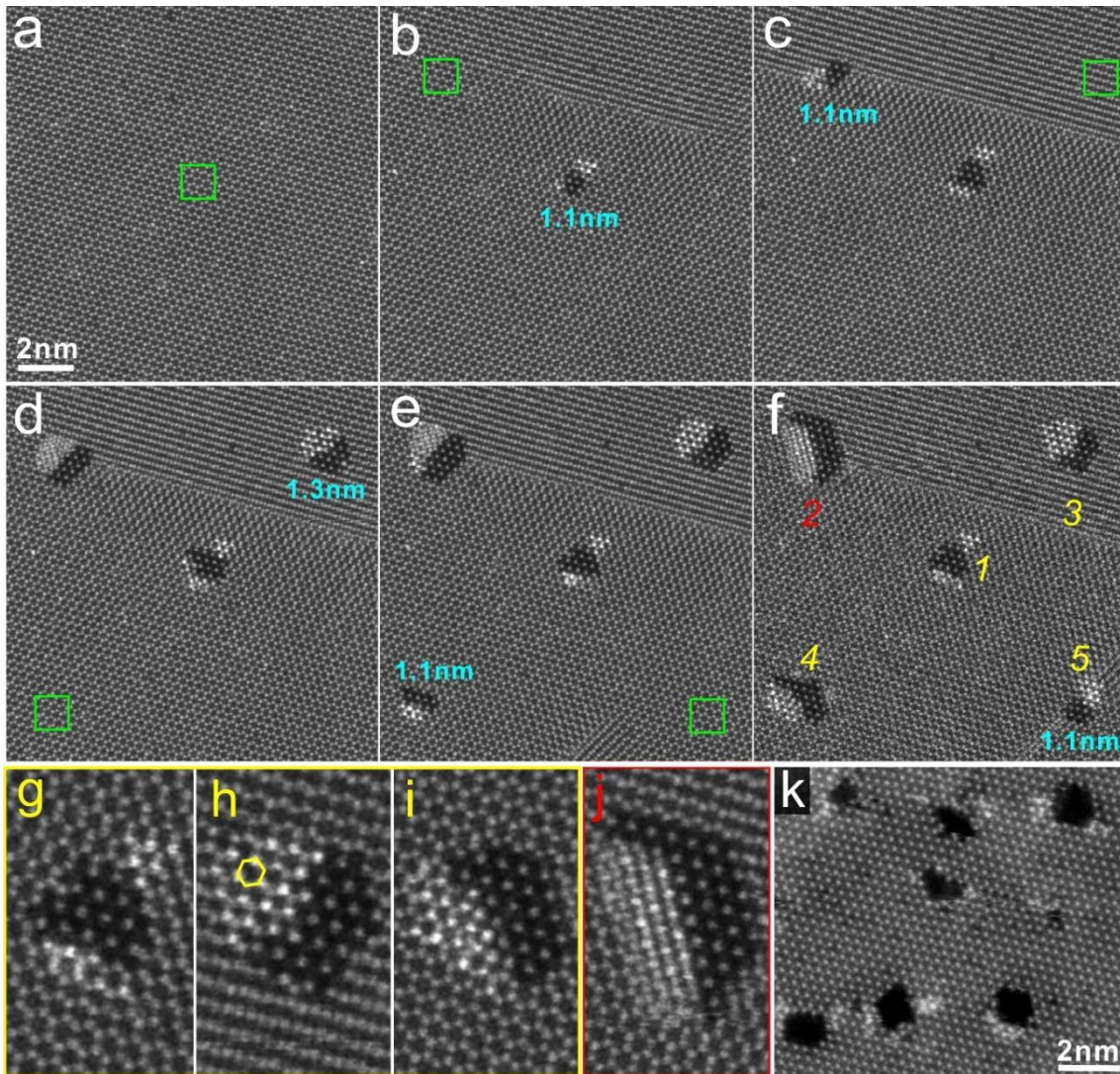


**Figure 5.2** (a–f) ADF-STEM image sequences showing the precise spatial control of the multiple atomically-thin nanowell arrays in a specified pattern, which are drilled one by one at bilayer WS<sub>2</sub> at 800 °C. The green boxes in (a–e) show the defined drilling regions of ~1.5 nm × 1.5 nm. The drilling time is ~40s each. (g–i) Magnified views of the nanowells with type-I edge numbered 1, 3, 4, respectively in (f). (j) Magnified view of the nanowell with type-II edge numbered 2 in (f). (k) ADF-STEM image of the monolayer WS<sub>2</sub> with drilled nanopore arrays for comparison.

## 5.2.2 Atomic Structures and Mechanisms of Nanowells

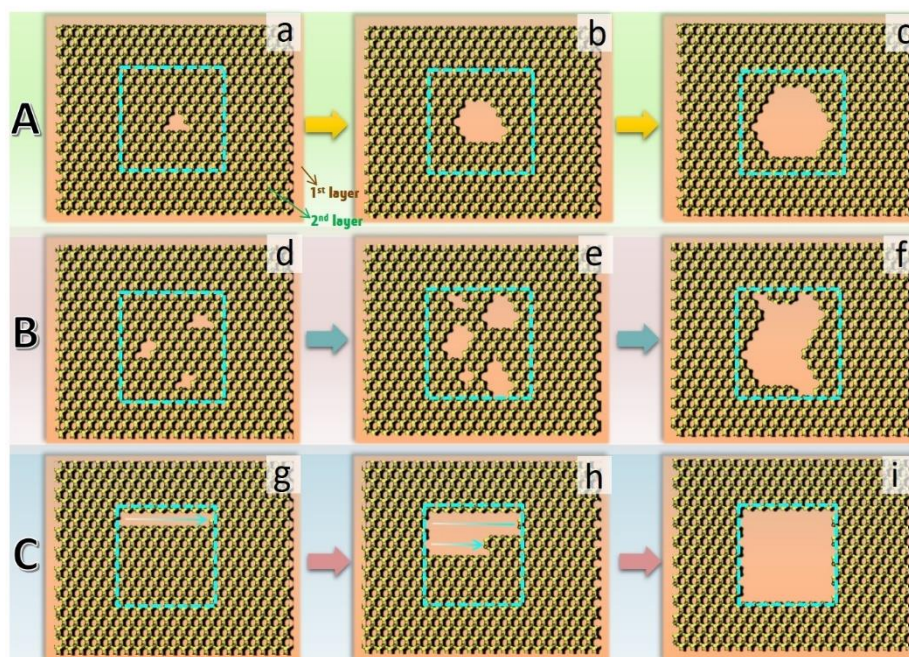


**Figure 5.3** Three sputtering dependent scenarios for the possible mechanisms of drilling nanowells in a bilayer region by raster scanning a focused electron beam in a predetermined boxed region. (a–c) Mechanism A (Close to the knock-on threshold). (d–f) Mechanism B (Moderately above the knock-on threshold). (g–i) Mechanism C (Well above the knock-on threshold).

When irradiating the confined region of a few-layered TMD continuously by a focused electron beam, there could be three possible nanowell formation mechanisms (Figure 5.3). For the first process (mechanism A, Figure 5.3a-c), it starts from the opening of a single nanovoid involving a couple of S vacancies, which then expands by further etching the edge atoms and evolves to be a faceted nanowell. This would be the likely scenario for an electron beam at the accelerating voltage close to the knock-on damage threshold (*e.g.*  $\sim 80\text{kV}$ ), *i.e.* when the transferred energy is close to or just overcomes the energy threshold for atomic displacement in monolayer  $\text{WS}_2$ . In scenario 2, if the electron beam transmits energy moderately above the sputtering threshold (*e.g.*  $100\text{-}150\text{kV}$ ), then a several tiny voids may be produced simultaneously, which can further expand and develop to be irregular shaped nanowells (mechanism B, Figure 5.3d-f). The third scenario is expected to occur if the beam is well-above the sputtering threshold (*e.g.*  $200\text{-}300\text{kV}$ ). Then during

a single scan pass of the electron beam, atoms are rapidly sputtered out, (mechanism C, Figure 5.3g-i), with the shape of the nanowell matching the scanned area. While in practice the squared pattern may be rarely found because of the tendency to form faceted voids in  $30^\circ/60^\circ/120^\circ$  angles with zigzag edges in  $\text{MoS}_2/\text{WS}_2$ , attributed to the more energetically favourable formation of zigzag edges with different reconstructed configurations as summarized in section 2.3.4.

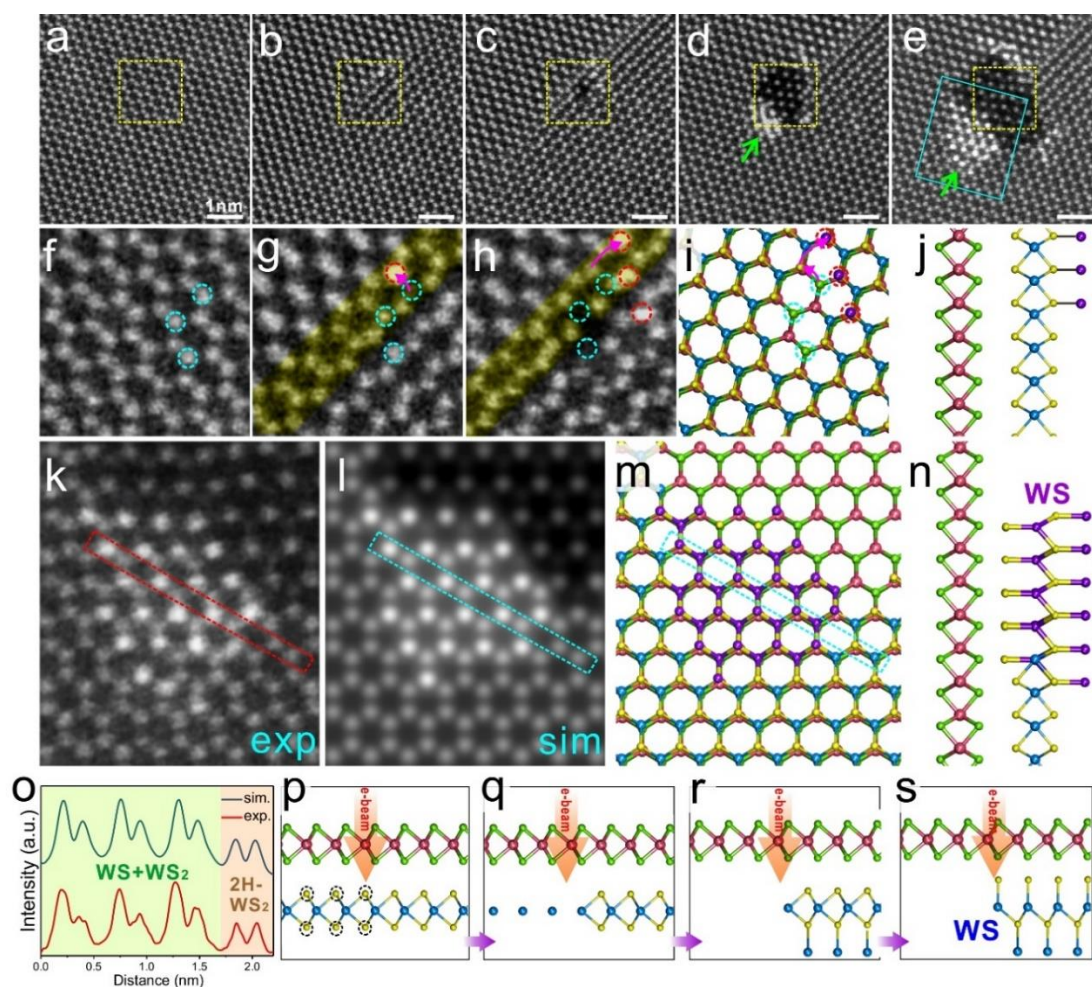


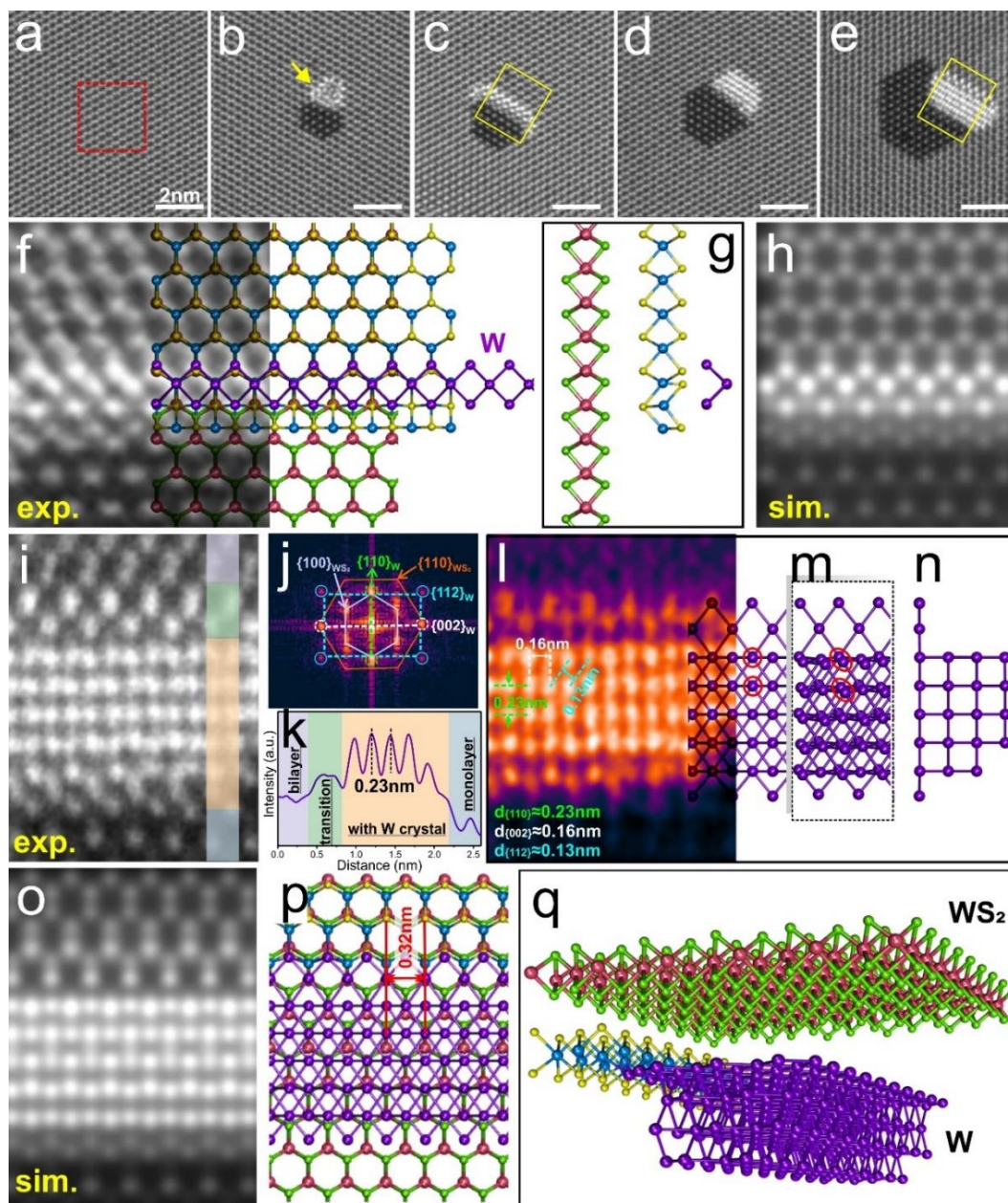
**Figure 5.4** Formation process of a typical nanowell with reconstructed epitaxial WS edge on bilayer  $\text{WS}_2$  drilled by focused beam at  $800^\circ\text{C}$ . (a–e) ADF-STEM image series showing the step-by-step drilling of a nanowell on bilayer  $\text{WS}_2$  in the same area. The beam is confined in a fixed region marked by dashed yellow box. The ADF-STEM images in (a–e) are recorded when drilled every 15 seconds. (f–h) Enlarged ADF-STEM images of the boxed regions in (a–c). The three W atoms marked by cyan circles in (f) are relocated onto the pink column in (h). The linear transparent yellow masks in (g,h) show the formed linear defects. (i) Atomic model based on the ADF-STEM image in (h), and (j) the side view of the model. (k) Magnified view of the blue-boxed region in (e), highlighting the reconstructed edge structure of the nanowell. (l) Simulated ADF-STEM image corresponding to (k), based on the atomic model in (m) with its side view in

(n). The purple spheres represent the W atoms ejected and reconstructed. (o) Intensity line plot profiles measured from the labelled regions of the experimental and simulated ADF-STEM images in (k,l) (p-s) Schematic illustration of the formation mechanism of the reconstructed epitaxial WS edge at the nanowell driven by focused beam.

In order to confirm the formation mechanism of the nanowells, the dynamic process was tracked step-by-step for one typical nanowell (type I). This is done by pausing the controlled boxed drilling process intermittently and then taking a wide view ADF-STEM image. The results in Figure 5.4 demonstrates a match for mechanism A in Figure 5.3, which is expected for an 80kV electron beam. Figure 5.4a-e shows the time-dependent ADF-STEM image series where the beam was limited to the centred yellow box ( $\sim 1.8\text{nm} \times 1.8\text{nm}$ ) at a slow scan rate of  $35 \mu\text{s}$  per pixel. The pristine clean  $\text{WS}_2$  film exhibits a 2H stacking type (AA' stacking). After the initial drilling of 15s (Figure 5.4b,g), there was an agglomeration of S linear vacancies. This then leads to the displacement of a single W atom adsorbed onto the surface of the neighbouring atom (pink circle in Figure 5.4g), which serves as the initiating site of the nanowell. When drilled for the second 15s (Figure 5.4h), an ultra-small nanowell was created with two more W atoms ejecting onto the nanowell-edge. This edge is different from the normal monolayer-bilayer step edge in the  $\text{WS}_2$  (Figure B2). These displaced W atoms were bonded onto S sites at the edge, which then triggered the nucleation of the defective structure composed of aggregated W atoms (marked by green arrow in Figure 5.4d). After further focused irradiation (Figure 5.4e), more W atoms became free and were released from the original positions with bond breaking, and at the high temperature of  $800^\circ\text{C}$ , those W atoms were re-aggregated and triggered to develop an epitaxial hexagonal WS crystal onto the  $\text{WS}_2$  edge. Figure B3 presents another example showing the same mechanism. This type-I reconstructed edge was magnified with atomic model in Figure 5.4k,m,n, and the multi-sliced simulation in Figure 5.4l shows good accordance as demonstrated by the intensity line profiles in Figure 5.4o. The number of the excessive W atoms also correlates with the total number that are

lost from the nanowell void. As another possibility, Figure 5.4k seems also like a tri-layer WS<sub>2</sub> in AA'A stacking. However, corresponding simulation is less matchable with the experimental (Figure B4). Moreover, the depletion of S in the nanowell region makes it less possible to form a third layer WS<sub>2</sub> with pristine stoichiometry, but more rationally to produce a S-deficient structure, *i.e.* the WS crystal.

Based on the ADF-STEM image series, the formation mechanism of the nanowell with reconstructed WS edge is illustrated in Figure 5.4p-s. When the electron beam hits the TMD bilayer, the bottom-layer atoms primarily suffer from the knock-on effect, because the energy thresholds for sputtering top-layer atoms facing the beam proved to be much higher, as the displaced atom can be 'stopped' by the supporting bottom layer.<sup>174</sup> Exposure to the beam in the narrow scanning window makes the S vacancies easily produced in a linear pathway, due to the comparatively low displacement threshold (the minimum initial kinetic energy of the recoil atom, ~6.5 eV for S in the TMDs lattice).<sup>173-</sup><sup>174</sup> When the surrounded S atoms are sputtered (Figure 5.4r), it becomes feasible to pop a single nanowell (*i.e.* to suddenly produce a single nanowell at a confined region) with W atoms ejected from the bottom layer which then attach at the pore edge. Triggered by further beam irradiation and thermal energy, those excessive W atoms interact with WS<sub>2</sub> at the edge and undergo structural reconfiguration to a 2D WS nanocrystal. The details of WS crystal structure are presented in Figure B5. The WS is also a hexagonal crystal but bulk material in nature. Previous study has shown the bulk crystal could grow epitaxially on layered TMDs through strong interfacial coupling.<sup>286</sup> Here, the 2D WS nanocrystal is a single atomic plane along the [001] direction, which is stabilized as an epitaxial 2D hexagonal monolayer onto the surface of the templating WS<sub>2</sub> beneath *via* interlayer interactions, decorating around the nanowell.



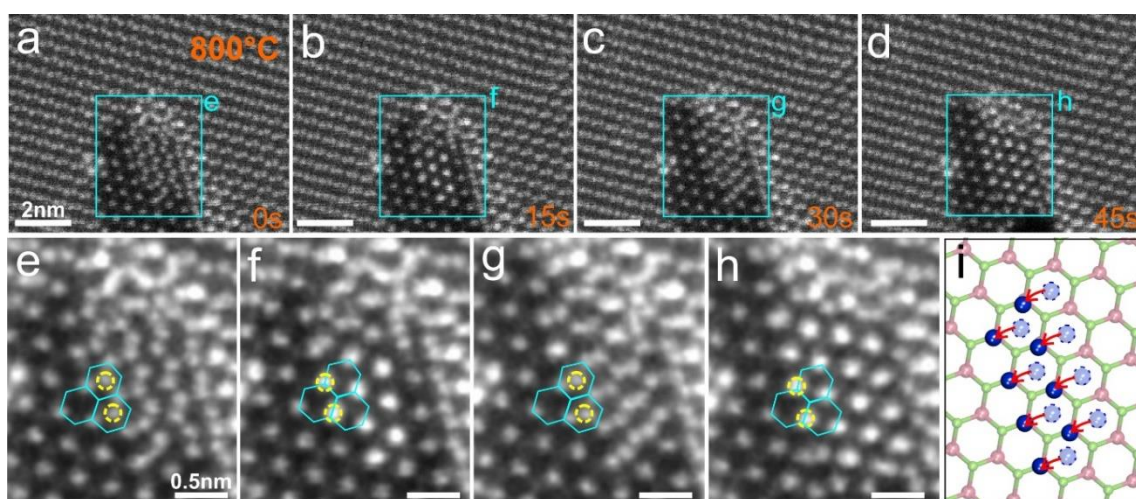
**Figure 5.5** Formation dynamics of the other type of nanowell with reconstructed edge of 2D tungsten (W) crystal *via* drilling bilayer WS<sub>2</sub> at 800 °C. (a–e) ADF-STEM image series showing the step-by-step drilling of a nanowell. The beam is confined in a fixed region marked by red box in (a), drilling out a sub-nanowell in (b) after 30s. The images in (c–e) are recorded when further drilled. (f) Magnified view of the boxed region in (c), with schematic atomic model overlaid and (g) side view. (h) Multi-slice simulation corresponding to (f). (i) Enlarged boxed region in (e). (j) Power spectrum by FFT of (i). Aligned spots between the cubic phase W crystal and WS<sub>2</sub> are indexed. (k) Intensity line plot profile obtained from the multi-coloured region in (i), and corresponding colours are used to mark the positions. (l) Reconstructed ADF-STEM image after applying a mask to the FFT of (j) to remove the WS<sub>2</sub> lattice contribution, showing only the 2D W crystal structure along [110] direction. Overlaid is the atomic model of the W crystal viewing from the [110] direction, with (m) its 3D perspective view, and (n) side view. The red circles manifest two W atoms at each column. (o) Multi-slice simulation corresponding to (i), based on the atomic model in (p). Scheme of 3D perspective side view of the model in (p).

Figure 5.5 analyses the dynamics of the other type of reconstructed metal-rich edges with changed phase on the drilled nanowell (type II). Firstly the amorphous metal cluster was formed at the edge by aggregated W atoms in Figure 5.5b, when the S atoms of one layer were bumped from the beam-focused region. These assembled W atoms then spread and uniformly adhered to the defective edge of the bottom layer, arising from the edge effect (Figure 5.5c). This is an intermediate state before recrystallization, where the bottom layer has the distorted S-deficient edge similar to the previous reports,<sup>104,168</sup> due to the loss of the S atoms around the void (Figure 5.5f). This exposed edge provides abundant defective sites for adsorb excessive W atoms, and the positions of the stacked W atom membrane (the purple atom model) is relative to the WS<sub>2</sub> lattice beneath (Figure 5.5f,g). The spread W membrane with non-stoichiometry was recently predicted to be the most energetically favourable pure metal monolayer which exhibits squared lattice.<sup>194</sup> The simulated ADF-STEM image *via* a multi-slice method accords well with the experimental image (Figure 5.5h). After intense beam stimulation with thermal annealing (800°C), the W-rich edge reconstructed to another orthogonal phase instead of the pristine hexagonal lattices, and showed stability which expanded without further structural change (Figure 5.5d,e). This crystal developed into a 2D pattern on the supported WS<sub>2</sub>, yielding homogeneous contrasts in the ADF-STEM image with atomic sharpness (Figure 5.5i). The 2D fast Fourier transform (FFT) of Figure 5.5i shows two different groups of spots: one group in hexagonal pattern containing two sets that belong to {100} and {110} of WS<sub>2</sub>, *i.e.* the zigzag and armchair directions, respectively, while the other group shows orthogonal patterns which can be assigned to {110}, {002}, and {112} of the tungsten (W) single crystal with a body centered cubic (bcc) structure viewing along [110] direction. The 2D tungsten (W) crystal is heteroepitaxially templated on the WS<sub>2</sub>, in which the {110}<sub>w</sub> is aligned with one zigzag direction of WS<sub>2</sub> and the {002}<sub>w</sub> is parallel

to the armchair direction. The line plot profiles obtained from Figure 5.5i show contrast intensities changing from bilayer WS<sub>2</sub>, transitional edge region, and the heteroepitaxial W crystal on WS<sub>2</sub>, to the monolayer WS<sub>2</sub>. The distance measuring from the line plot profile in W crystal region is ~0.23nm, corresponding to the interplanar spacings of {110} of the W crystal. The lattice structure of 2D W crystal is extracted by applying a mask to the 2D FFT to filter out the lattice contribution from hexagonal WS<sub>2</sub> (Figure 5.5l). The interplanar spacings of {100}<sub>w</sub> and {002}<sub>w</sub> and {112}<sub>w</sub> are measured to be ~0.23, ~0.16 and ~0.13 nm, respectively, consistent with that for bcc W single crystal. The atomic model of W crystal is overlaid on Figure 5.5l, where each column has two overlapped W atoms, giving the equivalent contrasts in the reconstructed ADF-STEM image. Figure 5.5o presents the simulated ADF-STEM image obtained from the atomic model of the W/WS<sub>2</sub> heterostructure (Figure 5.5p), with the schematic 3D model in Figure 5.5q. This localized phase change is a result of S depletion, electron stimulation, thermal energy, as well as the templating of supported WS<sub>2</sub> layer. According to the previous calculation, the formed metallic 2D metal membrane could be stabilized by charge transfer.<sup>194</sup> Besides, the good match between the d-spacing of {002}<sub>w</sub> with that of {110}<sub>ws2</sub> may also contribute to the stabilization of the heteroepitaxial structure.

Dynamics of 2D W metal atoms near the nanowells edge were observed at high temperature (Figure 5.6a-d). In a previous report, a 2D suspended pure transition metal (Mo) membrane was fabricated locally from monolayer MoSe<sub>2</sub> by electron beam sputtering at room temperature.<sup>193</sup> During the fast scanning ADF-STEM images, the W atoms quickly shifted from the hexagon void sites of the supported monolayer WS<sub>2</sub> onto its W sites (Figure 5.6e-h), then migrated back to the hexagon void sites followed by the W sites again. This demonstrates the 2D chemistry occurring within the atomically thin nanowells, where the edges provide the bonding pinning site and the interaction with the

bottom WS<sub>2</sub> under high temperature drives variations in the van der Waals stacking. This is different to what would occur in nanopores in monolayers without van der Waals interactions, and on the surface of a pristine 2D crystal there are no edge sites to bind the initial crystal formation. Some similar chemical interactions might be expected at monolayer-bilayer step-edges that occur naturally or randomly in crystals, but cannot be controlled in their location.



**Figure 5.6** (a–d) Time series of ADF-STEM images showing the dynamics of a 2D W cluster in a nanowell under electron beam at high temperature (800°C). (e–h) ADF-STEM images by fast scanning after (d). (e–h) Magnified views of the light blue boxed regions, showing the mobility of the W atoms on supported WS<sub>2</sub> at high temperature. (i) Atomic model showing the migration positions of the 2D W cluster.

For comparison, the continuous drilling at lower temperature (300°C) is conducted at a clean pristine WS<sub>2</sub> bilayer (Figure 5.7). Different to the high-temperature behaviour, the continuing drilling of 160s did not create a nanowell, while exerting local strains as marked by the yellow arrow in Figure 5.7b with the concentrating of beam-driven vacancies. Much longer irradiating time was needed for causing a pore, which produced a drilled-through bilayer hole straightforward instead of a nanowell. Figure 5.7f,g highlight the lattice structures, where the bilayer edges were distributed by W atoms with some dangling bonds. When zooming out after the bilayer hole formed, this drilling region was covered by beam-induced carbon contamination (Figure 5.7e), which could

protect the WS<sub>2</sub> and restrict the atoms displacement. In this case, the vacancies or atoms migration is impeded while the local non-orthogonal strains are accumulated which could cause out-of-plane distortion and finally punching a bilayer hole. In contrast, at the high-temperature, the amorphous carbon contamination can be avoided on WS<sub>2</sub>, and the high temperature facilitated the nucleation of the re-formed crystal in providing thermal energy and enabling vacancies migration and atoms displacement.

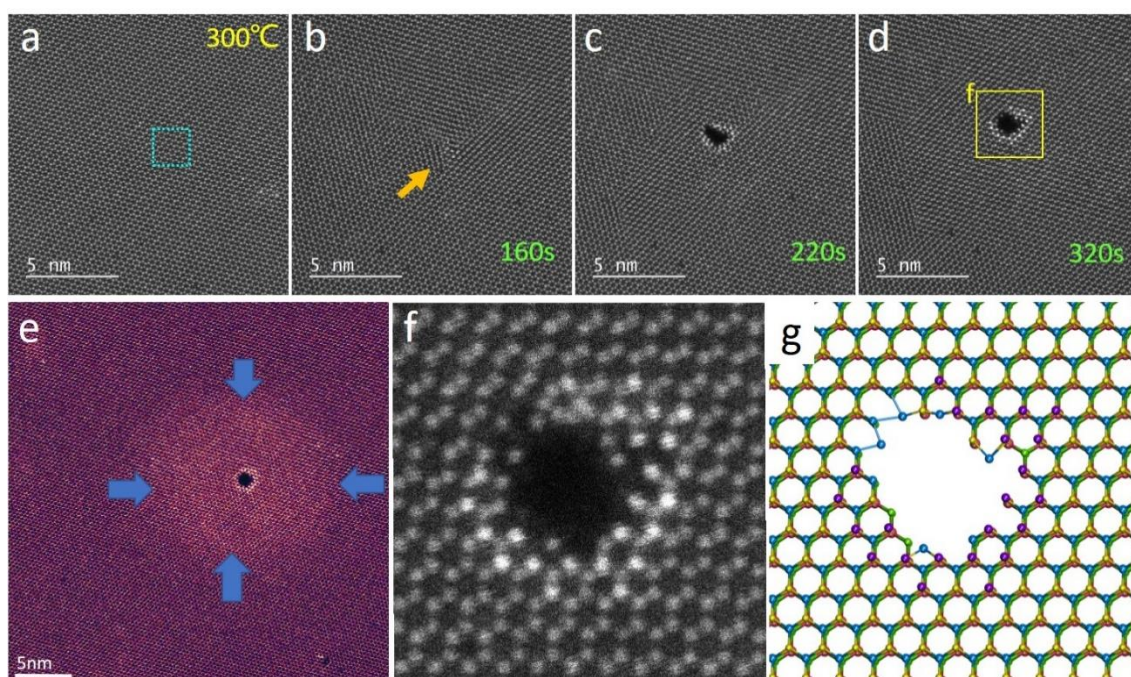


**Figure 5.7** Bilayer hole obtained when drilling at lower temperature of 300°C on bilayer WS<sub>2</sub>. (a–d) ADF-STEM image series taken at 300°C when the focused electron beam is confined in the fixed area marked by the dashed blue box in (a). (e) Zoomed-out ADF-STEM image from (d), showing the beam-induced carbon contamination after both layers are drilled through. The four arrows mark the position of contamination. (f) Magnified ADF-STEM image of the yellow-boxed region in (d). (g) Schematic atomic model corresponding to (f).

The precise control of the nanowell fabrication requires the manipulation of both the positions and sizes. The variation of the average sizes of nanowells created by adjusting the exposure time is presented in Figure 5.8. The nanowell sizes show the dose-dependent behaviour according to the plot graphs of the relationship between nanowell sizes (nm<sup>2</sup>) and the beam irradiation time for each of the examples (Figure 5.8f,g). Figure 5.8h shows a fitted linear plot of nanowell sizes as a function of average electron dose which was

adjusted from  $\sim 1.4 \times 10^8$  to  $\sim 2.3 \times 10^9 \text{ e}^{-1} \text{ nm}^{-2}$ . Here the average electron dose (D) is calculated by  $D = I \cdot T / A$ , using the beam current (I), beam illuminating area (A) and the irradiation time (T).<sup>287</sup> In this work I focused on the dynamics at varied dose, *i.e.* keeping the beam current density the same and adjusting the dwell time. If we consider the case of different dose rates, larger dose rate is speculated to speed up the evolution of nanowell, as the dose rate can determine how fast radiation damage progresses, which means it can affect the speed of the formation and growth of nanowell sizes.

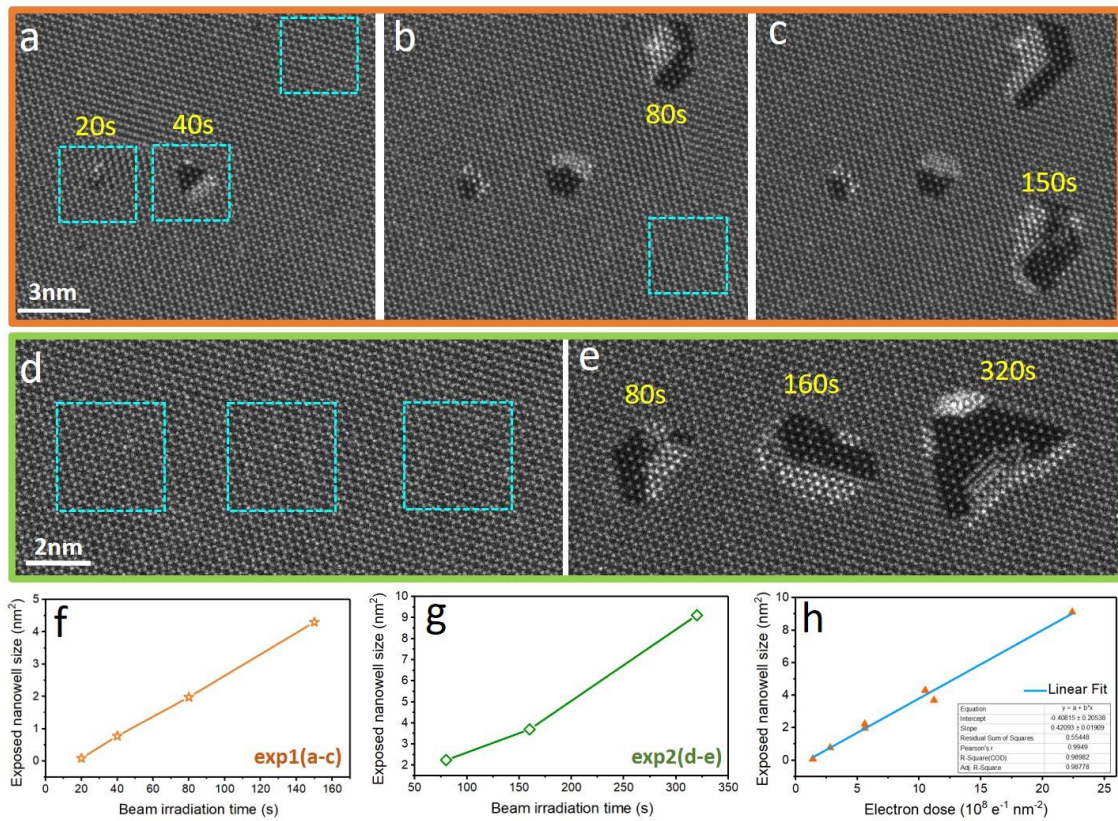


**Figure 5.8** Electron dose dependence of the nanowell drilling. (a–c) ADF-STEM image series showing the successive production of nanowells of varying sizes by controlling different exposure time within the same drilling area in bilayer WS<sub>2</sub> under high temperature of 800°C. (d–e) Another example of ADF-STEM image series showing the dose-varied drilling of different-sized nanowells. The three nanowells in (e) are produced from the same-sized drilling boxes shown in (d) after exposed for 80s, 150s and 320s, respectively. (f,g) Two line graphs corresponding to (a–c) and (d–e), respectively, showing the relationship between the nanowell sizes (nm<sup>2</sup>) and the beam irradiation time in the drilling boxes. The nanowell sizes are defined using the area of the exposed monolayer. (h) Linear fit plot of the exposed nanowell sizes (nm<sup>2</sup>) as a function of electron dose (10<sup>8</sup> e<sup>-1</sup> nm<sup>-2</sup>) obtained from all the nanowells in the two examples.

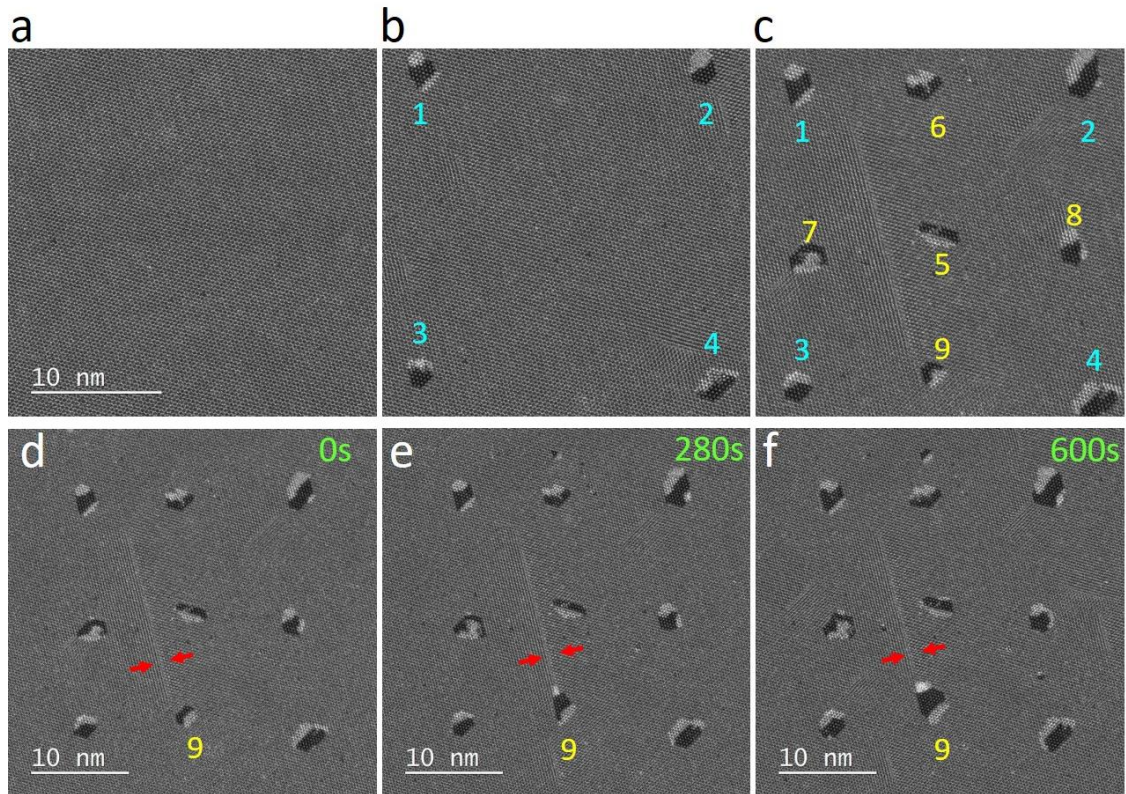


**Figure 5.9** The precisely controlled nanowell array in a WS<sub>2</sub> bilayer film at 800°C. (a–c) ADF-STEM images showing the drilling process of the nine-nanowell array pattern, where the number indicates the sequence of the drilling. The drilling time is ~45s each. (d–f) ADF-STEM images series when exposing the WS<sub>2</sub> film at the fast scanning mode for a certain time (280s, 600s), with the dwell time of 10 μs applied on 512×512 pixels, and the images were taken by 1024×1024 pixels with 15 μs per pixel.

The ability of accurate control of the nanowell array fabrication is further exhibited in Figure 5.9. The well-defined nine-nanowell array pattern was properly manufactured with the diameter of ~1.8nm each and average spacing of ~9 nm. After patterning, the fast scanning ADF-STEM imaging evaluates the nanowells stability, in which all the structures are maintained (Figure 5.9d-f). The nanowell labeled by number 9 has the largest expanding rate, mainly because it is at the end tip of extending line defect (red arrows in Figure 5.9d-f), where large compressive strain field exists, building up S vacancies much faster.<sup>117</sup> This manifests the size-retaining capability of the nanowells is normally high under the fast-scanning electron beam, while the effect from the line-defect environment also needs to be considered.

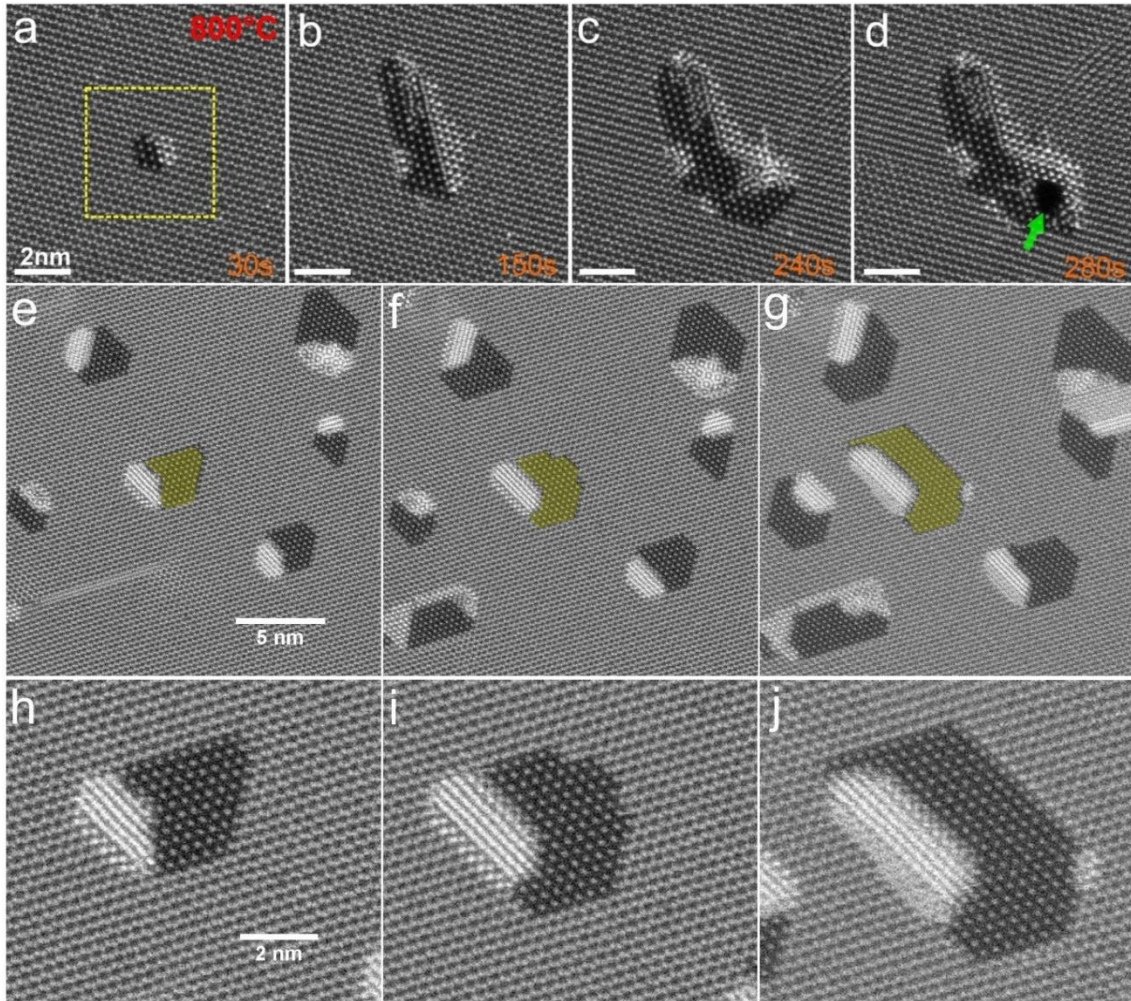


**Figure 5.10** Limits of the expansion of nanowells. Temperature = 800°C. (a–d) Series of ADF-STEM images taken after consecutive boxed drilling within the area defined by the yellow square in (a). A hole eventually opens up in (d), indicated by the green arrow. (e–g) Expansion of nanowell sizes by using large area electron beam exposure across the entire image. First a set of nanowells is drilled in several specific locations using small box of 1nm width. Then the entire area is continuously imaged, exposing the large area to electron irradiation and vacancy production. This leads to the nanowells slowly expanding without popping holes into the nanowells. Yellow shading indicates a central nanowell that expands and is shown in higher magnification in (h–j).

The final study investigated the limiting mechanisms of the continual expansion of the nanowells in size. Using a single boxed area for nanodrilling eventually leads to holes appearing in the nanowell (Figure 5.10a-d). The images in Figure 5.10a-d were taken after each consecutive drilling time. As the nanowell increases in size, more of the underlying monolayer is exposed to the 80keV beam, which statistically leads to holes forming in the exposed monolayer (Figure 5.10d). An alternative approach was then used, whereby

several nanowells were introduced in specific areas locally using a 1nm box to drill, and then these initial small nanowells are then expanded by exposing the larger area to the beam. This is essentially expanding the drilling box to create more vacancies that can migrate to the nanowells and result in enlargement. Figure 5.10e-g shows such a process, where the nanowells are enlarged to widths greater than 5nm. As the nanowells expand they begin to merge together, as seen in the top right corner of Figure 5.10e-g, shown in more detail in Figure 5.11.

### 5.3 Conclusion

In summary, the precise fabrication of nanowells in bilayer WS<sub>2</sub> is demonstrated by manipulating the electron beam conditions at 80 keV as the drilling tool, combined with an *in-situ* high temperature holder. Atomically thin etching from a given area is demonstrated with 2nm precision in location and 5nm separation distances between nearest neighbour nanowells. The mechanisms of nanowell formation is found to differ from the nanopore production in monolayers. High temperature of 800°C yields sufficient thermal energy, mobility of atoms and avoids covered amorphous carbon, which facilitates the metal atoms ejecting, migrating and reconstructing on edge for stabilizing the nanowell. The nanopore sizes show dose-dependent behaviours, offering the possibility of accurate manipulation of the size by adjusting exposure time and scanning areas. The methods to expand nanowells by large electron irradiation and their merging dynamics was revealed. It is possible that this technique could also be expanded in the future to mixed 2D vertical heterostructures, such as MoS<sub>2</sub>/WS<sub>2</sub> hetero-bilayers to make use of differences in electron beam damage rates for selective layer sputtering and patterning. The production of nanowells may give rise to opportunities for exploring surface chemistry in 2D confined environments.

## Chapter 6

### Defects and Grain Boundaries in 1T-Phase PtSe<sub>2</sub>

Most defects study to date have focused on the Mo or W based 2H-phase TMDs, but the structural research on the emerging noble metal TMDs, 1T-phase PtSe<sub>2</sub>, is still limited, which is also an essential member in TMD families and is playing an increasingly significant role in new 2D devices. In this chapter, I will move onto the understanding of defective structures in 1T-PtSe<sub>2</sub>. The atomic structures of point vacancies, stretched 1D defects, dislocations and grain boundaries (GBs) are systematically investigated in 1T-PtSe<sub>2</sub> monolayers, by using ADF-STEM at low accelerating voltage of 60kV. The dynamical process of those defects under electron beam is tracked and analysed for unveiling their evolution mechanism at the atomic level.

#### 6.1 Introduction

In the past several decades, TMDs of group VIB metal MX<sub>2</sub>, like M=Mo, W, and X=S, Se, typically with hexagonal 2H polytype, have been studied intensively in fundamental structures, properties, and applications.<sup>14,40,86</sup> They possess sizable band gaps in the range of 1.5–2.0 eV,<sup>31,288</sup> corresponding to the red to near infrared regions. While the wider range of optoelectronic applications require further exploration of novel 2D materials for full cover of the colour regions. The emerging noble metal TMDs, e.g. PtX<sub>2</sub>, have recently gained a lot of attention for expanding the 2D family, due to their fascinating properties such as the layer-controllable transition from metal to semiconductor, the notable carrier mobility, strong interlayer interaction, anisotropy, and ultrahigh air stability.<sup>289-298</sup> The tunable band gaps in the range of 0.25–1.6 eV of PtX<sub>2</sub> make up the gap between graphene

and most other TMDs, enabling their promising utilization in the desirable mid-infrared photonics and optoelectronics.<sup>299-302</sup> Lately, the growth of monolayer PtSe<sub>2</sub> has been experimentally realized through direct selenization of the thin Pt substrate.<sup>303</sup> Recent studies have also shown their high application potential in wide-ranging devices including spintronics, valleytronics, catalysis, and sensors.<sup>304-311</sup>

Differing from the common 2H-phase structures of Mo/W-based TMDs, the 2D PtX<sub>2</sub> crystal is preferably constructed in 1T polytype. Accordingly, their structural properties are supposed to be differentiated from those in 2H-TMDs. Understanding different defect structures in 1T-PtX<sub>2</sub> and their behaviours is vital for taking full advantage of them in tailoring materials properties. Theoretical studies have predicted the structures and stability of point defects in 1T-phase PtX<sub>2</sub>, as well as the affected electronic and magnetic properties,<sup>113,294,312-313</sup> while the experimental research addressing the defects in monolayer PtX<sub>2</sub> is still very limited so far, particularly for the intrinsic grain boundaries (GBs) that are ubiquitous in polycrystalline 2D materials. Several types of point defects were characterized by scanning tunneling microscopy (STM).<sup>110</sup> However, the atomic-level behaviours of defects and GBs in monolayer PtSe<sub>2</sub> have yet to be systematically investigated, which is crucial for exploiting the great potential of PtX<sub>2</sub> for extensive device applications.

In this chapter, I mainly use the atomic-resolution ADF-STEM at low accelerating voltage (60kV) for direct visualization and *in-situ* record of the defect and GB structures in monolayer 1T-PtSe<sub>2</sub> and their dynamic behaviours. The atomic structures of a varieties of defects and GBs have been identified, which are distinctly differentiated from those in the commonly found 2H-phase TMDs. I examine the how the structure transforms locally when excessive point vacancies are produced, and discuss the evolution mechanisms induced by the integrative behaviours of vacancies. Series of distinct dislocations are

directly observed in tilt-angle monolayer GBs with distinct 1T-feature configurations. On the basis of dislocation cores, the GB structures are investigated in terms of pathways of dislocation chain, different misorientation angles, and 2D strain fields induced.

## 6.2 Results and Discussion

### 6.2.1 Atomic Structures and Dynamics of Point Vacancies

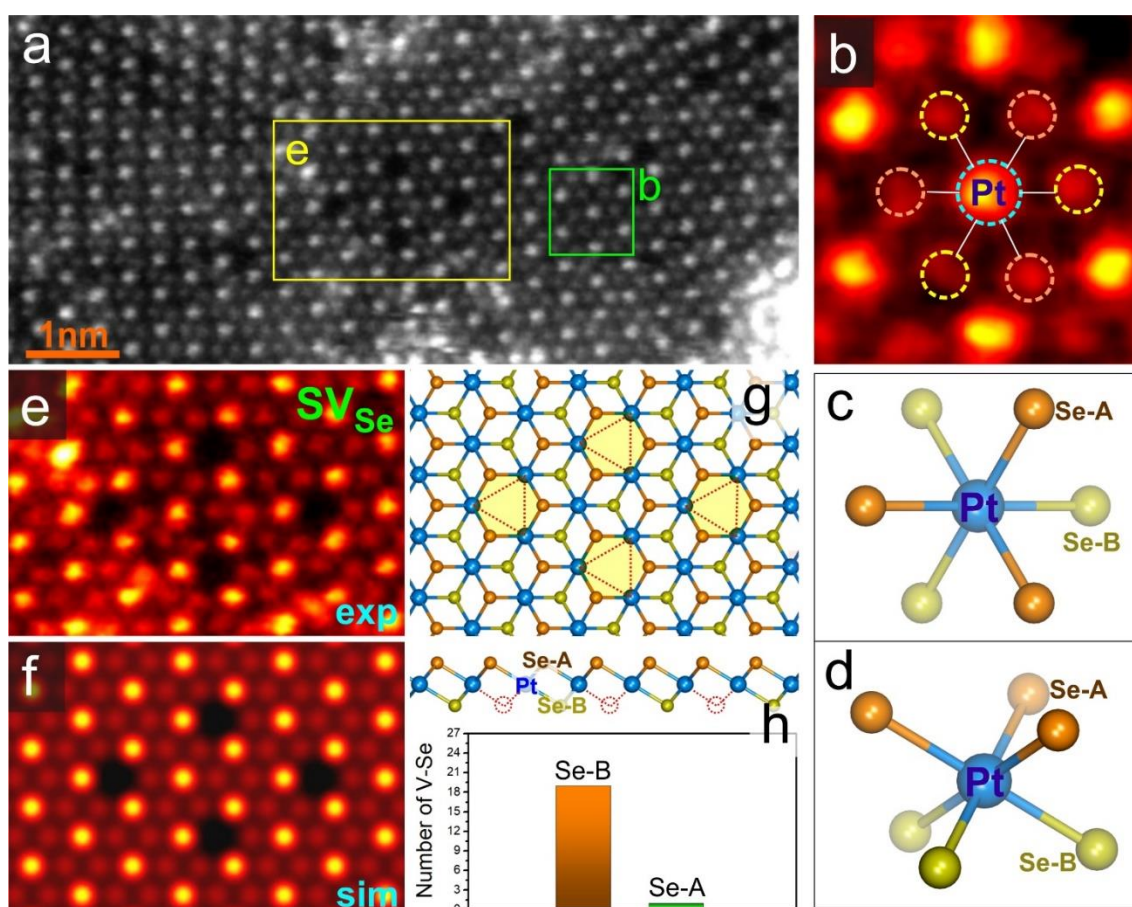


**Figure 6.1** Single Se point vacancies ( $V_{Se}$ ) of in monolayer  $PtSe_2$ . (a) ADF-STEM image of monolayer  $PtSe_2$  film containing isolated  $V_{Se}$ . (b) Enlarged STEM image in the green boxed region in (a). The circles highlight the relative positions of Pt and the surrounded six Se atoms. (c) Planar view and (d) 3D perspective view of the schematic atomic model corresponding to the marked atoms in (b), defining the A and B sites of Se atoms relative to the centred Pt, denoted as Se-A and Se-B, respectively. Pt: cyan, Se-A: gold, and Se-B: yellow spheres. (e) Enlarged view of the yellow boxed region in (a), showing four  $V_{Se}$ . (f) Multi-slice simulated ADF-STEM image corresponding to (e), with the atomic model in (g). (h) Histogram showing the statistics of the number of  $V_{Se}$  of the two different sub-lattice sites, examined from the ADF-STEM image in (a) with twenty  $V_{Se}$  counted in total.

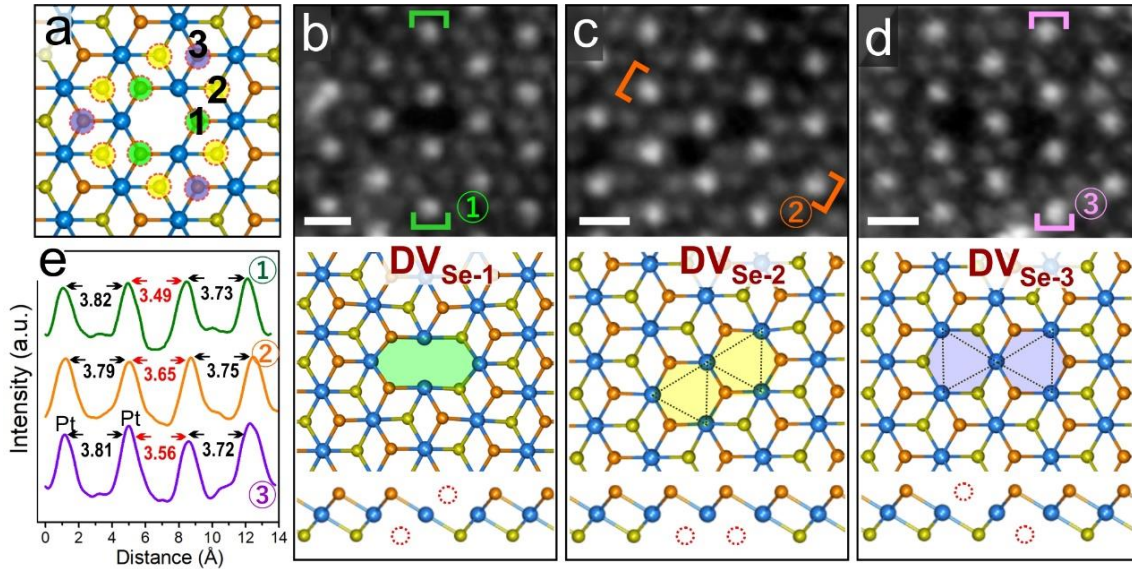


**Figure 6.2** Divacancies of Se ( $DV_{Se}$ ) in monolayer  $PtSe_2$ . (a) Schematic atomic model showing three possibility of  $DV_{Se}$  by losing three different Se atom positions next to a  $SV_{Se}$ , which are marked by green, yellow, and purple coloured circles with increased distance in the planar view relative to the  $SV_{Se}$ . (b-d) Experimental ADF-STEM images captured at monolayer  $PtSe_2$  showing examples of these three  $DV_{Se}$ ,  $DV_{Se-1/2/3}$ , with corresponding schematic atomic models displayed beneath, separately. Scale bars: 0.3nm. The vacancy columns are highlighted by green, yellow and purple shades in the planar models, respectively, with dashed circles in the side views marking the positions of the two lost Se atoms. (e) Intensity line plot profiles obtained from the marked regions in the ADF-STEM images in (b-d), respectively, measuring the Pt–Pt spacings of the lattices involving  $DV_{Se}$ .

Atomically thin  $PtSe_2$  films were grown as described in Section 3.2.3 in Chapter 3. Figure 6.1a shows an atomic-scale ADF-STEM image of a monolayer  $PtSe_2$  grain. It exhibits typical contrast characteristics of 1T-phase monolayers, where each contrast site is contributed by one atom only, and each Pt atom is surrounded by six Se atoms in the planar view (Figure 6.1b). There are two subgroups of Se atoms in 1T- $PtSe_2$ , denoted as Se-A and Se-B, according to their different sub-lattice positions relative to the Pt atoms (Figure 6.1c). These two different Se sites situate at top or bottom layers from the side view (Figure 6.1d). Here the imaging was conducted at a mildly heating condition of 200 °C for a balance between reducing contamination and maintaining pristine phase. Note that further heating treatment on  $PtSe_2$  above 500 °C will cause its phase transition to a new non-layered phase  $PtSe$ , as reported in the literature,<sup>210</sup> making it difficult to completely

remove carbonous contaminations *via* increasing temperature. This is different from the thermal stability of MoS<sub>2</sub> even at 1000°C which enables the use of high-temperature annealing.

For 2D TMDs, chalcogen vacancies are commonly generated due to their comparatively low displacement threshold energy (eg. ~6.4 eV for Se in the MoSe<sub>2</sub> lattice, which can be overcome by the energy transferred from electron beam of 80 keV ).<sup>174</sup> In Figure 6.1a, numerous Se point vacancies ( $V_{Se}$ ) are distributed, mainly induced by high-energy electron beam during imaging. Figure 6.1e clearly demonstrates the contrast feature of four  $V_{Se}$ , with qualitatively-matched simulation in Figure 6.1f. Note that all these four  $V_{Se}$  are derived from the loss of Se atoms at the same sub-lattice positions of Se-B (Figure 6.1g), which is also the most frequently observed  $V_{Se}$  site across this whole monolayer region according to the  $V_{Se}$  statistics in Figure 6.1h (Se-B: Se-A=19:1). The Se-B is supposed to be the bottom Se atom that primarily suffers from the knock-on effect of the beam according to the previous report proving the lower sputtering threshold of the bottom chalcogens.<sup>174</sup>

In 2D crystal monolayers, the vacancies can occur in pairs, forming the divacancies in the lattices. For the binary 2H-phase TMDs like MoS<sub>2</sub>, sulphur divacancies (DV) are created when the two sulphur atoms at the same column are lost. Here in the 1T-phase PtSe<sub>2</sub>, when one  $SV_{Se}$  is produced, there are three different Se atom sites right next to this  $SV_{Se}$  within one lattice unit (Figure 6.2a), which can be further ejected to form three types of  $DV_{Se}$ . Here all these three  $DV_{Se}$  structures commonly co-exist in the monolayer PtSe<sub>2</sub> in the observation (Figure 6.2b-d). More examples are given in Figure C1-3. In contrast to the discretely distributed  $SV_{Se}$  across the PtSe<sub>2</sub> which tend to lose Se atoms from the same sub-lattice site, *i.e.* the same Se layer, here the two missing Se atoms of  $DV_{Se}$  can be from the same sub-lattice site along the zig-zag direction ( $DV_{Se-2}$ ), or different sites in

the armchair direction ( $DV_{Se-1/3}$ ) (Figure 6.2b-d), which manifests the existed  $SV_{Se}$  could facilitate the ejection of its neighbouring Se atom when the incident beam hits. As the  $DV_{Se-3}$  has been predicted to possess lower relative energy,<sup>113</sup> the second Se is more likely to be ejected from different sub-lattice site separated by a Pt atom. The Pt–Pt spacings of the lattices around the  $DV_{Se}$  examined by intensity line plot profiles demonstrates the lattice contraction for all these  $DV_{Se}$  in slightly different extent (Figure 6.2e). The average Pt–Pt spacing along the [100] direction in pristine PtSe<sub>2</sub> is 3.76 Å, while it decreases to 3.49, 3.65, and 3.56 Å, for  $DV_{Se-1}$ ,  $DV_{Se-2}$ , and  $DV_{Se-3}$ , respectively. Note that the  $DV_{Se-1}$  has the largest lattice shrinkage by 7.2%, in which the two Se vacancies are from the same Pt–Se–Pt unit and has the nearest planar distance, jointly forming an 8-member void defect. The  $DV_{Se}$  example in Figure C1d also exhibits spacing shrinkage of similar extent. It can be inferred that the contraction of lattice spacings caused by the joint loss of two adjacent Se atoms can exert effects on the local strain field in the lattice.

Chalcogen point vacancies in 2D TMDs can be mobile under electron beam when the migration energy barriers are overcome. This mobility leads to a series of beam-induced defects dynamics, like the one-dimensional (1D) agglomeration of S vacancies and the resulted vacancy lines in 2H-phase MoS<sub>2</sub>.<sup>117,314</sup> The rapid beam-driven migration of  $V_{Se}$  is shown in monolayer PtSe<sub>2</sub> at a moderate heating temperature of 200°C at an *in-situ* heating stage (Figure 6.3). The moderate thermal condition can reduce the beam-induced contamination on PtSe<sub>2</sub> sample and help reveal the kinetic behaviours of  $V_{Se}$ . The dispersed  $V_{Se}$  at this vacancy-rich region has notable mobility under the beam, indicated by the fast migration of numerous  $V_{Se}$  positions with the increased  $V_{Se}$  number in Figure 6.3a-d. Detailed dynamical process is shown by several  $V_{Se}$  in the cropped region of  $\sim 3 \text{ \AA}^2$  area and atomic models in Figure 6.3e-l. The separate  $SV_{Se}$  keep moving randomly. At some stages, the  $SV_{Se}$  can temporarily pair to form a tri-vacancy connected

in by  $DV_{Se-3}$  (Figure 6.3g,k), or to generate a  $DV_{Se-2}$  (3h,l), while these are merely intermediate stages and the  $V_{Se}$  do not exhibit universal aggregation as they then further migrate away with more  $V_{Se}$  produced, which differs from the 1D vacancy accumulation behaviour in 2H-MoS<sub>2</sub>.

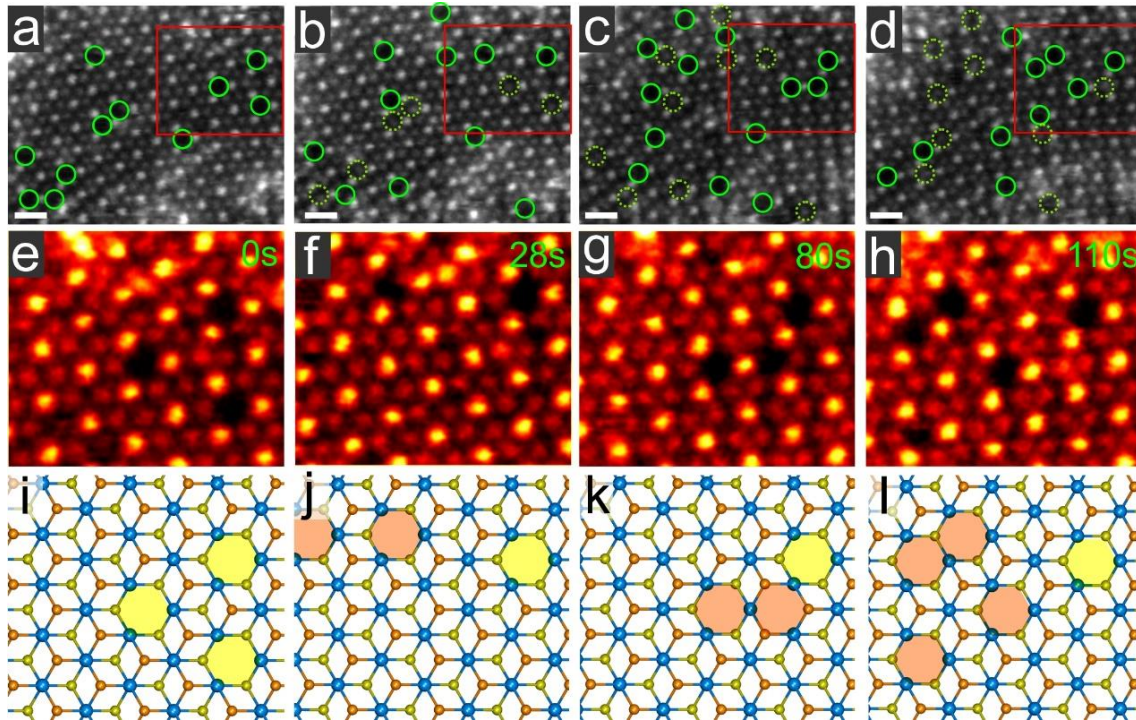


**Figure 6.3** Dynamics of Se point vacancies in monolayer PtSe<sub>2</sub> under electron beam at 60kV accelerating voltage. (a-d) Time series of ADF-STEM images of a monolayer PtSe<sub>2</sub> region showing the production and migration of  $V_{Se}$  driven by electron beam. The green circles highlight the positions of  $V_{Se}$ , and the dashed green circles mark the  $V_{Se}$  that have migrated away compared to the previous frame. Scale bars: 0.5nm. (e-h) Enlarged views of the boxed regions in (a-d), showing the detailed electron-driven dynamics of several  $V_{Se}$ , with (i-l) corresponding schematic atomic models. The shades highlights the  $V_{Se}$  columns, where the yellow shades represents the  $V_{Se}$  at original position, and the orange shades illustrates the migrating  $V_{Se}$ .

### 6.2.2 1D Stretched Defect Structures and Kinetics

For understanding the  $V_{Se}$  kinetic behaviours and how they affect the PtSe<sub>2</sub> structures, their dynamics under beam irradiation as well as the changing strain fields of the PtSe<sub>2</sub> lattices are examined using geometric phase analysis (GPA). Figure 6.4a,c,e,g show the time-dependent ADF-STEM image sequence of a monolayer PtSe<sub>2</sub>, with the 2D strain maps of the normal strain field component along x direction ( $\mathcal{E}_{xx}$ ) in Figure 6.4b,d,f,h,

respectively. The other strain field component maps with marks showing the reference area for GPA analysis are given in Figure C4-7.

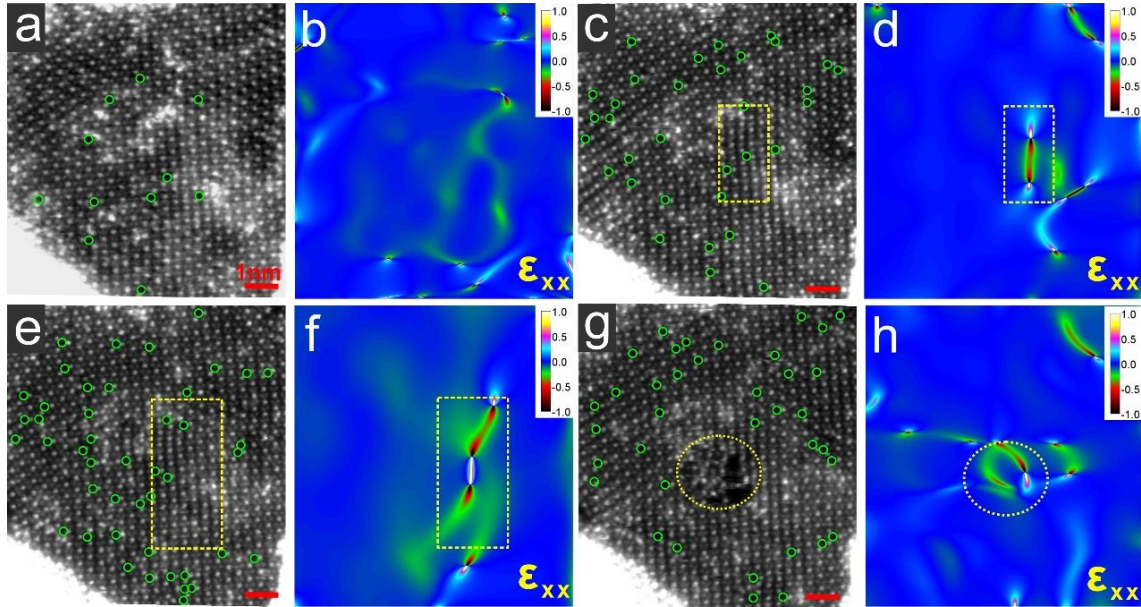


**Figure 6.4** Formation and evolution of linear defects at monolayer PtSe<sub>2</sub> with strain field analysis under electron beam. (a,c,e,g) Time series of ADF-STEM images of a monolayer PtSe<sub>2</sub> region showing dynamical process of the evolution of linear defects with the production and migration of V<sub>Se</sub> driven by electron beam. The images were taken with The green circles mark the beam-induced V<sub>Se</sub>. (b,d,f,h) 2D strain maps of  $\epsilon_{xx}$  corresponding to (a,c,e,g), respectively, with a colour scale ranging from  $-1.0$  to  $+1.0$ . The yellow boxes in (c-f) highlight the contractive strain fields caused by linear defects at the corresponding ADF-STEM images. The yellow dashed circles in (g,h) mark the pore popped at the formerly defective region.

At the initial frame (Figure 6.4a), a few V<sub>Se</sub> are induced during imaging while retaining the pristine PtSe<sub>2</sub> lattice structures, which shows homogeneous strain map overall with tiny variations (Figure 6.4b). When irradiated by beam, a high concentration of V<sub>Se</sub> are produced dispersedly as marked by green circles (Figure 6.4c). In its strain map, there occurs distinct linear strain field locally in the boxed area, corresponding to a linearly defective region stretched along zig-zag direction different from the pristine lattices, which gives compressive strain to the adjacent lattice (with colour black, red, and green in the map). It appears to be similar to the 1D strain distribution along the line defects in MoS<sub>2</sub>.<sup>115,117</sup> This distinct local strain field further extends (Figure 6.4f), which corresponds to the expansion of stretched region in PtSe<sub>2</sub> with the increase of

concentration of  $V_{\text{Se}}$  nearby (Figure 6.4e). After extended imaging, the local intense strain lead to the lattice break around the 1D defective structures, popping out a void in this region with strain fields dispersed (Figure 6.1g,h).

Figure 6.5 evaluates the detailed atomic structures of the regions with distinct strain fields where there occur linear defects. Line defects are one of the most typical beam-driven defects in the 2H-phase TMDs. For the 1T  $\text{PtSe}_2$ , the linear defects are deviated from the pristine lattices (Figure 6.5a-e), but they are not composed of rows of Se vacancies. Instead, there is a lattice distortion with the changed positions of two Se atoms sandwiching the Pt, breaking the perfect hexagonal symmetry, as compared in Figure 6.5b,c. Those two neighbouring Se atoms shifted to be closer in the x-y plane and almost overlapped from the planar view, which give composite contrast column in the same row with that of Pt in the ADF-STEM image, presenting 1D stretched lattices (Figure 6.5d). The simulated ADF-STEM image in Figure 6.5e corresponds well with the experimental. There is a lattice shrinkage in terms of in-plane atoms distance among those ‘lines’, where the Pt–Pt spacings in arm-chair direction have contracted by 11% from  $6.5\text{\AA}$  to  $5.8\text{\AA}$  according to the intensity line plot profile (Figure 6.5g). Generally, the lattice buckling is necessary in stabilizing 1D defects in 2H-TMDs including vacancy lines and grain boundaries.<sup>115,315</sup> Here, in order to maintain the Pt–Se bond length and the Pt–Pt distances, slight out-of-plane buckling should also be required to stabilize the structure (see the side view of Figure 6.5f). Based on the strain field analysis in Figure 6.4, these stretched defects resulting from lattice distortion are driven by the intense strain fields locally with the production of high concentration of Se vacancies nearby under the beam irradiation.

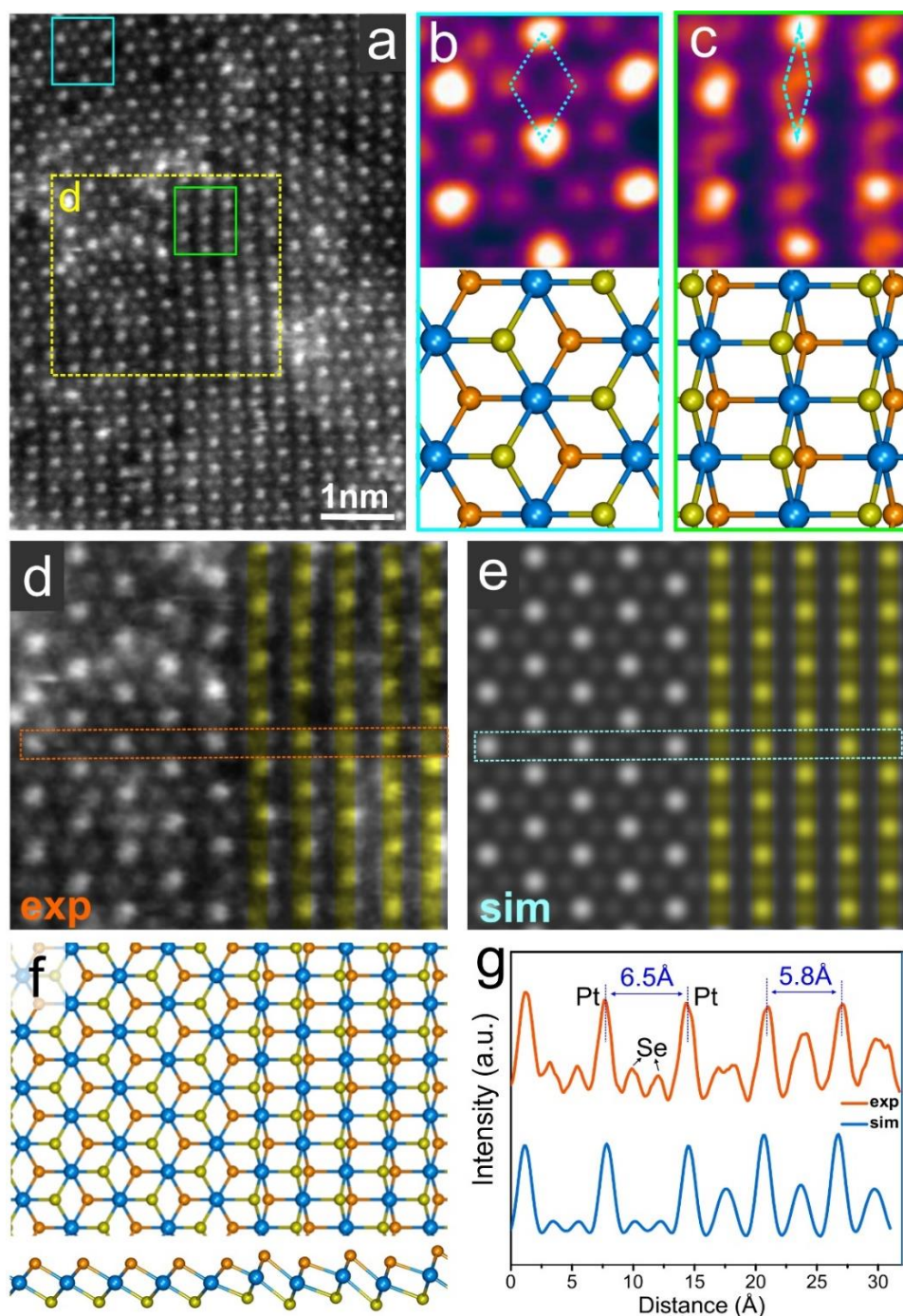


**Figure 6.5** Atomic structures of linearly stretched defects at monolayer PtSe<sub>2</sub> resulting from lattice distortion. (a) ADF-STEM image of a monolayer PtSe<sub>2</sub> embedded with a region of linear defects. (b,c) Enlarged views of the blue and green boxed regions in (a), with atomic models below, respectively, highlighting the shifted Se atoms in the (c) defective lattices compared to the (b) pristine lattices. (d) Magnified ADF-STEM image in the yellow dashed box in (a) showing the linear defect structures. The linearly defective region is highlighted by yellow shadow. (e) Multi-slice simulated ADF-STEM image corresponding to (d), with the atomic model of planar and side views in (f). (g) Intensity line plot profiles obtained from the marked regions in (d,e) for measuring the Pt-Pt spacings in pristine lattices and linear defective lattices.

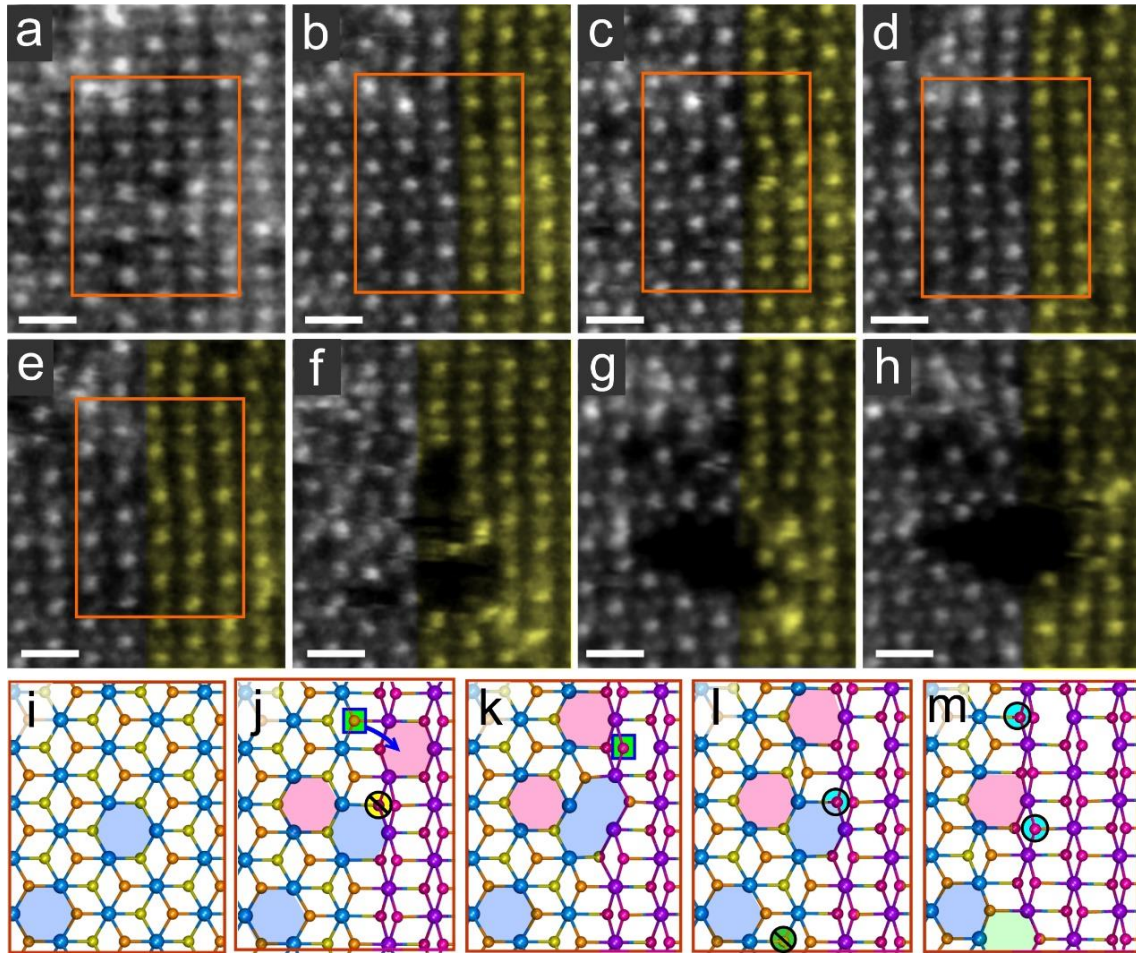


**Figure 6.6** (a-h) Time series of ADF-STEM images of a monolayer PtSe<sub>2</sub> region with linear defects, showing the detailed dynamical process of the interplay between Se point vacancies with linear defects. Scale bars: 0.5nm. The linearly defective regions are highlighted by yellow shadows. (i-m) Schematic atomic models corresponding to the lattices in boxed region in (a-e), with circles and arrows denoting the displacement of Se atoms. V<sub>Se</sub> columns are highlighted by colour shadows.

Figure 6.6 further illustrates the dynamical process of the interplay between V<sub>Se</sub> and linear defects at monolayer PtSe<sub>2</sub>. The schematic atomic models in Figure 6.6i-m elaborate this process corresponding to the frames in Figure 6.6a-e, highlighting the vacancy production and displacement. At the initial stage (Figure 6.6a,i), a few isolate V<sub>Se</sub> were produced. With the increase of local V<sub>Se</sub> concentration, the linear stretch occurs along the zig-zag direction accompanied by lattice contraction in the regions marked by colour shades (Figure 6.6b,j). Those V<sub>Se</sub> locally assemble to be divacancy (DV<sub>Se-2</sub>, Figure 6.6j), which further develop to be tri-vacancies with another Se missing, adopting the

configurations of  $DV_{Se-1}+ DV_{Se-2}$  in Figure 6.6c,k, causing increased local lattice distortion. There is a self-healing phenomenon of  $V_{Se}$  by capturing an excessive Se into the vacancy (Figure 6.6d,e,l,m), essentially attributed to the fast migration of  $V_{Se}$  and atom displacement, which at the same time leads to the expansion of the linearly stretched defects. After the series of vibrant interplay between the  $V_{Se}$  and the linear defects, the balance of metastable lattice rearrangement is finally broken due to increased strain, punching nano-voids adjacent to the linear defects (Figure 6.6f,g,h).

### 6.2.3 Dislocations and Grain Boundaries

Figure 6.7a presents an ADF-STEM image of monolayer/bilayer  $PtSe_2$  film containing a grain boundary (GB) between two grains of different orientations extending from monolayer to bilayer. Figure 6.7b reveal the two misoriented 1T-phase  $PtSe_2$  monolayers are atomically stitched together with the formation of a GB composed of a string of dislocation cores. The detailed atomic structure of the GB dislocation core is shown in Figure 6.7c, which is constructed by a five-fold ring and a Se inserted seven-fold ring ( $5|7_{+Se}$ ) separated by a distinctive Se–Se homoelemental bond in the middle. This type of  $5|7_{+Se}$  fold rings differentiates from the expected  $5|7$  dislocation structures that have been modelled and commonly observed in graphene, silicon, h-BN, and other hexagonal crystal structures like 2H-phase  $MoS_2$ .<sup>55,128,147,316-317</sup> It possesses a Se atom crossing inside the seven-fold ring showing distinct 1T feature. The comparison of them is further explained in Figure C8. The  $5|7_{+Se}$  dislocations is repeatedly formed along the GB (Figure 6.7d,e). The intersecting angle of the two monolayers is  $30^\circ$ , as indicated by the FFT spectra in Figure 6.7f, which is a special intersecting angle that makes lattice along the zigzag direction stitch with the armchair lattice (Figure 6.7g). This  $30^\circ$  GB causes the minimum rhombus units in the 1T-phase structure (highlighted by green shades

in Figure 6.7g) to be perpendicular at the two sides of the GB. In Figure 6.7d, these perpendicular rhombus motifs at the two sides develop at the same line in the lattice (see the green and blue lines across the 30° GB), which permits good crystal matching between the grains and ensures the homogeneity of the lattice structure.

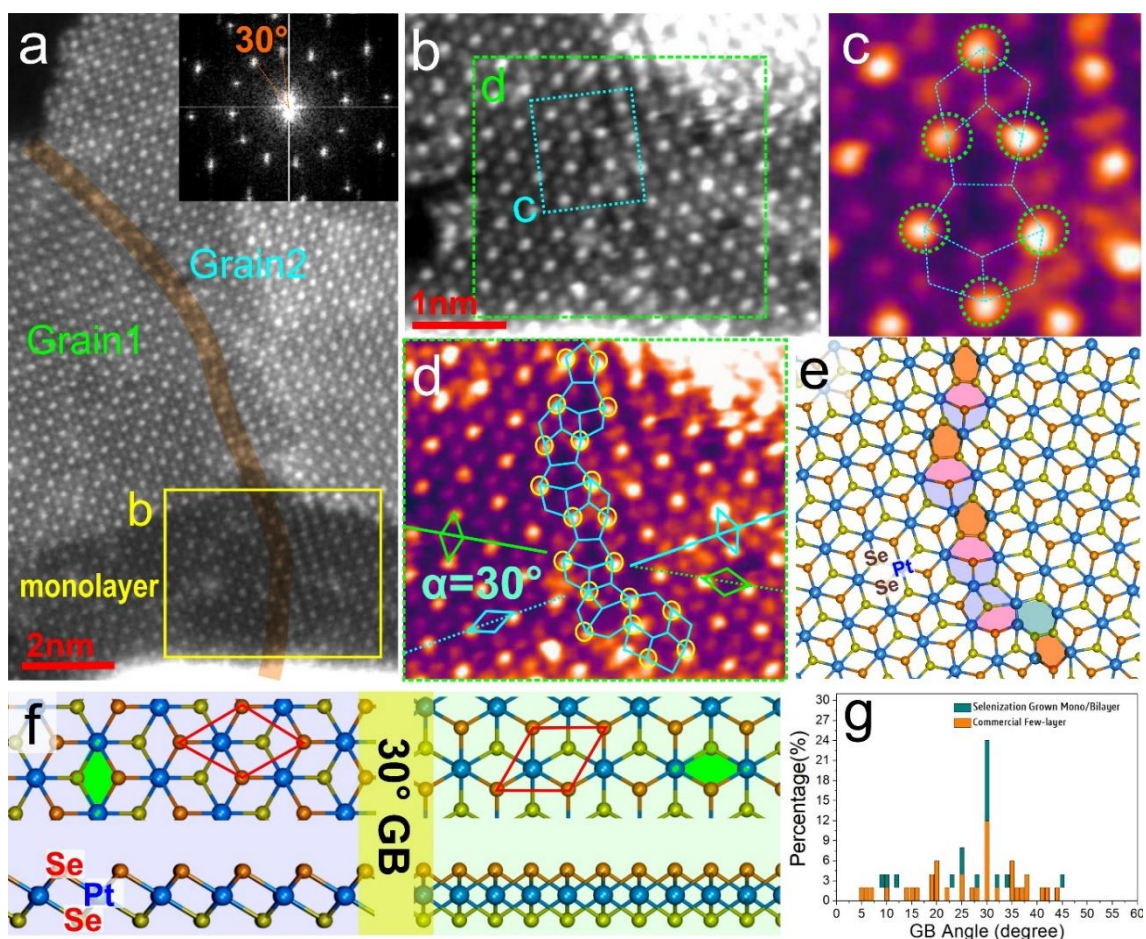


**Figure 6.7** GBs and dislocations in 2D layered PtSe<sub>2</sub> with tilt angle of 30°. (a) ADF-STEM image showing the GB formed between two tilt PtSe<sub>2</sub> grains, extending from monolayer to bilayers. (b) ADF-STEM image of the monolayer region in (a), showing the GB structure in monolayer PtSe<sub>2</sub> in atomic scale. Inset is the power spectrum by FFT, where two sets of spots have an angle of 30°. (c) Magnified view of the blue boxed region in (b), overlaid with schematic model illustrating the atomic structure of the dislocation core  $5[7_{+Se}]$  in the GB. The Pt atoms at the GB are marked by green circles, with blue lines indicating the bonds. (d) Enlarged view of the boxed region in (b), overlaid with schematic model showing the GB structure connected by a chain of dislocation cores. (e) Atomic model of Pt (blue) and Se (bronze and yellow) atoms corresponding to the ADF-STEM image in (d), with semi-transparent colour shades highlighting the lattice structure at the GB dislocation cores. (f) Schematic models in projection view (up) and side view (bottom) showing the lattice structures of two PtSe<sub>2</sub> grains with 30° tilt angle. (g) Histogram showing the statistics of the GB tilt angle distribution in polycrystalline PtSe<sub>2</sub> films. The samples examined include mono/bilayer PtSe<sub>2</sub> regions self-grown by selenization and the commercially bought few-layered PtSe<sub>2</sub>, with fifty GBs measured in total.

Note that the  $30^\circ$  GB is the most frequently occurred tilt GBs in our PtSe<sub>2</sub> sample grown by direct selenization of Pt on Si substrate, which makes up 37.5% among the monolayer/bilayer GBs, sharply larger than those of other angles (Figure C9,10). The major distribution of  $30^\circ$  GB is also found in the commercially bought few-layered PtSe<sub>2</sub> films on sapphire substrate (Figure C11,12). Figure 6.7g presents the integrated results of the GB angles distribution measured from these two samples, indicative of the predominance of  $30^\circ$  GB regardless of the layer numbers or substrates, which suggests the favourable  $30^\circ$  GB in polycrystalline PtSe<sub>2</sub> films grown by bottom-up methods, possibly arising from the atomic structure stability, good crystal matching and homogeneity in lattice with  $30^\circ$  GBs, and preferable growth in neighbouring zig-zag and arm-chair orientations.

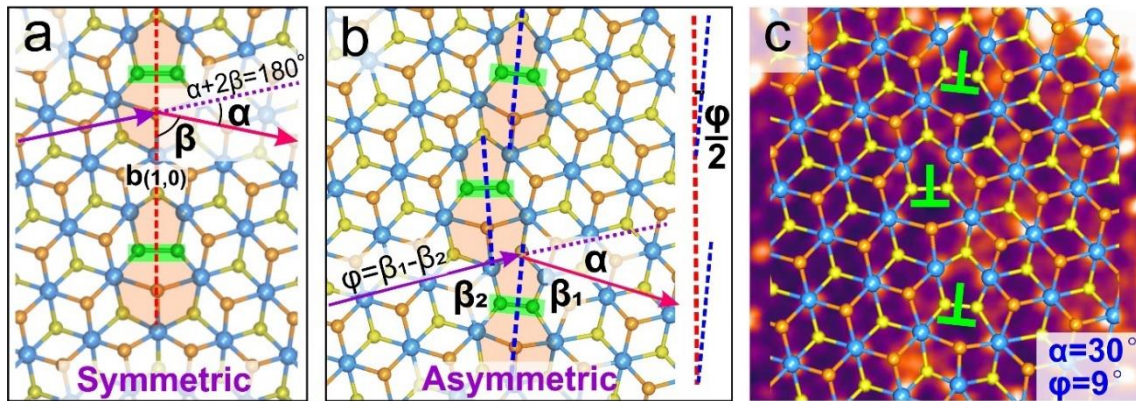


**Figure 6.8** (a,b) Schematic atomic models with parameters illustrating monolayer PtSe<sub>2</sub> GB structures constructed by  $5|7_{+Se}$  dislocation cores in (a) symmetric and (b) asymmetric pathways, respectively. Arrows in purple and pink colours manifest the two lattice orientations.  $\alpha$ : GB tilt angle.  $\beta$ : Angle between the dislocation core and lattice vector (1,0) in the stitched grains.  $\varphi$ : Deviation angle indicating the asymmetry of the GB dislocation core. (c) Experimental ADF-STEM image with atomic model overlaid, showing a monolayer PtSe<sub>2</sub> GB constructed from  $5|7_{+Se}$  dislocation cores in the asymmetric mode shown in (b). The positions of GB dislocation cores are indicated by green  $\perp$  marks.

The GB dislocation cores do not develop linearly but instead appear in a staggered way, as illustrated in Figure 6.7e. In order to describe the GB features in the 2D PtSe<sub>2</sub>, several parameters are defined, including the GB tilt angle ( $\alpha$ ) and the angle  $\beta$  between

the GB dislocation core central line and pristine grain lattice vector (1,0), which describes the GB extending direction. In the proposed symmetric GB atomic model with a linear row of  $5|7_{+Se}$  dislocation cores (Figure 6.8a), the two stitched grains have identical  $\beta$  ( $\beta_1=\beta_2$ ), while in the asymmetric GB arrangement (Figure 6.8b),  $\beta_1$  is not equivalent to  $\beta_2$ . A parameter  $\varphi$  is introduced to describe the deviation angle of the GB dislocation cores, which is defined as the difference between  $\beta_1$  and  $\beta_2$  ( $\varphi=\beta_1-\beta_2$ ), thus  $\varphi/2$  represents deviation between the dislocation central line and the symmetry line of the two misoriented lattice vectors. I did not observe the linear symmetric GB in our experiment. In a typical ADF-STEM image observed (Figure 6.8c), there is a small  $\varphi$  of  $9^\circ$  for the dislocation cores along the  $30^\circ$  GB. Besides, the dislocations are connected one after another without separation, different to the proposed symmetric model where there are half-lattice separations among the dislocations. The asymmetric mode is also found in another  $30^\circ$  GB in Figure C13 consisting of  $5|7_{+Se}$  dislocation core with a  $\varphi$  of  $18^\circ$ , manifesting the deviation angle can vary for the GB with the same tilt angle.

More types of dislocations are found at GBs in monolayer PtSe<sub>2</sub>. Figure 6.9a,b show a monolayer GB with a tilt angle of  $34^\circ$ , which develops along a nanoscale meandering pathway with turning angles of  $120^\circ$ , similar to other 2D TMDs.<sup>235,315</sup> The dislocation cores along the same extending direction are also connected staggerly (see the short red lines representing the connection between two sequential dislocations in Figure 6.9c). The GB along angle  $\beta$  of  $68^\circ$  are connected by stepped  $5|7_{+Se}$  dislocation cores with a small deviation angle ( $\varphi$ ) of  $\sim 10^\circ$ . The dislocation core units in the two directions vary in the atomic structures, mainly showing three types, denoted as i-iii in Figure 6.9d. These different basic edge dislocations can be formed by removing atoms from pristine PtSe<sub>2</sub> lattice along two lattice vectors, (1,0) and (0,1), as revealed in Figure 6.9f-k.

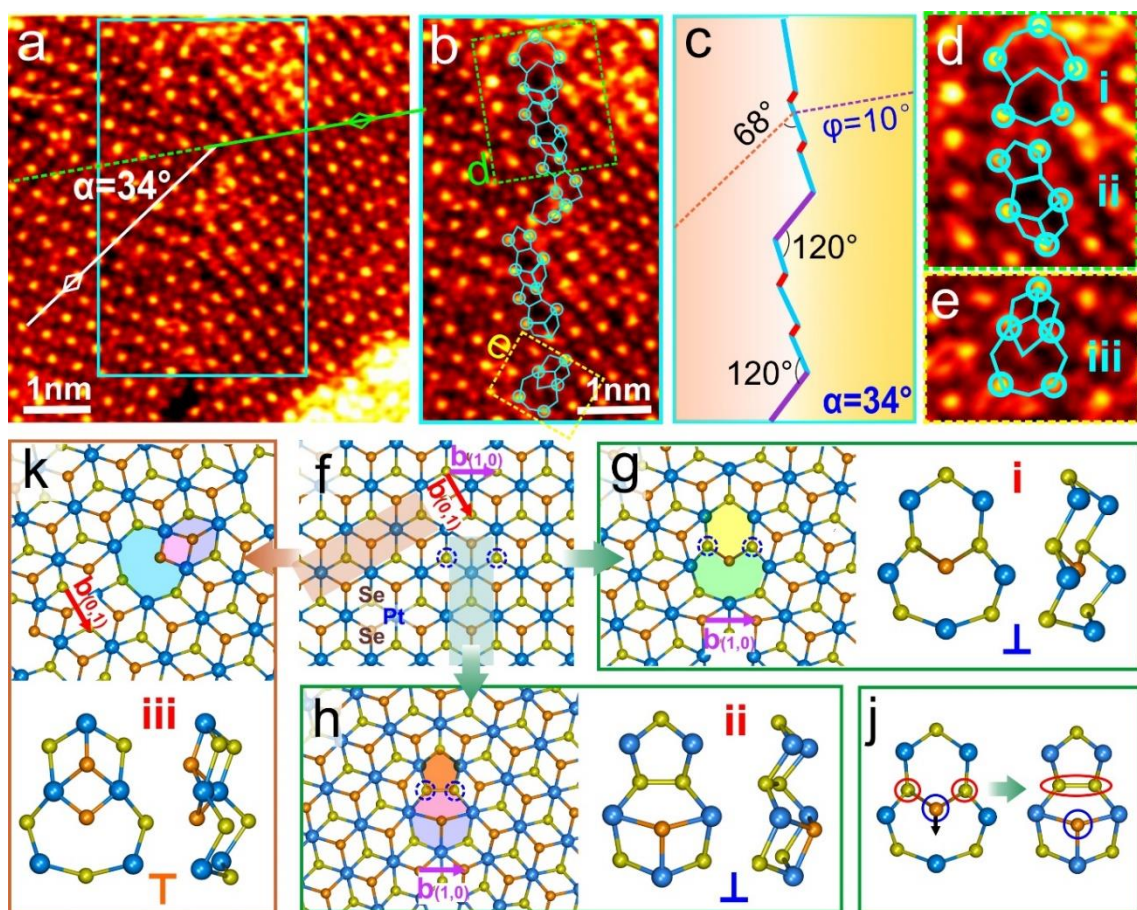


**Figure 6.9** Direct observation of various dislocations at monolayer PtSe<sub>2</sub> GB. (a) ADF-STEM image showing a GB formed in two monolayer PtSe<sub>2</sub> grains with tilt angle of 34°. (b) Enlarged view of the boxed region in (a), overlaid with schematic model showing the GB structure connected by a string of different dislocation cores, with (c) scheme showing the GB along a meandering pathway. The two dislocation cores extending directions with a turning angle of 120° are illustrated by light blue and purple lines, respectively. The short red lines represent the connection between two sequential dislocation cores. (d,e) Magnified views of different types of dislocation cores (i-iii) in the two boxed regions in (b), with schematic models showing the atomic structures. (f-k) Scheme of atomic models illustrating the formation of the observed edge dislocations (i-iii) by removal of the shaded atoms from the pristine PtSe<sub>2</sub> lattice in (f) along two lattice vectors. (g,h) Atomic models presenting the (g) 6|8, (h) 5|7<sub>+Se</sub> dislocation cores with Burgers vector of  $\mathbf{b}=(1,0)$ . (j) The transformation between the 6|8 and 5|7<sub>+Se</sub> dislocation cores. (k) Atomic model showing the 6<sub>+Se</sub>|8 dislocation core with Burgers vector of  $\mathbf{b}=(0,1)$ .

Type i-ii in Figure 6.9d correspond to the dislocation cores of 6|8 rings and 5|7<sub>+Se</sub> rings, respectively, with Burgers vector of  $\mathbf{b} (1,0)$ . Their atomic structures are illustrated in Figure 6.9g and h separately, tagged “⊥”, which are both Se-rich consisting of one (for 5|7<sub>+Se</sub> rings) or two (for 6|8 rings) Se–Se homoelemental bonds in the dislocation centre.

The planar view of 6|8 structure seems to resemble that of 6|8 dislocation in other hexagonal crystals like h-BN or 2H-phase TMDs, while the 6|8 dislocation in 2H lattice only consists of metal–chalcogen bonds, see Figure C14a,b.<sup>104,121,134,148,318</sup> The 6|8 and 5|7<sub>+Se</sub> dislocations have the same stoichiometry consisting of five Pt and six Se atoms in one motif, and can be interconverted by shifting the centred Se atom and re-bonding (Figure 6.9j). When removing the inverted plane of atoms, another category of edge dislocation of 6<sub>+Se</sub>|8 rings with Burgers vector of **b**(1,0) is created in Figure 6.9k, which is tagged “ $\top$ ”, corresponding to the observed one (iii) in Figure 6.9e. This 6<sub>+Se</sub>|8 rings differs from the 6|8 dislocation structures in other hexagonal crystals like 2H-phase MoS<sub>2</sub>, in light of its 1T structural feature having a Se atom crossing inside the six-fold ring, as compared in Figure C14b,c. Though all these three topologically different dislocations are observed in our experiments, the Se-rich 5|7<sub>+Se</sub> dislocations appear most frequently at the PtSe<sub>2</sub> GBs.

The special 60° GB is also found in 1T-phase PtSe<sub>2</sub>, as shown in Figure 6.10. For the typical 2H-phase TMDs like MoS<sub>2</sub> and WS<sub>2</sub>, the 60° GB is easily recognized because of the inverted contrasts in the bi-element honeycomb in the ADF-STEM image.<sup>104,129,134,147,314</sup> In contrast, rotating 60° of the 1T-phase monolayers also makes the lattice inverted, and is equivalent to interchanging the up-down positions of the two layers of chalcogen atoms (see the side view of atomic model in Figure C15), while in the planar view, the relative locations of metals and chalcogens do not change as they exhibit rhombus lattice arrangement, making the inverted 1T monolayer grains look the same in the ADF-STEM image (Figure C15).

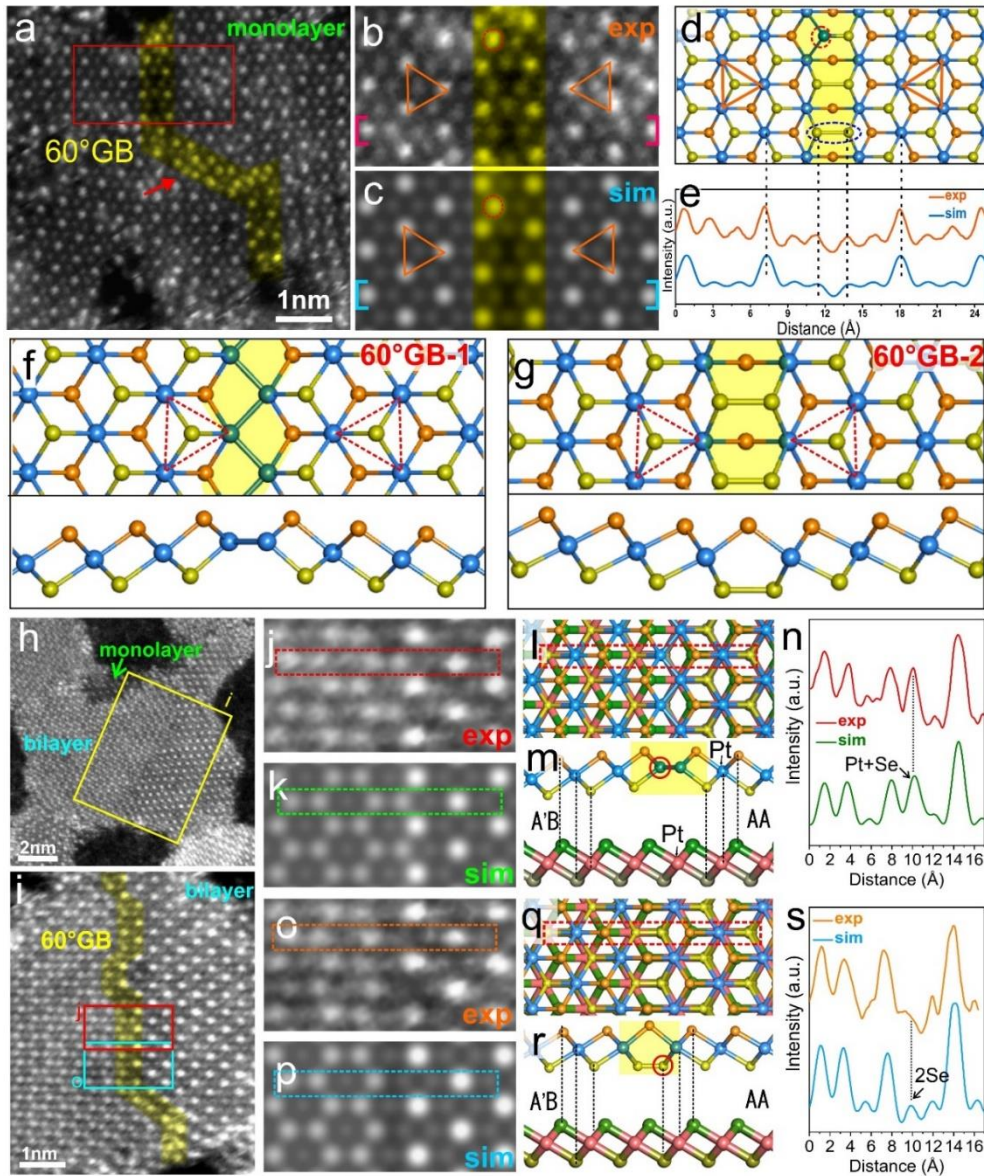


**Figure 6.10** Atomic structure of  $60^\circ$  GB in 2D PtSe<sub>2</sub>. (a) ADF-STEM image of a monolayer PtSe<sub>2</sub> with a  $60^\circ$  GB. (b) Enlarged view of the boxed region in (a), with yellow colour highlighting the  $60^\circ$  GB. (c) Multislice-simulated ADF-STEM image corresponding to (b), obtained from the schematic atomic model in (d). The yellow shade highlights the  $60^\circ$  GB connected by two types of dislocation cores. (e) Intensity line profile measured from the labelled regions in the experimental and simulated images in (b,c). (f,g) Atomic configurations of the two types of  $60^\circ$  GB. (f) Metal-rich GB. (g) Se-rich GB. (h,i) Overlapping  $60^\circ$  GB in bilayer PtSe<sub>2</sub> leading to two different stacking geometries. (h) ADF-STEM image of a bilayer PtSe<sub>2</sub> with overlapping  $60^\circ$  GB. (i) Zoomed-in ADF-STEM image with yellow shade highlighting the GB region. (j-n), (o-s) Detailed structures of two types of  $60^\circ$  GB. (j,o) Enlarged view of the red and blue boxes in (i). (k,p) Corresponding simulated ADF-STEM images corresponding to bilayer atomic configurations in (l,q), respectively, with (m,r) side views, respectively, which are obtained after conjugate gradient relaxation using the Stillinger-Weber potential. The metal-rich (l,m) and Se-rich (q,r)  $60^\circ$  GB at the 2<sup>nd</sup> layer are highlighted by yellow shades. (n) Intensity line plot profiles obtained from (j,k). (s) Intensity line plot profiles obtained from (o,p).

Though the inverted monolayer 1T grains cannot be directly determined on its own in the ADF-STEM image, I still observed the distinctive  $60^\circ$  GB structures serving as the mirror separating two inverted  $\text{PtSe}_2$  monolayers (Figure 6.10a,b). The atomic configuration of this structure is analysed by the atomic model and simulation in Figure 6.10c,d, where the simulation matches qualitatively with the experimental, as suggested by the obtained intensity line plot profile comparison in Figure 6.10e. This distinct  $60^\circ$  GB structure is constructed by alternate Pt–Se–Pt and Se–Se bonds, which build up chains of Se-rich symmetric trapezoid dislocations resembling the hourglass shape in the planar view, containing five-member ring each (see the side view Figure 6.10d). It can have derivative structure when one of the Se atom in the bridging Se–Se is substituted by a Pt atom (Figure 6.10f), forming an assembly of 4-member ring (rhombus) dislocations which constitute a metal-condensed asymmetric GB with a zigzag shape (see the upper region in Figure 6.10b-d). This  $60^\circ$  GB extends with  $120^\circ$  turning angles in the monolayer, forming a metal-rich row at the GB region marked by the red arrow in Figure 6.10a. For the bilayer  $\text{PtSe}_2$  films, the overlapping  $60^\circ$  GB at one layer leads to two stacking geometries, which forms a sharp border easily recognized between two grains with different contrast patterns in the ADF-STEM image (Figure 6.10h,i), similar to those reported in the 2H-phase TMD bilayer systems.<sup>141-143</sup> This anti-phase GB separates two bilayer grains adopting AA and A'B stacking configurations respectively (see the side views of atomic models in Figure 6.10m,r), which were calculated to be two most energetically favourable stackings in bilayer  $\text{PtSe}_2$ .<sup>294,319</sup> Overlapped on the pristine lattice at the first layer, the  $60^\circ$  GB on the second layer is composed of the two types of GB dislocation structures in accordance with those in the monolayer  $\text{PtSe}_2$ , the metal-rich zigzag GB (Figure 6.10j-m) and the Se-rich hourglass-like symmetric GB dislocations (Figure 6.10o-r). The intensity line profiles measured from the simulated and

experimental images match well for these two overlapping 60° GBs (Figure 6.10n,s). The line profiles of these two structures differ in the contrasts of columns Pt+Se (Figure 6.10n) or 2Se (Figure 6.10s), arising from different GB connecting atoms as marked by red circles in Figure 6.10m,r.

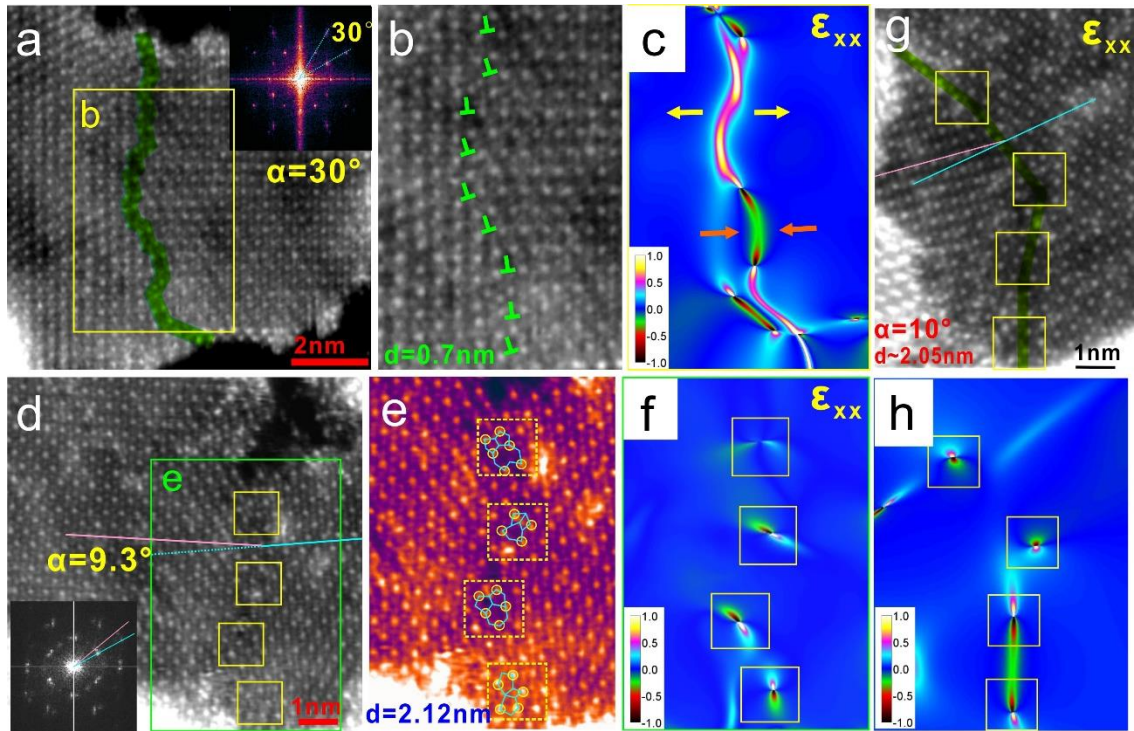


**Figure 6.11** Dislocation distributions in GBs with different misorientation angles. (a,b) ADF-STEM images showing a GBs with angle of 30°. The positions of a chain of 5|7<sub>+Se</sub> dislocation cores at the GB are indicated by green ⊥ marks individually in (b). (c) 2D strain maps of  $\epsilon_{xx}$  corresponding to (b), with a colour scale ranging from -1.0 to +1.0. (d,e) ADF-STEM images showing a GB with small tilt angle of 9.3°. (f) 2D strain maps of  $\epsilon_{xx}$  corresponding to (e). The dislocations in (e) are overlaid by schematic models corresponding to the positions of yellow boxes in (d,f). (g) ADF-STEM image showing a GB with small tilt angle of 10°. (h) 2D strain maps of  $\epsilon_{yy}$  corresponding to (g). Dislocation positions in (h,g) are marked by yellow boxes.

Figure 6.11 further investigates the dislocation distributions in GBs with different tilt angles and the effects on the strain in the lattice. For the 30°-tilt GB in Figure 6.11a, the chain of 5|7<sub>+Se</sub> dislocation cores are connected in succession along the extending direction (Figure 6.11b). The average spacing ( $d$ ) of the centres of dislocation cores is around 0.7nm, roughly doubles the lattice constant (0.37nm) of the primitive unit cell of

PtSe<sub>2</sub>. When evaluating the strain distribution for the monolayer PtSe<sub>2</sub> lattice containing GB by applying the GPA for the ADF-STEM image, it shows distinct strain fields narrowly localized at the GB region and extend linearly along the GB in the strain map of the normal component along x direction ( $\epsilon_{xx}$ ) (Figure 6.11c). The GB dislocation row mainly gives rise to tension strain fields with magnitude up to 100% to the adjacent lattice (marked by yellow arrows in Figure 6.11c) while can also generates contraction strain field of around 25% when the GB turns the extending direction (marked by orange arrows). In contrast, for the small-angle GB such as the 9.3°-tilt GB in Figure 6.11d, the dislocation cores appear discretely. The  $\epsilon_{xx}$  strain field surrounding each dislocation core on the GB exhibits a tension–compression dipole which is isolated with similar spatial dispersion (Figure 6.11f). Unlike the linear extended strain fields of the 30° GB, the strain fields of adjacent dislocations have no intersection with each other at the present spacings. Similar result is also seen in the 10°-tilt GB in Figure 6.11g,h. The other strain components are presented in Figure C16-18, respectively.

### 6.3 Conclusion

By using ADF-STEM direct imaging with single-atom resolution, this chapter studies detailed atomic structures of vacancies, stretched defects, dislocations and GBs in a typical 1T-phase TMD, 2D PtSe<sub>2</sub>, which are distinguished from the those defective structures in other hexagonal crystals like graphene, h-BN and 2H-phase TMDs (e.g. MoS<sub>2</sub>). The isolated V<sub>Se</sub> are highly mobile under beam irradiation, whose collective behaviours contribute to the re-arrangement of the PtSe<sub>2</sub> lattice. Distinct 1D deviated defects are found in 1T-PtSe<sub>2</sub> exhibiting 1T features without losing Se atom rows, which is distinguished from the typical line defects missing rows of chalcogens in 2H-phase TMDs. The main difference lies in the mechanism that in the PtSe<sub>2</sub> the increased

concentration of  $V_{Se}$  in a confined  $PtSe_2$  grain alters strain fields locally, triggering the formation of a special type of linearly stretched defect with contracted lattice distortion. For the GB structures, a special tilt angle of  $30^\circ$  is found where the lattice in armchair direction is stitched with that in the zig-zag direction, which is the most frequently occurred GB angle in polycrystalline  $PtSe_2$  films. Other GBs with different tilt angles are also directly observed in meandering pathways with various edge dislocation structures assembled, including  $5|7_{+Se}$ ,  $6|8$ , and  $6_{+Se}|8$  planar polygons which show distinct 1T-phase structural feature and possess Se-rich homoelemental bonds. Apart from the tilt GBs, the mirror twin GBs ( $60^\circ$  GBs) also formed in monolayer/bilayer  $PtSe_2$  grains, constructed by a string of metal-condensed asymmetric or Se-rich symmetric dislocations. Taking  $PtSe_2$  as an example, this systematic study of 1T-phase TMDs is expected to enrich our knowledge of defective structures in 2D binary lattices.

## Chapter 7

### Defects and Grain Boundaries in Thermally-Driven Pd<sub>2</sub>Se<sub>3</sub>

#### Monolayers

This chapter will further explore the atomic structure and dynamics of defects and grain boundaries (GBs) in a new 2D crystal, monolayer Pd<sub>2</sub>Se<sub>3</sub>, which is obtained by thermally controlled phase transformation from commercial PdSe<sub>2</sub> few-layers at an *in-situ* heating stage in annular dark field ADF-STEM. The *in-situ* observation during heating allows me to deduce the actual thermal degradation temperature and mechanisms for Pd<sub>2</sub>Se<sub>3</sub> monolayers forming reproducibly. The focus is then put on the defective structures of this thermally produced Pd<sub>2</sub>Se<sub>3</sub> monolayer by ADF-STEM imaging as well as their beam-driven dynamics. The defect configurations and dynamic behaviours observed in Pd<sub>2</sub>Se<sub>3</sub> are distinctly different from the typical MX<sub>2</sub> transition metal dichalcogenides (TMDs, M=Mo/W, X=S/Se) owing to the unique crystal structures.

#### 7.1 Introduction

2D materials have expanded rapidly beyond graphene over the past few years.<sup>15,23,320</sup> The semiconducting TMDs have advanced hugely in the opto-electronics using all 2D materials.<sup>1-3,18,31,85</sup> Further development, though, requires continual investigation of new 2D materials systems beyond those that are well known. Moreover, creating scalable methods to make new monolayers that do not exist as bulk layered materials provides access to new crystals yet to be fully explored.

Recently, it was found that electron beam irradiation can help transform few-layered PdSe<sub>2</sub> into monolayered Pd<sub>2</sub>Se<sub>3</sub> crystals.<sup>200-201</sup> This novel semiconducting Pd<sub>2</sub>Se<sub>3</sub>

monolayers are not found as bulk layered system and are formed by the loss of Se from the parent PdSe<sub>2</sub> few layered crystal and subsequent restructuring. Since the recent discovery of the new Pd<sub>2</sub>Se<sub>3</sub> monolayers, theoretical studies have predicted it to be a thermodynamically and kinetically stable semiconductor with indirect bandgap of 0.45 eV and carrier mobility of 178.02 cm<sup>2</sup>V<sup>-1</sup>s<sup>-1</sup>.<sup>321</sup> Moreover, monolayer Pd<sub>2</sub>Se<sub>3</sub> is calculated to be a highly efficient thermoelectric material owing to the high power factor and low lattice thermal conductivity which could not be fulfilled by the traditional TMD monolayers.<sup>322</sup> Its moderate bandgap, anisotropic transport properties and the excellent absorption in a wide range of solar spectrum render it a desirable new 2D material for (opto-)electronic industries.<sup>321,323</sup>

Device applications of new 2D materials require atomic understanding of their structures, particularly their defects such as point vacancies and GBs.<sup>104,134,150,324-325</sup> However, defects in monolayer Pd<sub>2</sub>Se<sub>3</sub> have yet to be systematically studied mainly due to the novelty of the material and the difficulty in material production. While new crystal phases can be created by electron beam irradiation, it does not provide scalable production techniques to advance the applications. The low melting point of PdSe<sub>2</sub> and its rich phase diagram makes it suitable for thermally induced Se loss by heating in vacuum and subsequent phase change. Transition metal dichalcogenides of MoS<sub>2</sub> or WS<sub>2</sub> lose S when heated in vacuum, which assemble into line vacancies before void formation occurs. The typical decomposition pathway from thermal heating is chalcogen loss and the formation of metal clusters. In PdSe<sub>2</sub> though, it is highly likely that thermally induced chalcogen loss will lead to a situation similar to the electron beam induced reactions, namely the formation of Pd<sub>2</sub>Se<sub>3</sub> monolayers.

In this chapter, the Pd<sub>2</sub>Se<sub>2</sub> monolayers are produced in a highly scalable way from few-layered PdSe<sub>2</sub> by using thermal stimulation at an *in-situ* heating stage loaded in the

STEM, which enables precise monitoring of the phase-change temperature of the material. It provides a systematic structural investigation of a variety of defects and GBs at the atomic level by using an aberration corrected ADF-STEM, and track their evolution driven by electron beam irradiation at a mild heating temperature of 200°C.

## 7.2 Results and Discussion

### 7.2.1 *In-Situ* High-Temperature Formation of Pd<sub>2</sub>Se<sub>3</sub> Monolayers

The Pd<sub>2</sub>Se<sub>3</sub> monolayers were obtained by heating the commercially bought PdSe<sub>2</sub> films by intentionally controlling the temperature up to 350 °C at the heating holder loaded in STEM with *in-situ* observation of the phase change, as shown in Figure 7.1a,b. In previous study the transformation from bilayer PdSe<sub>2</sub> films to Pd<sub>2</sub>Se<sub>3</sub> monolayers was initiated by high-energy electron beam.<sup>200-201</sup> It was suggested that the electron-beam induced Se vacancies reduced the distance between layers causing interlayer melding for thinning to Pd<sub>2</sub>Se<sub>3</sub> monolayers.<sup>200-201</sup> In this experiment, for eliminating the effect of electron beam, I blanked the beam when increasing the temperature slowly and found the thermal energy could also trigger this phase transformation. The heating condition promoted Se atoms loss which resulted in the interlayer fusion of layered PdSe<sub>2</sub> and structure reconstruction. The FFT in the Figure 7.1a,b inserts show similar spots of diffraction planes despite their different structure symmetries. A unit cell of monolayer Pd<sub>2</sub>Se<sub>3</sub> (a=5.95Å, b=6.15Å) includes four Pd atoms and six Se atoms, forming a lace-like structure (Figure 7.1e). The side view from x-direction shows an interlaced pentagonal configuration (Figure 7.1f). With two types of bonding modes, Se atoms can be classified to two subgroups, the cross bond-symmetric Se (Se<sub>A</sub>) which is bonded to four Pd atoms, and the dumbbell Se (Se<sub>B</sub>) which bonds to two Pd atoms and one neighbouring Se<sub>B</sub> (labelled in Figure 7.1e,f). Previous report has demonstrated the covalent nature of the

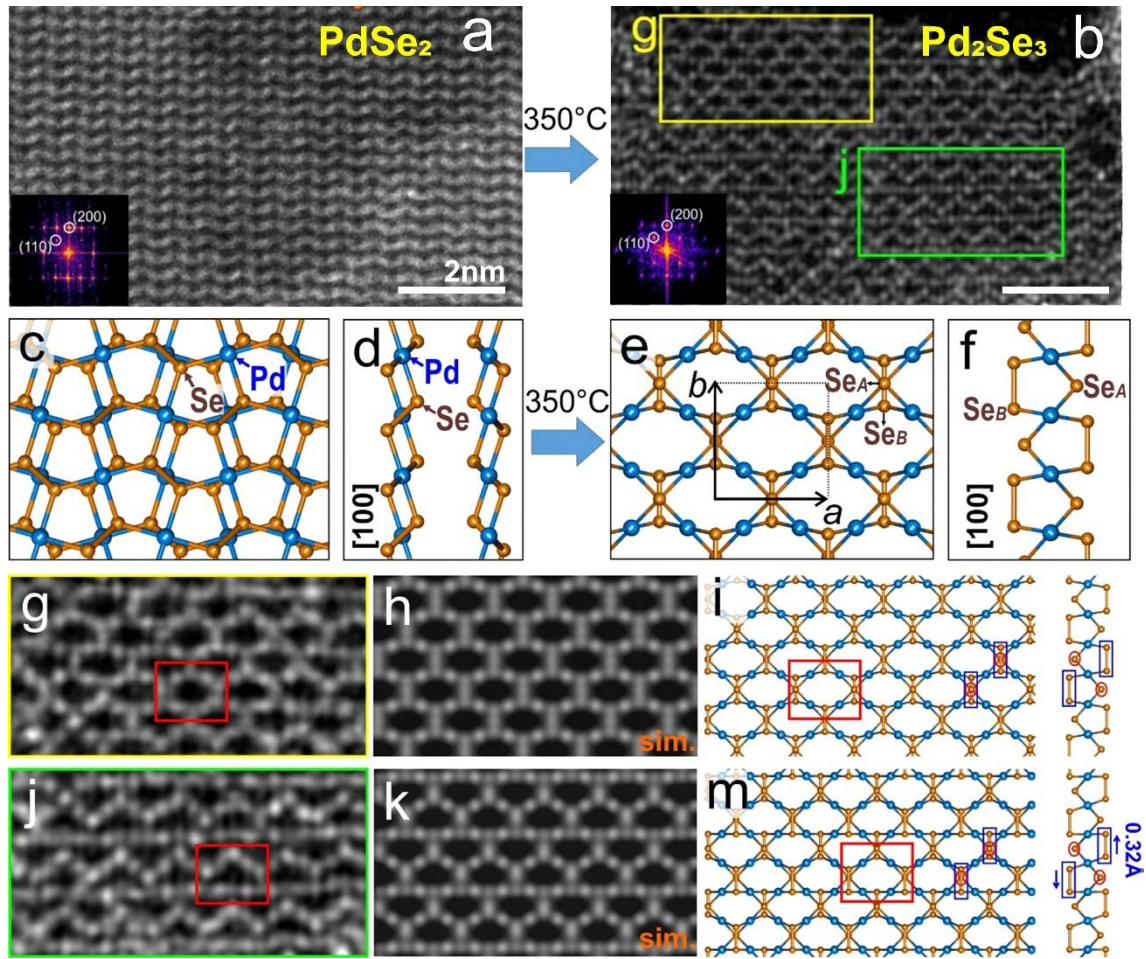


**Figure 7.1** (a,b) ADF-STEM images showing the transformation from (a) bilayer PdSe<sub>2</sub> film to (b) monolayer Pd<sub>2</sub>Se<sub>3</sub> when treated by *in-situ* heating at 350 °C. Inserts are the corresponding power spectra of FFT of the images. (c,d) Atomic model (Pd-cyan, Se-yellow) of the bilayer PdSe<sub>2</sub> of the front and side views. (e,f) Atomic model of the monolayer Pd<sub>2</sub>Se<sub>3</sub> of the front and side views. (g) Magnified view of the yellow box in (b), (h) multislice simulated ADF-STEM image and (i) corresponding atomic model of the pristine monolayer Pd<sub>2</sub>Se<sub>3</sub> structure. (j) Magnified view of the green box in (b), (k) multislice simulated ADF-STEM image and (m) corresponding atomic model of another basic structure of monolayer Pd<sub>2</sub>Se<sub>3</sub>.

In a monolayer Pd<sub>2</sub>Se<sub>3</sub> region (Figure 7.1b), two basic motifs are observed simultaneously as highlighted by the two boxes. One is the pristine structures like connected bulgy rectangles (Figure 7.1g-i), and the other one is the triangular-shaped structure with one straight line (Figure j-m) which in the previous reports was the main type of structures formed under beam.<sup>17-18</sup> The triangular-shaped structure can be formed by simply shifting the two dumbbell Se atom planes (blue boxes in Figure 7.1i,m) by

0.32Å. In this experiment, these two structures commonly coexist, manifesting they are both stable configurations, probably two local energy minima as monolayer Pd<sub>2</sub>Se<sub>3</sub>, see more examples in Figure D2.

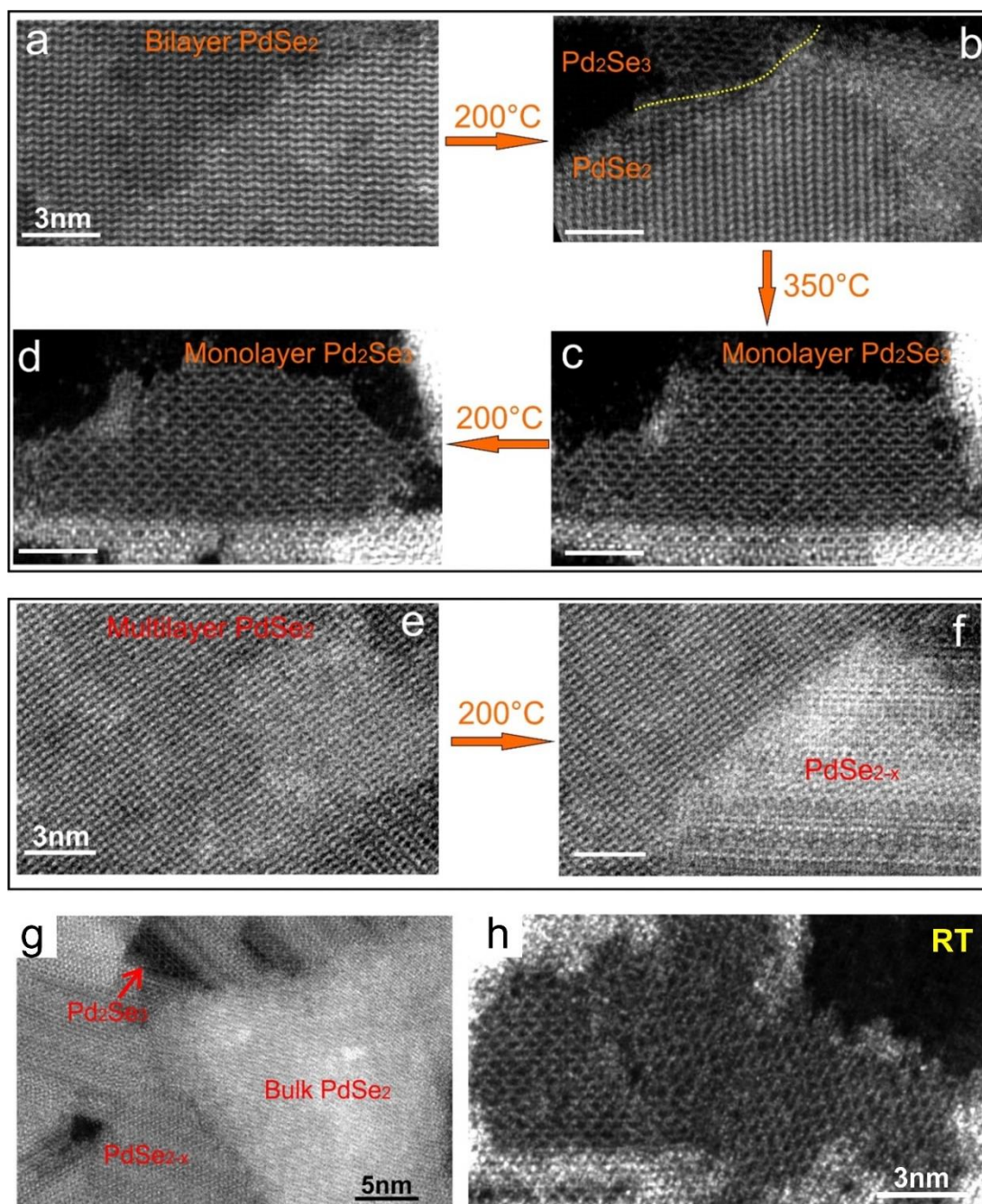


**Figure 7.2** (a-d) ADF-STEM images showing the transformation from PdSe<sub>2</sub> film to Pd<sub>2</sub>Se<sub>3</sub> by controlling temperature at the *in-situ* heating TEM chip. (e,f) Sequential ADF-STEM images showing the structural change in multilayer PdSe<sub>2</sub> films upon heating to 200 °C. (g) An ADF-STEM image showing the coexistence of monolayer Pd<sub>2</sub>Se<sub>3</sub>, thick PdSe<sub>2-x</sub>, and bulk PdSe<sub>2</sub> after partial phase transformation. (h) An ADF-STEM image of a Pd<sub>2</sub>Se<sub>3</sub> monolayer captured when cooled down to room temperature, showing the Pd<sub>2</sub>Se<sub>3</sub> exists stably.

Figure 7.2 further illustrates the phase change process under controlled *in-situ* heating. The structure of bilayer PdSe<sub>2</sub> started to change when heating to 200°C (Figure 7.2a-b), and the phase transformation to Pd<sub>2</sub>Se<sub>3</sub> monolayers quickly occurred at 350 °C so I decreased the temperature to 200 °C for ADF-STEM imaging after heating at 350 °C for 1 min (Figure 7.2c-d). Once cooled down, the Pd<sub>2</sub>Se<sub>3</sub> monolayer structures were maintained (see Figure 7.2h). The energy-dispersive X-ray spectroscopy (EDS) spectrum of the obtained Pd<sub>2</sub>Se<sub>3</sub> is given in Figure D1. As the PdSe<sub>2</sub> film thickness is not completely homogenous, the bilayer PdSe<sub>2</sub> region was fused to monolayer Pd<sub>2</sub>Se<sub>3</sub>, whilst the thicker PdSe<sub>2</sub> multilayer region changed to thick PdSe<sub>2-x</sub> complex (0<x<2) after phase transformation with Se atoms loss, as shown in Figure 7.2e,f (also see the brighter part below the monolayer region in Figure 7.2c,d). This phase transition mechanism is different from that in thermally driven phase change of 2D few-layered PtSe<sub>2</sub> into ultrathin 2D nonlayered PtSe crystals, as discussed in the section 2.4.2 in the literature review,<sup>210</sup> which involves lateral diffusion and atomic digestion following Se loss, forming PtSe crystals thicker than the original PtSe<sub>2</sub> layered precursors due to the stability of the 1:1 metal:chalcogen stoichiometry in Pt:Se.

### 7.2.2 Atomic Structures and Dynamics of Point and 1D Defects

Figure 7.3 showed the point defects and edge structures and their dynamics by *in-situ* ADF-STEM record. Different types of point defects are observed, constructed from dumbbell Se vacancies (V-Se<sub>B</sub>) and the adatoms, as highlighted by boxed regions Figure 7.3a-d. The cross-shape point defect in Figure 7.3h is caused by monovacancy at the Se<sub>B</sub> site (1) followed by the displacement of the other Se<sub>B</sub> (2) which stacks onto the Se<sub>A</sub> atom, forming 2Se atoms at the same column (Figure 7.3g-h). This mechanism is explained in detail in Figure D3. Under continuous beam irradiation, this defect became Se divacancy

as another Se was sputtered (Figure 7.3i), while it turned back to monovacancy after extended imaging (Figure 7.3j,k), suggesting the notable mobility of Se vacancies. The highly dynamic behaviour was also seen at the green boxed regions in Figure 7.3a-d. This composite point defect is produced by a V-Se<sub>B</sub> formation accompanied by trapping a Se adatom inside the squared Pd network (Figure 7.3m-n). Similar Se adatom was also observed the blue arrow region in Figure 7.3a. In the next frame, another Se<sub>B</sub> nearby (red circle in the atomic model of Figure 7.3n) was popped and the adatom underwent position displacement at the same time (Figure 7.3o). The constant beam illumination further stimulated the interplay between V-Se<sub>B</sub> and Se adatom, by which the adatom replenished the V-Se<sub>B</sub> in Figure 7.3p. Then another V-Se<sub>B</sub> was also repaired by capturing an extra Se probably coming from the edge (see the gradually consumed edge), exhibiting a self-healing phenomenon (Figure 7.3q). In the other word, the V-Se<sub>B</sub> migrated to the edge eventually. The pristine edge termination is atomically sharp and flat as highlighted by red rectangular in Figure 7.3a, with atomic model in Figure 7.3f and the corresponding simulation in Figure 7.3e. When irradiated by beam continuously, that edge was etched quickly instead of maintaining the flat configuration or forming the line vacancies, which could be attributed to the fast atom-by-atom edge etching by the beam spluttering with the fast migration of the vacancies to the edge simultaneously. This behaviour is distinguished from the Mo or W based hexagonal TMDs which often form line vacancies or stable holes when numerous chalcogen vacancies are produced, suggesting the possibly lower migrating energy of the Se vacancies in Pd<sub>2</sub>Se<sub>3</sub>. Figure D4 shows another example of the gradually consumed monolayer Pd<sub>2</sub>Se<sub>3</sub> as a result of the beam damage. Likewise, there are no line vacancies generated. With the lost Se atoms popped into the vacuum, the Pd atoms diffused away from the edge to randomly disperse as single atoms sticking onto the carbon substrate, or developed small amorphous metal clusters as a large number of

Pd atoms accumulated.

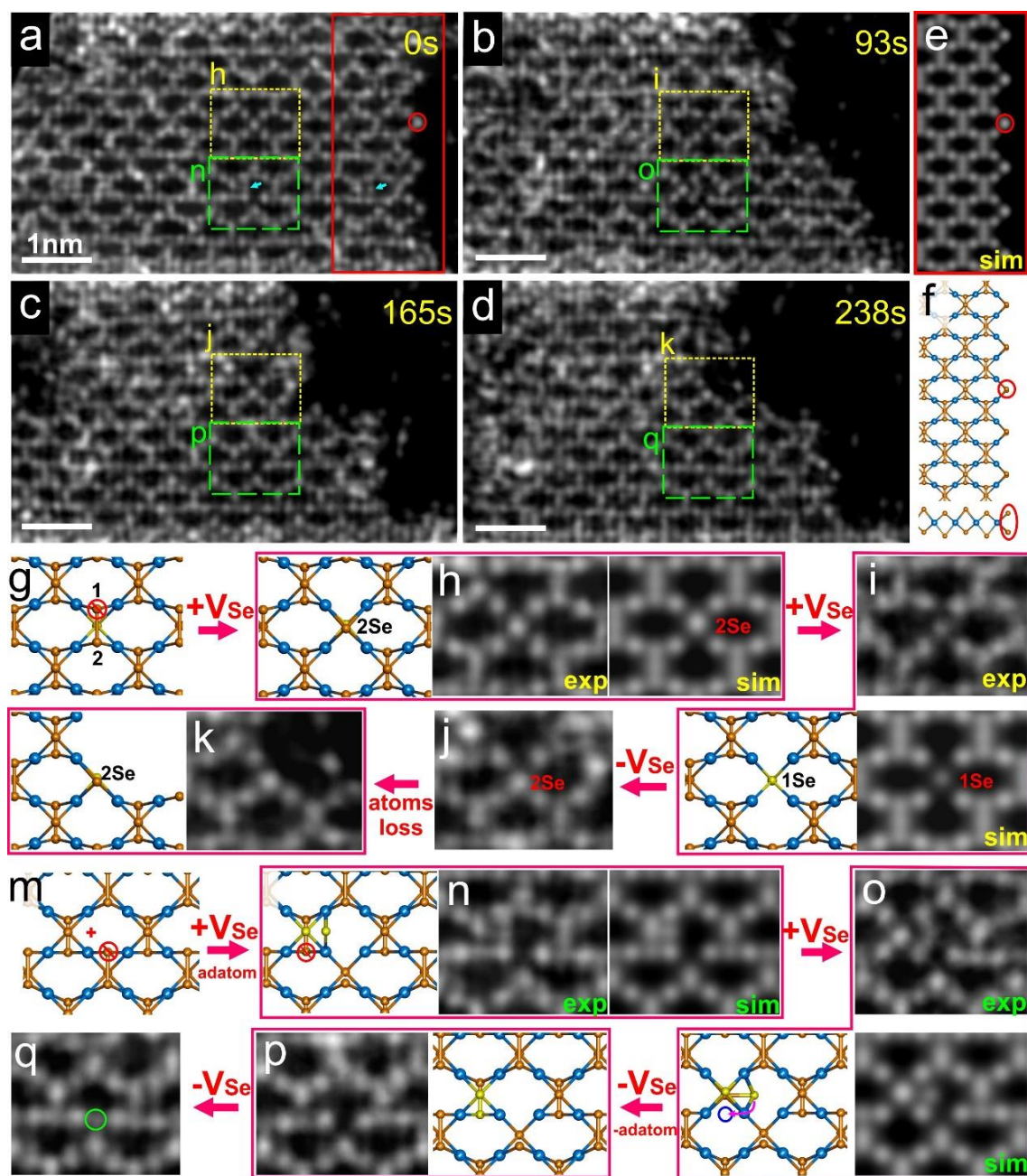


**Figure 7.3** Structures and dynamics of edge terminations, point defects and adatoms in Pd<sub>2</sub>Se<sub>3</sub> monolayers. (a-d) Time series of ADF-STEM images of a monolayer Pd<sub>2</sub>Se<sub>3</sub>. (e) Multislice simulated ADF-STEM image and (f) corresponding atomic model of the edge termination structure of the monolayer Pd<sub>2</sub>Se<sub>3</sub> marked by red rectangular in (a). (g-k) Dynamical process and mechanism of the cross-shape point defect caused by Se vacancies in the yellow boxed regions in (a-d) shown by magnified ADF-STEM images and corresponding atomic models illustration. (m-q) Evolvement of the point defect with adatom in the green boxed regions in (a-d) shown by magnified ADF-STEM images and corresponding atomic models illustration.

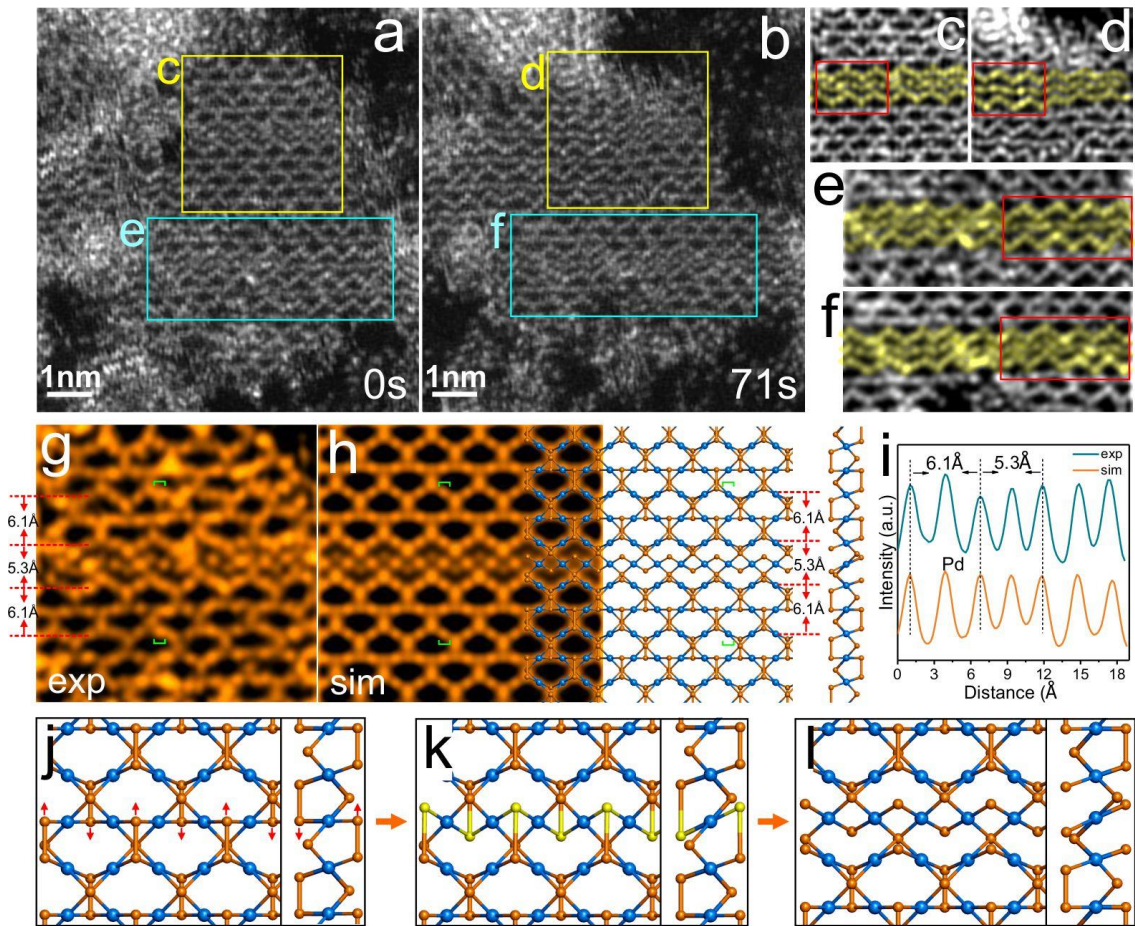


**Figure 7.4** (a,b) ADF-STEM image sequence of a Pd<sub>2</sub>Se<sub>3</sub> monolayer region with wave-like structure. (c-f) Magnified views of the yellow (c,d) and cyan (e,f) boxed regions in (a,b), where the wave-like structures are highlighted by yellow colour. (g) Experimental ADF-STEM image treated by noise-reduce filter and orange colour effects to highlight the wave-like structure, (h) multislice simulated ADF-STEM images with atomic model overlaid and the side view model. (i) Intensity line profile of the experimental and simulated ADF-STEM images measured from the regions labelled by green brackets in (g,h). (j-l) Schematic illustration of the formation mechanisms this structure.

The one-dimensional (1D) defects are often found in TMDs, which are the linear configurations that are deviated from the periodicity in the pristine lattice. Though the common types of line vacancies were not observed in Pd<sub>2</sub>Se<sub>3</sub>, a distinctive wave-like 1D structure was noticed in the boxed regions in Figure 7.4. The atoms involved in this wave-like structure were highlighted in Figure 7.4c-f. Note that the wave-like lattice can convert back to pristine structure stimulated by electron beam, which transformation is reversible, see the red boxed regions in Figure 7.4c-f, where the wave changed to pristine from (c)

to (d) while transformed back from (e) to (f). This atomic configuration is analysed in Figure 7.4g-h. As shown by the intensity line plot profile, the Pd atoms distances were compressed in the wave region. This narrow lattice shrinkage manifests the local compressive strain in Pd<sub>2</sub>Se<sub>3</sub>. The formation mechanism of this wave-like structure is illustrated in Figure 7.4j-l. The Se<sub>B</sub> atoms located along the same row of Pd atoms undergo the shifting in a staggered manner (j to k), followed by the bond breaking between two dumbbell Se<sub>B</sub> atoms (k to l), and it can turn back to pristine structure following reversed process. This flexible structure makes Pd<sub>2</sub>Se<sub>3</sub> adaptable to the local strains during a series of kinetic process motivated by electron beam.

### 7.2.3 Atomic Structures and Dynamics of Grain Boundaries

Differing from the hexagonal TMDs, the orthogonal feature and 180° symmetry of the monolayer Pd<sub>2</sub>Se<sub>3</sub> lattice structure determine two categories of GBs, the 90° GBs and the small angle tile GBs. The ADF-STEM image sequence in Figure 7.5a-f gives the direct observation and the dynamics of the 90° GBs formed between two perpendicular Pd<sub>2</sub>Se<sub>3</sub>. The 90° GBs are linked by stepped GB kinks, as marked by yellow colour in Figure 7.5g,h,k,l. Here the 90° GB is accompanied by the wave-like structure, suggesting the existence of local strain near the GB region. The meandering GB defect units are highlighted by blue and pink colours at different steps in the atomic model in Figure 7.5j,m, notably different from the GB structures in graphene, h-BN or other hexagonal MX<sub>2</sub> TMDs (*e.g.* MoS<sub>2</sub>) which are connected by numbers of dislocation cores (typically the 5/7 fold defect rings).<sup>91,128,134,145,147,326-327</sup> Here the Pd<sub>2</sub>Se<sub>3</sub> GB defects maintain the pristine stoichiometry and can be created by 90° bond rotation of the Se<sub>B</sub>-Se<sub>B</sub> covalent bond without losing atoms (Figure 7.5t,u). Such Stone-Wales bond rotations are abundantly observed in graphene defects,<sup>95,108,328</sup> which also help stabilize the vacancies

and are important in the vacancy dynamics. While in the  $\text{MX}_2$  TMDs like  $\text{MoS}_2$ , the bond rotation is much less common due to the bi-element feature of the bonds whose rotation involves three dimensional process.<sup>105</sup> Unlike the hexagonal TMDs, the existence of the covalent  $\text{Se}_B\text{-Se}_B$  bonds in  $\text{Pd}_2\text{Se}_3$  facilitates the Stone-Wales rotation, making it a significant process in  $\text{Pd}_2\text{Se}_3$  defects formation and dynamics. In the pristine  $\text{Pd}_2\text{Se}_3$  lattice, each unit of the lattice loop contains six  $\text{Se}_B$  atoms from the  $\text{Se}_B\text{-Se}_B$  dumbbells (Figure 7.5t). When one  $\text{Se}_B\text{-Se}_B$  bond rotates, there form two pairs of defect rings, containing 5  $\text{Se}_B$  and 7  $\text{Se}_B$  atoms respectively, shown by blue and yellow shades separately in the right panel in Figure 7.5t. If two neighboured  $\text{Se}_B\text{-Se}_B$  undergo bond rotations (Figure 7.5u), three types of defect loops are generated in pairs. The newly produced one includes 6  $\text{Se}_B$  atoms, denoted as 6' and highlighted by orange colour in Figure 7.5u. Various combination of these defect units enables the GB to extend along different directions, and further bond rotations can enrich the diversiform GB behaviours. When triggered by electron beam, the  $90^\circ$  GB migrated to the upper regions with the climb of the GB steps (Figure 7.5g to k). The lattice change was highlighted in the magnified ADF-STEM images in Figure 7.5n-o, with atomic models in Figure 7.5p-s illustrating the GB migration mechanism. The leaned wave-like structure was firstly converted to the pristine  $\text{Pd}_2\text{Se}_3$  lattices (Figure 7.5p to q), then the  $90^\circ$  GB migrated by one lattice unit through  $90^\circ$  bond rotation of the  $\text{Se}_B\text{-Se}_B$  at the GB lattices (Figure 7.5s), forming new GB steps in Figure 7.5r. This GB migration mechanism differs from that in other 2D TMDs which involves series of atoms rearrangement caused by mobile S vacancies/adatoms and significant lattice reconstruction,<sup>148</sup> but has commonality with the Stone-Wales rotation governed GB motion in graphene.<sup>327</sup> After continual beam irradiation, the GB region decomposed faster compared to pristine regions (Figure 7.5f), which could be attributed to the higher energy and atomic deformation stress locally.

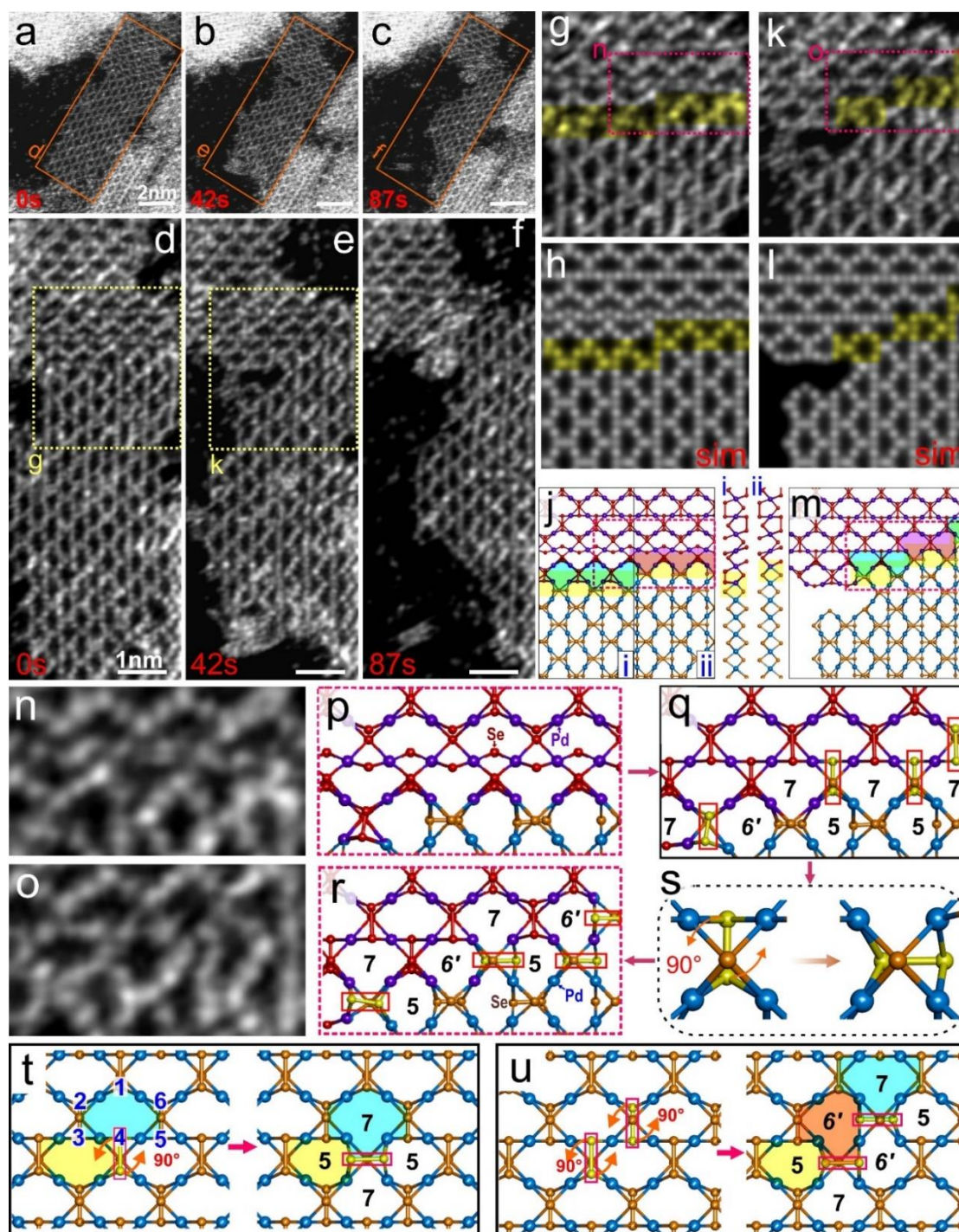


**Figure 7.5** (a-c) ADF-STEM image sequence of a  $\text{Pd}_2\text{Se}_3$  monolayer region with  $90^\circ$ GBs. (d-f) Zoomed-in ADF-STEM images in (a-c) showing the  $90^\circ$  GB dynamics. (g, k) Magnified views of the yellow boxed regions in (d,e) respectively with yellow colour highlighting the GB region, (h,l) multislice simulated ADF-STEM images and (j,m) corresponding atomic models. The atomic model in (j) is divided to two parts (i) and (ii) corresponding to the separate side views at the right panels. The stepped GB defect units in (j,m) are highlighted by blue and pink shades. (n,o) Magnified views of the yellow boxed regions in (g,k) with (p,r) corresponding atomic models. (q,s) Scheme showing the GB migration mechanism through  $90^\circ$  bound rotation. (t,u) Schematic illustration of the formation of different types of defect units at the  $90^\circ$  GB through  $90^\circ$  bond rotation of one (t) and two (u)  $\text{Se}_B\text{-Se}_B$  dumbbell bonds.

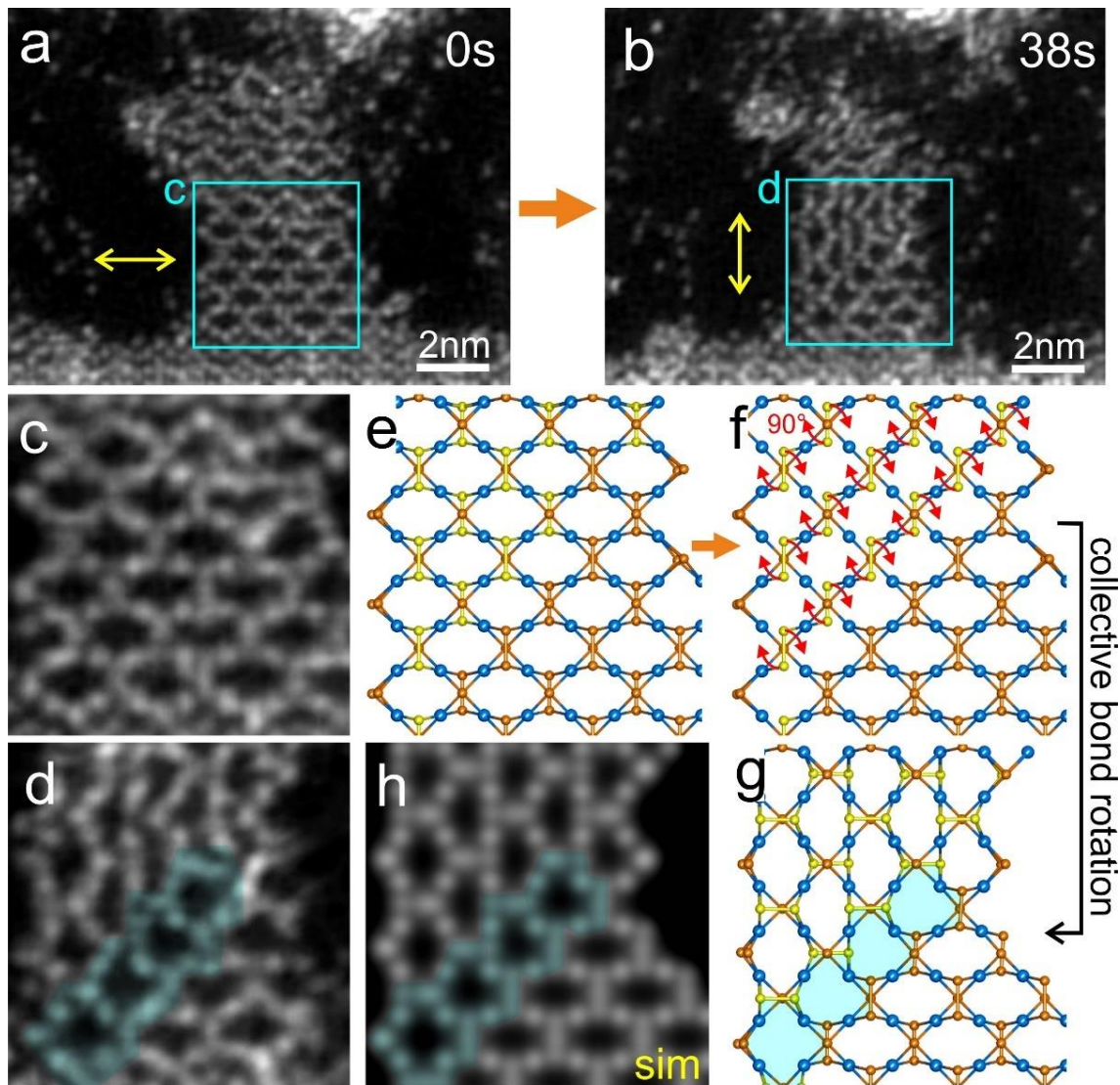


**Figure 7.6** (a,b) ADF-STEM image sequence showing the orientation inversion of partial  $\text{Pd}_2\text{Se}_3$  grain accompanied by GB formation under electron beam stimulation. (c,d) Enlarged views of the blue boxed regions in (a,b). (e-f) Schematic illustration of the evolution mechanism of the grain orientation inversion by collective  $90^\circ$  bond rotation. (e) Atomic model corresponding to (c). (g) Atomic model and (h) simulated ADF-STEM image corresponding to (d). The blue colour in (d,h,g) highlights the GB defects. Pd atoms are coloured with blue and Se in orange.

The  $90^\circ$  GBs can be created from pristine  $\text{Pd}_2\text{Se}_3$  monolayers when partial lattices inverted. Figure 7.6 shows the electron beam can stimulate the inversion of partial  $\text{Pd}_2\text{Se}_3$  grain, which is accompanied by formation of GB defects with the lattice orientation turned by  $90^\circ$  from Figure 7.6a to b. The atomic models in Figure 7.6e-g illustrate that the lattice inversion can be enabled by the collective  $90^\circ$  bond rotation of a group of

$\text{Se}_B\text{-Se}_B$  in a pristine  $\text{Pd}_2\text{Se}_3$  region, triggered by the high-energy electron beam. Considering the slight difference in the lattice parameters in two directions ( $a=5.95\text{\AA}$ ,  $b=6.15\text{\AA}$ ), this reconstruction should involve minor adjustment of the distances of Pd framework in the two directions, and can also bring about spread lattice strains in this region. After partial inversion, a chain of GB defect units are produced as an interface between the inverted and pristine grains, as highlighted by the light blue colour in Figure 7.6d,h,g. These GB defects corresponds to the 6' type as defined in Figure 7.5u, with two neighbouring  $\text{Se}_B\text{-Se}_B$  bonds rotated by  $90^\circ$ , which make the linear GB has the  $45^\circ$  angle to both grains that are perpendicularly stitched. The simulated ADF-STEM image in Figure 7.6h shows good accordance with the experimental image.

The distinct bonding characteristics between Pd and Se and adaptable feature of the lattice offer diverse configurations of GBs when several  $\text{Pd}_2\text{Se}_3$  grains merge together from various directions. Figure 7.7 presents a GB-rich region observed among four joint  $\text{Pd}_2\text{Se}_3$  monolayer grains (see the enlarged ADF-STEM image and corresponding schematic illustration in Figure 7.7b,c). The upper three monolayer  $\text{Pd}_2\text{Se}_3$  pieces are thinned from the top multilayer  $\text{PdSe}_2$  flake (the light blue area in Figure 7.7c) along different orientations as marked by the arrows in Figure 7.7c. Similar to the GB region in Figure 7.5, here the wave-like structure occurs (see the blue arrow in Figure 7.5b), serving as a buffer undertaking the local strain near the GB region. In the corner region when three sub-grains merge (Figure 7.7d), the GBs are connected by vacancy-involved square loops, which are constructed by the cross-shape defects with V- $\text{Se}_B$  formation (Figure 7.7j). These defects are the same as the point defect structure observed in Figure 7.3h. Owing to the merit of high symmetry, *i.e.* all-symmetric in four directions, the cross-shape defects can be compatible with the lattices coming from various angles, thus ideal for serving as the converging boundary structures that connect several grains. For the other

GB corner enlarged in Figure 7.7g, the structure is composed of the 5-6'-7 defect ring chain without vacancy formation, same as the structure denoted in Figure 7.5u.

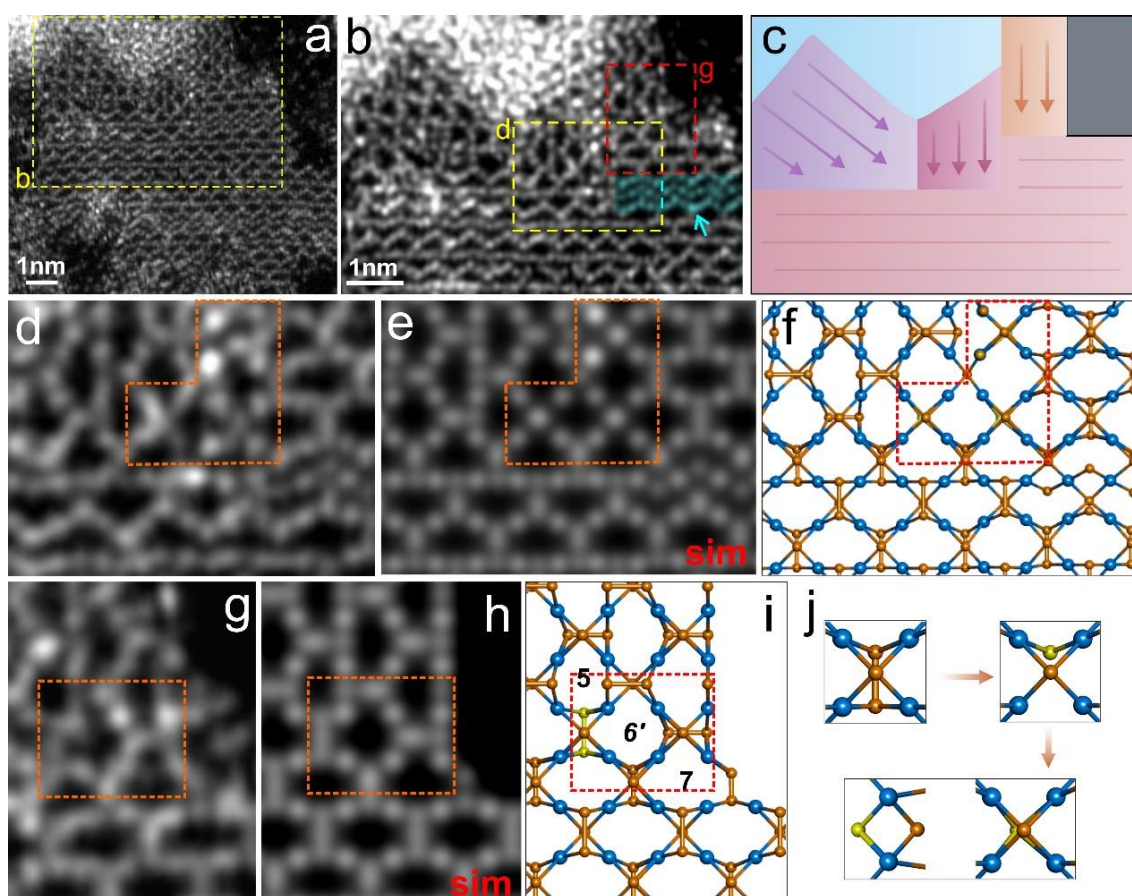


**Figure 7.7** (a) ADF-STEM image of a  $\text{Pd}_2\text{Se}_3$  monolayer with rich grain boundaries (GBs). (b) Zoomed-in image of boxed region in (a), with (c) scheme showing differently-oriented grains in this image. (d) Enlarged view of yellow box in (b) showing the corner connected by three grains, (e) multislice simulated ADF-STEM image and (f) corresponding atomic models. The dash lines mark the symmetric GB atoms. (j) Schematic illustration of the formation mechanism of this symmetric GB. (g) Enlarged view of red box in (b), (h) multislice simulated ADF-STEM image and (j) corresponding atomic models. The dashed box highlights the symmetric GB defect units formed by bond rotation. Pd atoms are coloured with blue and Se in orange.

Aside from the  $90^\circ$  GBs in two perpendicular grains, the small-angle tilt GBs are also observed in  $\text{Pd}_2\text{Se}_3$  monolayers. Figure 7.8 exhibits a GB structure between two differently oriented  $\text{Pd}_2\text{Se}_3$  monolayer films with an angle of  $45^\circ$ , as indicated by the FFT spectrum. The interface between these two grains is not a straight line or linear steps and chains of defect rings like the  $90^\circ$  GBs in Figure 7.5, but instead a transitional area involving a number of lattices and defects, as highlighted in the magnified GB region and

the corresponding atomic model in Figure 7.8b-d. This transitional GB region is constructed by a bunch of square lattices and large irregular loops connected by alternative Pd and Se atoms from two grains. Similar to the ones observed in the GB corner in Figure 7.6d, these all-symmetric squared lattices are also comprised of cross-shaped defects, making them adaptable to the orientation turning. The formation mechanism of this GB region is illustrated in Figure 7.8e-g. When two monolayer Pd<sub>2</sub>Se<sub>3</sub> grains develop toward each other with an angle of 45° along the green and pink arrows in Figure 7.8e, a group of Se<sub>B</sub> atoms near the edge are lost, and the protrude atoms in the edge of the two grains are approaching and bonded, when an area of cross-shaped defects formed with Se<sub>B</sub> vacancies (Figure 7.8f-g). With further atom positions re-arrangement, the 45° GB region is generated. Beside the commonly found cross-shape defect units which make up many defect structures in Pd<sub>2</sub>Se<sub>3</sub>, the large irregular defect loops that are not identical to each other also exist in these transitional GB regions. The formation of them between the two grains can further manifest the high adaptability of the Pd<sub>2</sub>Se<sub>3</sub> lattices which can yield multiple defects in different situations (*e.g.* random orientation changes and strain variations).

The GB dislocations in Pd<sub>2</sub>Se<sub>3</sub> can have a great variety of configurations locally as suggested by the captured structures in Figure 7.5-7.8, which are associated with random intersecting angles of two grains and flexible bonding modes between Pd and Se atoms. Whilst it may be difficult to affirm that those GB configurations commonly occur in large-scale 2D Pd<sub>2</sub>Se<sub>3</sub> sheets from the captured local structures of small grains. Aimed at validating their structural stability and analysing their possible formation conditions, further collaborative work is still under process with the supportive theoretical DFT calculations.

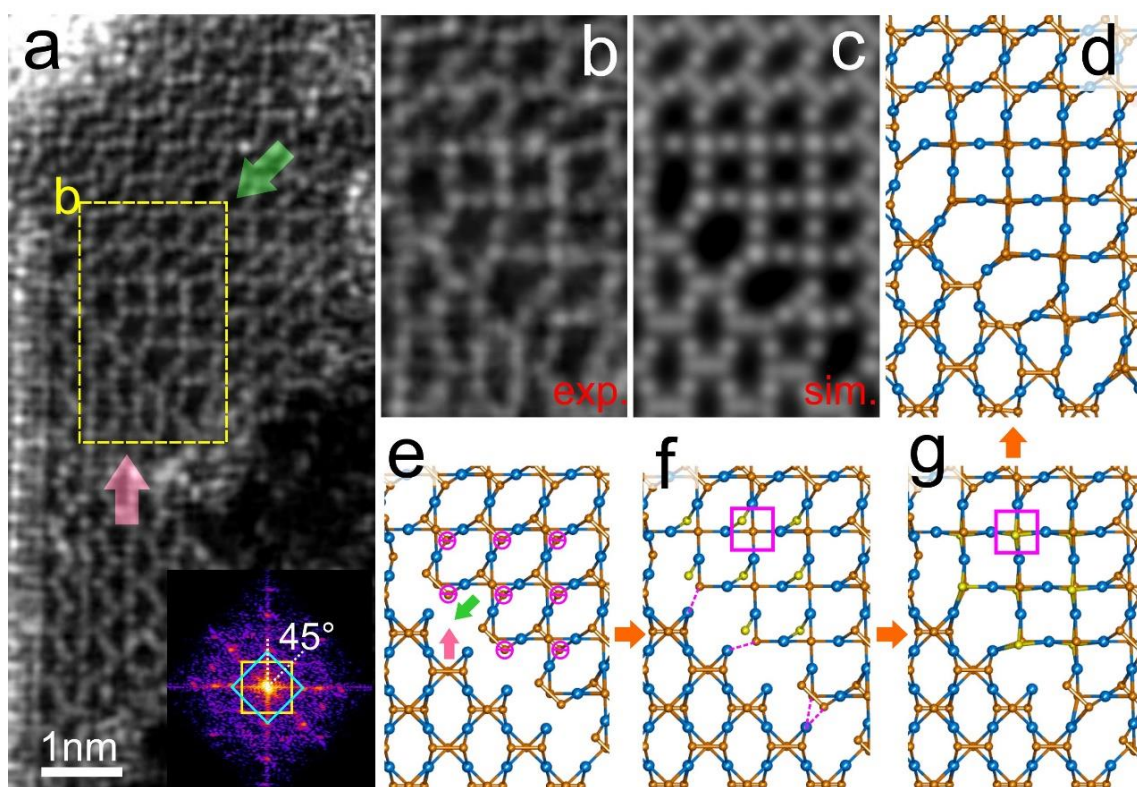


**Figure 7.8** (a) ADF-STEM image of a  $\text{Pd}_2\text{Se}_3$  monolayer region with a  $45^\circ$  grain boundary (GB). The inset is the power spectrum by FFT of the image, where two sets of spots have an angle of  $45^\circ$ . (b) Enlarged view of yellow box in (a) showing the structure of  $45^\circ$  GB region, (c) multislice simulated ADF-STEM image and (d) corresponding atomic model. (e-g) Schematic illustration of the formation mechanism of this GB region. Pd atoms are coloured with blue and Se in orange.

### 7.3 Conclusion

By using atomic-resolution direct ADF-STEM imaging, this chapter studies the atomic structures and electron-driven dynamics of various defects and GBs of monolayer  $\text{Pd}_2\text{Se}_3$ , which was obtained from  $\text{PdSe}_2$  crystals through controlling the *in-situ* heating temperature. The vacancies exhibit self-healing behaviour *via* migrating to the edge instead of forming line vacancies like other TMDs. An unusual 1D wave-like structure is formed with staggered shift of the  $\text{Se}_B\text{-Se}_B$  probably ascribed to the local strains, which often occurs near GBs serving as the strain buffer. Different types of GBs are observed in the  $\text{Pd}_2\text{Se}_3$  monolayers, including the  $90^\circ$  GB and small-angle tilt GB. The  $90^\circ$  GBs are

constructed by multiple defect units derived from the Stone-Wales (SW) rotations of the  $\text{Se}_B\text{-Se}_B$  without losing atoms, and can migrate *via* further bond rotations, in contrast to the much less common SW rotation in typical hexagonal TMDs with bi-element bonds only. The other highly symmetric square-shaped GB defects involving V- $\text{Se}_B$  also appear in the GB-rich corners and the tilt GB region, enabling the  $\text{Pd}_2\text{Se}_3$  to extend along various orientations. This study presents the diversity, adaptability and abundant electron-induced dynamics of the distinct monolayer  $\text{Pd}_2\text{Se}_3$  defects, which can enrich the structural knowledge of 2D materials, and offer more possibilities for exploiting versatile properties of 2D materials through defect engineering.

## Chapter 8

### Conclusion and Outlook

#### 8.1 Conclusion

The purpose of this doctorate project is to systematically establish a fundamental understanding of the defective structures in monolayer/bilayer TMDs at the atomic level by utilizing single-atom-resolution ADF-STEM. The TMDs studied in this project cover the typical hexagonal 2H phase TMDs (incl. MoS<sub>2</sub>, WS<sub>2</sub>), the emerging 1T phase noble metal TMD (PtSe<sub>2</sub>) as well as the new phase Pd<sub>2</sub>Se<sub>3</sub>. A variety of novel defect structures their dynamic are investigated, including point defects, linear defects, dislocations and grain boundaries (GBs). Targeting at exploring more possibility in tailored defects engineering, endeavour is also put in the *in-situ* modifications of 2D TMDs when doing ADF-STEM by using two techniques as the driving factors, electron beam patterning and high-temperature heating, focusing on the controllability and mechanism involved.

To begin with, Chapter 4 focuses on the GB-involved defect structures in the 2H phase TMDs, *i.e.* MoS<sub>2</sub> and WS<sub>2</sub> monolayer/bilayers, which are the most intensively studied 2D semiconductors and have demonstrated a plenty of appealing properties in 2D devices.<sup>13,73,329</sup> As a commonly found and a significant defect type in polycrystalline 2D TMDs, GBs have great influence on the electronic properties of materials. This chapter aims at contributing to a deep understanding of the GB-related defect structures. Two different GB-involved defective structures are studied at atomic level. One is the 60° GB-connected inversion domains (IDs) on monolayers, and the other is small-angle tilt-GB on bilayers. The *in-situ* high temperature defect behaviours are examined. Specifically, IDs formation and dynamics are demonstrated to be related to changed strain field caused

by electron beam irradiation with high-temperature heating. The dual GBs are proved to exist in the bilayer 2D TMDs, and can stay stable at high temperature of up to 700°C at least. The discovery of this dual bilayer GBs reveals the CVD synthesis mechanism and can help stimulate the controlled growth of the 2D bilayer interfaces.

Focused electron beam irradiation has high precision and control in creating nanoscale voids, with *in-situ* atomic resolution monitoring.<sup>270,281,330</sup> Motivated by this, the second part of my work utilizes the electron probe in the ADF-STEM at an accelerating voltage of 80 kV for the *in-situ* patterning of 2D TMDs apart from doing imaging, in particular manufacturing the atomically thin nanowell patterns in the bilayer WS<sub>2</sub>, combined with an *in-situ* heating holder. The controllable etching at the atomic level is demonstrated with 2 nm precision in location, showing dose-dependent behaviours for the sizes. High temperature here ensures mobility of atoms and avoids covered amorphous carbon, which proves to facilitate the well-defined nanowells production as compared with the drilled holes at room temperature. This systematic study addresses the detailed atomic configurations of the nanowells, and also reveals the mechanism involved in nanowells formation, evolution, and merging limits. The comprehensive framework provided in this part is promising to promote the *in-situ* electron beam patterning technique in manipulating TMD bilayer crystals.

Following the well-known 2H-phase MoS<sub>2</sub>/WS<sub>2</sub>, the final section of my project further works on the recently rising noble metal 2D TMDs. This section includes two topics in Chapter 6 and 7, focusing on the octahedral 1T-phase PtSe<sub>2</sub>, and the new phase pentagonal Pd<sub>2</sub>Se<sub>3</sub>, respectively, whose defects and GB structures and behaviours are found to be distinctly different from those commonly reported in other hexagonal 2D crystals like graphene, h-BN and 2H-phase TMDs.

For the 1T-PtSe<sub>2</sub>, single Se point vacancies ( $V_{Se}$ ) show preference of specific

production sites, which are highly mobile under electron beam. A new type of 1D stretched defects form with changed local strain fields caused by collective dynamic behaviours of isolated  $V_{Se}$ , showing different structures and mechanism in contrast to the 1D vacancy lines in 2H-phase  $MoS_2/WS_2$ . Distinct GB structures are found in misoriented  $PtSe_2$  grains with different angles. A special tilt angle of  $30^\circ$  is connected linearly by staggered GB dislocations asymmetrically with elongated strain fields, which is the most frequent GB angle in polycrystalline  $PtSe_2$ . The mirror twin GBs ( $60^\circ$  GBs) are also observed which cause the stacking diversity in bilayer  $PtSe_2$ . As the basic units for composing GB, various edge dislocations are classified, including  $5|7_{+Se}$ ,  $6|8$ , and  $6_{+Se}|8$  planar polygons which show distinct 1T-phase feature and possess Se-rich homoelemental bonds.

The other new 2D crystal,  $Pd_2Se_3$  monolayers, are created by thermally induced phase transformation of few-layered  $PdSe_2$  films in an *in-situ* heating holder in the STEM to promote Se loss. The distinct lattice structures, peculiar bonding modes, and particularly the existence of special covalent Se–Se dumbbell bonds (this type of Se is termed as  $Se_B$  in Chapter 7) make the  $Pd_2Se_3$  defect structures and behaviours distinctive. A variety of point vacancies, 1D defects and GBs structures are directly visualized in monolayer  $Pd_2Se_3$ , which show a series of dynamics triggered by electron beam. The fast migration of vacancies leads to self-healing of point vacancies and subsequent edge etching under beam irradiation. Specific defects for  $Pd_2Se_3$  are stabilized by the formation of Se–Se bonds, which can shift to buffer strain, forming a wave-like 1D defect. Bond rotations are also observed and play an important role in defect and GB dynamics in  $Pd_2Se_3$ . The GBs form in a meandering pathway and migrate by a sequence of Se–Se bond rotations without large scale vacancy formation. In the GB corners and tilted GBs, other highly symmetric vacancy defects also occur to adapt to the orientation change.

To sum up, this thesis presents comprehensive investigation on diverse defects of 2D TMDs of various phases at the atomic level, with particular interest in *in-situ* modification on the materials structures apart from the intrinsic defects study. Here the 2D TMDs ranges from the typical 2H-phase MoS<sub>2</sub>/WS<sub>2</sub> to the increasingly popular noble metal TMDs like 1T-PtSe<sub>2</sub> and the thermally driven unique Pd<sub>2</sub>Se<sub>3</sub>. Distinct defect structures and behaviours are compared for those TMDs taking different phases. These results give atomic level insights into a variety of defects in the 2D TMDs monolayers/bilayers, which will hopefully underpin the understanding of their structure-property correlation.

## 8.2 Future Outlook

There could be four directions as the rational evolution of my DPhil research. The first is to further investigate the controlled *in-situ* techniques for the intentional production of defects. This is of particular interest for the noble metal 2D TMDs like PtSe<sub>2</sub> and PdSe<sub>2</sub>/Pd<sub>2</sub>Se<sub>3</sub> which are becoming increasingly fascinating in devices while the defect study is still limited. The introduction of defects might be manipulated by the combination of focused electron beam and the thermal heating, and it should be worthwhile to examine what role the high temperature plays in the defect patterning process. Those defect creation mechanisms in the well-studied 2H-MoS<sub>2</sub>/WS<sub>2</sub> system can be taken as the reference. The second direction is to quantify the effects of the nano-engineered defects on the electrical properties of the TMDs, which can help guide the tailoring the material property through the modification on the lattice. This might be attained by utilising *in-situ* electrical measurements, for example, the *in-situ* test of the electric property of the nanochip overlapped by the PtSe<sub>2</sub> GBs. Thirdly, as an extension of the thermally-driven Pd<sub>2</sub>Se<sub>3</sub> study, it can be further explored whether the phase change is 100% reversible and how to realize this. For example, as the mechanism of Pd<sub>2</sub>Se<sub>3</sub> formation involves Se loss,

it might be able to recover to be the original layered PdSe<sub>2</sub> under Se-rich atmosphere at proper temperatures. This study is of significance because it can rationalize how to get any desired composition of the phases from the same material *via* controlling phase changes back and forth for specific uses in devices. Fourthly, it is promising to drive the creation of more types of new 2D materials by phase transition from layered or bulk transition-metal-based crystals through carefully controlling thermal conditions with *in-situ* monitoring, especially for those with rich phases in different atomic percentages.

## Appendix A Supporting Information of Chapter 4

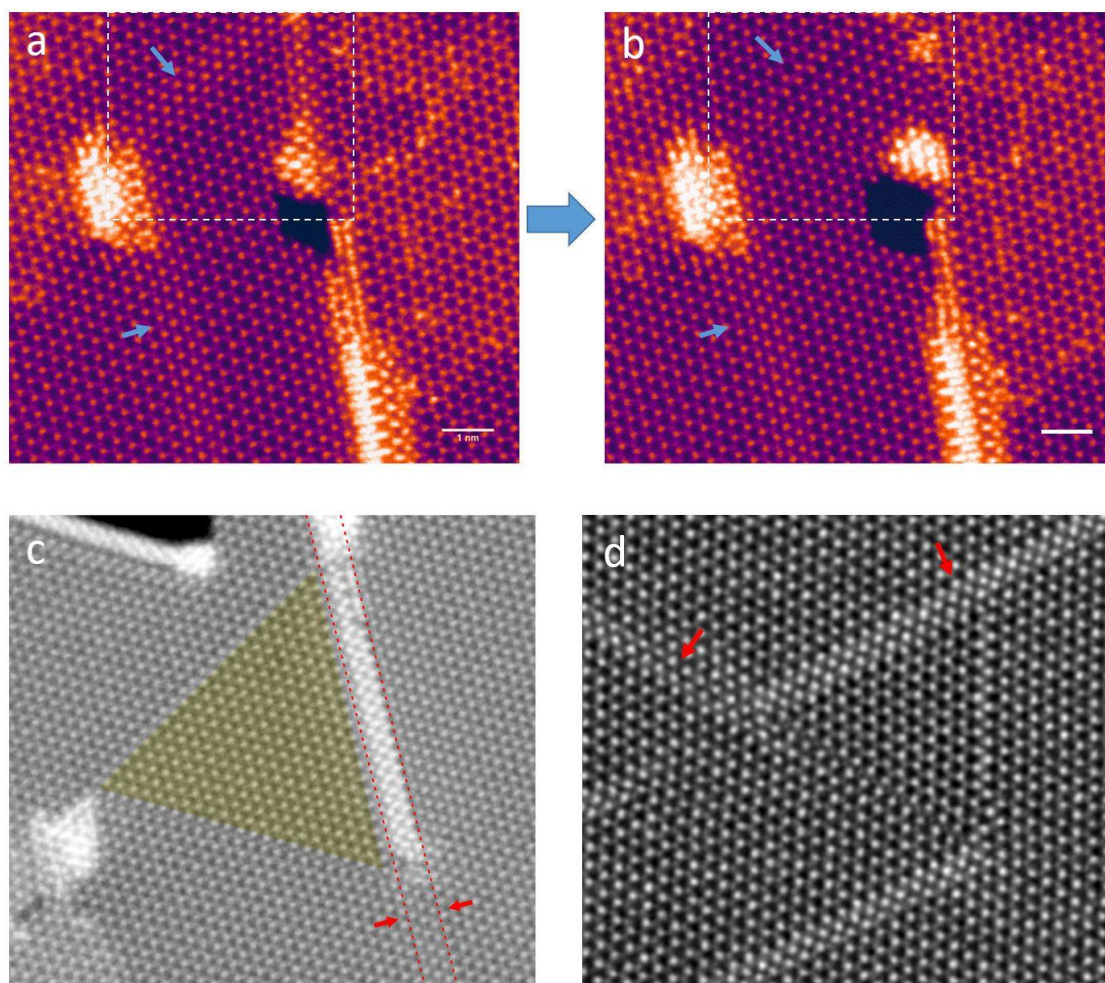


**Figure A1.** Some other examples of inversion domains (IDs) showing the presence of line defects nearby (marked by arrows), typically leaned on by the side of ID and serve as an extending line of the domain GB.

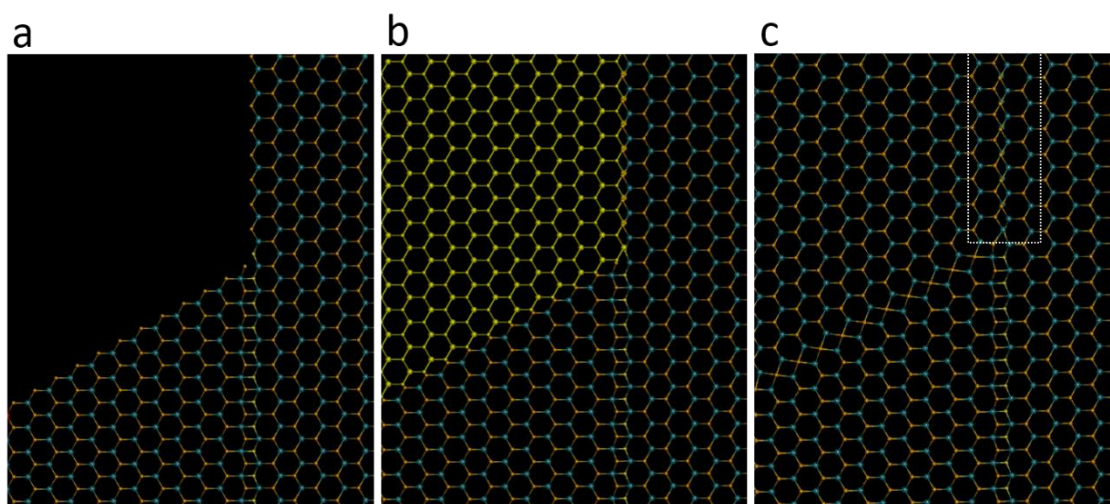


**Figure A2.** Schematic illustration by atomic models showing the MoS<sub>2</sub> lattice shrinkage required as a precondition to form an ID. (a) MoS<sub>2</sub> lattice only with 4|4E GB. The right side is pristine

lattice, and the left part is the inverted lattice. (b) Adding another segment of pristine MoS<sub>2</sub> lattice as highlighted, to form another GB with the inverted lattice. (c) The formed structure with a 4|4E GB and a 4|4P GB separating inverted domain and the pristine lattice. It is found that in order to create this structure, there should be a lattice shrinkage in the pristine MoS<sub>2</sub> lattice, as marked by the white dashed rectangular in (c). For the typical ID that is captured in our STEM experiment in the main article, this lattice shrinkage is produced by the 2SVL, which is the extended line of the evolved 4|4E GB.

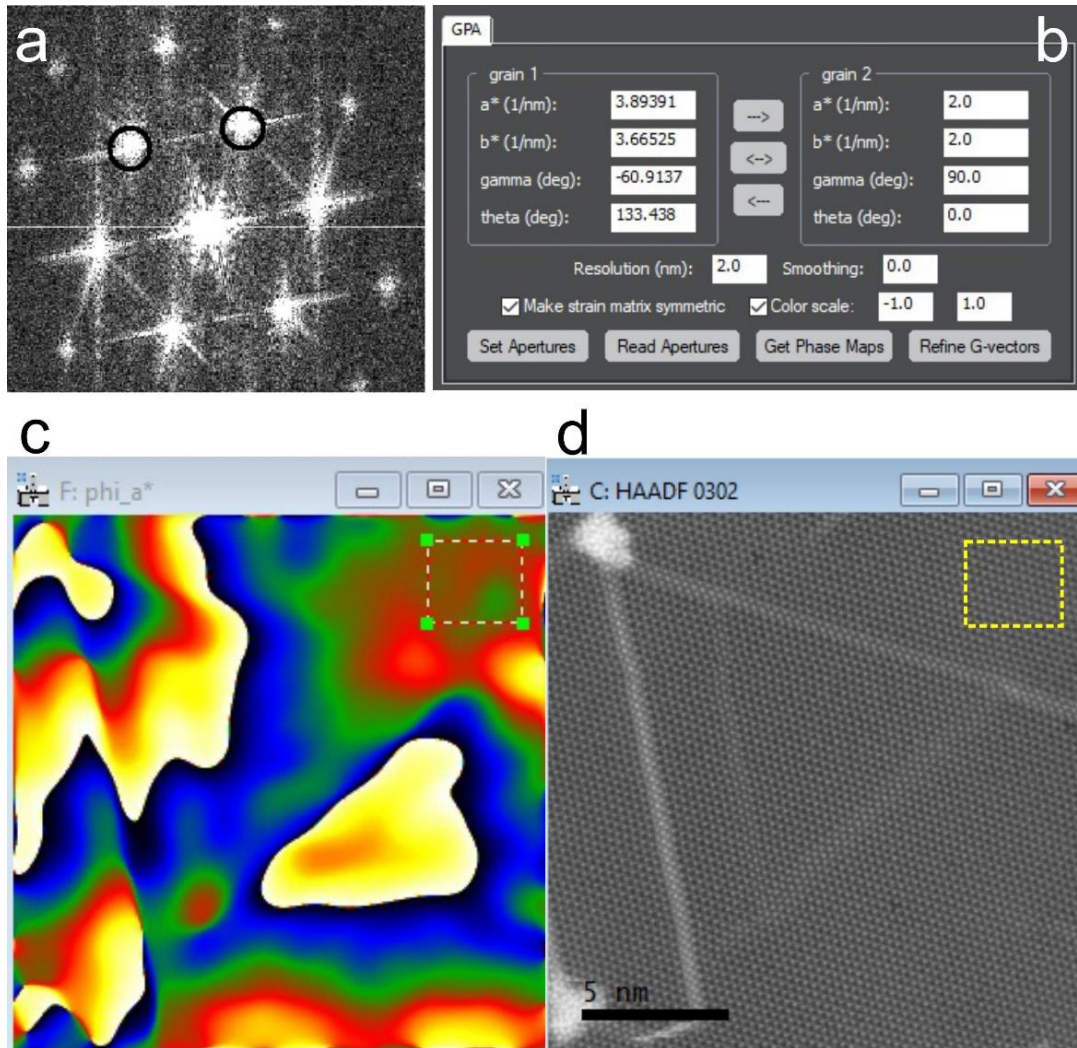


**Figure A3.** Parameters for using GPA analysis. (a) Two vectors selected. (b) Detailed parameters. (c,d) Referencing area chosen.

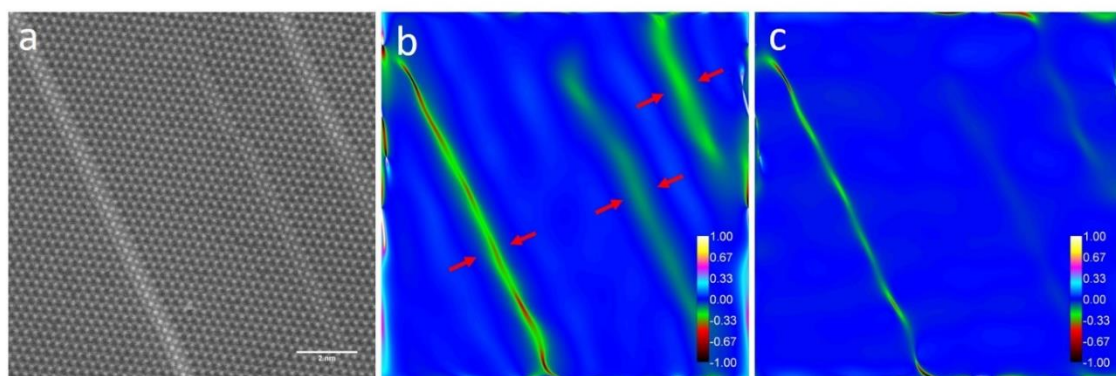


**Figure A4.** Supporting example showing the compressive strain fields of the line defects. (a) The ADF-STEM image of a MoS<sub>2</sub> monolayer consisting of three S vacancy defect lines. Scale bar: 2nm. (b, c) Strain components  $\epsilon_{xx}$  (b) and  $\epsilon_{yy}$  (c). The red arrows manifest the compressive strains caused by the line defects.

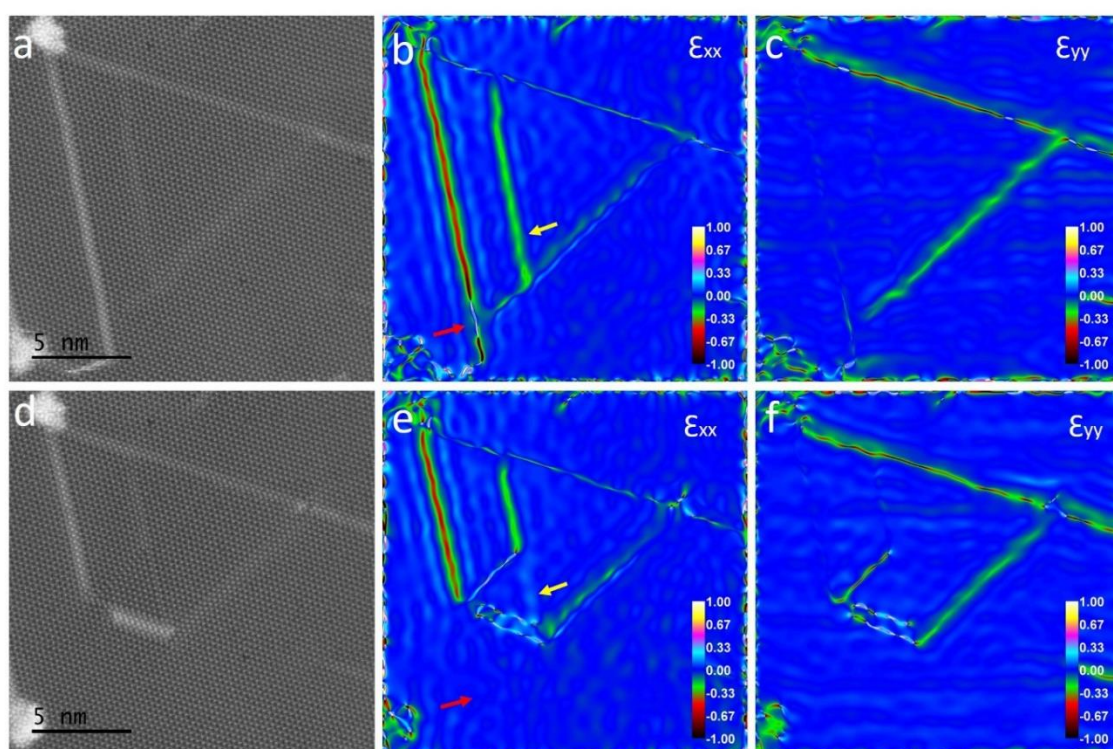


**Figure A5.** Strain fields of the lattices before (a-c) and after (d-f) the ID formation.

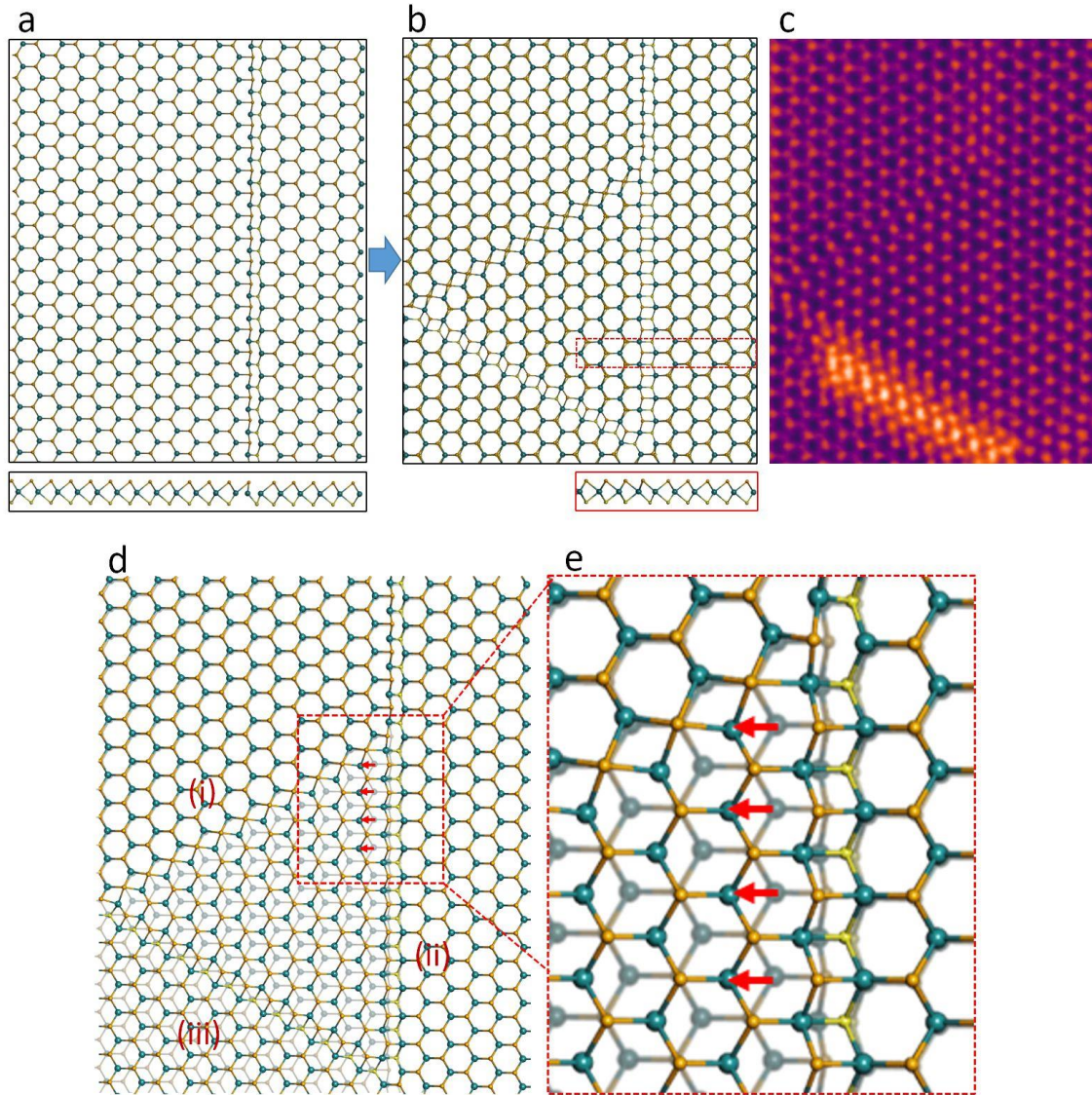


**Figure A6.** The schematic models showing the formation of a large ID starting from the MoS<sub>2</sub> lattice with a two-sulphur vacancy line (2SVL). (a) Monolayer MoS<sub>2</sub> lattice with a long 2SVL and the side view. (b) The formed ID along that 2SVL, with two different types of grain boundaries (GB). The 4|4 edge (4|4E) sharing GB (with the model side view beneath) evolves from the 2SVL, and the 4|4 point (4|4P) sharing GB forms in another side of the domain. (c) The ADF-STEM image of the ID corresponding to (b). (d) Image obtained by overlapping (a) and (b), showing how lattice changes when forming the ID. The original lattice is displayed in a half-transparent effect. For the lattice outside the ID in the model, region (i) and (ii) are kept unchanged while the pristine region (iii) need to shift leftward for nearly half lattice, which actually in the experimental data is not a pristine lattice area and the required shift is accommodated by the compact line defects in the bottom side of the ID in (c). (e) Expanded view of the red dashed box in (d), highlighting the atoms movement at a typical corner region intersected by 4|4E GB, 4|4P GB, and the 2SVL. The 4|4E GB evolves from the 2SVL structure in (a). The red arrows present the migration direction of Mo atoms in one side of the 2SVL, which shift half lattice, creating 4|4E GB and 4|4P GB simultaneously thus forming the ID.

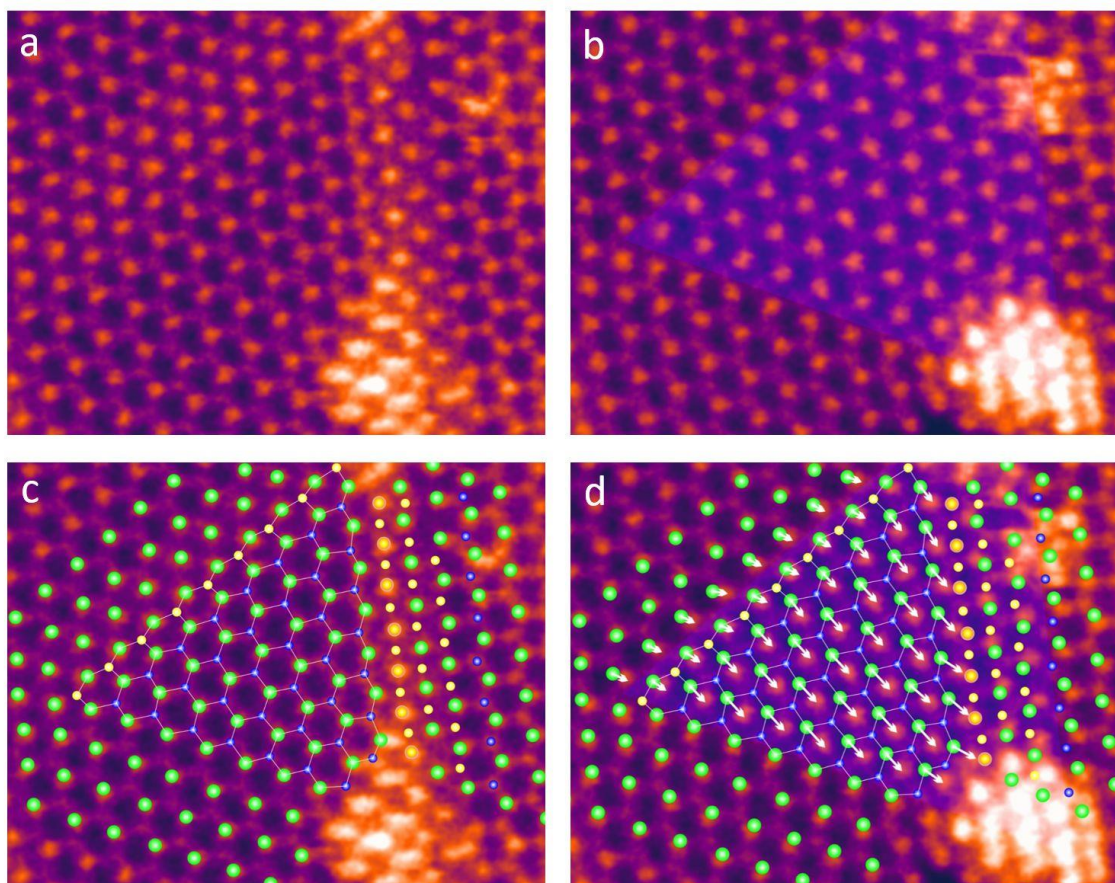


**Figure A7.** Another example illustrating the Mo atoms movement towards the defects area during the ID formation, while S atoms almost stay at their positions. (a,c) and (b,d) are the ADF-STEM images before and after the ID forms, respectively. (c) and (d) are the same frame as (a) and (b), separately, which are overlaid with schematic atoms marking their original positions, and the arrows in (d) indicate the displacement pathway of Mo atoms inside the ID.

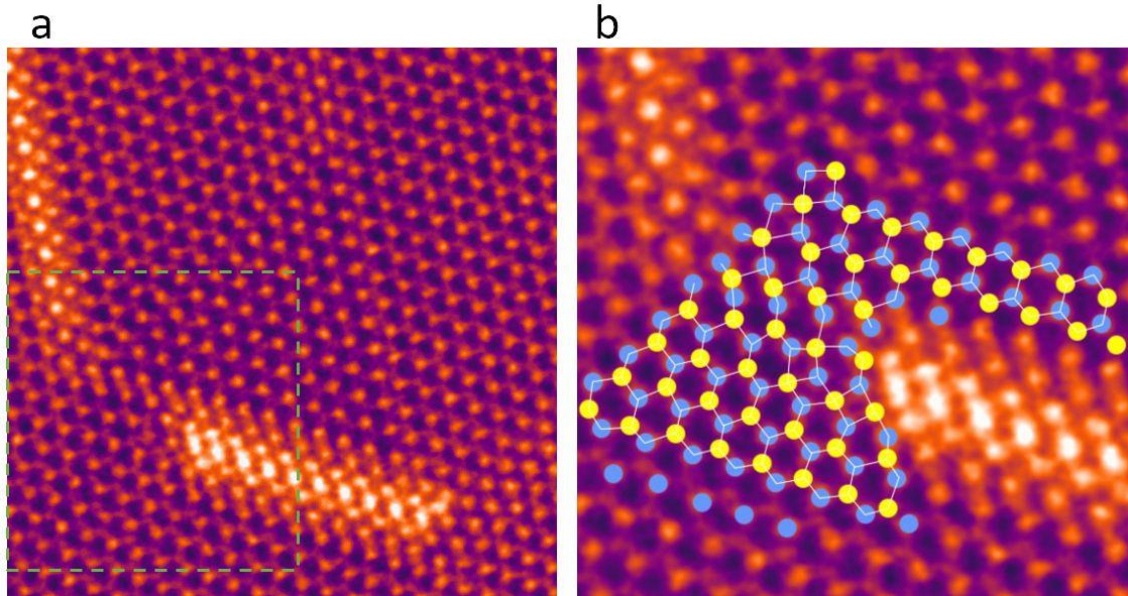


**Figure A8.** One corner structure of the ID, which is also at the intersection area of two compact multi-S line vacancies. (b) is the large view of the boxed region in (a), overlaid with schematic atomic models consisting of Mo (blue) and S (yellow) atoms.

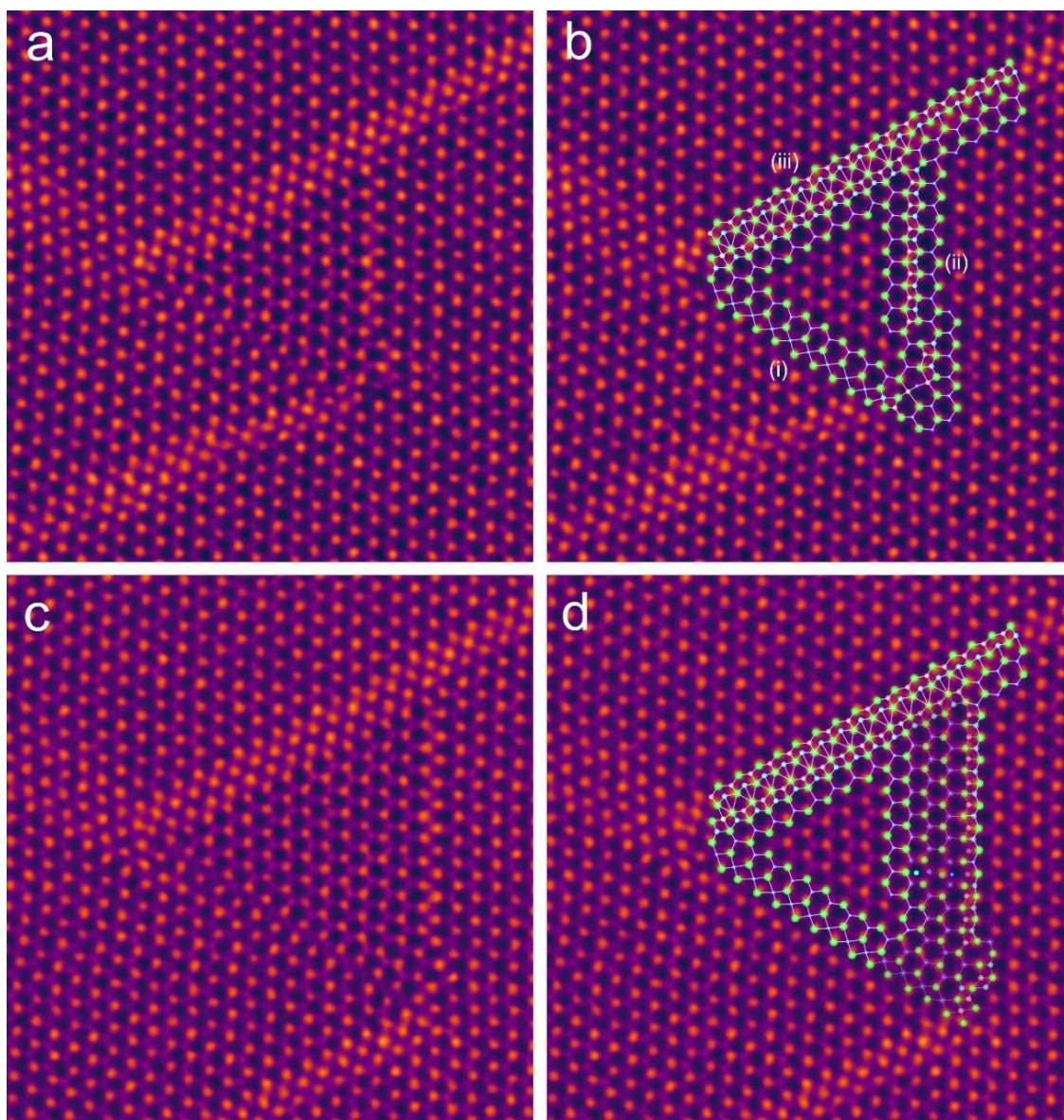


**Figure A9** ADF-STEM images of (a,b) original ID and (c,d) expanded ID. (b) and (d) are the same images as (a) and (c), respectively, with overlaid schematic atomic models interpreting the boundary structure of the ID.

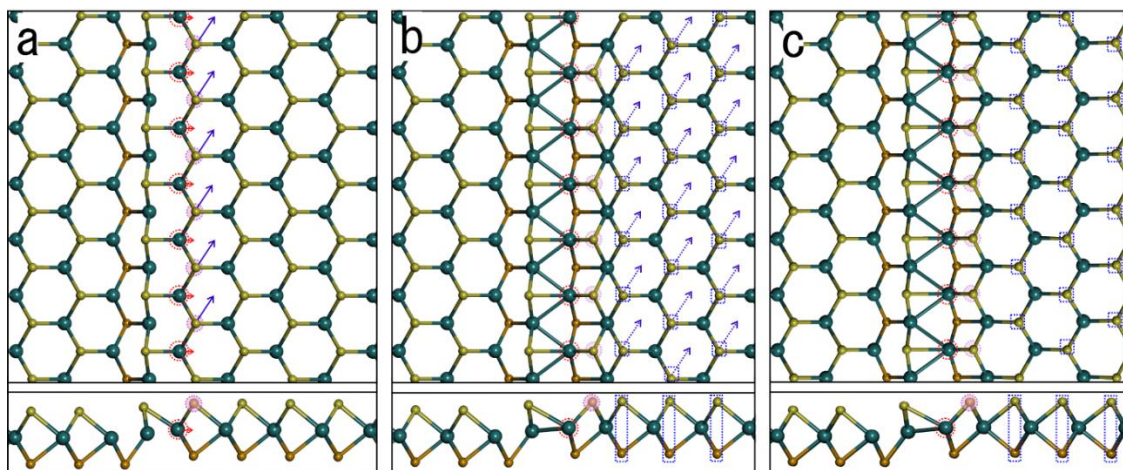


**Figure A10** Schematic illustration by atomic models showing the change when the MoS<sub>2</sub> lattice

at one side of the 2SVL is inverted, forming a 4|4E GB adjoining 2SVL structure, corresponding to the structure change near the 2SVL during ID expansion.

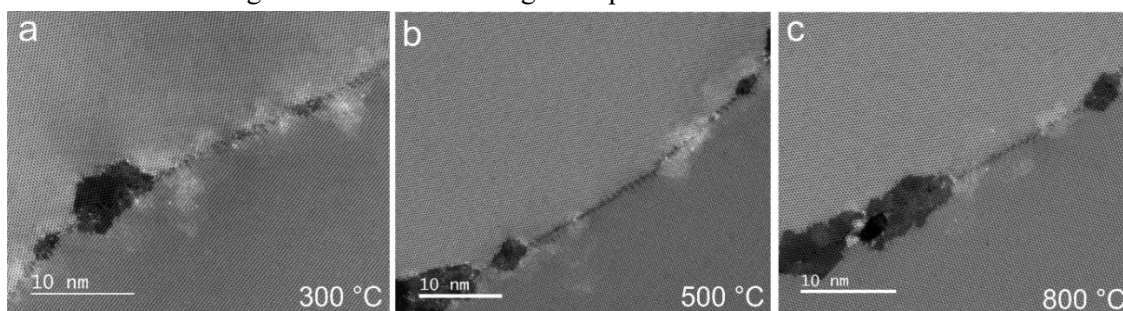


**Figure A11.** ADF-STEM images of **three areas along the extended grain boundary** in bilayer  $\text{WS}_2$  film. (a-c) are taken at different in-situ heating temperatures, 300, 500, 800 °C, respectively. The grain boundaries show the identical features in different temperatures without any structural changes. Surface contamination and beam induced contamination are reduced with temperature increasing.

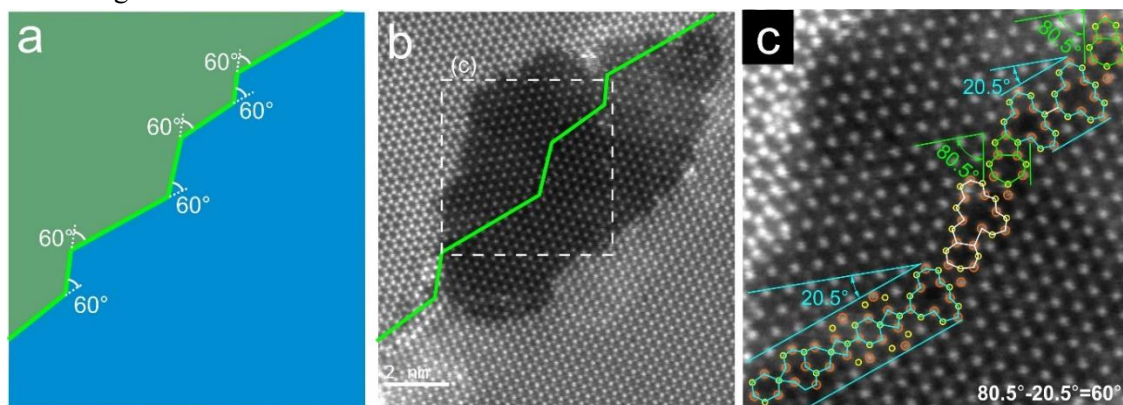


**Figure A12.** Meandering pathway in local  $\text{WS}_2$  GB region. (a) Schematic illustration showing the turning angles of  $60^\circ$  of the stepped GB in the ADF-STEM image in (b). (c) Enlarged view of the monolayer region in (b) showing the dislocation cores of at two different angle with the turning angle of  $60^\circ$ .

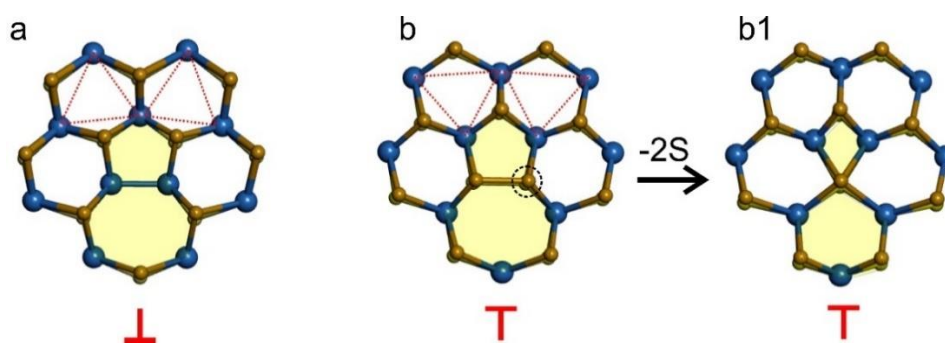


**Figure A13.** Schematic atomic models showing the sulfur-polar  $\top$  and metal-polar  $\perp$  monolayer dislocation GBs. (a, b) Basic 5|7 dislocation cores of sulfur- and metal-polar, respectively. Red triangles manifest the symmetry lattice on both sides of the GB. (b1) 4|6 dislocation cores derived from 5|7 defects by removing 2S atoms in (b).

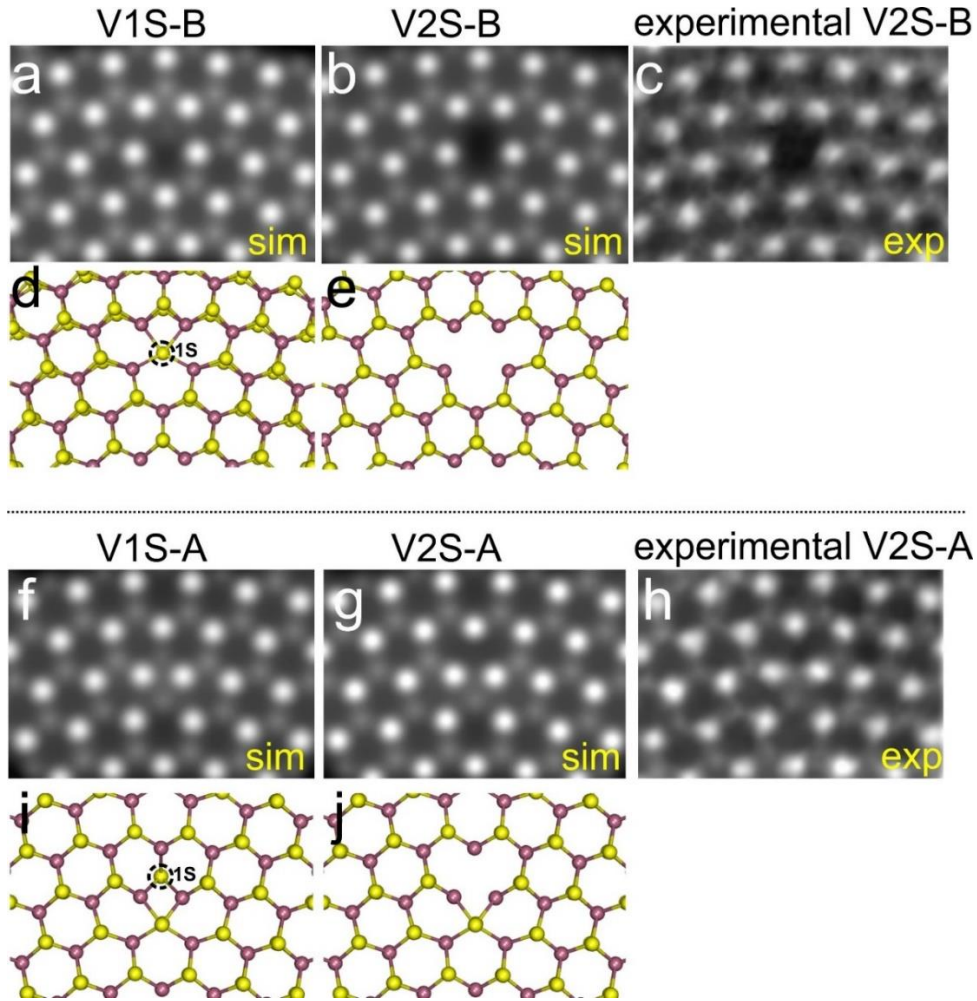


**Figure A14.** Comparison of the simulations and experimental ADF-STEM images of two S-vacancy derivatives of 4|6 GB dislocation cores, confirming the observed W-rich  $V_{2S}(B)$  and  $V_{2S}(A)$  GB structures in the first layer of this bilayer  $WS_2$ .

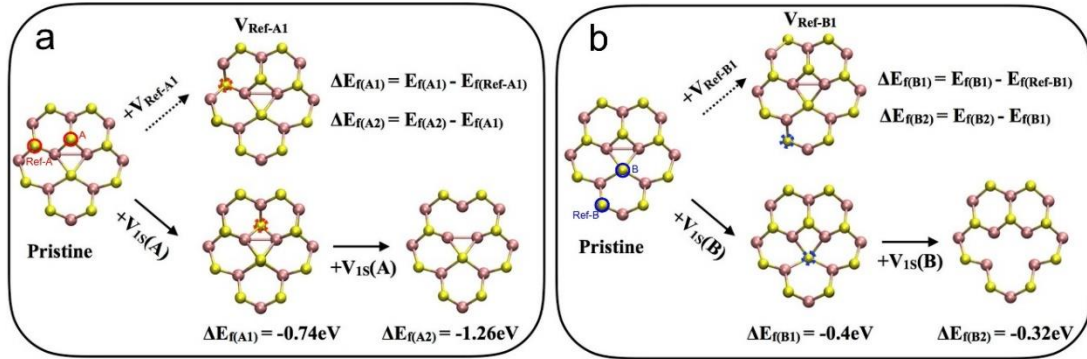


**Figure A15.** Schematics showing the defect formation energy of (a) type II and (b) III, compared to the nearest sulfur vacancy ( $V_{Ref-A1}$  or  $V_{Ref-B1}$ ). The results show the formation energy of A and B are both lower than the reference positions. Also, the formation of the next vacancy at the same position becomes smaller than the first one. The energy difference between 1st and 2nd vacancies with the position A (core type II) is about 1.3eV while the difference is not such significant about 0.3eV with the position B (core type III).

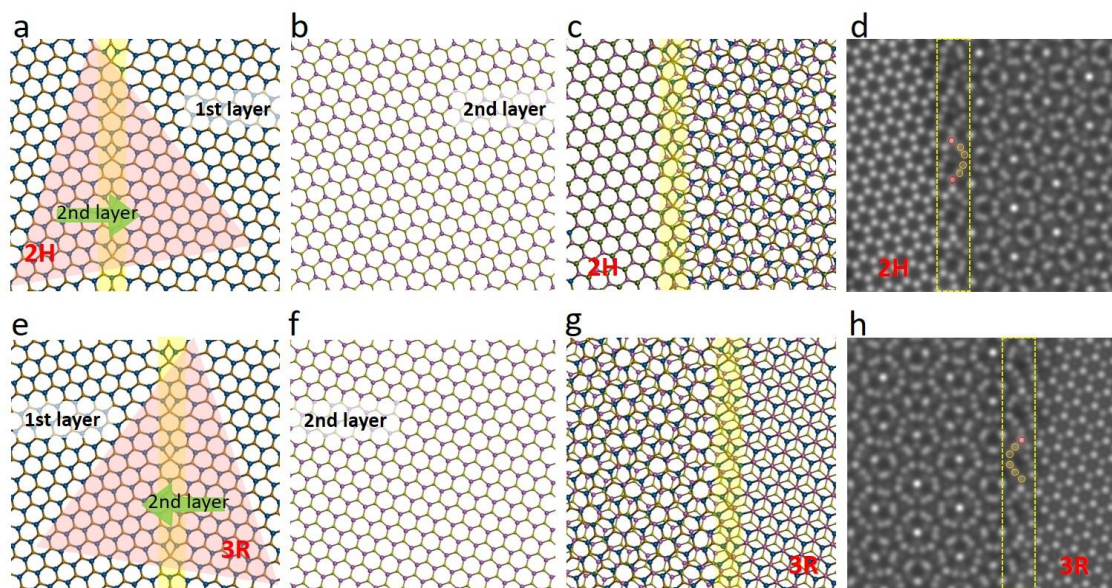


**Figure A16.** Schematics and simulations of the hypothesis that the 2<sup>nd</sup> layer with specific stacking continuously grows without changing lattice orientation, directly migrating across the 1<sup>st</sup>-layer GB. (a, e) The 2<sup>nd</sup>-layer domain adopts 2H(a) or 3R(e) stacking at one side of the 1<sup>st</sup>-layer GB, and directly overlays the 1<sup>st</sup>-layer GB which is highlighted by yellow. (b, f) 2<sup>nd</sup>-layer domain lattice overlaid on (a, e), respectively. (c, g) Atomic models of the stacked two layers, with 2H (c) or 3R (g) stacking at one side of 1<sup>st</sup>-layer GB and twisted stacking at the other side. The yellow masks overlaid mark the 1<sup>st</sup>-layer GB. (d, h) Simulated ADF-STEM image of (c) and (g), respectively. The overlaid GB regions highlighted by yellow dashed lines exhibit 6-member half-rings patterns, which differ with the stacking type. The inner sides of the half-rings are toward the 2H or 3R-stacked regions. The other sides, though, present turbostratically stacked patterns.

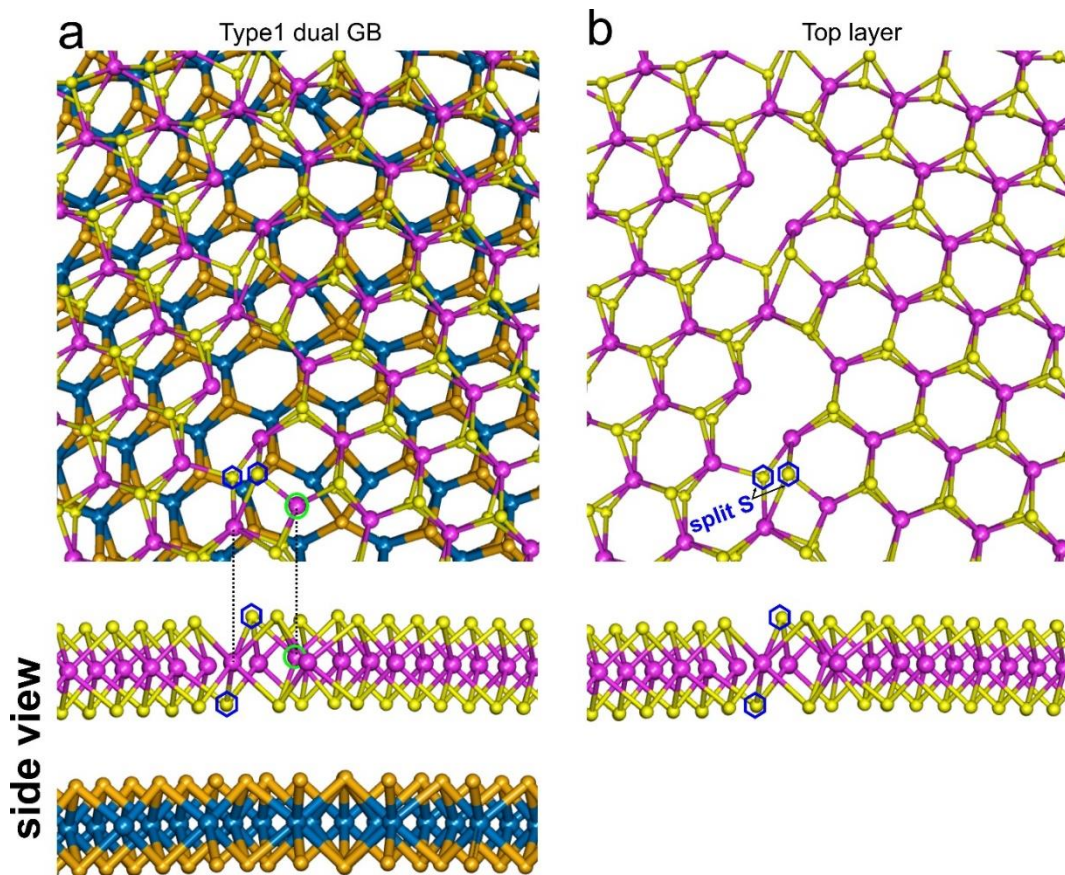


**Figure A17.** Perspective views at an angle of  $20^\circ$  and corresponding side views of the relaxed model showing the detailed atomic structures of the Type1 dual GB with split S atoms as the bridge.

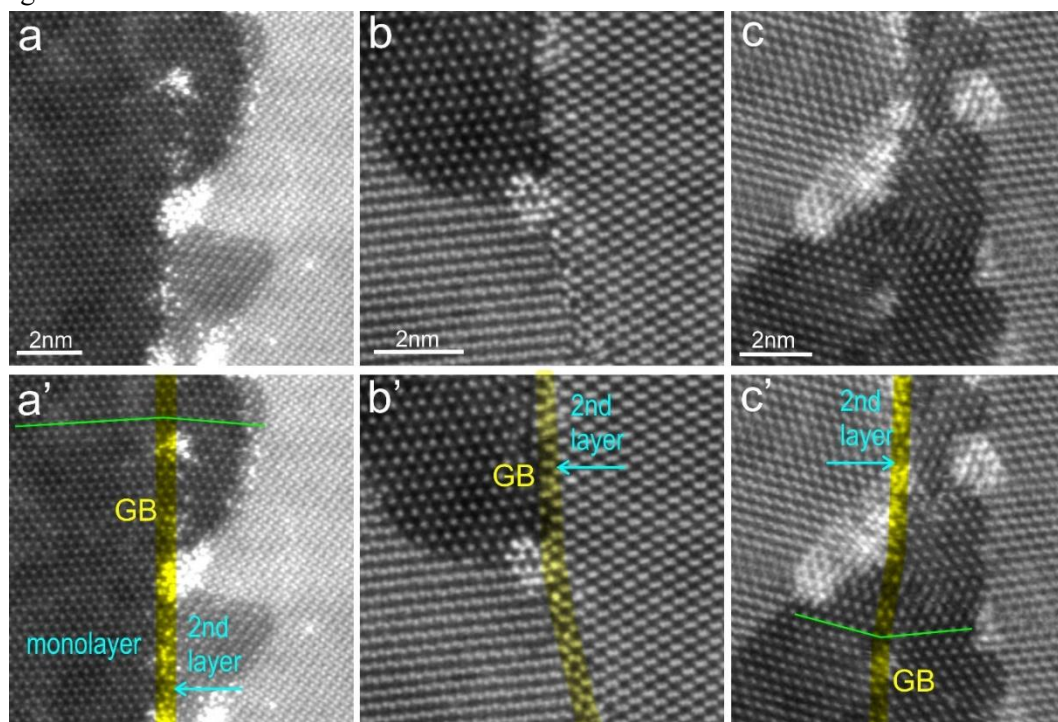


**Figure A18.** ADF-STEM images showing the secondary domain (second layer) stops growing when it reaches the location of the GB already formed in the underlying monolayer. (a-b) ADF-STEM images taken from (a) MoS<sub>2</sub>, (b,c) WS<sub>2</sub> films, with (a'-c') highlighting the small-angle tilt

GBs in the underlying monolayers. In these films, the second layers coming from one side stop at the bottom GB region instead of overlapping it.

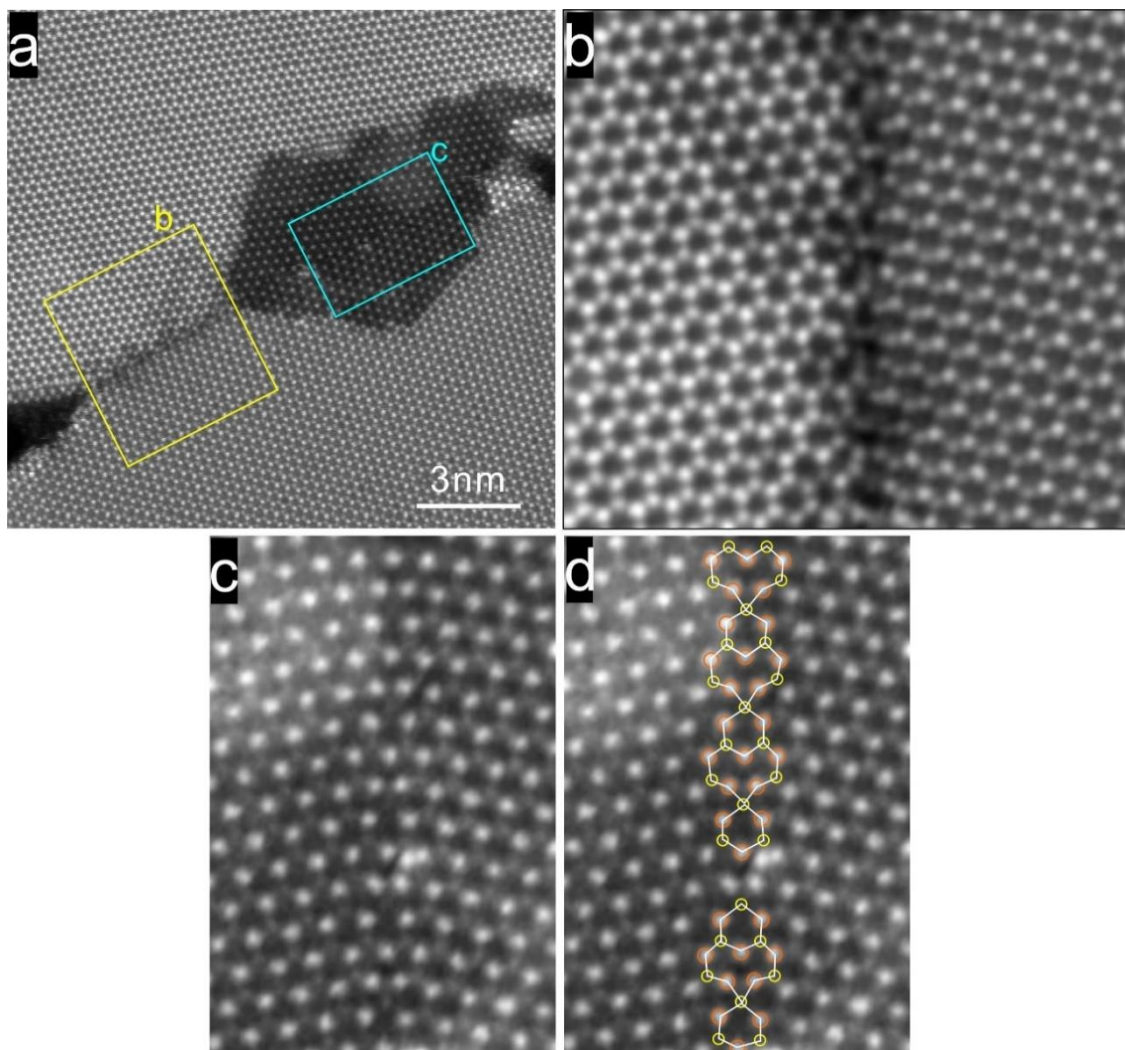


**Figure A19.** Supporting example showing another dual bilayer GB with type 2-ii pattern. (a) ADF-STEM image taken at accelerating voltage of 60 kV. (b) Enlarged view of the yellow boxed region in (a), showing the dual GB formed at 2H/3R interface in two bilayers with small angle of orientation difference. (c) Magnified view of the green boxed monolayer in (a), with schematic models overlaid in (d) showing the dislocation cores at the bottom layer GB.

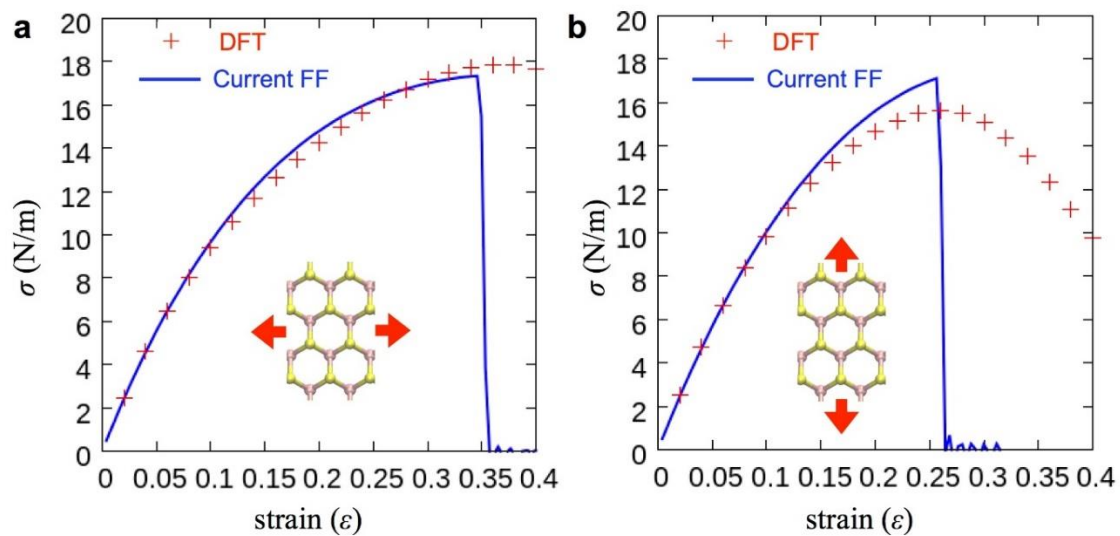


**Figure A20.** Stress-strain curves from MD and DFT under tensile loading along the zigzag (a) and armchair (b) directions. The details of the setting are the same as in the previous study.<sup>186</sup>

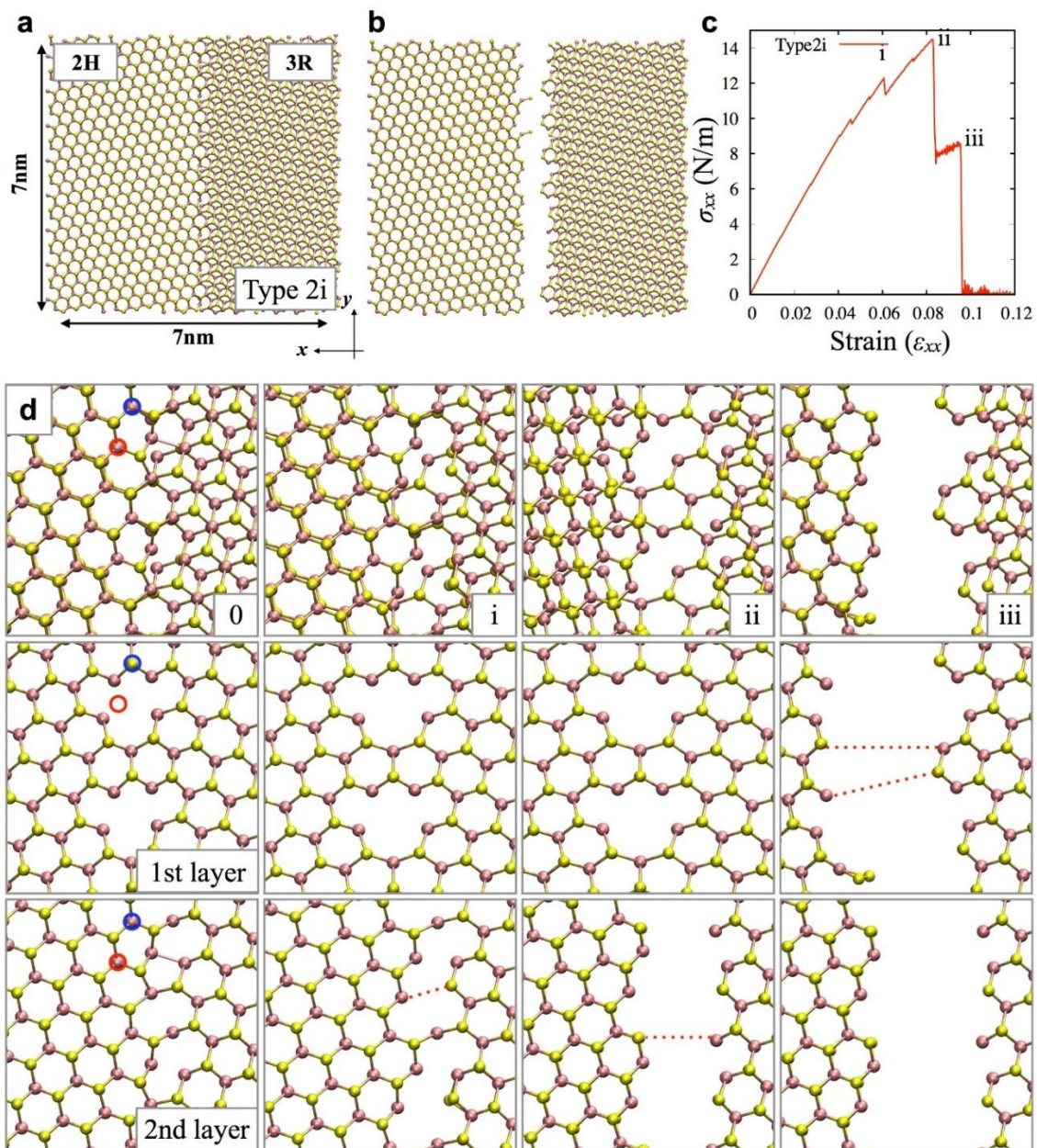


**Figure A21.** (a) Rebuilt model of Type2i through MD simulations with 7nm x 7nm size. (b) Snapshot of the model after both layers fail. (c) Stress-strain curve of the bilayer under tensile loading. There are several stages of failure (i- iii), which described more detail in **d**. (d) Detailed atomic structures of the MD model. The red lines indicate the bond breaks at the failure stage from i to iii described in the stress-strain curve.

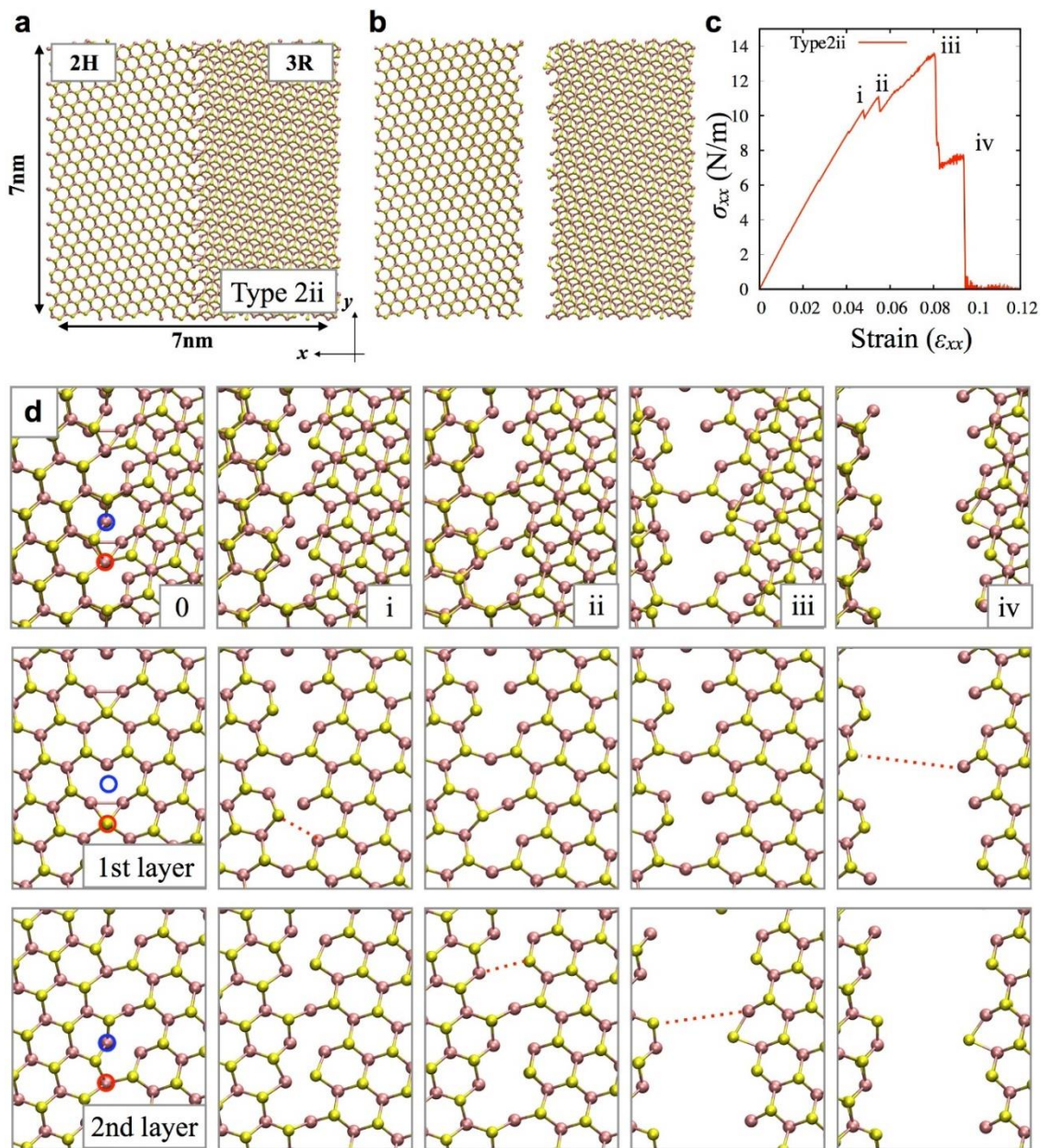


**Figure A22.** (a) Rebuilt model of Type2ii through MD simulations with 7nm x 7nm size. (b) Snapshot of the model after both layers fail. (c) Stress-strain curve of the bilayer under tensile loading. There are several stages of failure (i- iv), which described more detail in **d**. (d) Detailed atomic structures of the MD model. The red lines indicate the bond breaks at the failure stage from i to iv described in the stress-strain curve.

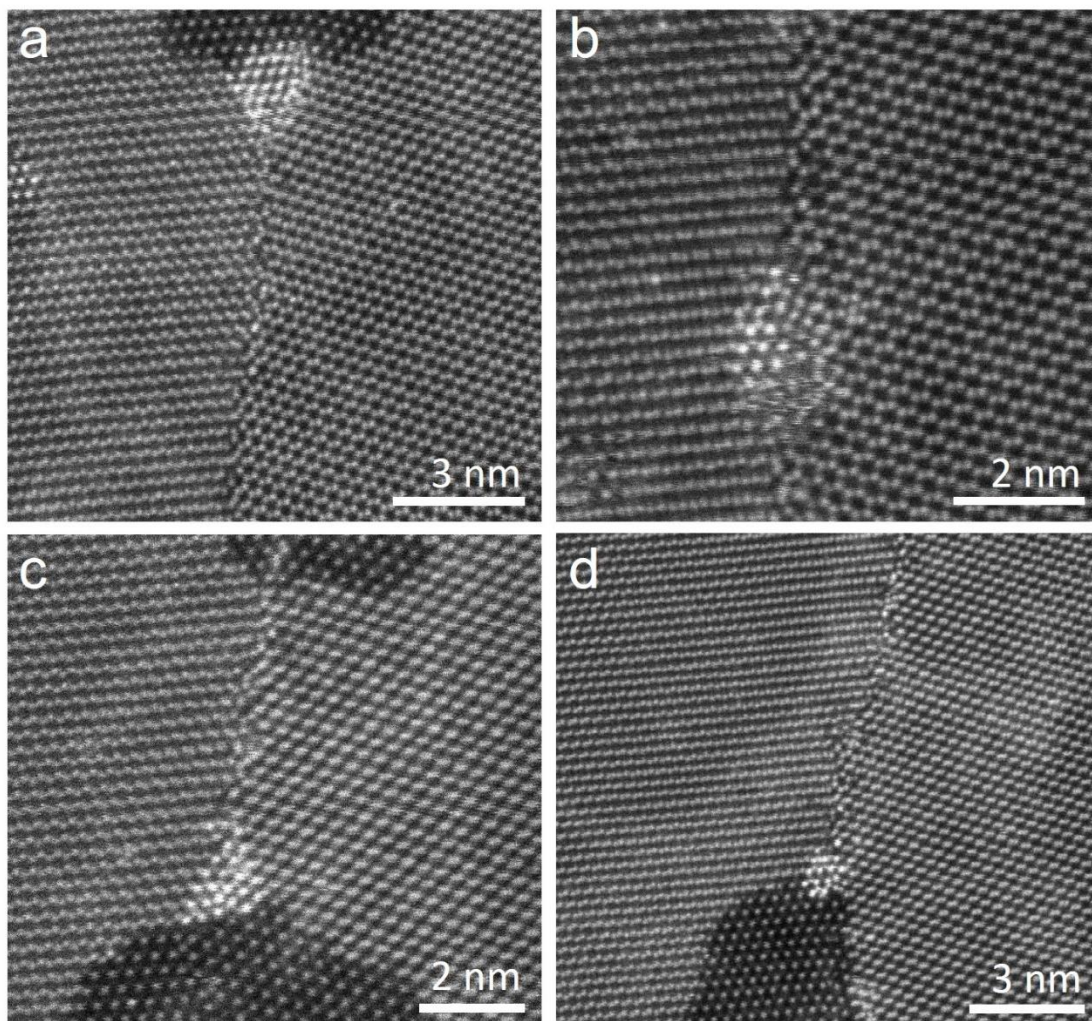


**Figure A23.** Several ADF-STEM images showing the atomically sharp dual GB can be also formed at shifted 2H/2H interface between two bilayers with small-angle lattice orientation difference. (a) and (b) show the same GB pattern. (c) and (d) exhibit more irregular patterns because of the random stitching of atoms from two top layers and the severe lattice translation (especially at the right side of GB shown in c and d) caused by intense local strain at the GB region.

## Appendix B Supporting Information of Chapter 5

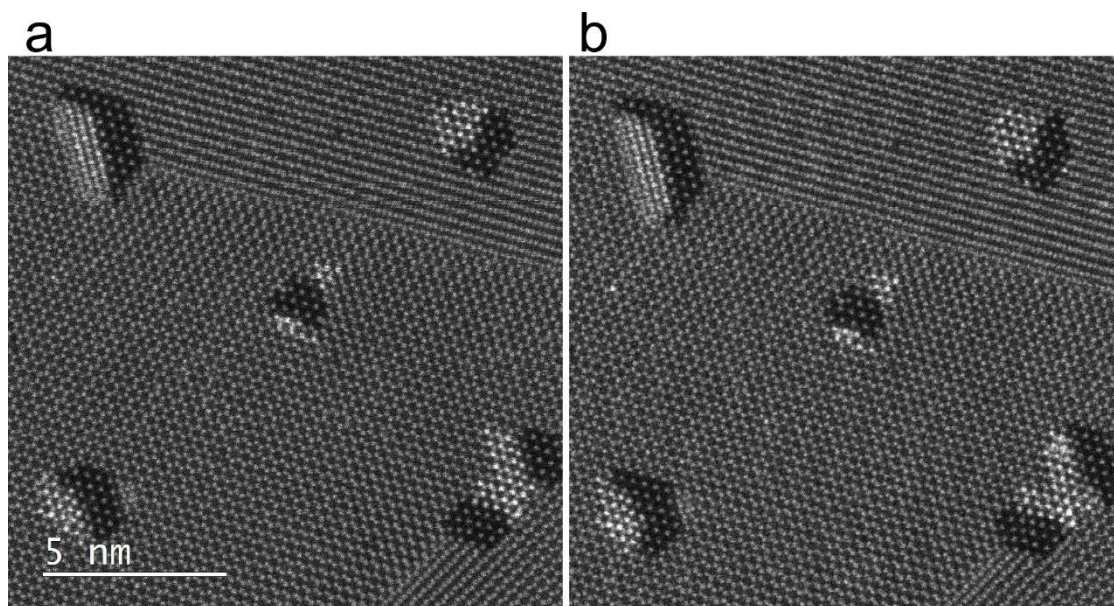


**Figure B1.** Two sequential ADF-STEM images taken of the nanowell array in Figure 5.2f to show the stability.

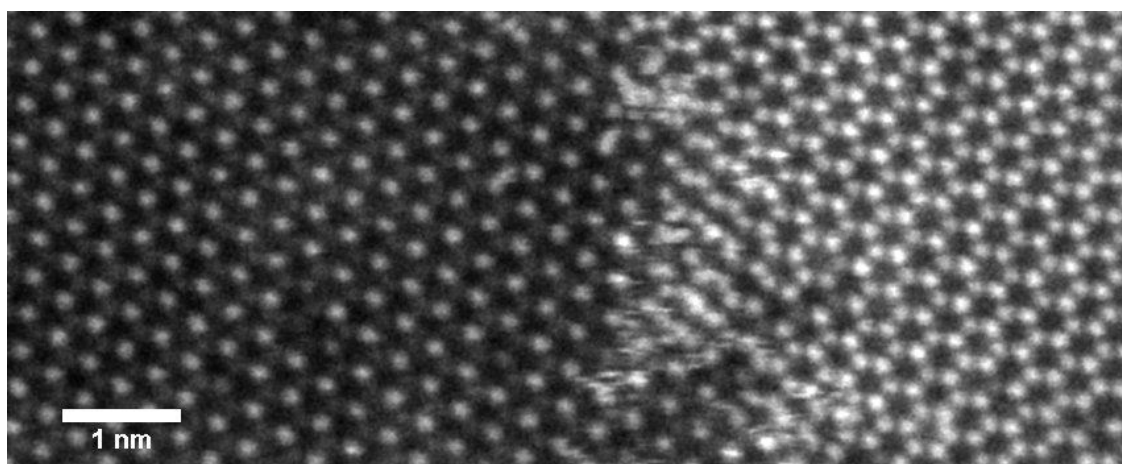


**Figure B2.** ADF-STEM image of the monolayer-bilayer step edge in the WS<sub>2</sub> sample

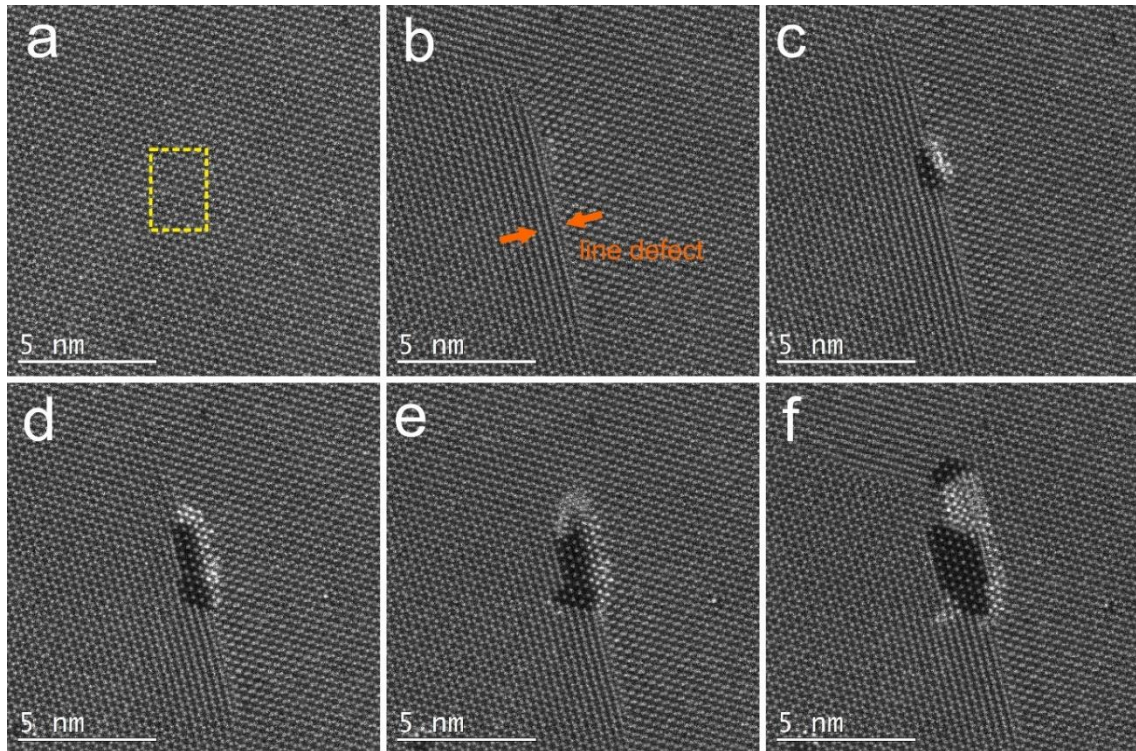


**Figure B3.** ADF-STEM image series showing another example of the formation and evolution of type-I nanowell drilled from bilayer WS<sub>2</sub> at high temperature of 800°C. The images from (a-f) were recorded when drilled every 15s within the fixed boxed region shown in (a). Similar to the typical nanowell in Figure 5.4 in the main article, line defect was firstly developed from the drilled region due to linear aggregation of S vacancies (b), then popping out a ultrasmall nanowell (c), developing reconstructed epitaxial edges (d), and growing in the sizes along the firstly formed S vacancy line when further drilled (f).

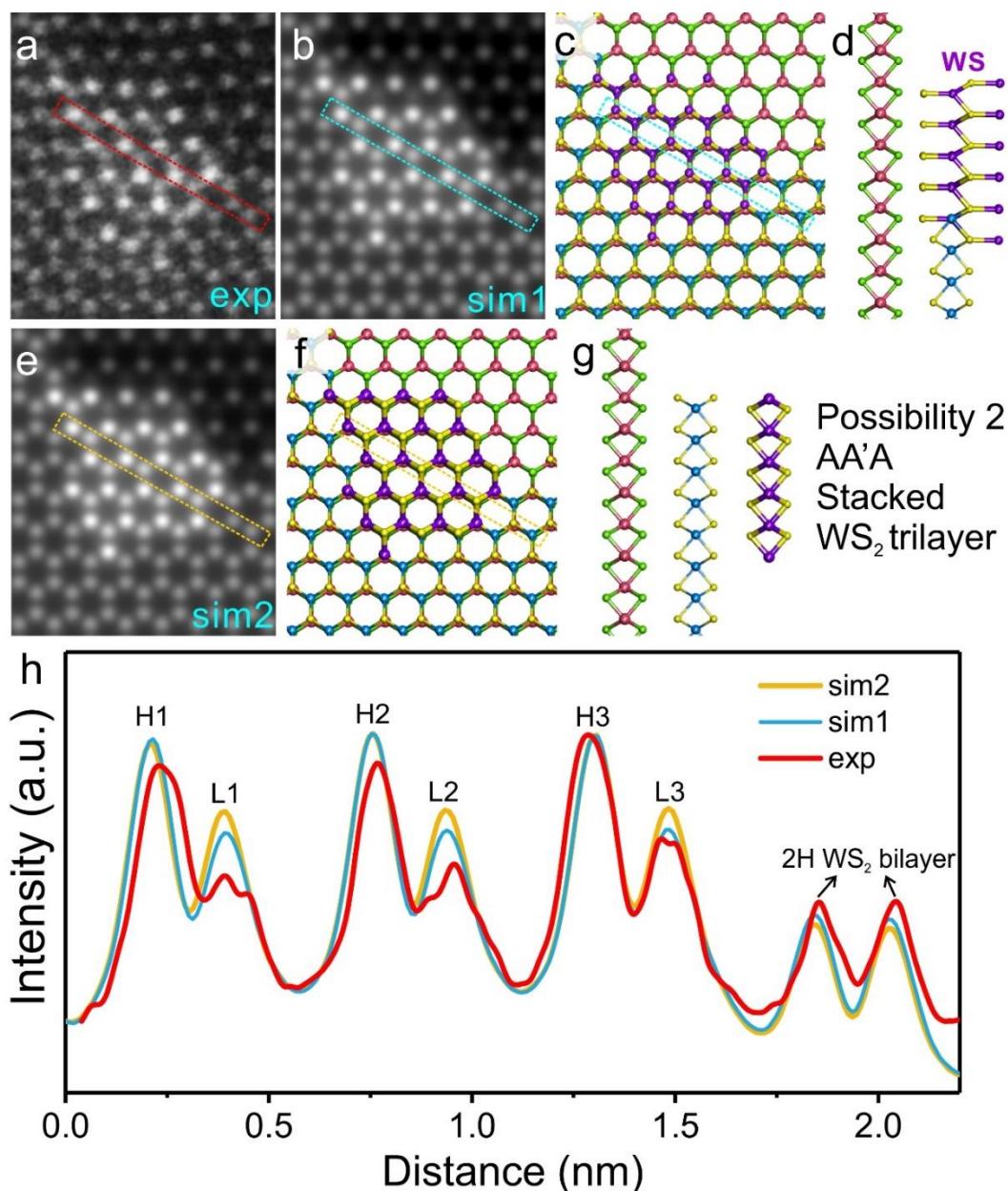


**Figure B4.** Comparison of the two simulations of the two possible configurations of the type-I nanowell edge. (a) Experimental ADF-STEM image. (b-d) Newly formed WS crystal on WS<sub>2</sub>, with (b) simulation, (c) atomic model and (d) its side view. (e-g) Possibility 2: a third layer WS<sub>2</sub> in AA'A stacking, with (e) simulation, (f) atomic model and (g) its side view. (h) Comparison of the intensity line plot profiles obtained from the atom columns marked in (a,b,e). The intensity is normalized using the high peak H3 as a standard. According to the ratios of H/L intensities (high/low peak intensities) in the profile, the simulation-1 which corresponds to WS crystal on WS<sub>2</sub> matches better with the experimental result.

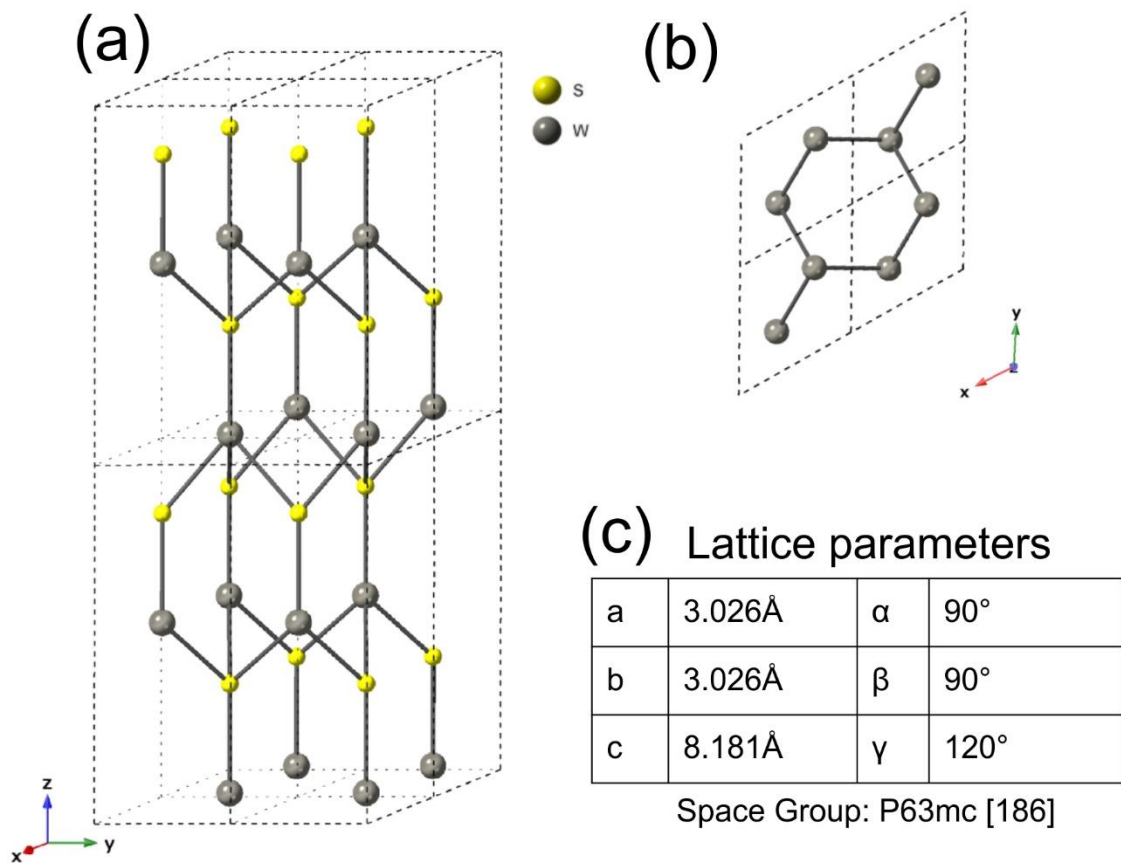


**Figure B5.** (a) 3D atomic model of the WS unit cells ( $2 \times 2 \times 2$ ), which adopts the hexagonal crystal structure. (b) Projection view of the hexagonal WS atomic model from the [001] direction. (c) Table showing the lattice parameters of the WS unit cell.

## Appendix C Supporting Information of Chapter 6

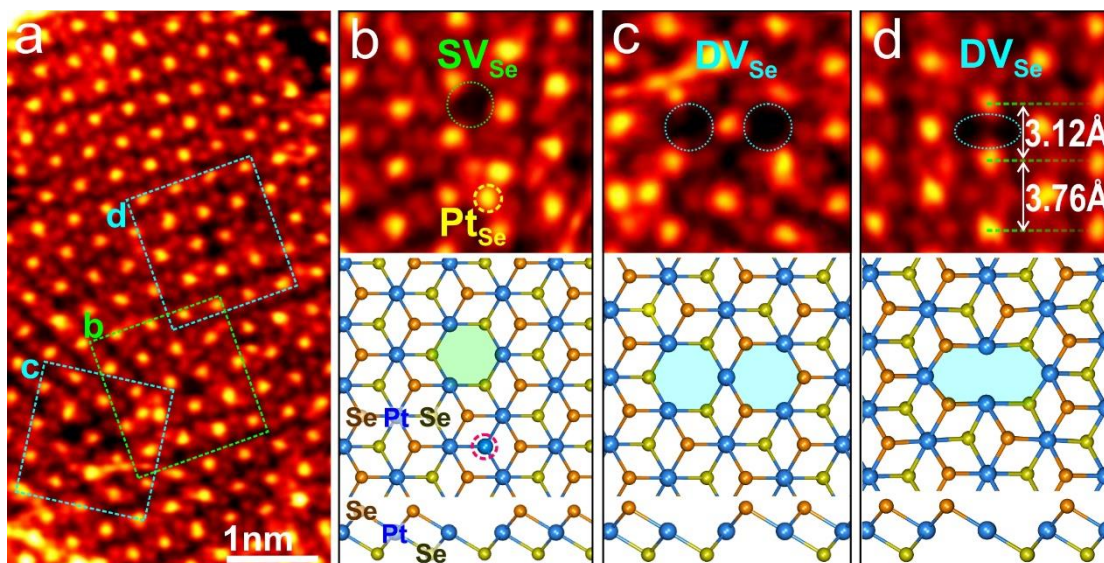


**Figure C1.** Supplementary example showing the point defect structures in monolayer PtSe<sub>2</sub>. (a) ADF-STEM image of monolayer PtSe<sub>2</sub> grain with Se point vacancies ( $V_{Se}$ ). (b-c) Enlarged views of the boxed regions in (a) with corresponding atomic models below showing the lattice structures of single vacancies ( $SV_{Se}$ ) and divacancies ( $DV_{Se}$ ). Pt-Pt spacings across the  $DV_{Se}$  are marked in (d), manifesting the resulted lattice contraction.

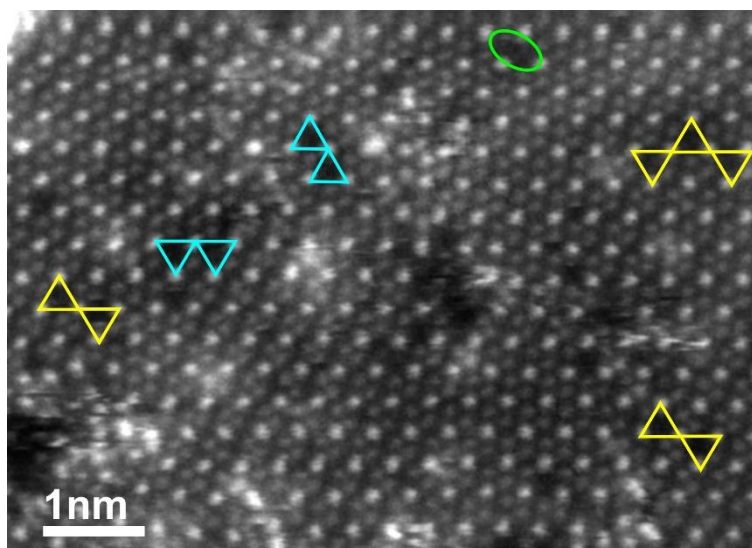


**Figure C2.** ADF-STEM image showing the co-existence of the three types of joint Se vacancy structures in monolayer PtSe<sub>2</sub>. The paired divacancies or tri-vacancies adapting  $DV_{Se-1}$ ,  $DV_{Se-2}$ ,  $DV_{Se-3}$  configurations are marked by green circle, blue triangle, and yellow triangles, respectively.

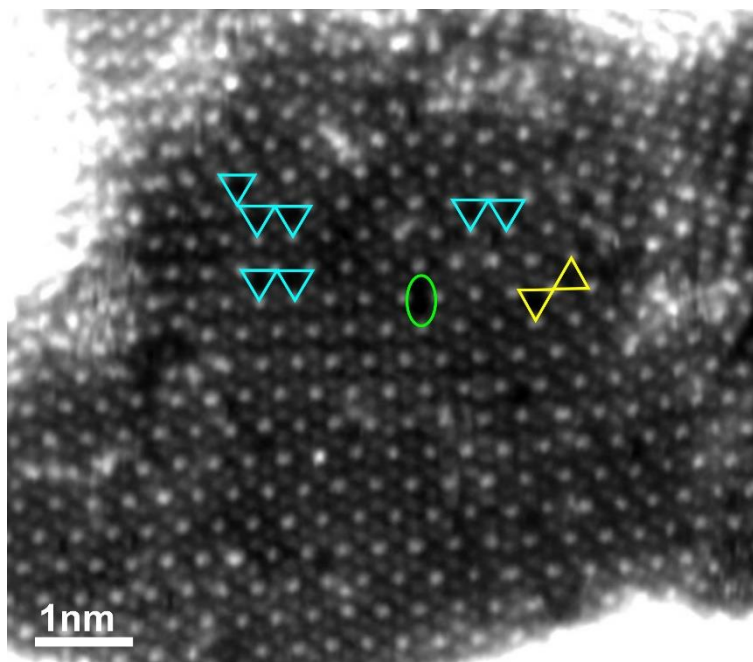


**Figure C3.** Another example of ADF-STEM image showing the co-existence of the three types of divacancies in monolayer PtSe<sub>2</sub>. The paired divacancies or tri-vacancies adapting DV<sub>Se-1</sub>, DV<sub>Se-2</sub>, DV<sub>Se-3</sub> configurations are marked by green circle, blue triangle, and yellow triangles, respectively.

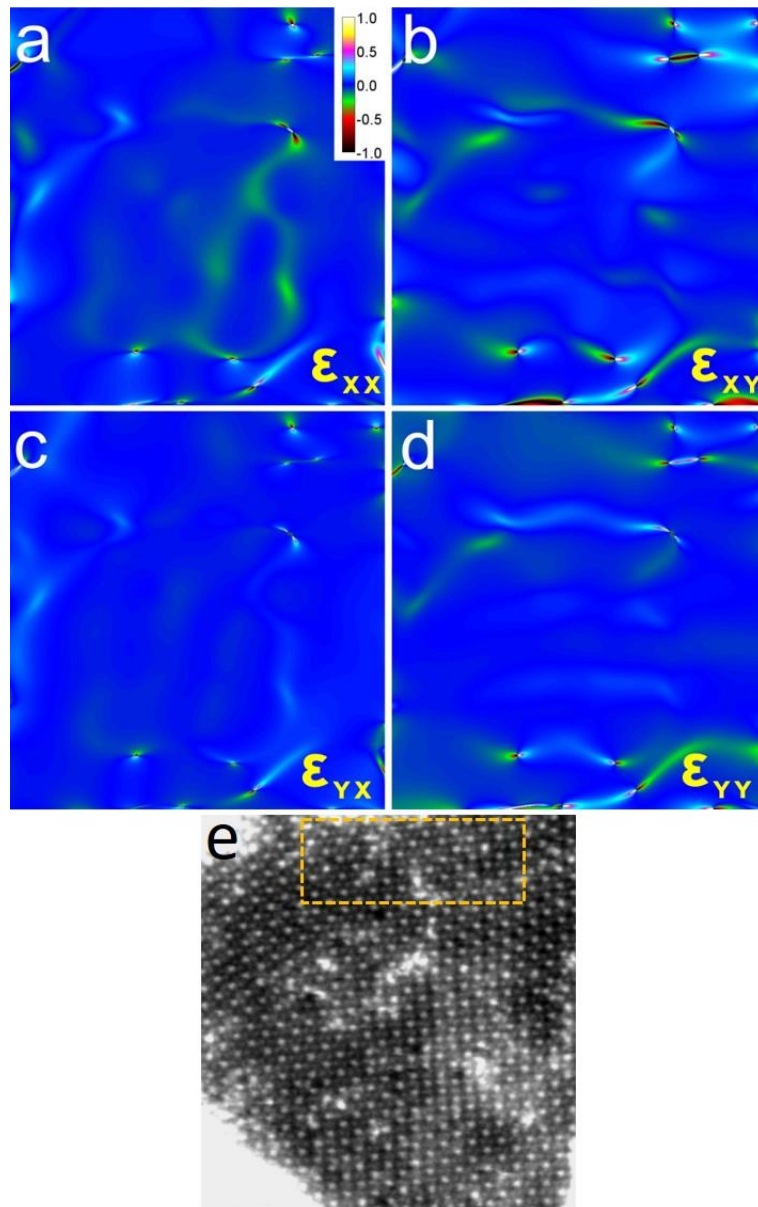


**Figure C4.** Strain components of (a)  $\epsilon_{xx}$ , (b)  $\epsilon_{xy}$ , (c)  $\epsilon_{yx}$  and (d)  $\epsilon_{yy}$  based on geometric phase analysis (GPA) corresponding to the ADF-STEM image in Figure 6.4(a) in the main text.  $\epsilon_{xx}$  and  $\epsilon_{yy}$  manifest the normal compression or tension fields in the  $x$ - $y$  plane.  $\epsilon_{xy}$  and  $\epsilon_{yx}$  indicate the 2D shear strain fields. (e) Corresponding ADF-STEM image, with the dashed rectangle indicating the reference area for GPA analysis.

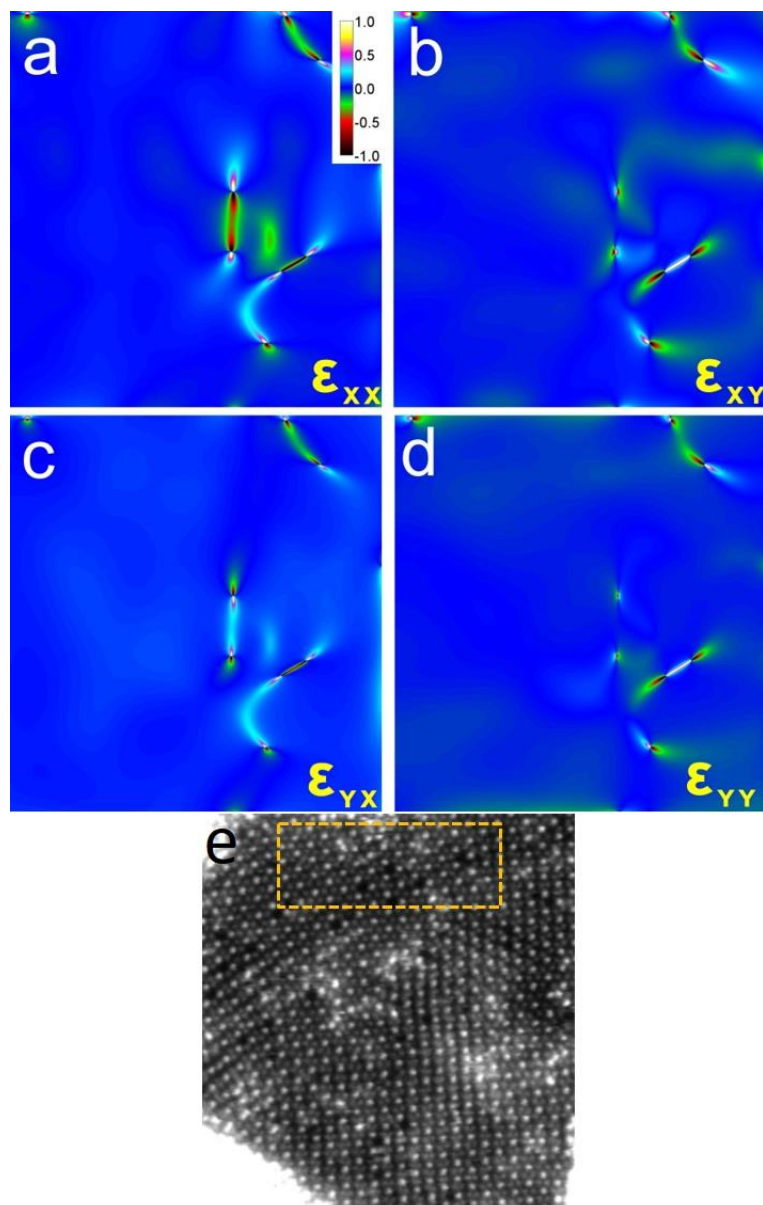


**Figure C5.** Strain components of (a)  $\epsilon_{xx}$ , (b)  $\epsilon_{xy}$ , (c)  $\epsilon_{yx}$  and (d)  $\epsilon_{yy}$  based on GPA corresponding to the ADF-STEM image in Figure 6.4(c) in the main text. (e) Corresponding ADF-STEM image, with the dashed rectangle indicating the reference area for GPA analysis.

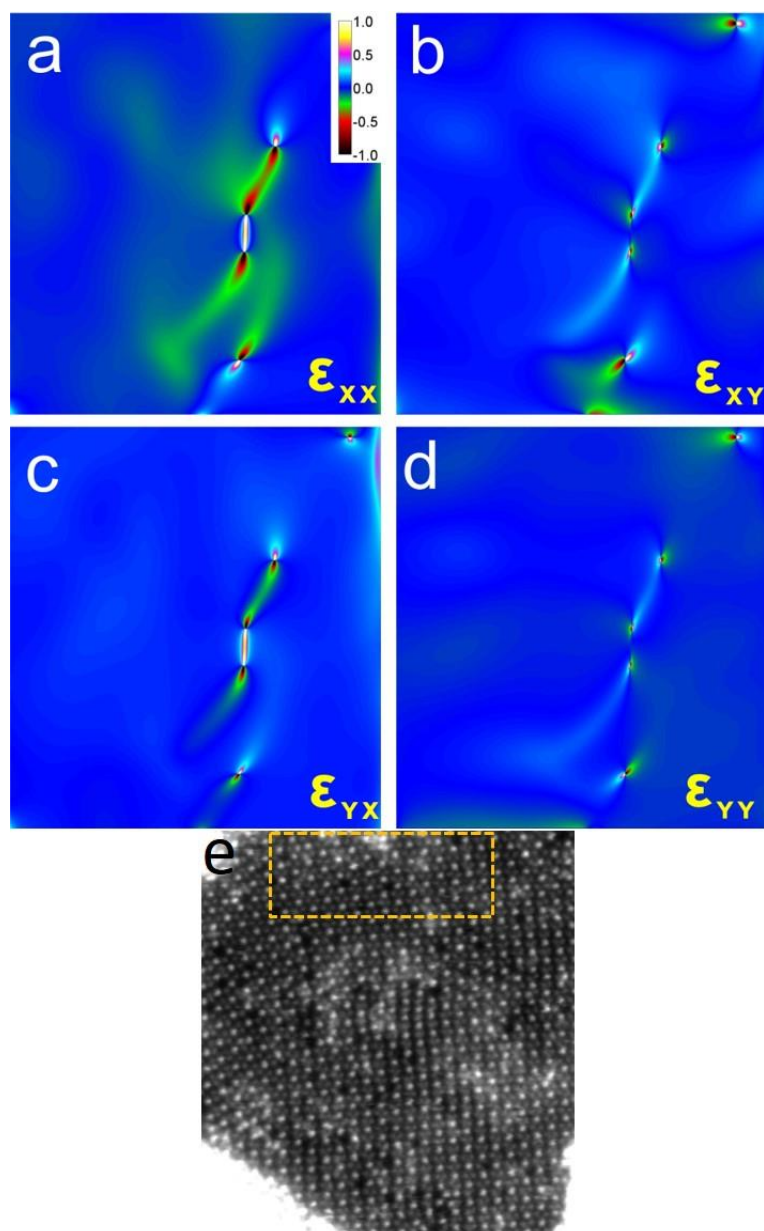


**Figure C6.** Strain components of (a)  $\epsilon_{xx}$ , (b)  $\epsilon_{xy}$ , (c)  $\epsilon_{yx}$  and (d)  $\epsilon_{yy}$  based on GPA corresponding to the ADF-STEM image in Figure 6.4(e) in the main text. (e) Corresponding ADF-STEM image, with the dashed rectangle indicating the reference area for GPA analysis.

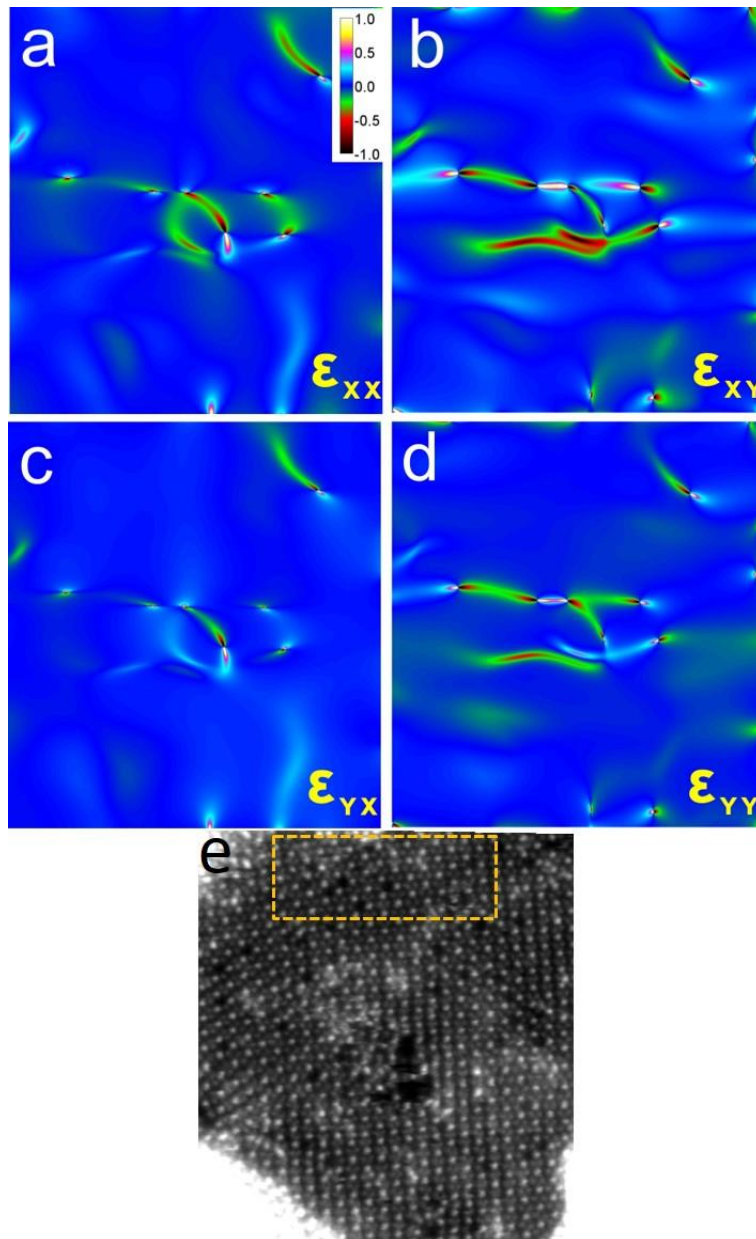


**Figure C7.** Strain components of (a)  $\epsilon_{xx}$ , (b)  $\epsilon_{xy}$ , (c)  $\epsilon_{yx}$  and (d)  $\epsilon_{yy}$  based on GPA corresponding to the ADF-STEM image in Figure 6.4(g) in the main text. (e) Corresponding ADF-STEM image, with the dashed rectangle indicating the reference area for GPA analysis.

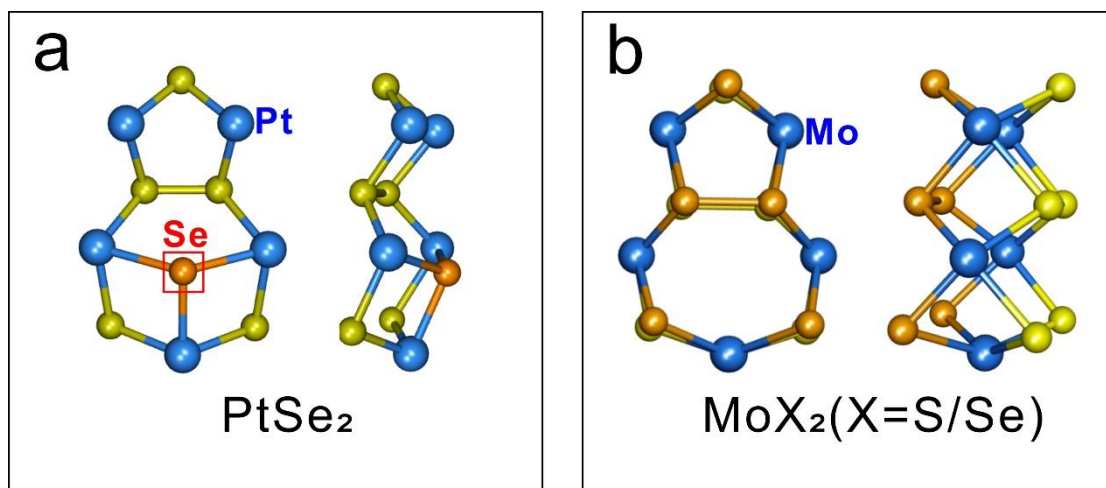


**Figure C8.** Comparison of the  $5\frac{1}{7}_{+Se}$  dislocation in 1T-phase PtSe<sub>2</sub> (a) and the commonly found  $5\frac{1}{7}$  dislocation structure in 2H-phase MoX<sub>2</sub> (b).

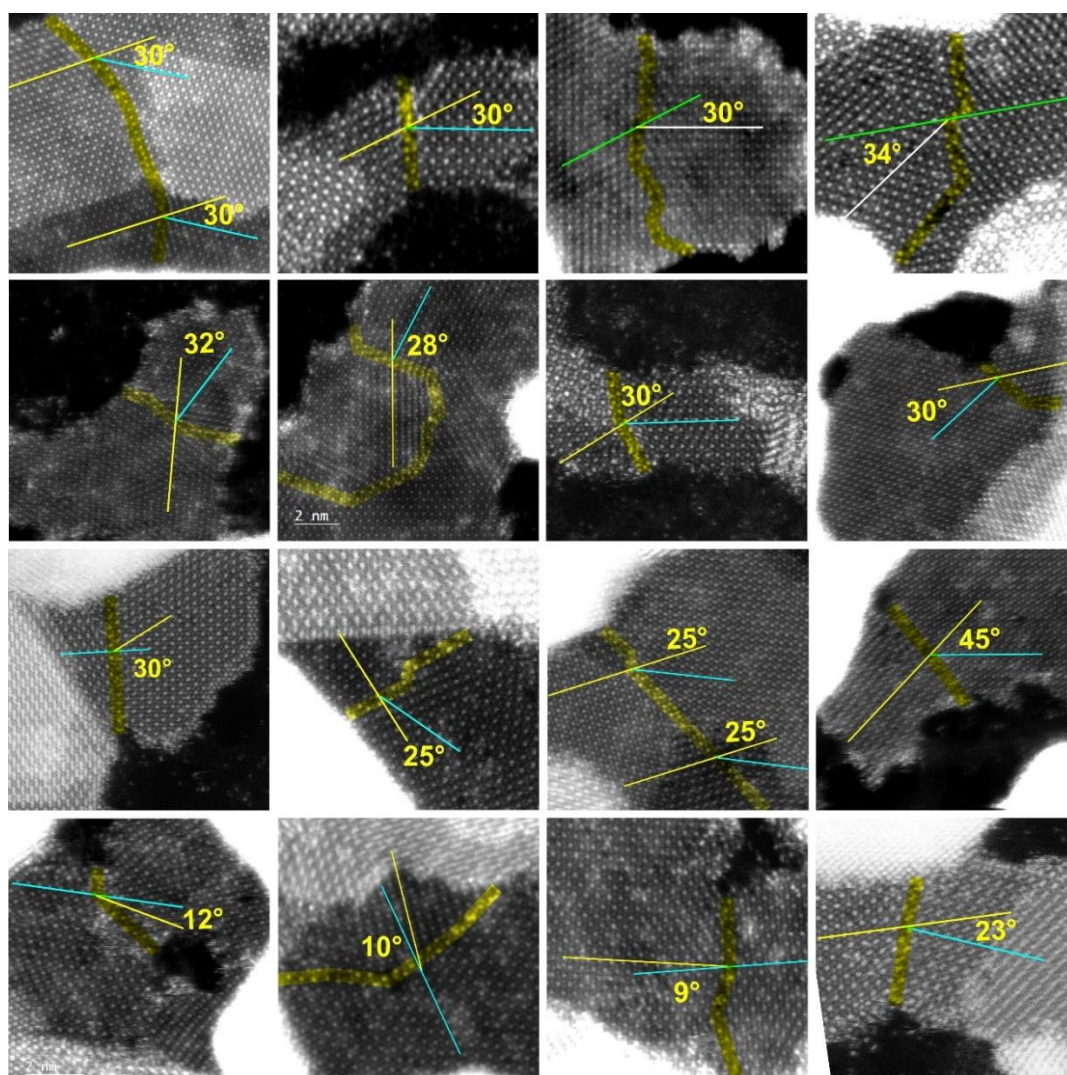


**Figure C9.** ADF-STEM images showing the observed tilt GBs (mirror twin GB not inclusive) in

our PtSe<sub>2</sub> samples grown by selenization method, with marks indicating their misorientation angles.

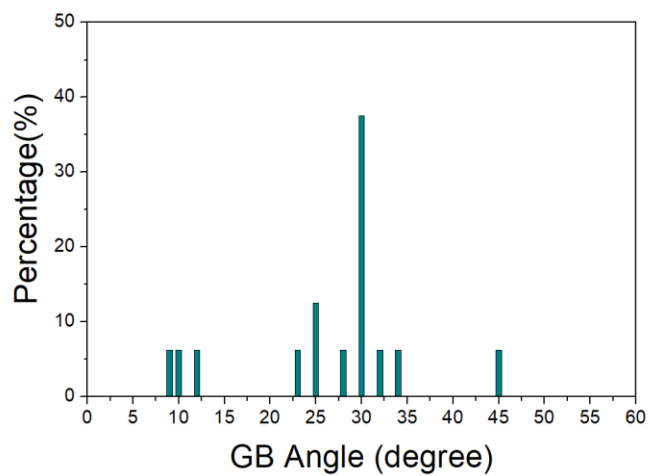


**Figure C10.** Histogram showing the percentages of tilt GB angles in our PtSe<sub>2</sub> sample, measured from the monolayer/bilayer GBs (number of 16 in total)) in Figure C9.

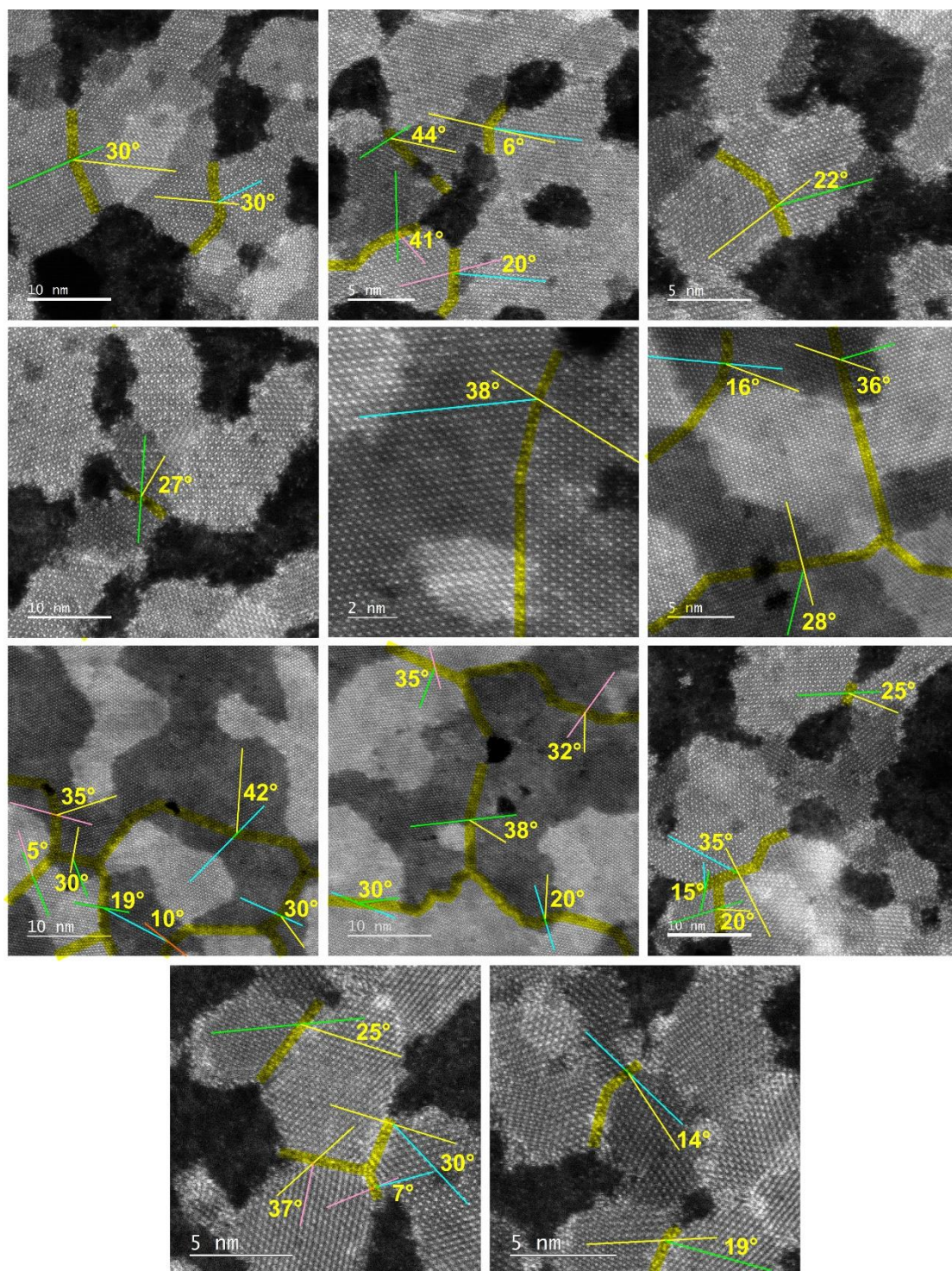


**Figure C11.** ADF-STEM images showing the observed tilt GBs (mirror twin GB not inclusive) in the commercially bought few-layered PtSe<sub>2</sub> samples grown by CVD method, with marks indicating their misorientation angles.

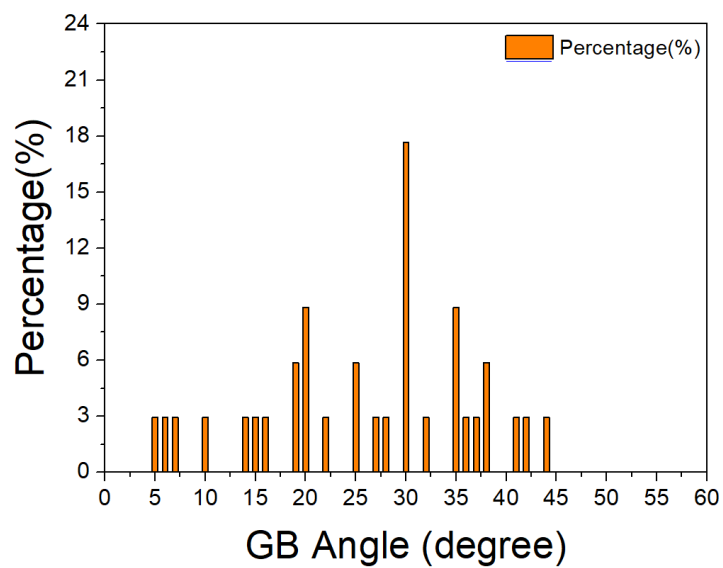


**Figure C12.** Histogram showing the percentages of tilt GB angles in the commercially bought few-layered PtSe<sub>2</sub> sample, measured from the GBs (number of 34 in total) in Figure C11.

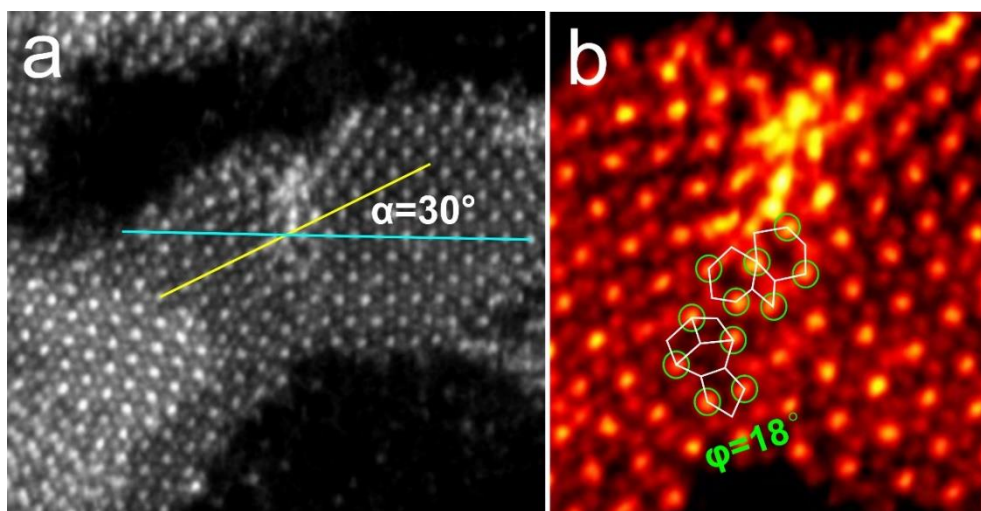


**Figure C13.** ADF-STEM images of a supplementary example showing the GB structure in monolayer PtSe<sub>2</sub> with a tilt angle of 30° and deviation angle of 18°.

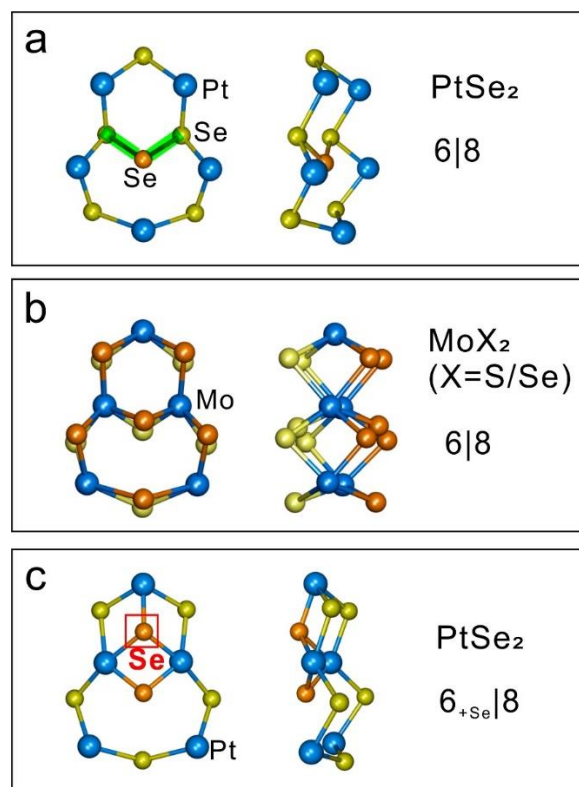


**Figure C14.** Comparison of the  $6|8$  dislocation in (a) 1T-phase PtSe<sub>2</sub> and (b) the commonly found  $6|8$  dislocation structure in 2H-phase MoX<sub>2</sub>, and (c)  $6_{+Se}|8$  dislocation in 1T-phase PtSe<sub>2</sub>. The green shades in (a) highlight the Se–Se bonds in the atomic model. The red box in (c) highlights the different Se positions due to the 1T structural feature compared to (b).

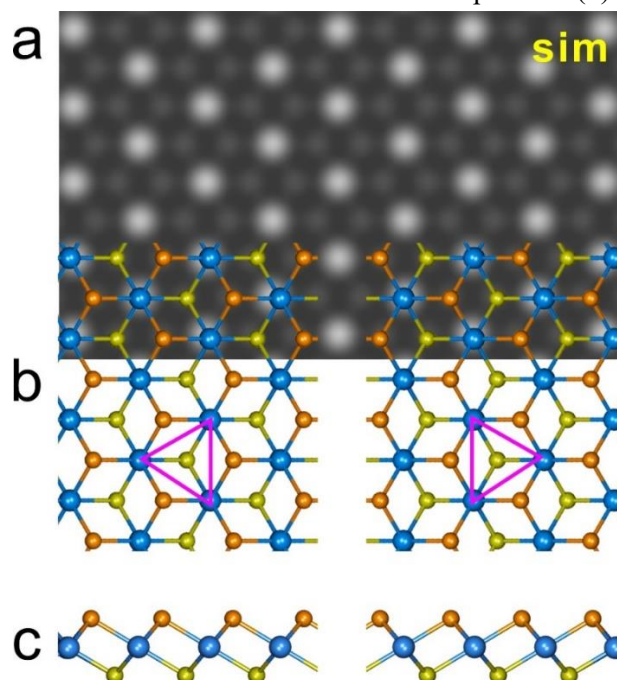


**Figure C15.** Scheme illustrating that the same contrast patterns in ADF-STEM image of the inverted PtSe<sub>2</sub> monolayer grains (*i.e.* rotated by 60°). (a) Multi-slice simulated ADF-STEM image, overlaid by (b) atomic model of two inverted PtSe<sub>2</sub> monolayer grains and (c) their side views.

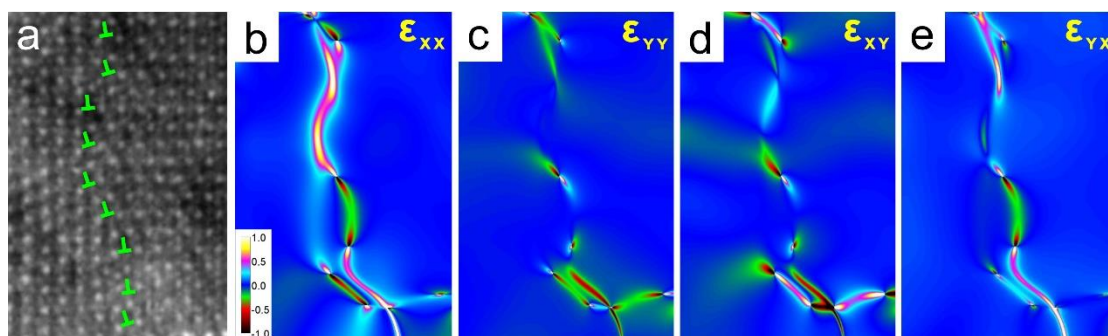


**Figure C16.** Strain components of (b)  $\epsilon_{xx}$  and (c)  $\epsilon_{yy}$  which manifest the normal compression or tension fields in the x–y plane, as well as (d)  $\epsilon_{xy}$  and (e)  $\epsilon_{yx}$  which indicate the 2D shear strain fields, based on geometric phase analysis corresponding to the ADF-STEM image in (a), as the supplementary to 30° GB in Figure 6.11(a-c) in the main text. The elongated linear strain field is mainly shown in the x direction ( $\epsilon_{xx}$ ), while that in the y direction ( $\epsilon_{yy}$ ) is ordered into a few positive–negative dipoles with much less magnitude.

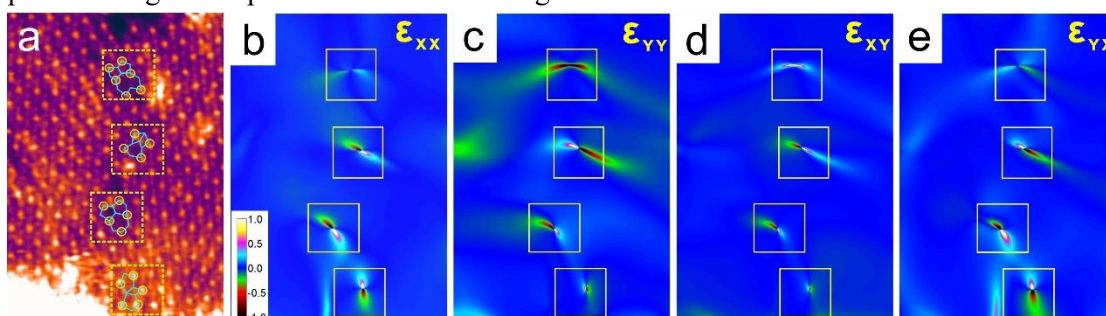


**Figure C17.** Strain components of normal strain fields (b)  $\epsilon_{xx}$  and (c)  $\epsilon_{yy}$  as well as the shear strain fields (d)  $\epsilon_{xy}$  and (e)  $\epsilon_{yx}$ , based on geometric phase analysis corresponding to the ADF-STEM image in (a), as the supplementary to 9.3° GB in Figure 6.11(d-f) in the main text.. All the four strain field components show the dispersed positive–negative dipoles with an approximately balanced magnitude around the dislocation cores along the small-angle GB.

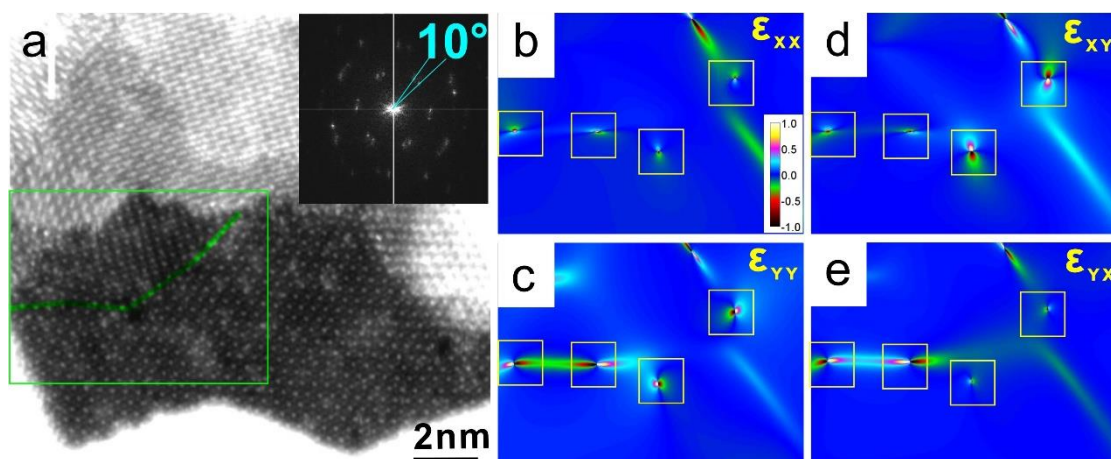


**Figure C18.** Strain components of normal strain fields (b)  $\epsilon_{xx}$  and (c)  $\epsilon_{yy}$  as well as the shear strain fields (d)  $\epsilon_{xy}$  and (e)  $\epsilon_{yx}$ , based on geometric phase (GPA) analysis corresponding to the green boxed region in (a), as the supplementary to 10° GB in Figure 6.11(g,h) in the main text. All the four strain field components show the dispersed positive–negative dipoles with an approximately balanced magnitude around the dislocation cores along the small-angle GB.

## Appendix D Supporting Information of Chapter 7

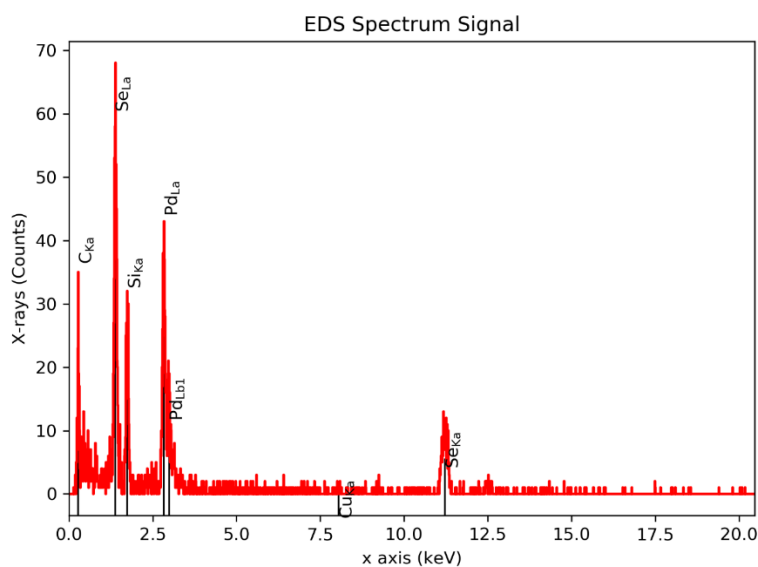


**Figure D1.** Energy-dispersive X-ray spectroscopy (EDS) spectrum of the obtained Pd<sub>2</sub>Se<sub>3</sub>

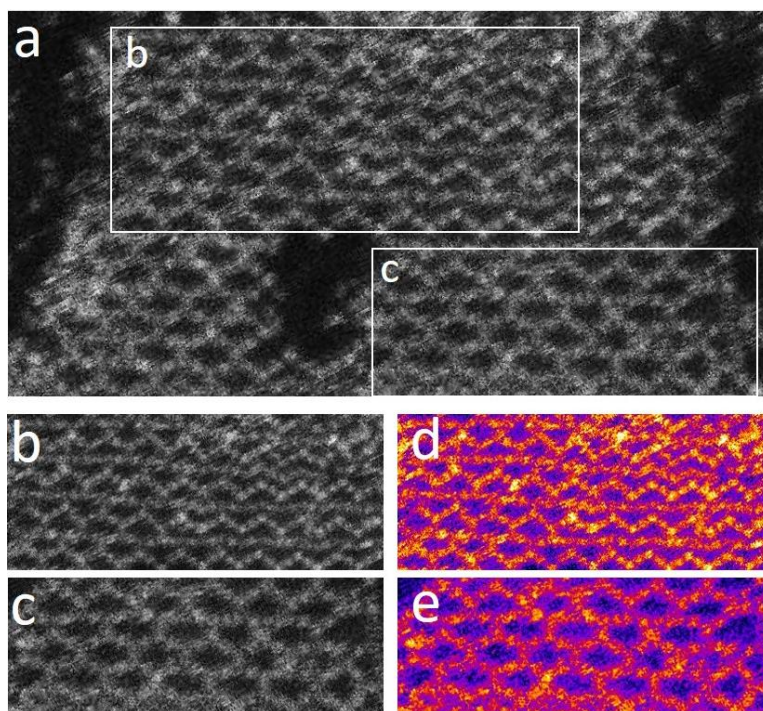


**Figure D2.** (a) ADF-STEM image showing the two basic structures coexist at a monolayer Pd<sub>2</sub>Se<sub>3</sub>. (b,c) Enlarged views from boxed regions in (a), (b) the triangular-shaped structure with straight lines, and (c) pristine structures. (d,e) Coloured (b,c) respectively with fire effect to increase the visual impact.

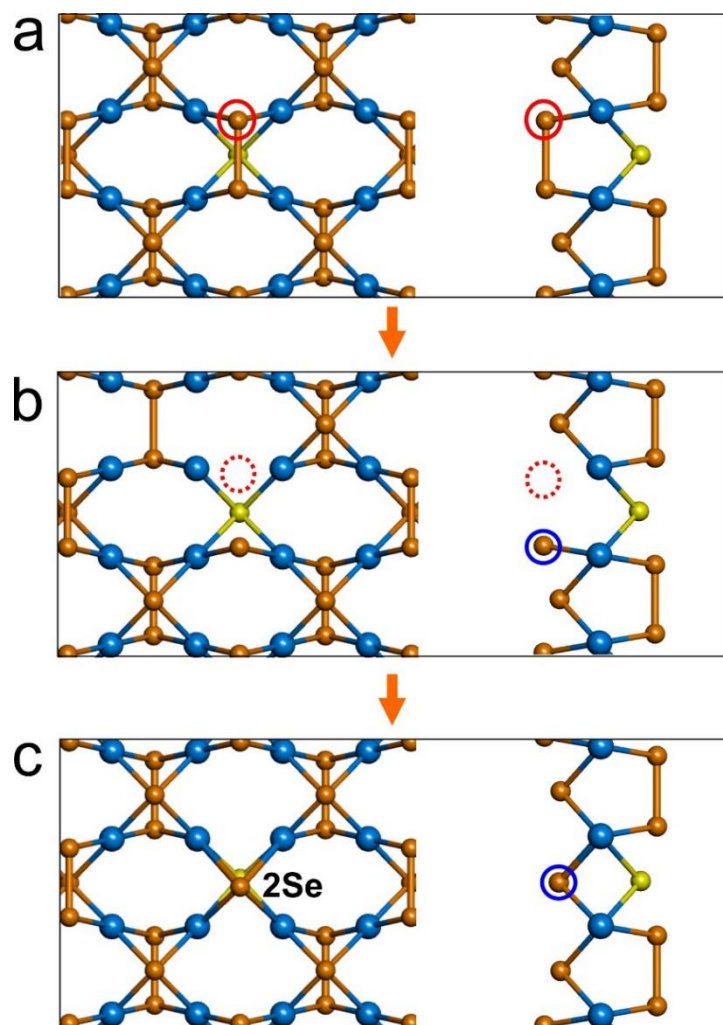


**Figure D3.** Schematic illustration of the detailed formation mechanism of the cross-shape point defect caused by Se vacancies. The right panels in (a-c) are corresponding side views of the atomic models.

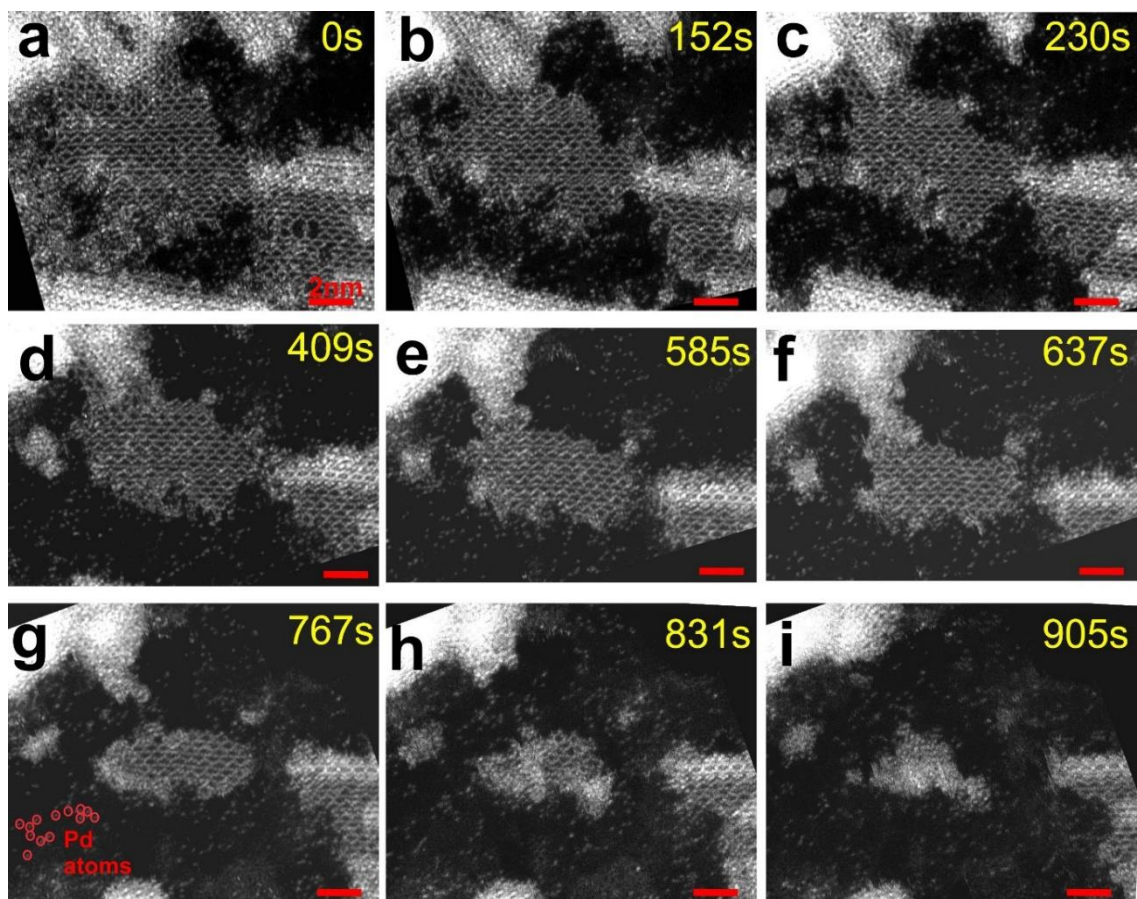


**Figure D4** (a-i) Time series of ADF-STEM image sequence within the duration of around 15 min, showing the dynamical process of a monolayer  $\text{Pd}_2\text{Se}_3$  when continuously irradiated by electron beam of 80 keV. The beam has induced the formation of numerous Se vacancies with the lost Se atoms popped into the vacuum. At the same time, the Pd atoms have diffused away from the edge and randomly dispersed as single atoms sticking onto the carbon substrate, or developed small amorphous metal clusters as a large number of Pd atoms accumulated.

## References

- (1) Radisavljevic, B.; Radenovic, A.; Brivio, J.; Giacometti, i. V.; Kis, A., Single-Layer MoS<sub>2</sub> Transistors. *Nat. Nanotechnol.* **2011**, *6*, 147-150.
- (2) Wang, Q. H.; Kalantar-Zadeh, K.; Kis, A.; Coleman, J. N.; Strano, M. S., Electronics and Optoelectronics of Two-Dimensional Transition Metal Dichalcogenides. *Nat. Nanotechnol.* **2012**, *7*, 699-172.
- (3) Manzeli, S.; Ovchinnikov, D.; Pasquier, D.; Yazyev, O. V.; Kis, A., 2D Transition Metal Dichalcogenides. *Nat. Rev. Mater.* **2017**, *2*, 17033.
- (4) Lin, Y.-C.; Li, S.; Komsa, H.-P.; Chang, L.-J.; Krasheninnikov, A. V.; Eda, G.; Suenaga, K., Revealing the Atomic Defects of WS<sub>2</sub> Governing Its Distinct Optical Emissions. *Adv. Funct. Mater.* **2018**, *28*.
- (5) Rhodes, D.; Chae, S. H.; Ribeiro-Palau, R.; Hone, J., Disorder in van der Waals heterostructures of 2D materials. *Nat. Mater.* **2019**, *18*, 541-549.
- (6) Kastl, C.; Koch, R. J.; Chen, C. T.; Eichhorn, J.; Ulstrup, S.; Bostwick, A.; Jozwiak, C.; Kuykendall, T. R.; Borys, N. J.; Toma, F. M.; Aloni, S.; Weber-Bargioni, A.; Rotenberg, E.; Schwartzberg, A. M., Effects of Defects on Band Structure and Excitons in WS<sub>2</sub> Revealed by Nanoscale Photoemission Spectroscopy. *ACS Nano* **2019**, *13*, 1284-1291.
- (7) Bonaccorso, F.; Colombo, L.; Yu, G.; Stoller, M.; Tozzini, V.; Ferrari, A. C.; Ruoff, R. S.; Pellegrini, V., Graphene, Related Two-Dimensional Crystals, and Hybrid Systems for Energy Conversion and Storage. *Science* **2015**, *347*, 1246501.
- (8) Novoselov, K. S.; Geim, A. K.; Morozov, S. V.; Jiang, D.; Zhang, Y.; Dubonos, S. V.; Grigorieva, I. V.; Firsov, A. A., Electric Field Effect in Atomically Thin Carbon Films. *Science* **2004**, *306*, 666-669.
- (9) Bhimanapati, G. R.; Lin, Z.; Meunier, V.; Jung, Y.; Cha, J.; Das, S.; Xiao, D.; Son, Y.; Strano, M. S.; Cooper, V. R., Recent Advances in Two-Dimensional Materials Beyond Graphene. *ACS Nano* **2015**, *9*, 11509-11539.
- (10) Wan, J.; Lacey, S. D.; Dai, J.; Bao, W.; Fuhrer, M. S.; Hu, L., Tuning Two-Dimensional Nanomaterials by Intercalation: Materials, Properties and Applications. *Chem. Soc. Rev.* **2016**, *45*, 6742-6765.
- (11) Stampfer, B.; Zhang, F.; Illarionov, Y. Y.; Knobloch, T.; Wu, P.; Walzl, M.; Grill, A.; Appenzeller, J.; Grasser, T., Characterization of Single Defects in Ultrascaled MoS<sub>2</sub> Field-Effect Transistors. *ACS Nano* **2018**, *12*, 5368-5375.
- (12) Li, H.; Yin, Z.; He, Q.; Li, H.; Huang, X.; Lu, G.; Fam, D. W. H.; Tok, A. I. Y.; Zhang, Q.; Zhang, H., Fabrication of Single- and Multilayer MoS<sub>2</sub> Film-Based Field-Effect Transistors for Sensing NO at Room Temperature. *Small* **2012**, *8*, 63-67.
- (13) Perea-López, N.; Elías, A. L.; Berkdemir, A.; Castro-Beltran, A.; Gutiérrez, H. R.; Feng, S.; Lv, R.; Hayashi, T.; López-Urías, F.; Ghosh, S.; Muchharla, B.; Talapatra, S.; Terrones, H.; Terrones, M., Photosensor Device Based on Few-Layered WS<sub>2</sub> Films. *Adv. Funct. Mater.* **2013**, *23*, 5511-5517.
- (14) Wang, H.; Li, C.; Fang, P.; Zhang, Z.; Zhang, J. Z., Synthesis, Properties, and Optoelectronic Applications of Two-Dimensional MoS<sub>2</sub> and MoS<sub>2</sub>-Based Heterostructures. *Chem. Soc. Rev.* **2018**, *47*, 6101-6127.
- (15) Liu, Z.; Lau, S. P.; Yan, F., Functionalized Graphene and Other Two-Dimensional Materials for Photovoltaic Devices: Device Design and Processing. *Chem. Soc. Rev.* **2015**, *44*, 5638-5679.

- (16) Tan, H.; Fan, Y.; Zhou, Y.; Chen, Q.; Xu, W.; Warner, J. H., Ultrathin 2D Photodetectors Utilizing Chemical Vapor Deposition Grown WS<sub>2</sub> with Graphene Electrodes. *ACS Nano* **2016**, *10*, 7866-7873.
- (17) Wang, S.; Pacios, M.; Bhaskaran, H.; Warner, J. H., Substrate Control for Large Area Continuous Films of Monolayer MoS<sub>2</sub> by Atmospheric Pressure Chemical Vapor Deposition. *Nanotechnology* **2016**, *27*, 085604.
- (18) Kappera, R.; Voiry, D.; Yalcin, S. E.; Branch, B.; Gupta, G.; Mohite, A. D.; Chhowalla, M., Phase-Engineered Low-Resistance Contacts for Ultrathin MoS<sub>2</sub> Transistors. *Nat. Mater.* **2014**, *13*, 1128–1134.
- (19) Lee, J.; Mak, K. F.; Shan, J., Electrical Control of the Valley Hall Effect in Bilayer MoS<sub>2</sub> Transistors. *Nat. Nanotechnol.* **2016**, *11*, 421.
- (20) Lee, C.; Wei, X.; Kysar, J. W.; Hone, J., Measurement of the Elastic Properties and Intrinsic Strength of Monolayer Graphene. *Science* **2008**, *321*, 385-388.
- (21) Nair, R. R.; Blake, P.; Grigorenko, A. N.; Novoselov, K. S.; Booth, T. J.; Stauber, T.; Peres, N. M.; Geim, A. K., Fine Structure Constant Defines Visual Transparency of Graphene. *Science* **2008**, *320*, 1308-1308.
- (22) Ghosh, S.; Bao, W.; Nika, D. L.; Subrina, S.; Pokatilov, E. P.; Lau, C. N.; Balandin, A. A., Dimensional Crossover of Thermal Transport in Few-Layer Graphene. *Nat. Mater.* **2010**, *9*, 555.
- (23) Tan, C.; Cao, X.; Wu, X.-J.; He, Q.; Yang, J.; Zhang, X.; Chen, J.; Zhao, W.; Han, S.; Nam, G.-H., Recent Advances in Ultrathin Two-Dimensional Nanomaterials. *Chem. Rev.* **2017**, *117*, 6225-6331.
- (24) Blake, P.; Brimicombe, P. D.; Nair, R. R.; Booth, T. J.; Jiang, D.; Schedin, F.; Ponomarenko, L. A.; Morozov, S. V.; Gleeson, H. F.; Hill, E. W., Graphene-Based Liquid Crystal Device. *Nano Lett.* **2008**, *8*, 1704-1708.
- (25) Das, S., Graphene: A Cathode Material of Choice for Aluminium-Ion Battery. *Angew. Chem. Int. Ed.* **2018**, *57*, 16606-16617.
- (26) Chen, H.; Xu, H.; Wang, S.; Huang, T.; Xi, J.; Cai, S.; Guo, F.; Xu, Z.; Gao, W.; Gao, C., Ultrafast All-Climate Aluminum-Graphene Battery with Quarter-Million Cycle Life. *Sci. Adv.* **2017**, *3*, eaao7233.
- (27) Li, Y.; Yan, K.; Lee, H.-W.; Lu, Z.; Liu, N.; Cui, Y., Growth of Conformal Graphene Cages on Micrometre-Sized Silicon Particles as Stable Battery Anodes. *Nat. Energy* **2016**, *1*, 15029.
- (28) Mendoza-Sanchez, B.; Gogotsi, Y., Synthesis of Two-Dimensional Materials for Capacitive Energy Storage. *Adv. Mater.* **2016**, *28*, 6104-35.
- (29) Miró, P.; Audiffred, M.; Heine, T., An Atlas of Two-Dimensional Materials. *Chem. Soc. Rev.* **2014**, *43*, 6537-6554.
- (30) Liu, G.; Debnath, B.; Pope, T. R.; Salguero, T. T.; Lake, R. K.; Balandin, A. A., A Charge-Density-Wave Oscillator Based on An Integrated Tantalum Disulfide–Boron Nitride–Graphene Device Operating at Room Temperature. *Nat. Nanotechnol.* **2016**, *11*, 845.
- (31) Duan, X.; Wang, C.; Pan, A.; Yu, R.; Duan, X., Two-Dimensional Transition Metal Dichalcogenides as Atomically Thin Semiconductors: Opportunities and Challenges. *Chem. Soc. Rev.* **2015**, *44*, 8859-8876.
- (32) Zhou, J.; Lin, J.; Huang, X.; Zhou, Y.; Chen, Y.; Xia, J.; Wang, H.; Xie, Y.; Yu, H.; Lei, J.; Wu, D.; Liu, F.; Fu, Q.; Zeng, Q.; Hsu, C. H.; Yang, C.; Lu, L.; Yu, T.; Shen, Z.; Lin, H.; Yakobson, B. I.; Liu, Q.; Suenaga, K.; Liu, G.; Liu, Z., A Library of Atomically Thin Metal Chalcogenides. *Nature* **2018**, *556*, 355-359.
- (33) Shi, Y.; Zhou, W.; Lu, A.-Y.; Fang, W.; Lee, Y.-H.; Hsu, A. L.; Kim, S. M.; Kim, K. K.; Yang,

- H. Y.; Li, L.-J.; Idrobo, J.-C.; Kong, J., Van Der Waals Epitaxy of MoS<sub>2</sub> Layers Using Graphene as Growth Templates. *Nano Lett.* **2012**, *12*, 2784-2791.
- (34) Shi, Y.; Li, H.; Li, L.-J., Recent Advances in Controlled Synthesis of Two-Dimensional Transition Metal Dichalcogenides *via* Vapour Deposition Techniques. *Chem. Soc. Rev.* **2015**, *44*, 2744-2756.
- (35) Chen, J.; Tang, W.; Tian, B.; Liu, B.; Zhao, X.; Liu, Y.; Ren, T.; Liu, W.; Geng, D.; Jeong, H. Y.; Shin, H. S.; Zhou, W.; Loh, K. P., Chemical Vapor Deposition of High-Quality Large-Sized MoS<sub>2</sub> Crystals on Silicon Dioxide Substrates. *Adv. Sci.* **2016**, *3*, 1500033.
- (36) Sheng, Y.; Tan, H.; Wang, X.; Warner, J. H., Hydrogen Addition for Centimeter-Sized Monolayer Tungsten Disulfide Continuous Films by Ambient Pressure Chemical Vapor Deposition. *Chem. Mater.* **2017**, *29*, 4904-4911.
- (37) Cai, L.; Shearer, M. J.; Zhao, Y.; Hu, Z.; Wang, F.; Zhang, Y.; Eliceiri, K. W.; Hamers, R. J.; Yan, W.; Wei, S.; Tang, M.; Jin, S., Chemically Derived Kirigami of WSe<sub>2</sub>. *J. Am. Chem. Soc.* **2018**, *140*, 10980-10987.
- (38) Zhao, B.; Dang, W.; Liu, Y.; Li, B.; Li, J.; Luo, J.; Zhang, Z.; Wu, R.; Ma, H.; Sun, G.; Huang, Y.; Duan, X.; Duan, X., Synthetic Control of Two-Dimensional NiTe<sub>2</sub> Single Crystals with Highly Uniform Thickness Distributions. *J. Am. Chem. Soc.* **2018**, *140*, 14217-14223.
- (39) Shao, G.; Xue, X.-X.; Zhou, X.; Xu, J.; Jin, Y.; Qi, S.; Liu, N.; Duan, H.; Wang, S.; Li, S.; Ouzounian, M.; Hu, T. S.; Luo, J.; Liu, S.; Feng, Y., Shape-Engineered Synthesis of Atomically Thin 1T-SnS<sub>2</sub> Catalyzed by Potassium Halides. *ACS Nano* **2019**, *13*, 8265-8274.
- (40) Lee, Y.-H.; Zhang, X.-Q.; Zhang, W.; Chang, M.-T.; Lin, C.-T.; Chang, K.-D.; Yu, Y.-C.; Wang, J. T.-W.; Chang, C.-S.; Li, L.-J.; Lin, T.-W., Synthesis of Large-Area MoS<sub>2</sub> Atomic Layers with Chemical Vapor Deposition. *Adv. Mater.* **2012**, *24*, 2320-2325.
- (41) Wang, S.; Rong, Y.; Fan, Y.; Pacios, M.; Bhaskaran, H.; He, K.; Warner, J. H., Shape Evolution of Monolayer MoS<sub>2</sub> Crystals Grown by Chemical Vapor Deposition. *Chem. Mater.* **2014**, *26*, 6371-6379.
- (42) Schmidt, H.; Wang, S.; Chu, L.; Toh, M.; Kumar, R.; Zhao, W.; Castro Neto, A. H.; Martin, J.; Adam, S.; Özyilmaz, B.; Eda, G., Transport Properties of Monolayer MoS<sub>2</sub> Grown by Chemical Vapor Deposition. *Nano Lett.* **2014**, *14*, 1909-1913.
- (43) Wang, X.; Gong, Y.; Shi, G.; Chow, W. L.; Keyshar, K.; Ye, G.; Vajtai, R.; Lou, J.; Liu, Z.; Ringe, E.; Tay, B. K.; Ajayan, P. M., Chemical Vapor Deposition Growth of Crystalline Monolayer MoSe<sub>2</sub>. *ACS Nano* **2014**, *8*, 5125-5131.
- (44) Cong, C.; Shang, J.; Wu, X.; Cao, B.; Peimyoo, N.; Qiu, C.; Sun, L.; Yu, T., Synthesis and Optical Properties of Large-Area Single-Crystalline 2D Semiconductor WS<sub>2</sub> Monolayer from Chemical Vapor Deposition. *Advanced Optical Materials* **2014**, *2*, 131-136.
- (45) Keyshar, K.; Gong, Y.; Ye, G.; Brunetto, G.; Zhou, W.; Cole, D. P.; Hackenberg, K.; He, Y.; Machado, L.; Kabbani, M.; Hart, A. H. C.; Li, B.; Galvao, D. S.; George, A.; Vajtai, R.; Tiwary, C. S.; Ajayan, P. M., Chemical Vapor Deposition of Monolayer Rhenium Disulfide (ReS<sub>2</sub>). *Adv. Mater.* **2015**, *27*, 4640-4648.
- (46) Wang, X.; Wang, P.; Wang, J.; Hu, W.; Zhou, X.; Guo, N.; Huang, H.; Sun, S.; Shen, H.; Lin, T., Ultrasensitive and Broadband MoS<sub>2</sub> Photodetector Driven by Ferroelectrics. *Adv. Mater.* **2015**, *27*, 6575-6581.
- (47) Qin, J. K.; Qiu, G.; He, W.; Jian, J.; Si, M. W.; Duan, Y. Q.; Charnas, A.; Zemlyanov, D. Y.; Wang, H. Y.; Shao, W. Z.; Zhen, L.; Xu, C. Y.; Ye, P. D., Epitaxial Growth of 1D Atomic Chain Based Se Nanoplates on Monolayer ReS<sub>2</sub> for High-Performance Photodetectors. *Adv. Funct. Mater.* **2018**, *28*, 1806254.

- (48) Tan, H.; Xu, W.; Sheng, Y.; Lau, C. S.; Fan, Y.; Chen, Q.; Tweedie, M.; Wang, X.; Zhou, Y.; Warner, J. H., Lateral Graphene-Contacted Vertically Stacked WS<sub>2</sub>/MoS<sub>2</sub> Hybrid Photodetectors with Large Gain. *Adv. Mater.* **2017**, *29*, 1702917.
- (49) Cai, Z.; Liu, B.; Zou, X.; Cheng, H. M., Chemical Vapor Deposition Growth and Applications of Two-Dimensional Materials and Their Heterostructures. *Chem. Rev.* **2018**, *118*, 6091-6133.
- (50) Li, G.; Zhang, Y.-Y.; Guo, H.; Huang, L.; Lu, H.; Lin, X.; Wang, Y.-L.; Du, S.; Gao, H.-J., Epitaxial Growth and Physical Properties of 2D Materials Beyond Graphene: From Monatomic Materials to Binary Compounds. *Chem. Soc. Rev.* **2018**, *47*, 6073-6100.
- (51) Kim, K. K.; Lee, H. S.; Lee, Y. H., Synthesis of Hexagonal Boron Nitride Heterostructures for 2D Van Der Waals Electronics. *Chem. Soc. Rev.* **2018**, *47*, 6342-6369.
- (52) Eda, G.; Fujita, T.; Yamaguchi, H.; Voiry, D.; Chen, M.; Chhowalla, M., Coherent Atomic and Electronic Heterostructures of Single-Layer MoS<sub>2</sub>. *ACS Nano* **2012**, *6*, 7311-7317.
- (53) Suenaga, K.; Ji, H. G.; Lin, Y.-C.; Vincent, T.; Maruyama, M.; Aji, A. S.; Shiratsuchi, Y.; Ding, D.; Kawahara, K.; Okada, S.; Panchal, V.; Kazakova, O.; Hibino, H.; Suenaga, K.; Ago, H., Surface-Mediated Aligned Growth of Monolayer MoS<sub>2</sub> and in-Plane Heterostructures with Graphene on Sapphire. *ACS Nano* **2018**, *12*, 10032-10044.
- (54) Zhang, C.; Chen, Y.; Huang, J.-K.; Wu, X.; Li, L.-J.; Yao, W.; Tersoff, J.; Shih, C.-K., Visualizing Band Offsets and Edge States in Bilayer–Monolayer Transition Metal Dichalcogenides Lateral Heterojunction. *Nat. Commun.* **2016**, *7*, 10349.
- (55) Warner, J. H.; Margine, E. R.; Mukai, M.; Robertson, A. W.; Giustino, F.; Kirkland, A. I., Dislocation-Driven Deformations in Graphene. *Science* **2012**, *337*, 209-212.
- (56) Hawkes, P. W., Aberration Correction Past and Present. *Philosophical Transactions of the Royal Society A: Mathematical, Physical and Engineering Sciences* **2009**, *367*, 3637-3664.
- (57) Krivanek, O. L.; Dellby, N.; Lupini, A. R., Towards Sub-Å Electron Beams. *Ultramicroscopy* **1999**, *78*, 1-11.
- (58) Dellby, N.; Bacon, N. J.; Hrnčirik, P.; Murfitt, M. F.; Skone, G. S.; Szilagy, Z. S.; Krivanek, O. L., Dedicated STEM for 200 to 40 keV Operation\*. *Eur. Phys. J. Appl. Phys.* **2011**, *54*, 33505.
- (59) Hawkes, P. W., The Correction of Electron Lens Aberrations. *Ultramicroscopy* **2015**, *156*, A1-A64.
- (60) Oxley, M. P.; Lupini, A. R.; Pennycook, S. J., Ultra-High Resolution Electron Microscopy. *Reports on Progress in Physics* **2016**, *80*, 026101.
- (61) Akashi, T.; Takahashi, Y.; Tanigaki, T.; Shimakura, T.; Kawasaki, T.; Furutsu, T.; Shinada, H.; Müller, H.; Haider, M.; Osakabe, N.; Tonomura, A., Aberration Corrected 1.2-MV Cold Field-Emission Transmission Electron Microscope with a Sub-50-pm Resolution. *Appl. Phys. Lett.* **2015**, *106*, 074101.
- (62) Lopatin, S.; Aljarb, A.; Roddatis, V.; Meyer, T.; Wan, Y.; Fu, J.-H.; Hedhili, M.; Han, Y.; Li, L.-J.; Tung, V., Aberration-corrected STEM imaging of 2D materials: Artifacts and practical applications of threefold astigmatism. *Sci. Adv.* **2020**, *6*, eabb8431.
- (63) Haider, M.; Uhlemann, S.; Schwan, E.; Rose, H.; Kabius, B.; Urban, K., Electron Microscopy Image Enhanced. *Nature* **1998**, *392*, 768-769.
- (64) Haider, M.; Rose, H.; Uhlemann, S.; Kabius, B.; Urban, K., Towards 0.1 nm Resolution with the First Spherically Corrected Transmission Electron Microscope. *Microscopy* **1998**, *47*, 395-405.
- (65) Batson, P. E.; Dellby, N.; Krivanek, O. L., Sub-ångstrom Resolution Using Aberration Corrected Electron Optics. *Nature* **2002**, *418*, 617-620.

- (66) Erni, R.; Rossell, M. D.; Kisielowski, C.; Dahmen, U., Atomic-Resolution Imaging with a Sub-50-pm Electron Probe. *Phys. Rev. Lett.* **2009**, *102*, 096101.
- (67) Sawada, H.; Tanishiro, Y.; Ohashi, N.; Tomita, T.; Hosokawa, F.; Kaneyama, T.; Kondo, Y.; Takayanagi, K., STEM Imaging of 47-pm-Separated Atomic Columns by a Spherical Aberration-Corrected Electron Microscope with a 300-kV Cold Field Emission Gun. *J. Electron Microsc.* **2009**, *58*, 357-361.
- (68) Meyer, J. C.; Kisielowski, C.; Erni, R.; Rossell, M. D.; Crommie, M.; Zettl, A., Direct Imaging of Lattice Atoms and Topological Defects in Graphene Membranes. *Nano Lett.* **2008**, *8*, 3582-3586.
- (69) Krivanek, O. L.; Chisholm, M. F.; Nicolosi, V.; Pennycook, T. J.; Corbin, G. J.; Dellby, N.; Murfitt, M. F.; Own, C. S.; Szilagy, Z. S.; Oxley, M. P.; Pantelides, S. T.; Pennycook, S. J., Atom-By-Atom Structural and Chemical Analysis by Annular Dark-Field Electron Microscopy. *Nature* **2010**, *464*, 571-574.
- (70) Wang, R.; Han, J.; Yang, B.; Wang, X.; Zhang, X.; Song, B., Defect Engineering in Metastable Phases of Transition-Metal Dichalcogenides for Electrochemical Applications. *Chem Asian J* **2020**, *15*, 3961-3972.
- (71) Schmidt, H.; Giustiniano, F.; Eda, G., Electronic Transport Properties of Transition Metal Dichalcogenide Field-Effect Devices: Surface and Interface Effects. *Chem. Soc. Rev.* **2015**, *44*, 7715-7736.
- (72) Chhowalla, M.; Shin, H. S.; Eda, G.; Li, L.-J.; Loh, K. P.; Zhang, H., The Chemistry of Two-Dimensional Layered Transition Metal Dichalcogenide Nanosheets. *Nat. Chem.* **2013**, *5*, 263.
- (73) Peng, J.; Liu, Y.; Luo, X.; Wu, J.; Lin, Y.; Guo, Y.; Zhao, J.; Wu, X.; Wu, C.; Xie, Y., High Phase Purity of Large-Sized 1T'-MoS<sub>2</sub> Monolayers with 2D Superconductivity. *Adv. Mater.* **2019**, *0*, 1900568.
- (74) Xu, H.; Han, D.; Bao, Y.; Cheng, F.; Ding, Z.; Tan, S. J. R.; Loh, K. P., Observation of Gap Opening in 1T' Phase MoS<sub>2</sub> Nanocrystals. *Nano Lett.* **2018**, *18*, 5085-5090.
- (75) Kan, M.; Wang, J. Y.; Li, X. W.; Zhang, S. H.; Li, Y. W.; Kawazoe, Y.; Sun, Q.; Jena, P., Structures and Phase Transition of a MoS<sub>2</sub> Monolayer. *J. Phys. Chem. C* **2014**, *118*, 1515-1522.
- (76) Duerloo, K.-A. N.; Li, Y.; Reed, E. J., Structural Phase Transitions in Two-Dimensional Mo- and W-Dichalcogenide Monolayers. *Nat. Commun.* **2014**, *5*, 4214.
- (77) Voiry, D.; Mohite, A.; Chhowalla, M., Phase Engineering of Transition Metal Dichalcogenides. *Chem. Soc. Rev.* **2015**, *44*, 2702-2712.
- (78) Py, M.; Haering, R., Structural Destabilization Induced by Lithium Intercalation in MoS<sub>2</sub> and Related Compounds. *Can. J. Phys.* **1983**, *61*, 76-84.
- (79) Lei, B.; Pan, Y.; Hu, Z.; Zhang, J.; Xiang, D.; Zheng, Y.; Guo, R.; Han, C.; Wang, L.; Lu, J.; Yang, L.; Chen, W., Direct Observation of Semiconductor-Metal Phase Transition in Bilayer Tungsten Diselenide Induced by Potassium Surface Functionalization. *ACS Nano* **2018**, *12*, 2070-2077.
- (80) Voiry, D.; Salehi, M.; Silva, R.; Fujita, T.; Chen, M.; Asefa, T.; Shenoy, V. B.; Eda, G.; Chhowalla, M., Conducting MoS<sub>2</sub> Nanosheets as Catalysts for Hydrogen Evolution Reaction. *Nano Lett.* **2013**, *13*, 6222-6227.
- (81) Liu, L.; Wu, J.; Wu, L.; Ye, M.; Liu, X.; Wang, Q.; Hou, S.; Lu, P.; Sun, L.; Zheng, J.; Xing, L.; Gu, L.; Jiang, X.; Xie, L.; Jiao, L., Phase-Selective Synthesis of 1T' MoS<sub>2</sub> Monolayers and Heterophase Bilayers. *Nat. Mater.* **2018**, *17*, 1108-1114.
- (82) Liu, K.; Zhang, L.; Cao, T.; Jin, C.; Qiu, D.; Zhou, Q.; Zettl, A.; Yang, P.; Louie, S. G.; Wang, F., Evolution of Interlayer Coupling in Twisted Molybdenum Disulfide Bilayers. *Nat. Commun.*

2014, 5, 4966.

- (83) Weston, A.; Zou, Y.; Enaldiev, V.; Summerfield, A.; Clark, N.; Zólyomi, V.; Graham, A.; Yelgel, C.; Magorrian, S.; Zhou, M.; Zultak, J.; Hopkinson, D.; Barinov, A.; Bointon, T. H.; Kretinin, A.; Wilson, N. R.; Beton, P. H.; Fal'ko, V. I.; Haigh, S. J.; Gorbachev, R., Atomic Reconstruction in Twisted Bilayers of Transition Metal Dichalcogenides. *Nat. Nanotechnol.* **2020**, *15*, 592-597.
- (84) Butler, S. Z.; Hollen, S. M.; Cao, L.; Cui, Y.; Gupta, J. A.; Gutiérrez, H. R.; Heinz, T. F.; Hong, S. S.; Huang, J.; Ismach, A. F., Progress, Challenges, and Opportunities in Two-Dimensional Materials Beyond Graphene. *ACS Nano* **2013**, *7*, 2898-2926.
- (85) Mak, K. F.; Lee, C.; Hone, J.; Shan, J.; Heinz, T. F., Atomically Thin MoS<sub>2</sub>: A New Direct-Gap Semiconductor. *Phys. Rev. Lett.* **2010**, *105*, 136805.
- (86) Splendiani, A.; Sun, L.; Zhang, Y.; Li, T.; Kim, J.; Chim, C.-Y.; Galli, G.; Wang, F., Emerging Photoluminescence in Monolayer MoS<sub>2</sub>. *Nano Lett.* **2010**, *10*, 1271-1275.
- (87) Ellis, J. K.; Lucero, M. J.; Scuseria, G. E., The Indirect to Direct Band Gap Transition in Multilayered MoS<sub>2</sub> as Predicted by Screened Hybrid Density Functional Theory. *Appl. Phys. Lett.* **2011**, *99*, 261908.
- (88) Kang, J.; Tongay, S.; Zhou, J.; Li, J.; Wu, J., Band Offsets and Heterostructures of Two-Dimensional Semiconductors. *Appl. Phys. Lett.* **2013**, *102*, 012111.
- (89) Robertson, A. W.; Bachmatiuk, A.; Wu, Y. A.; Schäffel, F.; Rellinghaus, B.; Büchner, B.; Rummeli, M. H.; Warner, J. H., Atomic Structure of Interconnected Few-Layer Graphene Domains. *ACS Nano* **2011**, *5*, 6610-6618.
- (90) Robertson, A. W.; Lee, G.-D.; He, K.; Fan, Y.; Allen, C. S.; Lee, S.; Kim, H.; Yoon, E.; Zheng, H.; Kirkland, A. I.; Warner, J. H., Partial Dislocations in Graphene and Their Atomic Level Migration Dynamics. *Nano Lett.* **2015**, *15*, 5950-5955.
- (91) Gong, C.; He, K.; Chen, Q.; Robertson, A. W.; Warner, J. H., *In Situ* High Temperature Atomic Level Studies of Large Closed Grain Boundary Loops in Graphene. *ACS Nano* **2016**, *10*, 9165-9173.
- (92) Robertson, A. W.; Montanari, B.; He, K.; Allen, C. S.; Wu, Y. A.; Harrison, N. M.; Kirkland, A. I.; Warner, J. H., Structural Reconstruction of the Graphene Monovacancy. *ACS Nano* **2013**, *7*, 4495-4502.
- (93) Robertson, A. W.; Lee, G.-D.; He, K.; Gong, C.; Chen, Q.; Yoon, E.; Kirkland, A. I.; Warner, J. H., Atomic Structure of Graphene Subnanometer Pores. *ACS Nano* **2015**, *9*, 11599-11607.
- (94) Gong, C.; He, K.; Robertson, A. W.; Yoon, E.; Lee, G.-D.; Warner, J. H., Spatially Dependent Lattice Deformations for Dislocations at the Edges of Graphene. *ACS Nano* **2014**, *9*, 656-662.
- (95) Robertson, A. W.; Lee, G.-D.; He, K.; Yoon, E.; Kirkland, A. I.; Warner, J. H., Stability and Dynamics of the Tetravacancy in Graphene. *Nano Lett.* **2014**, *14*, 1634-1642.
- (96) Griffin, E.; Mogg, L.; Hao, G. P.; Kalon, G.; Bacaksiz, C.; Lopez-Polin, G.; Zhou, T. Y.; Guarochico, V.; Cai, J.; Neumann, C.; Winter, A.; Mohn, M.; Lee, J. H.; Lin, J.; Kaiser, U.; Grigorieva, I. V.; Suenaga, K.; Ozyilmaz, B.; Cheng, H. M.; Ren, W.; Turchanin, A.; Peeters, F. M.; Geim, A. K.; Lozada-Hidalgo, M., Proton and Li-Ion Permeation through Graphene with Eight-Atom-Ring Defects. *ACS Nano* **2020**, *14*, 7280-7286.
- (97) Su, C.; Tripathi, M.; Yan, Q.-B.; Wang, Z.; Zhang, Z.; Hofer, C.; Wang, H.; Basile, L.; Su, G.; Dong, M.; Meyer, J. C.; Kotakoski, J.; Kong, J.; Idrobo, J.-C.; Susi, T.; Li, J., Engineering Single-Atom Dynamics with Electron Irradiation. *Sci. Adv.* **2019**, *5*, eaav2252.
- (98) Rummeli, M. H.; Ta, H. Q.; Mendes, R. G.; Gonzalez-Martinez, I. G.; Zhao, L.; Gao, J.; Fu, L.; Gemming, T.; Bachmatiuk, A.; Liu, Z., New Frontiers in Electron Beam-Driven Chemistry in

- and around Graphene. *Adv. Mater.* **2019**, *31*, 1800715.
- (99) Robertson, A. W.; Lee, G. D.; Lee, S.; Buntin, P.; Drexler, M.; Abdelhafiz, A. A.; Yoon, E.; Warner, J. H.; Alamgir, F. M., Atomic Structure and Dynamics of Epitaxial Platinum Bilayers on Graphene. *ACS Nano* **2019**, *13*, 12162-12170.
- (100) Govind Rajan, A.; Silmore, K. S.; Swett, J.; Robertson, A. W.; Warner, J. H.; Blankschtein, D.; Strano, M. S., Addressing the Isomer Cataloguing Problem for Nanopores in Two-Dimensional Materials. *Nat. Mater.* **2019**, *18*, 129-135.
- (101) Tripathi, M.; Mittelberger, A.; Pike, N. A.; Mangler, C.; Meyer, J. C.; Verstraete, M. J.; Kotakoski, J.; Susi, T., Electron-Beam Manipulation of Silicon Dopants in Graphene. *Nano Lett.* **2018**, *18*, 5319-5323.
- (102) Kotakoski, J.; Mangler, C.; Meyer, J. C., Imaging Atomic-Level Random Walk of a Point Defect in Graphene. *Nat. Commun.* **2014**, *5*, 3991.
- (103) Lee, J.; Zhou, W.; Pennycook, S. J.; Idrobo, J.-C.; Pantelides, S. T., Direct Visualization of Reversible Dynamics in a Si<sub>6</sub> Cluster Embedded in a Graphene Pore. *Nat. Commun.* **2013**, *4*, 1650.
- (104) Zhou, W.; Zou, X.; Najmaei, S.; Liu, Z.; Shi, Y.; Kong, J.; Lou, J.; Ajayan, P. M.; Yakobson, B. I.; Idrobo, J.-C., Intrinsic Structural Defects in Monolayer Molybdenum Disulfide. *Nano Lett.* **2013**, *13*, 2615-2622.
- (105) Lin, Y. C.; Bjorkman, T.; Komsa, H. P.; Teng, P. Y.; Yeh, C. H.; Huang, F. S.; Lin, K. H.; Jadcak, J.; Huang, Y. S.; Chiu, P. W.; Krasheninnikov, A. V.; Suenaga, K., Three-Fold Rotational Defects in Two-Dimensional Transition Metal Dichalcogenides. *Nat. Commun.* **2015**, *6*, 6736.
- (106) Ryu, G. H.; France-Lanord, A.; Wen, Y.; Zhou, S.; Grossman, J. C.; Warner, J. H., Atomic Structure and Dynamics of Self-Limiting Sub-Nanometer Pores in Monolayer WS<sub>2</sub>. *ACS Nano* **2018**, *12*, 11638-11647.
- (107) Hong, J.; Hu, Z.; Probert, M.; Li, K.; Lv, D.; Yang, X.; Gu, L.; Mao, N.; Feng, Q.; Xie, L.; Zhang, J.; Wu, D.; Zhang, Z.; Jin, C.; Ji, W.; Zhang, X.; Yuan, J.; Zhang, Z., Exploring Atomic Defects in Molybdenum Disulfide Monolayers. *Nat. Commun.* **2015**, *6*, 6293.
- (108) Chen, Q.; Robertson, A. W.; He, K.; Gong, C.; Yoon, E.; Lee, G.-D.; Warner, J. H., Atomic Level Distributed Strain within Graphene Divacancies from Bond Rotations. *ACS Nano* **2015**, *9*, 8599-8608.
- (109) Lee, G.-D.; Robertson, A. W.; Lee, S.; Lin, Y.-C.; Oh, J.-W.; Park, H.; Joo, Y.-C.; Yoon, E.; Suenaga, K.; Warner, J. H.; Ewels, C. P., Direct Observation and Catalytic Role of Mediator Atom in 2D Materials. *Sci. Adv.* **2020**, *6*, eaba4942.
- (110) Zheng, H.; Choi, Y.; Baniasadi, F.; Hu, D.; Jiao, L.; Park, K.; Tao, C., Visualization of Point Defects in Ultrathin Layered 1T-PtSe<sub>2</sub>. *2D Mater.* **2019**, *6*, 041005.
- (111) Zhang, Y.; Chen, X.; Huang, Y.; Zhang, C.; Li, F.; Shu, H., The Role of Intrinsic Defects in Electrocatalytic Activity of Monolayer VS<sub>2</sub> Basal Planes for the Hydrogen Evolution Reaction. *J. Phys. Chem. C* **2017**, *121*, 1530-1536.
- (112) Ali, A.; Zhang, J.-M.; Muhammad, I.; Shahid, I.; Ahmad, I., Modulating the Electronic, Magnetic and Optical Properties of 1T-SnSe<sub>2</sub> Monolayer by Defects: An Ab Initio Study. *Superlattices and Microstructures* **2020**, *145*, 106621.
- (113) Gao, J.; Cheng, Y.; Tian, T.; Hu, X.; Zeng, K.; Zhang, G.; Zhang, Y.-W., Structure, Stability, and Kinetics of Vacancy Defects in Monolayer PtSe<sub>2</sub>: A First-Principles Study. *ACS Omega* **2017**, *2*, 8640-8648.
- (114) Komsa, H.-P.; Kurasch, S.; Lehtinen, O.; Kaiser, U.; Krasheninnikov, A. V., From Point to Extended Defects in Two-Dimensional MoS<sub>2</sub>: Evolution of Atomic Structure under Electron Irradiation. *Phys. Rev. B* **2013**, *88*, 035301.

- (115) Wang, S.; Lee, G. D.; Lee, S.; Yoon, E.; Warner, J. H., Detailed Atomic Reconstruction of Extended Line Defects in Monolayer MoS<sub>2</sub>. *ACS Nano* **2016**, *10*, 5419–5430.
- (116) Ryu, G. H.; Lee, J.; Kim, N. Y.; Lee, Y.; Kim, Y.; Kim, M. J.; Lee, C.; Lee, Z., Line-Defect Mediated Formation of Hole and Mo Clusters in Monolayer Molybdenum Disulfide. *2D Mater.* **2016**, *3*, 014002.
- (117) Chen, Q.; Li, H.; Zhou, S.; Xu, W.; Chen, J.; Sawada, H.; Allen, C. S.; Kirkland, A. I.; Grossman, J. C.; Warner, J. H., Ultralong 1D Vacancy Channels for Rapid Atomic Migration During 2D Void Formation in Monolayer MoS<sub>2</sub>. *ACS Nano* **2018**, *12*, 7721-7730.
- (118) Liu, H.; Jiao, L.; Yang, F.; Cai, Y.; Wu, X.; Ho, W.; Gao, C.; Jia, J.; Wang, N.; Fan, H., Dense Network of One-Dimensional Midgap Metallic Modes in Monolayer MoSe<sub>2</sub> and Their Spatial Undulations. *Phys. Rev. Lett.* **2014**, *113*, 066105.
- (119) Kim, J. H.; Kim, S. Y.; Park, S. O.; Jung, G. Y.; Song, S.; Sohn, A.; Kim, S. W.; Kwak, S. K.; Kwon, S. Y.; Lee, Z., Antiphase Boundaries as Faceted Metallic Wires in 2D Transition Metal Dichalcogenides. *Adv. Sci.* **2020**, *7*, 2000788.
- (120) Zhu, J.; Wang, Z.-C.; Dai, H.; Wang, Q.; Yang, R.; Yu, H.; Liao, M.; Zhang, J.; Chen, W.; Wei, Z.; Li, N.; Du, L.; Shi, D.; Wang, W.; Zhang, L.; Jiang, Y.; Zhang, G., Boundary Activated Hydrogen Evolution Reaction on Monolayer MoS<sub>2</sub>. *Nat. Commun.* **2019**, *10*, 1348.
- (121) Ren, X.; Wang, X.; Jin, C., Atomic-Precision Fabrication of Quasi-Full-Space Grain Boundaries in Two-Dimensional Hexagonal Boron Nitride. *Nano Lett.* **2019**, *19*, 8581-8589.
- (122) Kondo, S.; Ishihara, A.; Tochigi, E.; Shibata, N.; Ikuhara, Y., Direct Observation of Atomic-Scale Fracture Path within Ceramic Grain Boundary Core. *Nat. Commun.* **2019**, *10*, 2112.
- (123) Ugeda, M. M.; Pulkin, A.; Tang, S.; Ryu, H.; Wu, Q.; Zhang, Y.; Wong, D.; Pedramrazi, Z.; Martín-Recio, A.; Chen, Y.; Wang, F.; Shen, Z.-X.; Mo, S.-K.; Yazyev, O. V.; Crommie, M. F., Observation of Topologically Protected States at Crystalline Phase Boundaries in Single-Layer WSe<sub>2</sub>. *Nat. Commun.* **2018**, *9*, 3401.
- (124) Hong, M.; Zhou, X.; Gao, N.; Jiang, S.; Xie, C.; Zhao, L.; Gao, Y.; Zhang, Z.; Yang, P.; Shi, Y.; Zhang, Q.; Liu, Z.; Zhao, J.; Zhang, Y., Identifying the Non-Identical Outermost Selenium Atoms and Invariable Band Gaps across the Grain Boundary of Anisotropic Rhenium Diselenide. *ACS Nano* **2018**, *12*, 10095-10103.
- (125) Hsieh, K.; Kochat, V.; Zhang, X.; Gong, Y.; Tiwary, C. S.; Ajayan, P. M.; Ghosh, A., Effect of Carrier Localization on Electrical Transport and Noise at Individual Grain Boundaries in Monolayer MoS<sub>2</sub>. *Nano Lett.* **2017**, *17*, 5452-5457.
- (126) Kochat, V.; Tiwary, C. S.; Biswas, T.; Ramalingam, G.; Hsieh, K.; Chattopadhyay, K.; Raghavan, S.; Jain, M.; Ghosh, A., Magnitude and Origin of Electrical Noise at Individual Grain Boundaries in Graphene. *Nano Lett.* **2016**, *16*, 562-567.
- (127) Kim, M. S.; Yun, S. J.; Lee, Y.; Seo, C.; Han, G. H.; Kim, K. K.; Lee, Y. H.; Kim, J., Biexciton Emission from Edges and Grain Boundaries of Triangular WS<sub>2</sub> Monolayers. *ACS Nano* **2016**, *10*, 2399-2405.
- (128) Liu, Y.; Zou, X.; Yakobson, B. I., Dislocations and Grain Boundaries in Two-Dimensional Boron Nitride. *ACS Nano* **2012**, *6*, 7053-7058.
- (129) Zou, X.; Yakobson, B. I., Metallic High-Angle Grain Boundaries in Monolayer Polycrystalline WS<sub>2</sub>. *Small* **2015**, *11*, 4503-4507.
- (130) Sangwan, V. K.; Jariwala, D.; Kim, I. S.; Chen, K.-S.; Marks, T. J.; Lauhon, L. J.; Hersam, M. C., Gate-Tunable Memristive Phenomena Mediated by Grain Boundaries in Single-Layer MoS<sub>2</sub>. *Nat. Nanotechnol.* **2015**, *10*, 403.
- (131) Park, S.; Kim, M. S.; Kim, H.; Lee, J.; Han, G. H.; Jung, J.; Kim, J., Spectroscopic

Visualization of Grain Boundaries of Monolayer Molybdenum Disulfide by Stacking Bilayers. *ACS Nano* **2015**, *9*, 11042-11048.

(132) Lehtinen, O.; Komsa, H.-P.; Pulkin, A.; Whitwick, M. B.; Chen, M.-W.; Lehnert, T.; Mohn, M. J.; Yazyev, O. V.; Kis, A.; Kaiser, U., Atomic Scale Microstructure and Properties of Se-Deficient Two-Dimensional MoSe<sub>2</sub>. *ACS Nano* **2015**, *9*, 3274-3283.

(133) Gao, N.; Guo, Y.; Zhou, S.; Bai, Y.; Zhao, J., Structures and Magnetic Properties of MoS<sub>2</sub> Grain Boundaries with Antisite Defects. *J. Phys. Chem. C* **2017**, *121*, 12261-12269.

(134) van der Zande, A. M.; Huang, P. Y.; Chenet, D. A.; Berkelbach, T. C.; You, Y.; Lee, G. H.; Heinz, T. F.; Reichman, D. R.; Muller, D. A.; Hone, J. C., Grains and Grain Boundaries in Highly Crystalline Monolayer Molybdenum Disulphide. *Nat. Mater.* **2013**, *12*, 554-561.

(135) Najmaei, S.; Amani, M.; Chin, M. L.; Liu, Z.; Birdwell, A. G.; O'Regan, T. P.; Ajayan, P. M.; Dubey, M.; Lou, J., Electrical Transport Properties of Polycrystalline Monolayer Molybdenum Disulfide. *ACS Nano* **2014**, *8*, 7930-7937.

(136) Rong, Y.; Sheng, Y.; Pacios, M.; Wang, X.; He, Z.; Bhaskaran, H.; Warner, J. H., Electroluminescence Dynamics across Grain Boundary Regions of Monolayer Tungsten Disulfide. *ACS Nano* **2015**, *10*, 1093-1100.

(137) Rong, Y.; He, K.; Pacios, M.; Robertson, A. W.; Bhaskaran, H.; Warner, J. H., Controlled Preferential Oxidation of Grain Boundaries in Monolayer Tungsten Disulfide for Direct Optical Imaging. *ACS Nano* **2015**, *9*, 3695-3703.

(138) Elibol, K.; Susi, T.; O'Brien, M.; Bayer, B. C.; Pennycook, T. J.; McEvoy, N.; Duesberg, G. S.; Meyer, J. C.; Kotakoski, J., Grain Boundary-Mediated Nanopores in Molybdenum Disulfide Grown by Chemical Vapor Deposition. *Nanoscale* **2017**, *9*, 1591-1598.

(139) Wang, S.; Sawada, H.; Han, X.; Zhou, S.; Li, S.; Guo, Z. X.; Kirkland, A. I.; Warner, J. H., Preferential Pt Nanocluster Seeding at Grain Boundary Dislocations in Polycrystalline Monolayer MoS<sub>2</sub>. *ACS Nano* **2018**, *12*, 5626-5636.

(140) Lin, Y.-C.; Yeh, C.-H.; Lin, H.-C.; Siao, M.-D.; Liu, Z.; Nakajima, H.; Okazaki, T.; Chou, M.-Y.; Suenaga, K.; Chiu, P.-W., Stable 1T Tungsten Disulfide Monolayer and Its Junctions: Growth and Atomic Structures. *ACS Nano* **2018**, *12*, 12080-12088.

(141) Yan, A.; Ong, C. S.; Qiu, D. Y.; Ophus, C.; Ciston, J.; Merino, C.; Louie, S. G.; Zettl, A., Dynamics of Symmetry-Breaking Stacking Boundaries in Bilayer MoS<sub>2</sub>. *J. Phys. Chem. C* **2017**, *121*, 22559-22566.

(142) Hong, J.; Wang, C.; Liu, H.; Ren, X.; Chen, J.; Wang, G.; Jia, J.; Xie, M.; Jin, C.; Ji, W.; Yuan, J.; Zhang, Z., Inversion Domain Boundary Induced Stacking and Bandstructure Diversity in Bilayer MoSe<sub>2</sub>. *Nano Lett.* **2017**, *17*, 6653-6660.

(143) Zhao, X.; Ding, Z.; Chen, J.; Dan, J.; Poh, S. M.; Fu, W.; Pennycook, S. J.; Zhou, W.; Loh, K. P., Strain Modulation by Van Der Waals Coupling in Bilayer Transition Metal Dichalcogenide. *ACS Nano* **2018**, *12*, 1940-1948.

(144) Han, Y.; Li, M.-Y.; Jung, G.-S.; Marsalis, M. A.; Qin, Z.; Buehler, M. J.; Li, L.-J.; Muller, D. A., Sub-Nanometre Channels Embedded in Two-Dimensional Materials. *Nat. Mater.* **2017**, *17*, 129.

(145) Najmaei, S.; Liu, Z.; Zhou, W.; Zou, X.; Shi, G.; Lei, S.; Yakobson, B. I.; Idrobo, J. C.; Ajayan, P. M.; Lou, J., Vapour Phase Growth and Grain Boundary Structure of Molybdenum Disulphide Atomic Layers. *Nat. Mater.* **2013**, *12*, 754-759.

(146) Zhang, Z.; Zou, X.; Crespi, V. H.; Yakobson, B. I., Intrinsic Magnetism of Grain Boundaries in Two-Dimensional Metal Dichalcogenides. *ACS Nano* **2013**, *7*, 10475-10481.

(147) Zou, X.; Liu, Y.; Yakobson, B. I., Predicting Dislocations and Grain Boundaries in Two-

- Dimensional Metal-Disulfides from the First Principles. *Nano Lett.* **2012**, *13*, 253-258.
- (148) Azizi, A.; Zou, X.; Ercius, P.; Zhang, Z.; Elías, A. L.; Perea-López, N.; Stone, G.; Terrones, M.; Yakobson, B. I.; Alem, N., Dislocation Motion and Grain Boundary Migration in Two-Dimensional Tungsten Disulfide. *Nat. Commun.* **2014**, *5*, 4867.
- (149) Batzill, M., Mirror Twin Grain Boundaries in Molybdenum Dichalcogenides. *J Phys Condens Matter* **2018**, *30*, 493001.
- (150) Barja, S.; Wickenburg, S.; Liu, Z.-F.; Zhang, Y.; Ryu, H.; Ugeda, Miguel M.; Hussain, Z.; Shen, Z.-X.; Mo, S.-K.; Wong, E.; Salmeron, Miquel B.; Wang, F.; Crommie, M. F.; Ogletree, D. F.; Neaton, Jeffrey B.; Weber-Bargioni, A., Charge Density Wave Order in 1D Mirror Twin Boundaries of Single-Layer MoSe<sub>2</sub>. *Nat. Phys.* **2016**, *12*, 751–756.
- (151) Zhou, S.; Wang, S.; Shi, Z.; Sawada, H.; Kirkland, A. I.; Li, J.; Warner, J. H., Atomically Sharp Interlayer Stacking Shifts at Anti-Phase Grain Boundaries in Overlapping MoS<sub>2</sub> Secondary Layers. *Nanoscale* **2018**, *10*, 16692-16702.
- (152) Wang, Y.; Cong, C.; Yang, W.; Shang, J.; Peimyoo, N.; Chen, Y.; Kang, J.; Wang, J.; Huang, W.; Yu, T., Strain-Induced Direct–Indirect Bandgap Transition and Phonon Modulation in Monolayer WS<sub>2</sub>. *Nano Res.* **2015**, *8*, 2562-2572.
- (153) Yun, W. S.; Han, S.; Hong, S. C.; Kim, I. G.; Lee, J., Thickness and Strain Effects on Electronic Structures of Transition Metal Dichalcogenides: 2H-MX<sub>2</sub> Semiconductors (M= Mo, W; X= S, Se, Te). *Phys. Rev. B* **2012**, *85*, 033305.
- (154) Bollinger, M.; Jacobsen, K. W.; Nørskov, J. K., Atomic and Electronic Structure of MoS<sub>2</sub> Nanoparticles. *Phys. Rev. B* **2003**, *67*, 085410.
- (155) Cui, P.; Zeng, J.; Peng, H.; Choi, J.-H.; Li, Z.; Zeng, C.; Shih, C.-K.; Perdew, J. P.; Zhang, Z., Predictive Design of Intrinsic Half-Metallicity in Zigzag Tungsten Dichalcogenide Nanoribbons. *Phys. Rev. B* **2019**, *100*, 195304.
- (156) Pezo, A.; Lima, M. P.; Costa, M.; Fazzio, A., Electronic Transport Properties of MoS<sub>2</sub> Nanoribbons Embedded in Butadiene Solvent. *Phys. Chem. Chem. Phys.* **2019**, *21*, 11359-11366.
- (157) Fei, Z.; Palomaki, T.; Wu, S.; Zhao, W.; Cai, X.; Sun, B.; Nguyen, P.; Finney, J.; Xu, X.; Cobden, D. H., Edge Conduction in Monolayer WTe<sub>2</sub>. *Nat. Phys.* **2017**, *13*, 677.
- (158) Li, G.; Zhang, D.; Qiao, Q.; Yu, Y.; Peterson, D.; Zafar, A.; Kumar, R.; Curtarolo, S.; Hunte, F.; Shannon, S., All the Catalytic Active Sites of MoS<sub>2</sub> for Hydrogen Evolution. *J. Am. Chem. Soc.* **2016**, *138*, 16632-16638.
- (159) Cao, D.; Shen, T.; Liang, P.; Chen, X.; Shu, H., Role of Chemical Potential in Flake Shape and Edge Properties of Monolayer MoS<sub>2</sub>. *J. Phys. Chem. C* **2015**, *119*, 4294-4301.
- (160) Hansen, L. P.; Ramasse, Q. M.; Kisielowski, C.; Brorson, M.; Johnson, E.; Topsøe, H.; Helveg, S., Atomic-Scale Edge Structures on Industrial-Style MoS<sub>2</sub> Nanocatalysts. *Angew. Chem. Int. Ed.* **2011**, *50*, 10153-10156.
- (161) Kumar, P.; Chatterjee, D.; Maeda, T.; Roy, A.; Kaneko, K.; Balakrishnan, V., Scalable Faceted Voids with Luminescent Enhanced Edges in WS<sub>2</sub> Monolayers. *Nanoscale* **2018**, *10*, 16321-16331.
- (162) Li, Y.; Zhou, Z.; Zhang, S.; Chen, Z., MoS<sub>2</sub> Nanoribbons: High Stability and Unusual Electronic and Magnetic Properties. *J. Am. Chem. Soc.* **2008**, *130*, 16739-16744.
- (163) Yue, Q.; Chang, S.; Kang, J.; Zhang, X.; Shao, Z.; Qin, S.; Li, J., Bandgap Tuning in Armchair MoS<sub>2</sub> nanoribbon. *J. Phys.: Condens. Matter* **2012**, *24*, 335501.
- (164) Lauritsen, J. V.; Kibsgaard, J.; Helveg, S.; Topsøe, H.; Clausen, B. S.; Lægsgaard, E.; Besenbacher, F., Size-Dependent Structure of MoS<sub>2</sub> Nanocrystals. *Nat. Nanotechnol.* **2007**, *2*, 53.
- (165) Chianelli, R. R.; Siadati, M. H.; De la Rosa, M. P.; Berhault, G.; Wilcoxon, J. P.; Bearden

- Jr, R.; Abrams, B. L., Catalytic Properties of Single Layers of Transition Metal Sulfide Catalytic Materials. *Catal. Rev.* **2006**, *48*, 1-41.
- (166) Helveg, S.; Lauritsen, J. V.; Lægsgaard, E.; Stensgaard, I.; Nørskov, J. K.; Clausen, B.; Topsøe, H.; Besenbacher, F., Atomic-Scale Structure of Single-Layer MoS<sub>2</sub> Nanoclusters. *Phys. Rev. Lett.* **2000**, *84*, 951.
- (167) Chen, Q.; Li, H.; Xu, W.; Wang, S.; Sawada, H.; Allen, C. S.; Kirkland, A. I.; Grossman, J. C.; Warner, J. H., Atomically Flat Zigzag Edges in Monolayer MoS<sub>2</sub> by Thermal Annealing. *Nano Lett.* **2017**, *17*, 5502-5507.
- (168) Zhao, X.; Fu, D.; Ding, Z.; Zhang, Y. Y.; Wan, D.; Tan, S. J. R.; Chen, Z.; Leng, K.; Dan, J.; Fu, W.; Geng, D.; Song, P.; Du, Y.; Venkatesan, T.; Pantelides, S. T.; Pennycook, S. J.; Zhou, W.; Loh, K. P., Mo-Terminated Edge Reconstructions in Nanoporous Molybdenum Disulfide Film. *Nano Lett.* **2018**, *18*, 482-490.
- (169) Egerton, R. F.; Li, P.; Malac, M., Radiation damage in the TEM and SEM. *Micron* **2004**, *35*, 399-409.
- (170) Egerton, R. F., Control of radiation damage in the TEM. *Ultramicroscopy* **2013**, *127*, 100-108.
- (171) Susi, T.; Meyer, J. C.; Kotakoski, J., Quantifying Transmission Electron Microscopy Irradiation Effects Using Two-Dimensional Materials. *Nat. Rev. Phys.* **2019**, *1*, 397-405.
- (172) Zan, R.; Ramasse, Q. M.; Jalil, R.; Georgiou, T.; Bangert, U.; Novoselov, K. S., Control of Radiation Damage in MoS<sub>2</sub> by Graphene Encapsulation. *ACS Nano* **2013**, *7*, 10167-10174.
- (173) Liu, X.; Xu, T.; Wu, X.; Zhang, Z.; Yu, J.; Qiu, H.; Hong, J.-H.; Jin, C.-H.; Li, J.-X.; Wang, X.-R.; Sun, L.-T.; Guo, W., Top-Down Fabrication of Sub-Nanometre Semiconducting Nanoribbons Derived from Molybdenum Disulfide Sheets. *Nat. Commun.* **2013**, *4*, 1776.
- (174) Komsa, H.-P.; Kotakoski, J.; Kurasch, S.; Lehtinen, O.; Kaiser, U.; Krasheninnikov, A. V., Two-Dimensional Transition Metal Dichalcogenides under Electron Irradiation: Defect Production and Doping. *Phys. Rev. Lett.* **2012**, *109*, 035503.
- (175) Algara-Siller, G.; Kurasch, S.; Sedighi, M.; Lehtinen, O.; Kaiser, U., The Pristine Atomic Structure of MoS<sub>2</sub> Monolayer Protected from Electron Radiation Damage by Graphene. *Appl. Phys. Lett.* **2013**, *103*, 203107.
- (176) Hopkinson, D. G.; Zólyomi, V.; Rooney, A. P.; Clark, N.; Terry, D. J.; Hamer, M.; Lewis, D. J.; Allen, C. S.; Kirkland, A. I.; Andreev, Y.; Kudrynskiy, Z.; Kovalyuk, Z.; Patané, A.; Fal'ko, V. I.; Gorbachev, R.; Haigh, S. J., Formation and Healing of Defects in Atomically Thin GaSe and InSe. *ACS Nano* **2019**, *13*, 5112-5123.
- (177) Nguyen, L.; Komsa, H.-P.; Khestanova, E.; Kashtiban, R. J.; Peters, J. J. P.; Lawlor, S.; Sanchez, A. M.; Sloan, J.; Gorbachev, R. V.; Grigorieva, I. V.; Krasheninnikov, A. V.; Haigh, S. J., Atomic Defects and Doping of Monolayer NbSe<sub>2</sub>. *ACS Nano* **2017**, *11*, 2894-2904.
- (178) Kretschmer, S.; Lehnert, T.; Kaiser, U.; Krasheninnikov, A. V., Formation of Defects in Two-Dimensional MoS<sub>2</sub> in the Transmission Electron Microscope at Electron Energies Below the Knock-on Threshold: The Role of Electronic Excitations. *Nano Lett.* **2020**, *20*, 2865-2870.
- (179) Lin, Z.; Carvalho, B. R.; Kahn, E.; Lv, R.; Rao, R.; Terrones, H.; Pimenta, M. A.; Terrones, M., Defect Engineering of Two-Dimensional Transition Metal Dichalcogenides. *2D Mater.* **2016**, *3*, 022002.
- (180) Lehnert, T.; Lehtinen, O.; Algara-Siller, G.; Kaiser, U., Electron Radiation Damage Mechanisms in 2D MoSe<sub>2</sub>. *Appl. Phys. Lett.* **2017**, *110*, 033106.
- (181) Lin, J.; Pantelides, S. T.; Zhou, W., Vacancy-Induced Formation and Growth of Inversion Domains in Transition-Metal Dichalcogenide Monolayer. *ACS Nano* **2015**, *9*, 5189-5197.

- (182) Lin, Y.-C.; Dumcenco, D. O.; Huang, Y.-S.; Suenaga, K., Atomic Mechanism of the Semiconducting-to-Metallic Phase Transition in Single-Layered MoS<sub>2</sub>. *Nat. Nanotechnol.* **2014**, *9*, 391–396.
- (183) Sang, X.; Li, X.; Zhao, W.; Dong, J.; Rouleau, C. M.; Geohegan, D. B.; Ding, F.; Xiao, K.; Unocic, R. R., *In Situ* Edge Engineering in Two-Dimensional Transition Metal Dichalcogenides. *Nat. Commun.* **2018**, *9*, 2051.
- (184) Wang, S.; Li, H.; Sawada, H.; Allen, C. S.; Kirkland, A. I.; Grossman, J. C.; Warner, J. H., Atomic Structure and Formation Mechanism of Sub-Nanometer Pores in 2D Monolayer MoS<sub>2</sub>. *Nanoscale* **2017**, *9*, 6417-6426.
- (185) Wang, S.; Qin, Z.; Jung, G. S.; Martin-Martinez, F. J.; Zhang, K.; Buehler, M. J.; Warner, J. H., Atomically Sharp Crack Tips in Monolayer MoS<sub>2</sub> and Their Enhanced Toughness by Vacancy Defects. *ACS Nano* **2016**, *10*, 9831-9839.
- (186) Jung, G. S.; Wang, S.; Qin, Z.; Martin-Martinez, F. J.; Warner, J. H.; Buehler, M. J., Interlocking Friction Governs the Mechanical Fracture of Bilayer MoS<sub>2</sub>. *ACS Nano* **2018**, *12*, 3600-3608.
- (187) Shen, Y.; Xu, T.; Tan, X.; He, L.; Yin, K.; Wan, N.; Sun, L., *In Situ* Repair of 2D Chalcogenides under Electron Beam Irradiation. *Adv. Mater.* **2018**, *30*, 1705954.
- (188) Brehm, J. A.; Lin, J.; Zhou, J.; Sims, H.; Liu, Z.; Pantelides, S. T.; Suenaga, K., Electron-Beam-Induced Synthesis of Hexagonal 1H-MoSe<sub>2</sub> from Square β-FeSe Decorated with Mo Adatoms. *Nano Lett.* **2018**, *18*, 2016-2020.
- (189) Dyck, O.; Kim, S.; Jimenez-Izal, E.; Alexandrova, A. N.; Kalinin, S. V.; Jesse, S., Building Structures Atom by Atom via Electron Beam Manipulation. *Small* **2018**, *14*, 1801771.
- (190) Kretschmer, S.; Komsa, H.-P.; Bøggild, P.; Krasheninnikov, A. V., Structural Transformations in Two-Dimensional Transition-Metal Dichalcogenide MoS<sub>2</sub> under an Electron Beam: Insights from First-Principles Calculations. *J. Phys. Chem. Lett.* **2017**, *8*, 3061-3067.
- (191) Lin, J.; Cretu, O.; Zhou, W.; Suenaga, K.; Prasai, D.; Bolotin, K. I.; Cuong, N. T.; Otani, M.; Okada, S.; Lupini, A. R.; Idrobo, J.-C.; Caudel, D.; Burger, A.; Ghimire, N. J.; Yan, J.; Mandrus, D. G.; Pennycook, S. J.; Pantelides, S. T., Flexible Metallic Nanowires with Self-Adaptive Contacts to Semiconducting Transition-Metal Dichalcogenide Monolayers. *Nat. Nanotechnol.* **2014**, *9*, 436.
- (192) Koh, A. L.; Wang, S.; Ataca, C.; Grossman, J. C.; Sinclair, R.; Warner, J. H., Torsional Deformations in Subnanometer MoS Interconnecting Wires. *Nano Lett.* **2016**, *16*, 1210-1217.
- (193) Zhao, X.; Dan, J.; Chen, J.; Ding, Z.; Zhou, W.; Loh, K. P.; Pennycook, S. J., Atom-by-Atom Fabrication of Monolayer Molybdenum Membranes. *Adv. Mater.* **2018**, *30*, 1707281.
- (194) Joseph, T.; Ghorbani-Asl, M.; Kvashnin, A. G.; Larionov, K. V.; Popov, Z. I.; Sorokin, P. B.; Krasheninnikov, A. V., Non-Stoichiometric Phases of Two-Dimensional Transition-Metal Dichalcogenides: From Chalcogen Vacancies to Pure Metal Membranes. *J. Phys. Chem. Lett.* **2019**, *10*, 6492-6498.
- (195) Ke, J.-A.; Garaj, S.; Gradečak, S., Nanopores in 2D MoS<sub>2</sub>: Defect-Mediated Formation and Density Modulation. *ACS Appl. Mater. Interfaces* **2019**, *11*, 26228-26234.
- (196) Park, H. J.; Ryu, G. H.; Lee, Z., Hole Defects on Two-Dimensional Materials Formed by Electron Beam Irradiation: Toward Nanopore Devices. *Appl. Microsc.* **2015**, *45*, 107-114.
- (197) Huang, W.; Wang, X.; Ji, X.; Zhang, Z.; Jin, C., *In-Situ* Fabrication of Mo<sub>6</sub>S<sub>6</sub>-Nanowire-Terminated Edges in Monolayer Molybdenum Disulfide. *Nano Res.* **2018**, *11*, 5849-5857.
- (198) Sutter, E.; Huang, Y.; Komsa, H. P.; Ghorbani-Asl, M.; Krasheninnikov, A. V.; Sutter, P., Electron-Beam Induced Transformations of Layered Tin Dichalcogenides. *Nano Lett.* **2016**, *16*,

4410-4416.

- (199) Wang, X.; Guan, X.; Ren, X.; Liu, T.; Huang, W.; Cao, J.; Jin, C., Deriving 2D  $M_2X_3$  ( $M = Mo, W, X = S, Se$ ) by Periodic Assembly of Chalcogen Vacancy Lines in Their  $MX_2$  Counterparts. *Nanoscale* **2020**, *12*, 8285-8293.
- (200) Lin, J.; Zuluaga, S.; Yu, P.; Liu, Z.; Pantelides, S. T.; Suenaga, K., Novel  $Pd_2Se_3$  Two-Dimensional Phase Driven by Interlayer Fusion in Layered  $PdSe_2$ . *Phys. Rev. Lett.* **2017**, *119*, 016101.
- (201) Sebastian, Z.; Junhao, L.; Kazu, S.; Sokrates, T. P., Two-Dimensional  $PdSe_2$ - $Pd_2Se_3$  Junctions Can Serve as Nanowires. *2D Mater.* **2018**, *5*, 035025.
- (202) Egerton, R. F., Beam-Induced Motion of Adatoms in the Transmission Electron Microscope. *Microscopy and Microanalysis* **2013**, *19*, 479-486.
- (203) Meyer, J. C.; Eder, F.; Kurasch, S.; Skakalova, V.; Kotakoski, J.; Park, H. J.; Roth, S.; Chuvilin, A.; Eyhusen, S.; Benner, G.; Krasheninnikov, A. V.; Kaiser, U., Accurate Measurement of Electron Beam Induced Displacement Cross Sections for Single-Layer Graphene. *Phys. Rev. Lett.* **2012**, *108*, 196102.
- (204) Chirita Mihaila, A. I.; Susi, T.; Kotakoski, J., Influence of Temperature on the Displacement Threshold Energy in Graphene. *Sci. Rep.* **2019**, *9*, 12981.
- (205) Zhu, H.; Wang, Q.; Cheng, L.; Addou, R.; Kim, J.; Kim, M. J.; Wallace, R. M., Defects and Surface Structural Stability of  $MoTe_2$  under Vacuum Annealing. *ACS Nano* **2017**, *11*, 11005-11014.
- (206) Zhao, X.; Ji, Y.; Chen, J.; Fu, W.; Dan, J.; Liu, Y.; Pennycook, S. J.; Zhou, W.; Loh, K. P., Healing of Planar Defects in 2D Materials via Grain Boundary Sliding. *Adv. Mater.* **2019**, 1900237.
- (207) Zhu, H.; Wang, Q.; Zhang, C.; Addou, R.; Cho, K.; Wallace, R. M.; Kim, M. J., New  $Mo_6Te_6$  Sub-Nanometer-Diameter Nanowire Phase from 2H- $MoTe_2$ . *Adv. Mater.* **2017**, *29*, 1606264.
- (208) Yu, Y.; Wang, G.; Tan, Y.; Wu, N.; Zhang, X.-A.; Qin, S., Phase-Controlled Growth of One-Dimensional  $Mo_6Te_6$  Nanowires and Two-Dimensional  $MoTe_2$  Ultrathin Films Heterostructures. *Nano Lett.* **2018**, *18*, 675-681.
- (209) Wang, Q.; Zhu, H.; Zhang, C.; Addou, R.; Cho, K.; Wallace, R. M.; Kim, M. J., *In Situ* Heating Study of 2H- $MoTe_2$  to  $Mo_6Te_6$  Nanowire Phase Transition. *Microscopy and Microanalysis* **2017**, *23*, 1764-1765.
- (210) Ryu, G. H.; Chen, J.; Wen, Y.; Warner, J. H., *In-Situ* Atomic-Scale Dynamics of Thermally Driven Phase Transition of 2D Few-Layered 1T  $PtSe_2$  into Ultrathin 2D Nonlayered  $PtSe$  Crystals. *Chem. Mater.* **2019**, *31*, 9895-9903.
- (211) Pennycook, S. J.; Boatner, L. A., Chemically Sensitive Structure-Imaging with a Scanning Transmission Electron Microscope. *Nature* **1988**, *336*, 565.
- (212) Voyles, P. M.; Muller, D. A.; Grazul, J. L.; Citrin, P. H.; Gossmann, H. J. L., Atomic-Scale Imaging of Individual Dopant Atoms and Clusters in Highly N-Type Bulk Si. *Nature* **2002**, *416*, 826.
- (213) Singhal, A.; Yang, J. C.; Gibson, J. M., Stem-Based Mass Spectroscopy of Supported Re Clusters. *Ultramicroscopy* **1997**, *67*, 191-206.
- (214) SAXTON, W. O., Observation of Lens Aberrations for Very High-Resolution Electron Microscopy. I. Theory. *Journal of Microscopy* **1995**, *179*, 201-213.
- (215) Saxton, W. O., Observation of Lens Aberrations for High Resolution Electron Microscopy II: Simple Expressions for Optimal Estimates. *Ultramicroscopy* **2015**, *151*, 168-177.

- (216) Müller, H.; Uhlemann, S.; Hartel, P.; Haider, M., Advancing the Hexapole Cs-Corrector for the Scanning Transmission Electron Microscope. *Microscopy and Microanalysis* **2006**, *12*, 442.
- (217) Cowley, J. M.; Moodie, A. F., The Scattering of Electrons by Atoms and Crystals. I. A New Theoretical Approach. *Acta Crystallographica* **1957**, *10*, 609-619.
- (218) Goodman, P.; Moodie, A. F., Numerical Evaluations of N-Beam Wave Functions in Electron Scattering by the Multi-Slice Method. *Acta Crystallographica Section A* **1974**, *30*, 280-290.
- (219) Ophus, C., A Fast Image Simulation Algorithm for Scanning Transmission Electron Microscopy. *Advanced Structural and Chemical Imaging* **2017**, *3*, 13.
- (220) Hýtch, M.; Snoeck, E.; Kilaas, R., Quantitative Measurement of Displacement and Strain Fields from Hrem Micrographs. *Ultramicroscopy* **1998**, *74*, 131-146.
- (221) Hýtch, M. J.; Putaux, J.-L.; Pénisson, J.-M., Measurement of the Displacement Field of Dislocations to 0.03 Å by Electron Microscopy. *Nature* **2003**, *423*, 270–273.
- (222) Plimpton, S., Fast Parallel Algorithms for Short-Range Molecular Dynamics. *J. Comput. Phys.* **1995**, *117*, 1-19.
- (223) Liang, T.; Phillpot, S. R.; Sinnott, S. B., Parametrization of a Reactive Many-Body Potential for Mo-S Systems. *Phys. Rev. B* **2009**, *79*, 245110.
- (224) Stewart, J. A.; Spearot, D. E., Atomistic Simulations of Nanoindentation on the Basal Plane of Crystalline Molybdenum Disulfide (MoS<sub>2</sub>). *Modelling and Simulation in Materials Science and Engineering* **2013**, *21*, 045003.
- (225) He, J.; Hummer, K.; Franchini, C., Stacking Effects on the Electronic and Optical Properties of Bilayer Transition Metal Dichalcogenides MoS<sub>2</sub>, MoSe<sub>2</sub>, WS<sub>2</sub>, and WSe<sub>2</sub>. *Phys. Rev. B* **2014**, *89*, 075409.
- (226) Grimme, S., Semiempirical GGA-Type Density Functional Constructed with a Long-Range Dispersion Correction. *J. Comput. Chem.* **2006**, *27*, 1787-1799.
- (227) Klimeš, J.; Bowler, D. R.; Michaelides, A., Van Der Waals Density Functionals Applied to Solids. *Phys. Rev. B* **2011**, *83*, 195131.
- (228) Giannozzi, P.; Baroni, S.; Bonini, N.; Calandra, M.; Car, R.; Cavazzoni, C.; Ceresoli, D.; Chiarotti, G. L.; Cococcioni, M.; Dabo, I.; Dal Corso, A.; de Gironcoli, S.; Fabris, S.; Fratesi, G.; Gebauer, R.; Gerstmann, U.; Gougoussis, C.; Kokalj, A.; Lazzeri, M.; Martin-Samos, L.; Marzari, N.; Mauri, F.; Mazzarello, R.; Paolini, S.; Pasquarello, A.; Paulatto, L.; Sbraccia, C.; Scandolo, S.; Sclauzero, G.; Seitsonen, A. P.; Smogunov, A.; Umari, P.; Wentzcovitch, R. M., Quantum Espresso: A Modular and Open-Source Software Project for Quantum Simulations of Materials. *J. Phys.: Condens. Matter* **2009**, *21*, 395502.
- (229) Perdew, J. P.; Burke, K.; Ernzerhof, M., Generalized Gradient Approximation Made Simple. *Phys. Rev. Lett.* **1996**, *77*, 3865-3868.
- (230) Troullier, N.; Martins, J. L., Efficient Pseudopotentials for Plane-Wave Calculations. *Phys. Rev. B* **1991**, *43*, 1993-2006.
- (231) Komsa, H.-P.; Krasheninnikov, A. V., Native Defects in Bulk and Monolayer MoS<sub>2</sub> from First Principles. *Phys. Rev. B* **2015**, *91*, 125304.
- (232) Sensoy, M. G.; Vinichenko, D.; Chen, W.; Friend, C. M.; Kaxiras, E., Strain Effects on the Behavior of Isolated and Paired Sulfur Vacancy Defects in Monolayer MoS<sub>2</sub>. *Phys. Rev. B* **2017**, *95*, 014106.
- (233) Zhou, Y.; Tan, H.; Sheng, Y.; Fan, Y.; Xu, W.; Warner, J. H., Utilizing Interlayer Excitons in Bilayer WS<sub>2</sub> for Increased Photovoltaic Response in Ultrathin Graphene Vertical Cross-Bar

Photodetecting Tunneling Transistors. *ACS Nano* **2018**, *12*, 4669-4677.

- (234) Tang, S.-Y.; Medina, H.; Yen, Y.-T.; Chen, C.-W.; Yang, T.-Y.; Wei, K.-H.; Chueh, Y.-L., Enhanced Photocarrier Generation with Selectable Wavelengths by M-Decorated-M-Decorated-CuInS<sub>2</sub> Nanocrystals (M = Au and Pt) Synthesized in a Single Surfactant Process on MoS<sub>2</sub> Bilayers. *Small* **2019**, *15*, 1803529.
- (235) Liu, Z.; Amani, M.; Najmaei, S.; Xu, Q.; Zou, X.; Zhou, W.; Yu, T.; Qiu, C.; Birdwell, A. G.; Crowne, F. J.; Vajtai, R.; Yakobson, B. I.; Xia, Z.; Dubey, M.; Ajayan, P. M.; Lou, J., Strain and Structure Heterogeneity in MoS<sub>2</sub> Atomic Layers Grown by Chemical Vapour Deposition. *Nat. Commun.* **2014**, *5*, 5246.
- (236) Cheng, J.; Jiang, T.; Ji, Q.; Zhang, Y.; Li, Z.; Shan, Y.; Zhang, Y.; Gong, X.; Liu, W.; Wu, S., Kinetic Nature of Grain Boundary Formation in as-Grown MoS<sub>2</sub> Monolayers. *Adv. Mater.* **2015**, *27*, 4069-4074.
- (237) Keerthi, A.; Geim, A. K.; Janardanan, A.; Rooney, A. P.; Esfandiari, A.; Hu, S.; Dar, S. A.; Grigorieva, I. V.; Haigh, S. J.; Wang, F. C.; Radha, B., Ballistic Molecular Transport through Two-Dimensional Channels. *Nature* **2018**, *558*, 420-424.
- (238) Mouterde, T.; Keerthi, A.; Poggioli, A. R.; Dar, S. A.; Siria, A.; Geim, A. K.; Bocquet, L.; Radha, B., Molecular Streaming and Its Voltage Control in Ångström-Scale Channels. *Nature* **2019**, *567*, 87-90.
- (239) Marbach, S.; Dean, D. S.; Bocquet, L., Transport and Dispersion across Wiggling Nanopores. *Nat. Phys.* **2018**, *14*, 1108-1113.
- (240) Sahu, S.; Zwolak, M., Colloquium: Ionic Phenomena in Nanoscale Pores through 2D Materials. *Rev. Mod. Phys.* **2019**, *91*, 021004.
- (241) Arjmandi-Tash, H.; Belyaeva, L. A.; Schneider, G. F., Single Molecule Detection with Graphene and Other Two-Dimensional Materials: Nanopores and Beyond. *Chem. Soc. Rev.* **2016**, *45*, 476-493.
- (242) Danda, G.; Masih Das, P.; Chou, Y.-C.; Mlack, J. T.; Parkin, W. M.; Naylor, C. H.; Fujisawa, K.; Zhang, T.; Fulton, L. B.; Terrones, M.; Johnson, A. T. C.; Drndić, M., Monolayer WS<sub>2</sub> Nanopores for DNA Translocation with Light-Adjustable Sizes. *ACS Nano* **2017**, *11*, 1937-1945.
- (243) Gethers, M. L.; Thomas, J. C.; Jiang, S.; Weiss, N. O.; Duan, X.; Goddard, W. A.; Weiss, P. S., Holey Graphene as a Weed Barrier for Molecules. *ACS Nano* **2015**, *9*, 10909-10915.
- (244) Rodríguez-Manzo, J. A.; Puster, M.; Nicolăi, A.; Meunier, V.; Drndić, M., DNA Translocation in Nanometer Thick Silicon Nanopores. *ACS Nano* **2015**, *9*, 6555-6564.
- (245) Cohen-Tanugi, D.; Grossman, J. C., Water Desalination across Nanoporous Graphene. *Nano Lett.* **2012**, *12*, 3602-3608.
- (246) Surwade, S. P.; Smirnov, S. N.; Vlassiuk, I. V.; Unocic, R. R.; Veith, G. M.; Dai, S.; Mahurin, S. M., Water Desalination Using Nanoporous Single-Layer Graphene. *Nat. Nanotechnol.* **2015**, *10*, 459.
- (247) Heiranian, M.; Farimani, A. B.; Aluru, N. R., Water Desalination with a Single-Layer MoS<sub>2</sub> Nanopore. *Nat. Commun.* **2015**, *6*, 8616.
- (248) Min, S. K.; Kim, W. Y.; Cho, Y.; Kim, K. S., Fast DNA Sequencing with a Graphene-Based Nanochannel Device. *Nat. Nanotechnol.* **2011**, *6*, 162-165.
- (249) Feng, J.; Liu, K.; Graf, M.; Dumcenco, D.; Kis, A.; Di Ventura, M.; Radenovic, A., Observation of Ionic Coulomb Blockade In nanopores. *Nat. Mater.* **2016**, *15*, 850.
- (250) Liu, K.; Feng, J.; Kis, A.; Radenovic, A., Atomically Thin Molybdenum Disulfide Nanopores with High Sensitivity for DNA Translocation. *ACS Nano* **2014**, *8*, 2504-2511.
- (251) Wilson, J.; Aksimentiev, A., Water-Compression Gating of Nanopore Transport. *Phys. Rev.*

*Lett.* **2018**, *120*, 268101.

- (252) Gopinadhan, K.; Hu, S.; Esfandiar, A.; Lozada-Hidalgo, M.; Wang, F. C.; Yang, Q.; Tyurnina, A. V.; Keerthi, A.; Radha, B.; Geim, A. K., Complete Steric Exclusion of Ions and Proton Transport through Confined Monolayer Water. *Science* **2019**, *363*, 145-148.
- (253) Pérez, M. D. B.; Nicolai, A.; Delarue, P.; Meunier, V.; Drndić, M.; Senet, P., Improved Model of Ionic Transport in 2D MoS<sub>2</sub> Membranes with Sub-5nm Pores. *Appl. Phys. Lett.* **2019**, *114*, 023107.
- (254) Feng, J.; Liu, K.; Bulushev, R. D.; Khlybov, S.; Dumcenco, D.; Kis, A.; Radenovic, A., Identification of Single Nucleotides in MoS<sub>2</sub> Nanopores. *Nat. Nanotechnol.* **2015**, *10*, 1070.
- (255) Warner, J. H.; Rummeli, M. H.; Bachmatiuk, A.; Wilson, M.; Büchner, B., Examining Co-Based Nanocrystals on Graphene Using Low-Voltage Aberration-Corrected Transmission Electron Microscopy. *ACS Nano* **2010**, *4*, 470-476.
- (256) Hong, J.; Pan, Y.; Hu, Z.; Lv, D.; Jin, C.; Ji, W.; Yuan, J.; Zhang, Z., Direct Imaging of Kinetic Pathways of Atomic Diffusion in Monolayer Molybdenum Disulfide. *Nano Lett.* **2017**, *17*, 3383-3390.
- (257) Li, H.; Wang, S.; Sawada, H.; Han, G. G.; Samuels, T.; Allen, C. S.; Kirkland, A. I.; Grossman, J. C.; Warner, J. H., Atomic Structure and Dynamics of Single Platinum Atom Interactions with Monolayer MoS<sub>2</sub>. *ACS Nano* **2017**, *11*, 3392-3403.
- (258) Lehtinen, P. O.; Foster, A. S.; Ayuela, A.; Krasheninnikov, A.; Nordlund, K.; Nieminen, R. M., Magnetic Properties and Diffusion of Adatoms on a Graphene Sheet. *Phys. Rev. Lett.* **2003**, *91*, 017202.
- (259) Kim, K.; Lee, H.-B.-R.; Johnson, R. W.; Tanskanen, J. T.; Liu, N.; Kim, M.-G.; Pang, C.; Ahn, C.; Bent, S. F.; Bao, Z., Selective Metal Deposition at Graphene Line Defects by Atomic Layer Deposition. *Nat. Commun.* **2014**, *5*, 4781.
- (260) Ho, C. H.; Chen, W. H.; Tiong, K. K.; Lee, K. Y.; Gloter, A.; Zobelli, A.; Stephan, O.; Tizei, L. H. G., Interplay between Cr Dopants and Vacancy Clustering in the Structural and Optical Properties of WSe<sub>2</sub>. *ACS Nano* **2017**, *11*, 11162-11168.
- (261) Lin, Y. C.; Dumcenco, D. O.; Komsa, H. P.; Niimi, Y.; Krasheninnikov, A. V.; Huang, Y. S.; Suenaga, K., Properties of Individual Dopant Atoms in Single-Layer MoS<sub>2</sub>: Atomic Structure, Migration, and Enhanced Reactivity. *Adv. Mater.* **2014**, *26*, 2857-2861.
- (262) Li, W.; Guo, M.; Zhang, G.; Zhang, Y.-W., Edge-Specific Au/Ag Functionalization-Induced Conductive Paths in Armchair MoS<sub>2</sub> Nanoribbons. *Chem. Mater.* **2014**, *26*, 5625-5631.
- (263) Wang, S.; Sawada, H.; Chen, Q.; Han, G. G. D.; Allen, C.; Kirkland, A. I.; Warner, J. H., *In Situ* Atomic-Scale Studies of the Formation of Epitaxial Pt Nanocrystals on Monolayer Molybdenum Disulfide. *ACS Nano* **2017**, *11*, 9057-9067.
- (264) Abdelhafiz, A.; Vitale, A.; Joiner, C.; Vogel, E.; Alamgir, F. M., Layer-by-Layer Evolution of Structure, Strain, and Activity for the Oxygen Evolution Reaction in Graphene-Templated Pt Monolayers. *ACS Appl. Mater. Interfaces* **2015**, *7*, 6180-6188.
- (265) Zhao, J.; Deng, Q.; Bachmatiuk, A.; Sandeep, G.; Popov, A.; Eckert, J.; Rummeli, M. H., Free-Standing Single-Atom-Thick Iron Membranes Suspended in Graphene Pores. *Science* **2014**, *343*, 1228-1232.
- (266) Tapasztó, L.; Dobrik, G.; Lambin, P.; Biró, L. P., Tailoring the Atomic Structure of Graphene Nanoribbons by Scanning Tunneling Microscope Lithography. *Nat. Nanotechnol.* **2008**, *3*, 397-401.
- (267) Lee, S.; Yang, F.; Suh, J.; Yang, S.; Lee, Y.; Li, G.; Sung Choe, H.; Suslu, A.; Chen, Y.; Ko, C.; Park, J.; Liu, K.; Li, J.; Hippalgaonkar, K.; Urban, J. J.; Tongay, S.; Wu, J., Anisotropic in-

Plane Thermal Conductivity of Black Phosphorus Nanoribbons at Temperatures Higher Than 100 K. *Nat. Commun.* **2015**, *6*, 8573.

(268) White, D. L.; Burkert, S. C.; Hwang, S. I.; Star, A., Holey Graphene Metal Nanoparticle Composites *via* Crystalline Polymer Templated Etching. *Nano Lett.* **2019**, *19*, 2824-2831.

(269) Feng, J.; Liu, K.; Graf, M.; Lihter, M.; Bulushev, R. D.; Dumcenco, D.; Alexander, D. T. L.; Krasnozhan, D.; Vuletic, T.; Kis, A.; Radenovic, A., Electrochemical Reaction in Single Layer MoS<sub>2</sub>: Nanopores Opened Atom by Atom. *Nano Lett.* **2015**, *15*, 3431-3438.

(270) Song, B.; Schneider, G. F.; Xu, Q.; Pandraud, G.; Dekker, C.; Zandbergen, H., Atomic-Scale Electron-Beam Sculpting of Near-Defect-Free Graphene Nanostructures. *Nano Lett.* **2011**, *11*, 2247-2250.

(271) Emmrich, D.; Beyer, A.; Nadzeyka, A.; Bauerdick, S.; Meyer, J. C.; Kotakoski, J.; Götzhäuser, A., Nanopore Fabrication and Characterization by Helium Ion Microscopy. *Appl. Phys. Lett.* **2016**, *108*, 163103.

(272) Xia, D.; Huynh, C.; McVey, S.; Kobler, A.; Stern, L.; Yuan, Z.; Ling, X. S., Rapid Fabrication of Solid-State Nanopores with High Reproducibility over a Large Area Using a Helium Ion Microscope. *Nanoscale* **2018**, *10*, 5198-5204.

(273) Meyer, J. C.; Chuvilin, A.; Algara-Siller, G.; Biskupek, J.; Kaiser, U., Selective Sputtering and Atomic Resolution Imaging of Atomically Thin Boron Nitride Membranes. *Nano Lett.* **2009**, *9*, 2683-2689.

(274) Abbas, A. N.; Liu, G.; Liu, B.; Zhang, L.; Liu, H.; Ohlberg, D.; Wu, W.; Zhou, C., Patterning, Characterization, and Chemical Sensing Applications of Graphene Nanoribbon Arrays Down to 5 nm Using Helium Ion Beam Lithography. *ACS Nano* **2014**, *8*, 1538-1546.

(275) Liu, L.; Shi, J.; Li, M.; Yu, P.; Yang, T.; Li, G., Fabrication of Sub-Micrometer-Sized MoS<sub>2</sub> Thin-Film Transistor by Phase Mode AFM Lithography. *Small* **2018**, *14*, 1803273.

(276) Byun, I.-S.; Yoon, D.; Choi, J. S.; Hwang, I.; Lee, D. H.; Lee, M. J.; Kawai, T.; Son, Y.-W.; Jia, Q.; Cheong, H.; Park, B. H., Nanoscale Lithography on Monolayer Graphene Using Hydrogenation and Oxidation. *ACS Nano* **2011**, *5*, 6417-6424.

(277) Masubuchi, S.; Ono, M.; Yoshida, K.; Hirakawa, K.; Machida, T., Fabrication of Graphene Nanoribbon by Local Anodic Oxidation Lithography Using Atomic Force Microscope. *Appl. Phys. Lett.* **2009**, *94*, 082107.

(278) Chen, S.; Kim, S.; Chen, W.; Yuan, J.; Bashir, R.; Lou, J.; van der Zande, A. M.; King, W. P., Monolayer MoS<sub>2</sub> Nanoribbon Transistors Fabricated by Scanning Probe Lithography. *Nano Lett.* **2019**, *19*, 2092-2098.

(279) Hudak, B. M.; Song, J.; Sims, H.; Troparevsky, M. C.; Humble, T. S.; Pantelides, S. T.; Snijders, P. C.; Lupini, A. R., Directed Atom-by-Atom Assembly of Dopants in Silicon. *ACS Nano* **2018**, *12*, 5873-5879.

(280) Xu, Q.; Wu, M.-Y.; Schneider, G. F.; Houben, L.; Malladi, S. K.; Dekker, C.; Yucelen, E.; Dunin-Borkowski, R. E.; Zandbergen, H. W., Controllable Atomic Scale Patterning of Freestanding Monolayer Graphene at Elevated Temperature. *ACS Nano* **2013**, *7*, 1566-1572.

(281) Börrnert, F.; Fu, L.; Gorantla, S.; Knupfer, M.; Büchner, B.; Rummeli, M. H., Programmable Sub-Nanometer Sculpting of Graphene with Electron Beams. *ACS Nano* **2012**, *6*, 10327-10334.

(282) Fischbein, M. D.; Drndić, M., Electron Beam Nanosculpting of Suspended Graphene Sheets. *Appl. Phys. Lett.* **2008**, *93*, 113107.

(283) Xu, T.; Xie, X.; Yin, K.; Sun, J.; He, L.; Sun, L., Controllable Atomic-Scale Sculpting and Deposition of Carbon Nanostructures on Graphene. *Small* **2014**, *10*, 1724-1728.

- (284) Masih Das, P.; Danda, G.; Cupo, A.; Parkin, W. M.; Liang, L.; Kharche, N.; Ling, X.; Huang, S.; Dresselhaus, M. S.; Meunier, V.; Drndić, M., Controlled Sculpture of Black Phosphorus Nanoribbons. *ACS Nano* **2016**, *10*, 5687-5695.
- (285) Rodríguez-Manzo, J. A.; Qi, Z. J.; Crook, A.; Ahn, J.-H.; Johnson, A. T. C.; Drndić, M., *In Situ* Transmission Electron Microscopy Modulation of Transport in Graphene Nanoribbons. *ACS Nano* **2016**, *10*, 4004-4010.
- (286) Wang, S.; Li, H.; Zhang, J.; Guo, S.; Xu, W.; Grossman, J. C.; Warner, J. H., Epitaxial Templating of Two-Dimensional Metal Chloride Nanocrystals on Monolayer Molybdenum Disulfide. *ACS Nano* **2017**, *11*, 6404-6415.
- (287) Puster, M.; Rodríguez-Manzo, J. A.; Balan, A.; Drndić, M., Toward Sensitive Graphene Nanoribbon–Nanopore Devices by Preventing Electron Beam-Induced Damage. *ACS Nano* **2013**, *7*, 11283-11289.
- (288) Schwierz, F.; Pezoldt, J.; Granzner, R., Two-Dimensional Materials and Their Prospects in Transistor Electronics. *Nanoscale* **2015**, *7*, 8261-8283.
- (289) Villaos, R. A. B.; Crisostomo, C. P.; Huang, Z.-Q.; Huang, S.-M.; Padama, A. A. B.; Albao, M. A.; Lin, H.; Chuang, F.-C., Thickness Dependent Electronic Properties of Pt Dichalcogenides. *npj 2D Materials and Applications* **2019**, *3*, 2.
- (290) Shawkat, M. S.; Gil, J.; Han, S. S.; Ko, T.-J.; Wang, M.; Dev, D.; Kwon, J.; Lee, G.-H.; Oh, K. H.; Chung, H.-S.; Roy, T.; Jung, Y.; Jung, Y., Thickness-Independent Semiconducting-to-Metallic Conversion in Wafer-Scale Two-Dimensional PtSe<sub>2</sub> Layers by Plasma-Driven Chalcogen Defect Engineering. *ACS Appl. Mater. Interfaces* **2020**, *12*, 14341-14351.
- (291) Wang, G.; Wang, K.; McEvoy, N.; Bai, Z.; Cullen, C. P.; Murphy, C. N.; McManus, J. B.; Magan, J. J.; Smith, C. M.; Duesberg, G. S.; Kaminer, I.; Wang, J.; Blau, W. J., Ultrafast Carrier Dynamics and Bandgap Renormalization in Layered PtSe<sub>2</sub>. *Small* **2019**, *15*, 1902728.
- (292) Roman, K.; Agnieszka, K.; Thomas, H., *Two-Dimensional Noble-Metal Dichalcogenides and Phosphochalcogenides*. ChemRxiv.: 2019.
- (293) Sajjad, M.; Singh, N.; Schwingenschlögl, U., Strongly Bound Excitons in Monolayer PtS<sub>2</sub> and PtSe<sub>2</sub>. *Appl. Phys. Lett.* **2018**, *112*, 043101.
- (294) Kandemir, A.; Akbali, B.; Kahraman, Z.; Badalov, S. V.; Ozcan, M.; Iyikanat, F.; Sahin, H., Structural, Electronic and Phononic Properties of PtSe<sub>2</sub>: From Monolayer to Bulk. *Semicond. Sci. Technol.* **2018**, *33*, 085002.
- (295) Zhao, Y.; Qiao, J.; Yu, Z.; Yu, P.; Xu, K.; Lau, S. P.; Zhou, W.; Liu, Z.; Wang, X.; Ji, W.; Chai, Y., High-Electron-Mobility and Air-Stable 2D Layered PtSe<sub>2</sub> FETs. *Adv. Mater.* **2017**, *29*.
- (296) Yao, W.; Wang, E.; Huang, H.; Deng, K.; Yan, M.; Zhang, K.; Miyamoto, K.; Okuda, T.; Li, L.; Wang, Y.; Gao, H.; Liu, C.; Duan, W.; Zhou, S., Direct Observation of Spin-Layer Locking by Local Rashba Effect in Monolayer Semiconducting PtSe<sub>2</sub> Film. *Nat. Commun.* **2017**, *8*, 14216.
- (297) Zhao, Y.; Qiao, J.; Yu, P.; Hu, Z.; Lin, Z.; Lau, S. P.; Liu, Z.; Ji, W.; Chai, Y., Extraordinarily Strong Interlayer Interaction in 2D Layered PtS<sub>2</sub>. *Adv. Mater.* **2016**, *28*, 2399-2407.
- (298) Miró, P.; Ghorbani-Asl, M.; Heine, T., Two Dimensional Materials Beyond MoS<sub>2</sub>: Noble-Transition-Metal Dichalcogenides. *Angew. Chem. Int. Ed.* **2014**, *53*, 3015-3018.
- (299) Yu, X.; Yu, P.; Wu, D.; Singh, B.; Zeng, Q.; Lin, H.; Zhou, W.; Lin, J.; Suenaga, K.; Liu, Z.; Wang, Q. J., Atomically Thin Noble Metal Dichalcogenide: A Broadband Mid-Infrared Semiconductor. *Nat. Commun.* **2018**, *9*, 1545.
- (300) Pi, L.; Li, L.; Liu, K.; Zhang, Q.; Li, H.; Zhai, T., Recent Progress on 2D Noble-Transition-Metal Dichalcogenides. *Adv. Funct. Mater.* *0*, 1904932.
- (301) Wang, Z.; Li, Q.; Besenbacher, F.; Dong, M., Facile Synthesis of Single Crystal PtSe<sub>2</sub>

- Nanosheets for Nanoscale Electronics. *Adv. Mater.* **2016**, *28*, 10224-10229.
- (302) Wang, Z.; Wang, P.; Wang, F.; Ye, J. F.; He, T.; Wu, F.; Peng, M.; Wu, P. S.; Chen, Y. F.; Zhong, F.; Xie, R. Z.; Cui, Z. Z.; Shen, L.; Zhang, Q. H.; Gu, L.; Luo, M.; Wang, Y.; Chen, H. W.; Zhou, P.; Pan, A. L.; Zhou, X. H.; Zhang, L. L.; Hu, W. D., A Noble Metal Dichalcogenide for High-Performance Field-Effect Transistors and Broadband Photodetectors. *Adv. Funct. Mater.* **2020**, *30*, 1907945.
- (303) Wang, Y.; Li, L.; Yao, W.; Song, S.; Sun, J. T.; Pan, J.; Ren, X.; Li, C.; Okunishi, E.; Wang, Y. Q.; Wang, E.; Shao, Y.; Zhang, Y. Y.; Yang, H. T.; Schwier, E. F.; Iwasawa, H.; Shimada, K.; Taniguchi, M.; Cheng, Z.; Zhou, S.; Du, S.; Pennycook, S. J.; Pantelides, S. T.; Gao, H. J., Monolayer PtSe<sub>2</sub>, a New Semiconducting Transition-Metal-Dichalcogenide, Epitaxially Grown by Direct Selenization of Pt. *Nano Lett.* **2015**, *15*, 4013-8.
- (304) Hu, D.; Zhao, T.; Ping, X.; Zheng, H.; Xing, L.; Liu, X.; Zheng, J.; Sun, L.; Gu, L.; Tao, C.; Wang, D.; Jiao, L., Unveiling the Layer-Dependent Catalytic Activity of PtSe<sub>2</sub> Atomic Crystals for the Hydrogen Evolution Reaction. *Angew. Chem. Int. Ed. Engl.* **2019**, *58*, 6977-6981.
- (305) Boland, C. S.; Coileáin, C. Ó.; Wagner, S.; McManus, J. B.; Cullen, C. P.; Lemme, M. C.; Duesberg, G. S.; McEvoy, N., PtSe<sub>2</sub> Grown Directly on Polymer Foil for Use as a Robust Piezoresistive Sensor. *2D Mater.* **2019**, *6*, 045029.
- (306) Wagner, S.; Yim, C.; McEvoy, N.; Kataria, S.; Yokaribas, V.; Kuc, A.; Pindl, S.; Fritzen, C.-P.; Heine, T.; Duesberg, G. S.; Lemme, M. C., Highly Sensitive Electromechanical Piezoresistive Pressure Sensors Based on Large-Area Layered PtSe<sub>2</sub> Films. *Nano Lett.* **2018**, *18*, 3738-3745.
- (307) Yim, C.; Lee, K.; McEvoy, N.; O'Brien, M.; Riazimehr, S.; Berner, N. C.; Cullen, C. P.; Kotakoski, J.; Meyer, J. C.; Lemme, M. C.; Duesberg, G. S., High-Performance Hybrid Electronic Devices from Layered PtSe<sub>2</sub> Films Grown at Low Temperature. *ACS Nano* **2016**, *10*, 9550-9558.
- (308) Chia, X.; Adriano, A.; Lazar, P.; Sofer, Z.; Luxa, J.; Pumera, M., Layered Platinum Dichalcogenides (PtS<sub>2</sub>, PtSe<sub>2</sub>, and PtTe<sub>2</sub>) Electrocatalysis: Monotonic Dependence on the Chalcogen Size. *Adv. Funct. Mater.* **2016**, *26*, 4306-4318.
- (309) Wang, G.; Wang, Z.; McEvoy, N.; Fan, P.; Blau, W. J., Layered PtSe<sub>2</sub> for Sensing, Photonic, and (Opto-)Electronic Applications. *Adv. Mater.* **2021**, *33*, 2004070.
- (310) Yang, Y.; Li, J.; Choi, S.; Jeon, S.; Cho, J. H.; Lee, B. H.; Lee, S., High-Responsivity PtSe<sub>2</sub> Photodetector Enhanced by Photogating Effect. *Appl. Phys. Lett.* **2021**, *118*, 013103.
- (311) Das, T.; Yang, E.; Seo, J. E.; Kim, J. H.; Park, E.; Kim, M.; Seo, D.; Kwak, J. Y.; Chang, J., Doping-Free All PtSe<sub>2</sub> Transistor via Thickness-Modulated Phase Transition. *ACS Appl. Mater. Interfaces* **2021**, *13*, 1861-1871.
- (312) Yong, X.; Zhang, J.; Ma, X., Effects of Intrinsic Defects on the Photocatalytic Water-Splitting Activities of PtSe<sub>2</sub>. *Int. J. Hydrog. Energy* **2020**, *45*, 8549-8557.
- (313) Avsar, A.; Cheon, C.-Y.; Pizzochero, M.; Tripathi, M.; Ciarrocchi, A.; Yazyev, O. V.; Kis, A., Probing Magnetism in Atomically Thin Semiconducting PtSe<sub>2</sub>. *Nat. Commun.* **2020**, *11*, 4806.
- (314) Chen, J.; Zhou, S.; Wen, Y.; Ryu, G. H.; Allen, C.; Lu, Y.; Kirkland, A. I.; Warner, J. H., *In Situ* High Temperature Atomic Level Dynamics of Large Inversion Domain Formations in Monolayer MoS<sub>2</sub>. *Nanoscale* **2019**, *11*, 1901-1913.
- (315) Chen, J.; Jung, G. S.; Ryu, G. H.; Chang, R.-J.; Zhou, S.; Wen, Y.; Buehler, M. J.; Warner, J. H., Atomically Sharp Dual Grain Boundaries in 2D WS<sub>2</sub> Bilayers. *Small* **2019**, 1902590.
- (316) Dienel, T.; Kawai, S.; Söde, H.; Feng, X.; Müllen, K.; Ruffieux, P.; Fasel, R.; Gröning, O., Resolving Atomic Connectivity in Graphene Nanostructure Junctions. *Nano Lett.* **2015**, *15*, 5185-5190.

- (317) Bennetto, J.; Nunes, R. W.; Vanderbilt, D., Period-Doubled Structure for the 90° Partial Dislocation in Silicon. *Phys. Rev. Lett.* **1997**, *79*, 245-248.
- (318) Zhu, C.; Yu, M.; Zhou, J.; He, Y.; Zeng, Q.; Deng, Y.; Guo, S.; Xu, M.; Shi, J.; Zhou, W.; Sun, L.; Wang, L.; Hu, Z.; Zhang, Z.; Guo, W.; Liu, Z., Strain-Driven Growth of Ultra-Long Two-Dimensional Nano-Channels. *Nat. Commun.* **2020**, *11*, 772.
- (319) Fang, L.; Liang, W.; Feng, Q.; Luo, S.-N., Structural Engineering of Bilayer PtSe<sub>2</sub> Thin Films: A First-Principles Study. *J. Phys.: Condens. Matter* **2019**, *31*, 455001.
- (320) Lee, J. S.; Choi, S. H.; Yun, S. J.; Kim, Y. I.; Boandoh, S.; Park, J.-H.; Shin, B. G.; Ko, H.; Lee, S. H.; Kim, Y.-M.; Lee, Y. H.; Kim, K. K.; Kim, S. M., Wafer-Scale Single-Crystal Hexagonal Boron Nitride Film via Self-Collimated Grain Formation. *Science* **2018**, *362*, 817-821.
- (321) Zhu, X.; Li, F.; Wang, Y.; Qiao, M.; Li, Y., Pd<sub>2</sub>Se<sub>3</sub> Monolayer: A Novel Two-Dimensional Material with Excellent Electronic, Transport, and Optical Properties. *J. Mater. Chem. C* **2018**, *6*, 4494-4500.
- (322) Naghavi, S. S.; He, J.; Xia, Y.; Wolverton, C., Pd<sub>2</sub>Se<sub>3</sub> Monolayer: A Promising Two-Dimensional Thermoelectric Material with Ultralow Lattice Thermal Conductivity and High Power Factor. *Chem. Mater.* **2018**, *30*, 5639-5647.
- (323) Li, X.; Zhang, S.; Guo, Y.; Wang, F. Q.; Wang, Q., Physical Properties and Photovoltaic Application of Semiconducting Pd<sub>2</sub>Se<sub>3</sub> Monolayer. *Nanomaterials* **2018**, *8*, 832.
- (324) Wang, S.; Robertson, A.; Warner, J. H., Atomic Structure of Defects and Dopants in 2D Layered Transition Metal Dichalcogenides. *Chem. Soc. Rev.* **2018**, *47*, 6764-6794.
- (325) Huang, Y. L.; Chen, Y.; Zhang, W.; Quek, S. Y.; Chen, C.-H.; Li, L.-J.; Hsu, W.-T.; Chang, W.-H.; Zheng, Y. J.; Chen, W.; Wee, A. T. S., Bandgap Tunability at Single-Layer Molybdenum Disulfide Grain Boundaries. *Nat. Commun.* **2015**, *6*, 6298.
- (326) Huang, P. Y.; Ruiz-Vargas, C. S.; van der Zande, A. M.; Whitney, W. S.; Levendorf, M. P.; Kevek, J. W.; Garg, S.; Alden, J. S.; Hustedt, C. J.; Zhu, Y.; Park, J.; McEuen, P. L.; Muller, D. A., Grains and Grain Boundaries in Single-Layer Graphene Atomic Patchwork Quilts. *Nature* **2011**, *469*, 389-392.
- (327) Kurasch, S.; Kotakoski, J.; Lehtinen, O.; Skákalová, V.; Smet, J.; Krill, C. E.; Krasheninnikov, A. V.; Kaiser, U., Atom-by-Atom Observation of Grain Boundary Migration in Graphene. *Nano Lett.* **2012**, *12*, 3168-3173.
- (328) Li, L.; Reich, S.; Robertson, J., Defect Energies of Graphite: Density-Functional Calculations. *Phys. Rev. B* **2005**, *72*, 184109.
- (329) Kim, J. S.; Kim, J.; Zhao, J.; Kim, S.; Lee, J. H.; Jin, Y.; Choi, H.; Moon, B. H.; Bae, J. J.; Lee, Y. H., Electrical transport properties of polymorphic MoS<sub>2</sub>. *ACS Nano* **2016**, *10*, 7500-7506.
- (330) Rodriguez-Manzo, J. A.; Banhart, F., Creation of Individual Vacancies in Carbon Nanotubes by Using an Electron Beam of 1 Å Diameter. *Nano Lett.* **2009**, *9*, 2285-2289.